

# **Properties and dynamics of excited charge carriers in colloidal nanocrystals studied via optical and terahertz pump-probe spectroscopy**

**Dissertation**

submitted to the Department of Chemistry,  
Faculty of Mathematics, Informatics and Natural Sciences  
of the University of Hamburg

in conformity with the requirements for  
the degree of *Doctor Rerum Naturalium* (Dr. rer. nat.)

by  
**Yannic Uwe Stächelin**  
Hamburg, 2024



*This work was conducted between May 2020 and July 2024 under the supervision of Holger Lange at the Institute of Physical Chemistry, Department of Chemistry, Faculty of Mathematics, Informatics and Natural Sciences, University of Hamburg.*

1<sup>st</sup> Reviewer: Prof. Dr. Holger Lange  
2<sup>nd</sup> Reviewer: Prof. Dr. Gabriel Bester  
3<sup>rd</sup> Reviewer: Prof. Dr. Matias Bargheer

Oral defense committee:  
Prof. Dr. Markus Gühr  
Prof. Dr. Dorota Koziej  
Prof. Dr. Holger Lange

Date of submission: 26.07.2024  
Date of oral defense: 18.10.2024  
Date of print release: 29.10.2024



# List of publications

- Yannic U. Staechelin, Dominik Hoening, Florian Schulz and Holger Lange. Size-dependent Electron-Phonon Coupling in Monocrystalline Gold Nanoparticles. *ACS Photonics* **2021**, 8, 752-757.
- Yannic U. Staechelin, Michael Deffner, Sonja Krohn, Christian Castillo Delgadillo, Jan Steffen Niehaus and Holger Lange. Carrier localization in zero-dimensional and one-dimensional CdSe-CdS heterostructures. *The Journal of Chemical Physics* **2022**, 156, 061102.
- Jannik Rebmann, Hans Werners, Florian Johst, Marcel Dohrmann, Yannic U. Staechelin, Christian Strelow, Alf Mews and Tobias Kipp. Cation Exchange during the Synthesis of Colloidal Type-II ZnSe-Dot/CdS-Rod Nanocrystals. *Chemistry of Materials* **2023**, 35, 1238-1248.
- Yannic U. Staechelin, Tobias Kroh, Franz X. Kärtner and Holger Lange. Impact of Pump Beam Spot Size on Semiconductor Carrier Dynamics in Optical-Pump-Terahertz-Probe Spectroscopy. *Journal of the Optical Society of America B* **2023**, 40 (8), 2058-2063.
- Soenke Wengler-Rust, Yannic U. Staechelin, Holger Lange and Horst Weller. Electron Donor-Specific Surface Interactions Promote the Photocatalytic Activity of Metal-Semiconductor Nanohybrids. *Small*, **2024**, 20, 2401388
- Shivani Kesarwani, Sabrina Juergensen, Yannic U. Staechelin, Stephanie Reich, Florian Schulz and Holger Lange. Incorporation strategy for organic dyes into gold nanoparticle superlattices. *The Journal of Chemical Physics* **2024**, 161, 044702.
- Jose de Jesus Velazquez-Garcia, Krishnayan Basuroy, Joanne Wong, Serhiy Demeshko, Franc Meyer, Insik Kim, Robert Henning, Yannic U. Staechelin, Holger Lange and Simone Techert. Out-of-Equilibrium Dynamics of a Grid-Like Fe(II) Spin Crossover Dimer Triggered by Two-Photon Excitation. *Chemical Science* **2024**, 15, 13531-13540.



# Abstract

Colloidal nanocrystals are extensively studied for their unique, size-dependent optical and electronic properties, enabling possible applications in photocatalysis, solar cells or light-emitting devices as well as providing a platform for studying fundamental physical phenomena such as light-matter coupling or superfluorescence. The optical properties of metal nanoparticles are dictated by the localized surface plasmon resonance, a collective vibration of the conduction band electrons, that falls into the optical frequency region for gold. Research on gold nanoparticles focuses on the utilization of highly excited electrons that are generated during the dephasing of the plasmon oscillation. Semiconducting nanocrystals have recently attracted the attention of a wider public, since the Nobel Prize in Chemistry in 2023 was devoted to research on their size-tunable band gap. Material parameters such as size, shape and composition have a significant effect on the optical and electronic properties of excited charge carriers. Therefore, with smart design, multi-component nanocrystals can be tailored for specific functions, such as efficient charge separation for photocatalytic applications or efficient charge recombination for light-emitting devices. Ultrafast lasers allow to study the properties and dynamics of optically excited charge carriers *via* various pump-probe spectroscopic methods and hence help to make smart design choices for optimizing nanocrystals towards the various applications. This thesis aims to contribute to the understanding of how the nanocrystal's material parameters like size, shape, crystallinity or surface chemistry alter the dynamics of optically excited carriers. To do so, both metal and semiconductor nanocrystals as well as hybrid nanostructures that combine the properties of multiple components were studied *via* optical-pump-optical-probe (transient absorption) and optical-pump-terahertz-probe spectroscopy.

Employing transient absorption spectroscopy, it could be shown that in gold nanoparticles, the electron-phonon coupling constant is a size-dependent quantity. However, the size dependency can only be observed in monocrystalline particles, as in polycrystalline particles, it is blurred due to efficient electron-surface scattering at internal grain boundaries. In a second study, it has been shown that in order to enable strong optical interaction of gold nanoparticles with dyes, carefully designing the dye and applying it to the nanoparticle's surface is crucial.

In a project focusing on semiconductor nanocrystals, the charge carrier localization in spherical and elongated CdSe-CdS core-shell nanocrystals was compared. Employing a combination of transient absorption and optical-pump-terahertz-probe spectroscopy, it could be shown that shell-excited carriers are mobile in elongated particles for hundreds of picoseconds, whereas they quickly form bound electron-hole pairs in spherical particles. Furthermore, hybrid semiconductor-metal nanoparticles were studied for their photocatalytic hydrogen generation, whereby it was shown that ionic electron donating agents scavenge holes from the photocatalyst faster than alcoholic ones due to their enhanced surface activity, thereby enabling fast charge carrier dynamics and efficient hydrogen generation.

Finally, in a technical study on optical-pump-terahertz-probe spectroscopy, spectral distortions in the acquired data caused by too small pump beam spot sizes were discussed. A plain model was set up to account for such distortions and different experimental implementations were compared.





# Zusammenfassung

Kolloidale Nanokristalle werden aufgrund ihrer einzigartigen, größenabhängigen optischen und elektronischen Eigenschaften intensiv erforscht. Mögliche Anwendungsfelder sind die Photokatalyse, Solarzellen oder Licht-emittierende Bauteile. Außerdem können mittels kolloidaler Nanokristalle fundamentale physikalische Phänomene wie die Wechselwirkung von Licht und Materie oder Superfluoreszenz studiert werden. Die optischen Eigenschaften von Metall-Nanokristallen werden von der lokalisierten Oberflächenplasmonenresonanz, einer kollektiven Schwingung der Leitungsbandelektronen, die im Falle von Gold in den optischen Frequenzbereich fällt, bestimmt. Forschung an Goldnanopartikeln konzentriert sich auf die Nutzung hochangeregter Elektronen, welche durch die Dephasierung der Plasmonenschwingung erzeugt werden. Halbleitenden Nanokristalle haben neulich die Aufmerksamkeit einer breiteren Öffentlichkeit auf sich gezogen, da der Nobelpreis für Chemie im Jahre 2023 der Erforschung ihrer größenabhängigen Bandlücke gewidmet wurde. Größe, Form und Zusammensetzung der Nanokristalle beeinflussen die optischen und elektronischen Eigenschaften angeregter Ladungsträger stark, wodurch hybride Nanokristalle, die aus mehreren Materialien bestehen, durch geschicktes Design für spezifische Anwendungen optimiert werden können. Ultrakurze Laserpulse ermöglichen die Erforschung der Eigenschaften und Dynamik von optisch angeregten Ladungsträgern mittels verschiedener Anregungs-Abfrage-Techniken (engl. *pump-probe*). Diese Disseration versucht, zum Verständnis des Einflusses der Materialparameter auf die Dynamik optisch angeregter Ladungsträger in kolloidalen Nanokristallen beizutragen. Metallische, halbleitende sowie hybride Nanopartikel wurden mittels optischer *pump-probe* Experimente (Transiente Absorptionsspektroskopie) sowie Experimente mit Abfrage im Terahertz-Spektralbereich studiert.

Mittels Transienter Absorptionsspektroskopie konnte gezeigt werden, dass die Elektron-Phonon-Kopplung in Goldnanopartikeln größenabhängig ist. Dies wird allerdings nur in monokristalline Partikeln beobachtet. In polykristallinen Partikeln sorgen innere Oberflächen und Korngrenzen für effektive Elektron-Oberflächen-Streuung und überdecken dadurch die Größenabhängigkeit der Elektron-Phonon Kopplung. Eine zweite Studie an Goldnanopartikeln zeigt, dass starke optische Wechselwirkungen zwischen den Nanopartikeln und einem Farbstoff erzeugt werden können, wenn der Farbstoff gezielt auf der Partikeloberfläche angebracht wird.

In einem weiteren Projekt wurde die Lokalisierung der Ladungsträger in sphärischen und elongierten CdSe-CdS Kern-Schale Nanokristallen untersucht. Eine Kombination aus *pump-probe* Experimenten mit optischer und Terahertz-Abfrage wurde genutzt um zu zeigen, dass Ladungsträger, die in der Schale erzeugt werden, in elongierten Nanokristallen mehrere hundert Pikosekunden lang mobil sind, wobei in sphärischen Nanokristallen innerhalb weniger Pikosekunden gebundene Elektron-Loch-Paare gebildet werden. Außerdem wurden hybride Metal-Halbleiter-Partikel auf deren photokatalytische Eigenschaften untersucht. Es konnte gezeigt werden, dass ionische Elektronendonatoren aufgrund ihrer Oberflächenaktivität Löcher schneller aus den Partikeln entfernen als alkoholische Elektronendonatoren, wodurch schnellere Ladungsträgerdynamik und effektivere Wasserstoff-Produktion ermöglicht wird.

In einer technischen Studie über *pump-probe* Experimente mit optischer Anregung und Abfrage im Terahertz-Spektralbereich wurden spektrale Verzerrungen in den gemessenen Daten diskutiert, die durch zu kleine Strahlprofile der Anregungspulse entstehen. Ein einfaches Modell wurde vorgestellt, mit dem diese Verzerrungen korrigiert werden können.



# Contents

<b>List of publications</b>	<b>i</b>
<b>Abstract</b>	<b>iii</b>
<b>Zusammenfassung</b>	<b>v</b>
<b>1 Introduction</b>	<b>1</b>
<b>2 Pump-probe spectroscopy with ultrafast laser pulses</b>	<b>5</b>
2.1 Ultrafast lasers . . . . .	5
2.2 Transient absorption spectroscopy . . . . .	8
2.3 Terahertz spectroscopy . . . . .	12
2.3.1 Terahertz time-domain spectroscopy . . . . .	12
2.3.2 Optical-pump-terahertz-probe spectroscopy . . . . .	16
2.3.3 Physical models of terahertz conductivity . . . . .	19
2.3.4 Terahertz-pump-optical-probe spectroscopy . . . . .	22
<b>3 Hot electron dynamics in gold nanoparticles</b>	<b>23</b>
3.1 Optical properties of bulk metals . . . . .	23
3.2 Localized surface plasmon resonance in gold nanoparticles . . . . .	25
3.3 Hot electron dynamics . . . . .	29
3.3.1 Transient absorption experiments on gold nanoparticles . . . . .	29
3.3.2 Plasmon dephasing and hot electron generation . . . . .	31
3.3.3 Electron-electron scattering . . . . .	32
3.3.4 Electron-phonon scattering . . . . .	33
3.3.5 Phonon coupling to the environment . . . . .	36
<b>4 Charge carrier dynamics in semiconductor nanocrystals</b>	<b>37</b>
4.1 Optical properties of bulk and nanoscale semiconductors . . . . .	37
4.2 Different types of colloidal semiconductor nanocrystals . . . . .	39
4.3 Charge carrier dynamics . . . . .	42
4.3.1 Transient absorption experiments on semiconductor nanocrystals . . . . .	42
4.3.2 Relaxation processes . . . . .	45
4.3.3 Optical-pump-terahertz-probe experiments on semiconductor nanocrystals	51
<b>5 Synopsis</b>	<b>55</b>
5.1 Motivation . . . . .	55
5.2 Size-dependent electron-phonon coupling in monocrystalline gold nanoparticles .	56
5.3 Carrier localization in zero-dimensional and one-dimensional CdSe-CdS hetero- structures . . . . .	64

5.4	Impact of pump beam spot size on semiconductor carrier dynamics in optical-pump-terahertz-probe spectroscopy . . . . .	74
5.5	Cation exchange during the synthesis of colloidal type-II ZnSe-dot/CdS-rod nanocrystals . . . . .	84
5.6	Electron donor-specific surface interactions promote the photocatalytic activity of metal-semiconductor nanohybrids . . . . .	96
5.7	Incorporation strategy for organic dyes into gold nanoparticle superlattices . . . . .	108
<b>6</b>	<b>Unpublished results</b>	<b>119</b>
6.1	Terahertz-induced Stark effect in CdSe nanoplatelets . . . . .	119
6.2	Collective properties of giant-shell quantum dots . . . . .	126
<b>7</b>	<b>Summary</b>	<b>135</b>
	<b>References</b>	<b>139</b>
<b>A</b>	<b>Appendix</b>	<b>157</b>
A.1	Technical aspects of transient absorption spectroscopy . . . . .	157
A.2	Supporting information for Chapter 5.2 . . . . .	162
A.3	Supporting information for Chapter 5.4 . . . . .	176
A.4	Supporting information for Chapter 5.6 . . . . .	182
A.5	Supporting information for Chapter 5.7 . . . . .	196
A.6	Supporting information for Chapter 6.2 . . . . .	204
A.7	List of chemicals . . . . .	206
A.8	List of abbreviations . . . . .	217
A.9	List of Figures . . . . .	218
	<b>Acknowledgements</b>	<b>221</b>

# 1. Introduction

Colloidal nanocrystal (NC) science is an ever expanding field located at the interface of chemistry, physics and material science. Many decades of intense research have produced sophisticated, wet-chemical synthesis routes that allow to produce a plethora of colloidal NCs of different shapes and compositions.<sup>1</sup> The huge interest in these materials is due to their structural versatility as well as their unique optical properties. Although the physical phenomena at work are fundamentally different, both semiconductor and metal NCs exhibit size-dependent optical properties that differ significantly from their bulk counterparts, making them interesting candidates for a variety of applications.

As the use of solar energy becomes increasingly more important in nowadays technologies, a huge body of research is dedicated to the application of NCs in photovoltaics and photocatalysis.<sup>2-6</sup> NCs interacting with the entire solar spectrum can nowadays be synthesized with ease.<sup>7-10</sup> Material development for application in solar-energy harvesting requires an in-depth understanding of the behavior of the charge carriers in NCs after the absorption of light. For example in the case of photocatalysis, efficient charge-carrier separation must be achieved by cleverly constructing the nanocatalysts.<sup>11,12</sup>

Their tunable optical properties, narrow linewidths and bright emission make semiconductor NCs interesting for application in light-emitting devices. Especially spherical NCs, also known as quantum dots (QDs), have gained large attention. In displays, QDs can be used as color converters excited by light-emitting diodes (LEDs) or in QD LEDs that are directly driven by an applied bias.<sup>13-15</sup> Also, QDs are promising candidates for solution-processable gain media for lasing applications.<sup>16-18</sup>

Colloidal NCs are also used as platforms to study fundamental optical phenomena. QDs are studied for their potential in quantum light generation, specifically for applications such as superfluorescence<sup>19-21</sup> or as single-photon sources.<sup>22,23</sup> Supercrystals of metal NCs have been used to enter the deep-strong light-matter coupling regime.<sup>24</sup> Hybrid semiconductor-metal structures enable studying exciton-plasmon coupling.<sup>25,26</sup>

## **Pump-probe spectroscopy**

To allow targeted material development for any optical application, it is crucial to understand the behavior of excited charge carriers in the NC of interest. After the absorption of a photon by any material, a cascade of events takes place, until eventually the absorbed energy is dissipated, re-emitted or used in a chemical reaction. Time-resolved pump-probe

experiments are used to study such processes. A short, intense radiation pulse, the so-called pump pulse, transfers the sample of interest into its excited state. The subsequent cascade of events, that eventually leads to the relaxation of the system back to its ground state, is studied using a second radiation pulse, the so-called probe pulse, that travels through the sample a certain delay time after the pump pulse. The probe pulse is recorded after interacting with the sample, both with and without prior excitation of the sample by the pump pulse. From this, pump pulse-induced changes in the sample's interaction with the probe pulse can be recorded. By varying the delay time between pump and probe pulse, the relaxation of the sample can be followed.<sup>27,28</sup> The time resolution of such experiments should be high relative to the duration of the processes of interest and is effectively limited by the pulse duration of both pump and probe pulse.

The first pump-probe experiments were conducted using two rare-gas flash lamps triggered by mechanical shutters. George Porter introduced the concept of flash photolysis in 1950 to study fast chemical reactions with millisecond time resolution<sup>29</sup> and was awarded the Nobel Prize in Chemistry for his invention in 1967.<sup>30</sup> Nowadays, lasers are used to provide both pump and probe pulses. The development of pulsed lasers opened the door towards time-resolved measurement techniques with ever-increasing time resolutions, currently culminating in attosecond time resolution.<sup>31</sup> In 2023, the Nobel Prize in Physics was awarded to Ferenc Krausz, Pierre Agostini and Anne L'Huillier "for experimental methods that generate attosecond pulses of light for the study of electron dynamics in matter".<sup>32</sup>

In this work, optical pump pulses are used to excite charge carriers in the sample of interest in combination with probe pulses covering different ranges of the electromagnetic spectrum. Optical probe pulses allow to investigate the occupation of electronic states, whereas, from experiments with probe pulses in the far-infrared, the so-called terahertz (THz) regime, information about the electrical properties of excited charge carriers can be extracted. If identical excitation conditions in both experiments are carefully assured, optical-pump-optical-probe spectroscopy, also referred to as transient absorption (TA), and optical-pump-terahertz-probe spectroscopy (OPTP) can be used as complementary techniques and deliver directly comparable time traces, allowing to gain information none of the two techniques could deliver on their own.

## Semiconductor nanocrystals

In macroscopic semiconductors, the band gap energy  $E_g$ , which is the energy difference between the valence band and conduction band, is a fixed, material-dependent constant. In direct band gap semiconductors, an electron that was previously excited to the conduction band can relax to the valence band by emission of a photon carrying the energy  $h\nu = E_g$ . However, in nanometer-sized semiconductor crystals consisting of around 100 to 10,000 atoms, electronic states are quantized and the band gap energy is size-dependent. This is due to the so-called quantum confinement effect, *i.e.* the electrons feeling the boundaries of the material. The particle-in-a-box model can well explain the increasing emitted photon energy with decreasing particle size.

In 1981, Aleksei Ekimov demonstrated experimentally that the optical properties of nanoscale CuCl crystals in a glass matrix change with size.<sup>33</sup> Louis Brus *et al.* were the first to demonstrate the quantum size effect in colloidal NCs, as they managed to synthesize 4.5 nm colloidal CdS NCs that grew to 12.5 nm due to Ostwald ripening whilst sitting on the lab bench for a day in 1983.<sup>34</sup> Interest in what became known as QDs grew, but it was not until 1993 when Mounji Bawendi *et al.* published a new synthesis protocol for cadmium chalcogenide NCs, that high-quality colloidal QDs became readily available.<sup>35</sup> In the following years, synthesis protocols were further refined, paving the way toward QDs with ever-increasing optical properties.<sup>1</sup> In 2023, Ekimov, Brus and Bawendi were awarded the Nobel Prize in Chemistry "for the discovery and synthesis of quantum dots".<sup>37</sup>

## Metal nanoparticles

Unlike semiconductors, metals, owing to their partly filled conduction band and the high density of electronic states, exhibit less pronounced quantum size effects in the nanometer size regime. Significant spacing of energy levels is observed at much smaller particle sizes of 100 atoms or less,<sup>38,39</sup> which rather fall into the range of molecular clusters than colloidal NC science. Still, gold nanoparticles<sup>2</sup> (AuNPs) exhibit unique, size-dependent optical properties, which are caused by a surface effect rather than quantum size effects. The so-called localized surface plasmon resonance (LSPR), a collective oscillation of conduction band electrons induced by the interaction with optical light, leads to a strong absorption in the visible part of the electromagnetic spectrum and gives dispersions of AuNPs their characteristic red color. In fact, AuNPs have been used for colouring of glass since ancient times.<sup>41</sup> In the middle of the 19th century, Michael Faraday was the first to relate the red colour of AuNP dispersions to the particle size.<sup>42,43</sup> Gustav Mie was able to theoretically describe the optical properties of small spheres in 1908, a concept that became known as the Mie theory and is still valid today.<sup>44</sup> Dephasing of the LSPR excites few electrons far above the Fermi level.<sup>45,46</sup> These so-called hot electrons are nowadays heavily studied for their use in photocatalysis.<sup>47,48</sup>

## Hybrid colloidal nanocrystals

Hybrid colloidal NCs, also referred to as nanohybrids, consist of several materials within a single particle. The functionalities of the components can be combined to achieve a certain electronic behavior. The combination of several semiconducting materials with differing valence and conduction band energies allows the engineering of the band gap, which can for example be used to separate charge carriers.<sup>49</sup> Metal-semiconductor hybrids can combine the efficient light absorption of semiconductors with the catalytically active surfaces of metals.<sup>50</sup>

---

<sup>1</sup>The reader is referred to the "Scientific Background to the Nobel Prize in Chemistry 2023; Quantum Dots - Seeds of Nanoscience" by the Nobel Committee of Chemistry for a comprehensive read of the historical developments that led to today's research on QDs.<sup>36</sup>

<sup>2</sup>Although colloidal metal nanostructures usually also possess a crystalline lattice, they are often referred to as *nanoparticles*, whereas semiconductor nanostructures are referred to as *nanocrystals*.<sup>40</sup>

**Structure of this thesis**

This thesis aims to contribute to the research field of charge carrier dynamics in colloidal NCs. Chapter 2 discusses the two main experimental techniques employed in this thesis, namely TA and OPTP. Chapter 3 and 4 discuss the basics of the optical properties as well as the current understanding of charge carrier dynamics in metal and semiconductor NCs, respectively. Chapter 5 forms the main part of this thesis, presenting articles that were published in international, peer-reviewed journals and were first- or co-authored by the author of this thesis. Chapter 6 describes some yet unpublished results. Eventually, the thesis is summarized in Chapter 7.



## 2. Pump-probe spectroscopy with ultrafast laser pulses

Extensive literature exists on the generation, properties and manipulation of ultrashort laser pulses.<sup>51–53</sup> Here, a brief summary of the basics necessary to understand the operating principle of the setups employed in this work is given, followed by a description of TA and OPTP. THz spectroscopy is explained in more detail, as it is generally less well known in the colloidal NC community.

### 2.1 Ultrafast lasers

#### Generation and amplification of femtosecond laser pulses

Femtosecond laser systems usually comprise three units. A seed laser provides femtosecond laser pulses with a high repetition rate and low pulse energy. A high-intensity pump laser of longer pulse duration is used to amplify the femtosecond pulses provided by the seed laser. The amplification takes place in a regenerative amplifier *via* so-called chirped-pulse amplification (CPA).

The seed laser generates femtosecond laser pulses by a technique called mode-locking. Lasers exhibit all the resonance frequencies of the laser cavity. By locking these frequencies in phase, the output is not constant with time, but shows a periodic repetition of maxima, resulting from the constructive interference of the different longitudinal cavity modes. In the case of active mode-locking, an acousto-optical modulator is placed inside the cavity to introduce time-dependent losses. These losses are modulated with a sinusoidal function and synchronized to the time of a resonator round-trip. All radiation experiences losses, except the pulses traveling through the modulator at times where losses are minimal. This leads to a concentration of the radiation in the time interval of lowest loss. Using this technique, a pulse duration of 35 fs can be obtained routinely from titanium sapphire oscillators. The repetition rate of these oscillators is given by the inverse of the cavity round-trip time ( $f = c/2L$ , where  $c$  is the speed of light and  $L$  is the cavity length) and is usually in the MHz regime.<sup>54</sup>

For many applications, the pulse energies of lasers with MHz repetition rate are too low. Therefore, CPA is applied. To amplify the seed pulses, they are stretched in time using a grating, effectively lowering the pulse's peak intensity and thereby preventing damage to

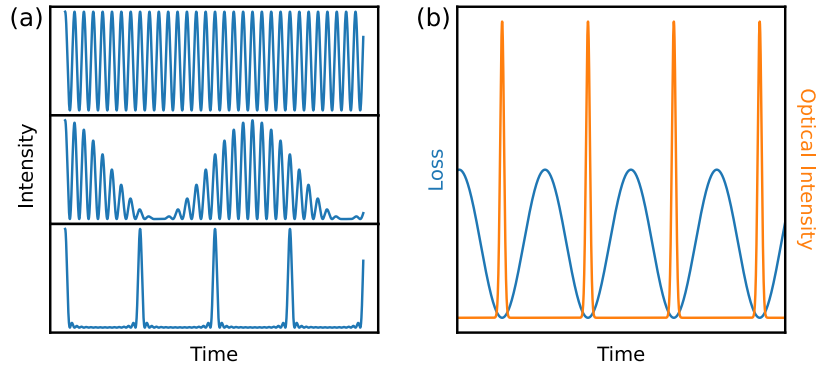


**Figure 2.1:** (a) The emergence of pulsed laser output shown from the mode-locked superposition of laser modes. Upper part: single laser mode. Middle part: two laser modes in phase. Lower part: four laser modes in phase. (b) Schematic presentation of active mode-locking. The optical intensity concentrates in times with minimal loss generated by the acousto-optical modulator.

the medium crystal. A Pockels cell placed at the entrance of the amplification cavity lowers the seed laser pulse rate to the kHz regime. A second, high-intensity laser pumps a gain medium. The seed pulse is spatially overlapped with the pump pulse in the gain medium and is trapped inside the amplification cavity to travel through the amplification medium several times, before being released. A second grating is used to re-compress the amplified pulses, yielding femtosecond laser pulses with exceptionally high pulse energies.<sup>55</sup> In 2018, Donna Strickland and Gérard Mourou were awarded the Nobel Prize in Physics for the development of the CPA technique.<sup>56</sup>

In the setup used in this work, the seed laser was an 800 nm, 35 fs titanium sapphire mode-locked laser with a repetition rate of 84 MHz (*MaiTai*, *Spectra Physics*). The chirped pulse amplifier (*Spitfire Ace-35F*, *Spectra Physics*, pumped by an *Empower 45*, *Spectra Physics*) provided 6 mJ pulses at a repetition rate of 1 kHz, which were split into two beams of 3 mJ each before being compressed by two independent compressors to 35 fs pulse duration.

### Properties of femtosecond laser pulses

The electric field of a laser pulse can be described as an electromagnetic wave with a Gaussian envelope

$$E(t) = E_0 \exp\left(-\frac{t^2}{2\sigma^2}\right) \cos(\omega_0 t + \phi(t)). \quad (2.1)$$

Due to the time-bandwidth product  $\Delta t \Delta \omega \geq \frac{1}{2}$ , short laser pulses are not monochromatic but have a certain spectral bandwidth. The velocity of the plain wave components of the pulse is called phase velocity  $v_{ph}(\omega)$ , whereas the velocity of the envelope is called group velocity  $v_{gr}(\omega_0)$ . When traveling through a dispersive medium, the different spectral components of the pulse travel at different speeds, which leads to a temporal broadening of the pulse. High frequencies are usually slower than low frequencies (*i.e.* the red part of the pulse runs ahead, while the blue part is trailing), which is referred to as positive chirp (or up-chirp). Using gratings or prisms, negative chirp (or down-chirp) can be established (*i.e.* the blue part runs ahead, the red part is trailing).<sup>51</sup>

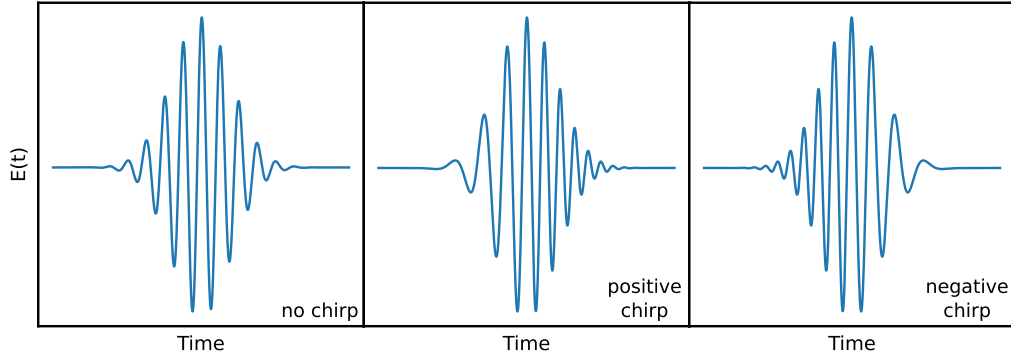


**Figure 2.2:** Schematic time evolution of linearly chirped pulses.

### Manipulation of the wavelength *via* nonlinear processes

CPA-based laser sources are usually limited to a narrow spectral range not suitable for many experiments. Using nonlinear optical processes, a broader spectral range is accessible, allowing to tune both pump and probe beams to the desired wavelength. In linear optics, the induced electric polarization  $P$  of a material depends linearly on the applied electric field  $E$

$$P = \chi_E E, \quad (2.2)$$

where  $\chi_E$  is the electric susceptibility. In nonlinear optical media and at high electric field strength generated by high power laser pulses, this relationship is no longer linear

$$P = (\chi_1 + \chi_2 E + \chi_3 E^2 + \dots)E. \quad (2.3)$$

The optical electric field of a laser beam can be described as

$$E = E_0 \cos(\omega t). \quad (2.4)$$

When two optical electric fields  $E_1$  and  $E_2$  with frequencies  $\omega_1$  and  $\omega_2$  are impinging onto the nonlinear medium, the second-order nonlinear polarization can be written as<sup>57</sup>

$$P_2 = \chi_2 E_1 E_2 \quad (2.5)$$

$$P_2 = \chi_2 \frac{E_1 E_2}{2} ((1 + \cos(2\omega_1 t)) + (1 + \cos(2\omega_2 t)) + \cos(\omega_1 - \omega_2)t + \cos(\omega_1 + \omega_2)t). \quad (2.6)$$

The first two terms in the bracket ( $2\omega_1$  and  $2\omega_2$ ) in Equation (2.6) describe second harmonic generation (SHG) of  $E_1$  and  $E_2$ , respectively, a process in which two photons of equal frequency turn into a single photon of doubled frequency inside a nonlinear medium. The intensity with which the second harmonic is generated  $I_{2\omega}$  can be described as<sup>51</sup>

$$I_{2\omega} = \frac{2^7 \pi^3 \omega^2 \chi^2 l^2}{n^3 c^2} I_\omega^2 \left( \frac{\sin(\Delta k l / 2)}{\Delta k l / 2} \right)^2, \quad (2.7)$$

where  $\omega$  is the frequency of the incoming photon,  $I_\omega$  is the intensity of the incoming beam,  $\chi^2$  is the second-order nonlinear susceptibility,  $l$  is the length of the material,  $n$  is the index of refraction and  $c$  is the speed of light. The dephasing quantity  $\Delta k$  is defined as the difference of the wave vectors of the fundamental beam  $k_1$  and its second harmonic  $k_2$ ,  $\Delta k = k_2 - 2k_1$ . The fundamental generates its second harmonic at any point along the propagation axis. If the phases of two photons of the second harmonic generated at different points along the propagation axis do not match, they interfere destructively. Therefore, to ensure constructive interference, *i.e.* efficient second harmonic generation, phase matching must be ensured ( $\Delta k$  close to zero). Birefringent crystals are used for this purpose, as they exhibit identical refractive indices for fundamental and second harmonic at a certain angle, the so-called phase matching angle (*i.e.*  $\Delta k = 0$ ).<sup>51</sup>

As described by the third and fourth term in Equation (2.6), both the difference and the sum of the incoming frequencies can be generated ( $\omega_1 - \omega_2$ : difference frequency generation (DFG).  $\omega_1 + \omega_2$ : sum frequency generation (SFG)). In optical parametric amplification, a weak pulse  $\omega_1$  (*signal*) is intensified at the expense of a stronger pump pulse  $\omega_2$ . Energy conservation requires the creation of a third frequency  $\omega_3 = \omega_2 - \omega_1$  (*idler*).<sup>57</sup>

In this work, an optical parametric amplifier (OPA) (*TOPAS Prime, Light Conversion*) was used to tune the pump photon wavelength across the visible spectrum. SHG is used to generate 400 nm pump photons in a  $\beta$ -barium borate (BBO) crystal from the laser fundamental of 800 nm.

Spectrally broad continua can be generated from short laser pulses *via* self-phase modulation (SPM), a third-order nonlinear optical effect.<sup>51,58</sup> It is used in OPAs for the generation of the weak pulse  $\omega_1$  and in TA to generate white-light probe pulses.

Combining these non-linear effects provides great control over the wavelengths of laser pulses generated from a single source, enabling versatile pump and probe pulses for time-resolved experiments.

## 2.2 Transient absorption spectroscopy

The term transient absorption spectroscopy is usually used for optical-pump-optical-probe experiments driven by femtosecond lasers. The laser beam is split into two parts, a high-intensity pump pulse and a weak probe pulse. The wavelength of the pump pulse is usually tuned to match the absorption spectrum of the sample of interest by either OPA or SHG. The weak probe pulse travels over a mechanical delay stage to set the pump-probe delay time and is then focused into a transparent medium to generate a spectrally broad continuum to be able to probe the entire optical spectrum at once using a spectrometer. A chopper is used to block every other pump pulse, whereby the absorption of the sample is always measured alternately with and without optical excitation. Figure 2.3 schematically shows the employed TA setup.

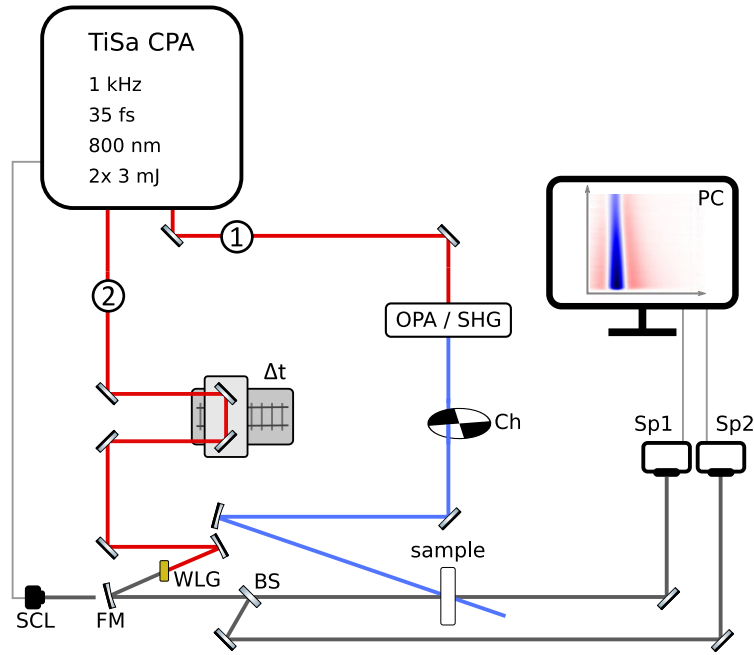


**Figure 2.3:** Schematic of the TA setup used in this thesis. 1: pump beam path, 2: probe beam path, TiSa CPA: titanium sapphire chirped-pulse amplifier, Ch: chopper, WLG: white-light generation crystal, SCL: supercontinuum laser, FM: flipped mirror, BS: beamsplitter, Sp1: main spectrometer, Sp2: reference spectrometer, PC: computer for data acquisition. The supercontinuum laser is used for long delay time TA measurements and is electronically connected to the femtosecond laser source to set the time delay between the femtosecond pump and the supercontinuum probe pulse.

In TA, the measured quantity  $\Delta A$  is the difference of the sample's absorption in its excited and ground state <sup>1</sup>

$$\Delta A = A_{exc} - A_{gr}. \quad (2.8)$$

The absorption  $A$  can be calculated *via* the Beer-Lambert law

$$A = \log_{10} \left( \frac{I_0}{I} \right), \quad (2.9)$$

where  $I_0$  and  $I$  are the spectral intensities of the incoming white-light beam and the beam transmitted through the sample, respectively. Inserting Equation (2.9) into Equation (2.8), it becomes obvious that  $I_0$  can be canceled from the equation, given that the spectral intensity of the incoming probe beam is stable.

$$\Delta A = \log_{10} \left( \frac{I_0}{I_{exc}} \right) - \log_{10} \left( \frac{I_0}{I_{gr}} \right) = \log_{10} \left( \frac{I_{gr}}{I_{exc}} \right) \quad (2.10)$$

As the white-light probe pulse is generated from nonlinear processes, the obtained spectra are highly dependent on the incoming pulse energy. Small fluctuations in the laser output

<sup>1</sup>Note that sometimes the transient difference transmission  $\Delta T/T$  is used, which is opposite in sign compared to  $\Delta A$ .

energy can therefore lead to considerable fluctuations in the white-light spectral intensity, giving the main source of noise in the experiment. Some TA setups are thus equipped with a second spectrometer, which acts as a reference channel for the probe pulse, measuring the fluctuations in the white-light spectrum. In this case,  $\Delta A$  is calculated from

$$\Delta A = \log_{10} \left( \frac{I_{gr}}{I_{exc}} \cdot \frac{I_{gr,ref}}{I_{exc,ref}} \right). \quad (2.11)$$

Figure 2.4 exemplarily shows TA data of CdSe-CdS QDs. The mechanisms leading to contrast in TA experiments of such QDs are discussed in Chapter 4.3.1.

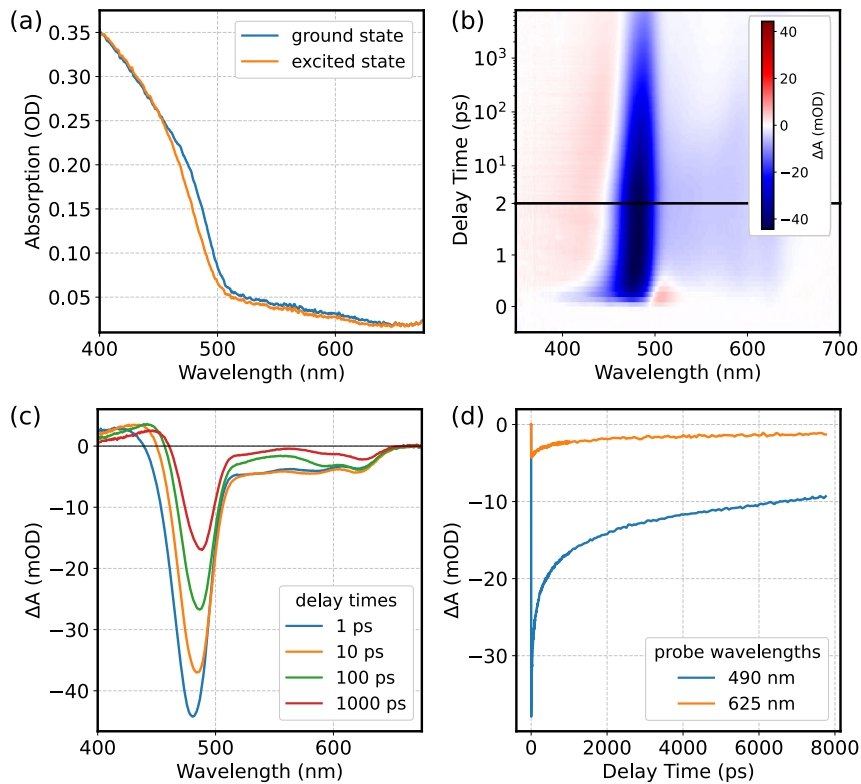


**Figure 2.4:** Exemplary TA data of CdSe-CdS QDs. (a) Absorption in the ground and excited state. (b) TA map. (c) Differential spectra at certain delay times. (d) Time traces at certain probe wavelengths.

### Long-delay time transient absorption spectroscopy

As the delay between pump and probe pulse is set using a computer-controlled mechanical delay stage in TA, the maximum achievable delay time is usually a few nanoseconds, practically limited by the length of the delay stage. To achieve longer delay times, electronically triggered supercontinuum lasers can be used as a probe source. The upper delay time limit is then determined only by the pump laser repetition rate. Here, TA experiments with SPM-generated probe pulses are referred to as fs-TA (to stress the shortest delays accessible), while measurements with a supercontinuum laser probe pulse are referred to as  $\mu$ s-TA (to stress the longest delays accessible). If there is an overlap between the longest delay times accessible

by the fs-TA experiment and the shortest delay times of the  $\mu\text{s}$ -TA experiment, a sample can be studied with the same pump conditions in both configurations and the data can be overlaid. This is exemplarily shown for measurements taken on CdSe-CdS QDs in Figure 2.5.

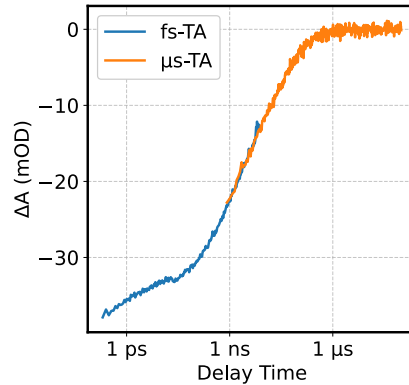


**Figure 2.5:** TA dynamics of CdSe-CdS QDs probed at the main bleach feature with both fs-TA and  $\mu\text{s}$ -TA. The x-axis is plotted with a logarithmic scale to better visualize the timescales. The two data sets overlap in the single-digit nanosecond regime. The rise of both measurements is cropped for better visualization.

In the studies presented in this thesis, a commercial fs-TA setup was used (*HELIOS, Ultrafast Systems*) in combination with a commercial supercontinuum probe laser (*EOS, Ultrafast Systems*). The time resolution of the fs-TA is on the order of 100 fs (*cf.* Chapter A.1). The longest delay time achievable with the femtosecond probe is around 7.5 ns. The shortest delay time accessible with the supercontinuum probe is around 1 ns, and the longest (limited by the 1 kHz repetition rate of the fs-laser) is 400  $\mu\text{s}$ . Hence, more than nine orders of magnitude are covered by combining the two probe sources.

## 2.3 Terahertz spectroscopy

THz radiation covers the part of the electromagnetic spectrum between the electronically accessible microwaves and the optically accessible infrared radiation. It is usually defined to range from 0.1 THz (which corresponds to a photon energy of 0.41 meV and a wavelength of 3 mm) to several tens of THz (10 THz correspond to 41 meV and 30  $\mu\text{m}$ , respectively). Not being well accessible by both standard electronic and optical means, THz radiation has been challenging to work with for a long time. In recent years, great efforts have been made to research both THz sources and detectors, seeking to close what is known as the "THz gap". With femtosecond laser sources being increasingly available to researchers, spectroscopy in the THz spectral region gained growing attention. Nowadays, THz spectroscopy is widely used to study energetic transitions in the meV range as well as (photo)conductivity of various materials.<sup>59,60</sup> THz time-domain spectroscopy (THz-TDS) relies on the coherent generation and detection of THz radiation. THz-TDS differs from most other spectroscopic methods in that it does not measure the intensity of light in the frequency domain but rather the electric field of light in the time domain. By Fourier transformation, the time domain data can be transferred into the frequency domain to give the complex conductivity of a sample.<sup>61</sup> Experiments in a pump-probe fashion, such as OPTP spectroscopy, allow to study the photoinduced conductivity as well as relaxation times of photoexcited charge carriers with sub-picosecond time resolution.<sup>62</sup>

### 2.3.1 Terahertz time-domain spectroscopy

#### Terahertz generation by optical rectification

Optical rectification is a widespread method to generate THz radiation from femtosecond near-infrared (NIR) laser pulses using crystals with nonlinear optical properties. As it is a second-order non-linear effect, it can be described by Equation (2.6). In the case when  $\omega_1 = \omega_2$ , both second harmonic and a direct current (DC) polarization are generated. As the optical field of the NIR pulse has a time dependence, the DC polarization is also time-dependent and resembles the envelope of the NIR pulse rather than an actual constant DC level. This change in polarization is effectively a current generating THz radiation.<sup>63</sup> The bandwidth of the generated THz pulse depends on the bandwidth of the femtosecond laser pulse, the phase matching between the femtosecond pulse and the generated THz pulse as well as optical phonon resonances of the employed nonlinear material. Generally, thicker crystals lead to higher THz intensities, but narrower THz spectra due to destructive interference of the high THz frequencies.<sup>64</sup> In this work, ZnTe crystals were used for THz generation, providing THz pulses that cover a frequency range of roughly 0.1 to 2 THz.

#### Terahertz detection by electro-optical sampling

THz pulses can be detected using electro-optical sampling (EOS), which is the inverse process of optical rectification. To do so, the THz pulse is focused onto a nonlinear crystal, where it is spatially and temporarily overlaid with a femtosecond optical sampling pulse. The electric field of the THz pulse induces a birefringence to the crystal, *i.e.* the crystal



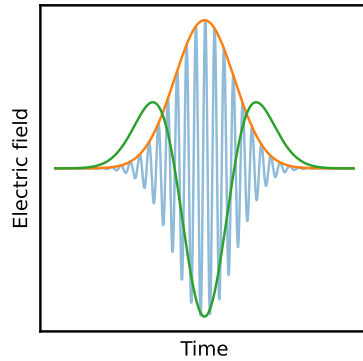


**Figure 2.6:** Optical rectification: Electric field of the incoming femtosecond pulse (blue), the induced polarization (envelope of the femtosecond pulse, orange), electric field of the emitted THz pulse (green).

has different refractive indices along the different crystal axes. This effectively changes the polarization of the passing femtosecond sampling pulse from linear polarization to elliptical polarization. The change in polarization of the femtosecond sampling pulse is measured as depicted in Figure 2.7. A quarter-wave plate changes the polarization from linear to circular. The beam is then split into two linearly polarized beams with perpendicular polarization using a Wollaston prism. The change in polarization is measured by a pair of balanced photodiodes with a lock-in amplifier set to the frequency of a chopper that blocks every other THz pulse.<sup>61</sup>

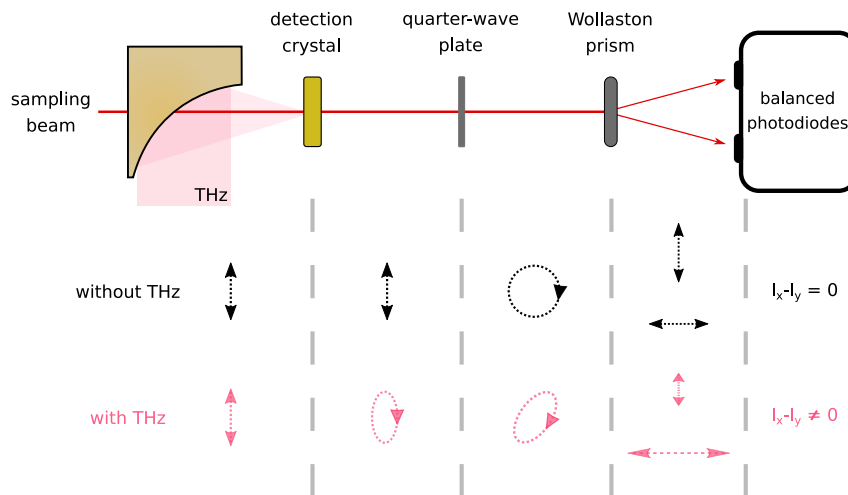


**Figure 2.7:** Schematic representation of an EOS-setup. The dotted arrows depict the polarisation of the sampling beam at each respective stage of the setup. Adapted with permission from Peiponen.<sup>63</sup>

To reconstruct the THz electric field in the time domain, the change in polarization is measured at different time delays between the short femtosecond sampling pulse and the picosecond THz pulse using a mechanical delay stage, as illustrated in Figure 2.8. The measured signal  $S(\tau)$  is a convolution of the THz pulses electric field  $E_{THz}(\tau)$  and the

femtosecond sampling pulse  $E_{\text{sampling}}(\tau)$ . If the pulse duration of the sampling pulse is much shorter than the pulse duration of the THz pulse, the sampling pulse can be regarded as a delta function and the measured signal  $S(\tau)$  is directly proportional to the THz electric field  $E_{\text{THz}}(\tau)$ .<sup>60</sup>

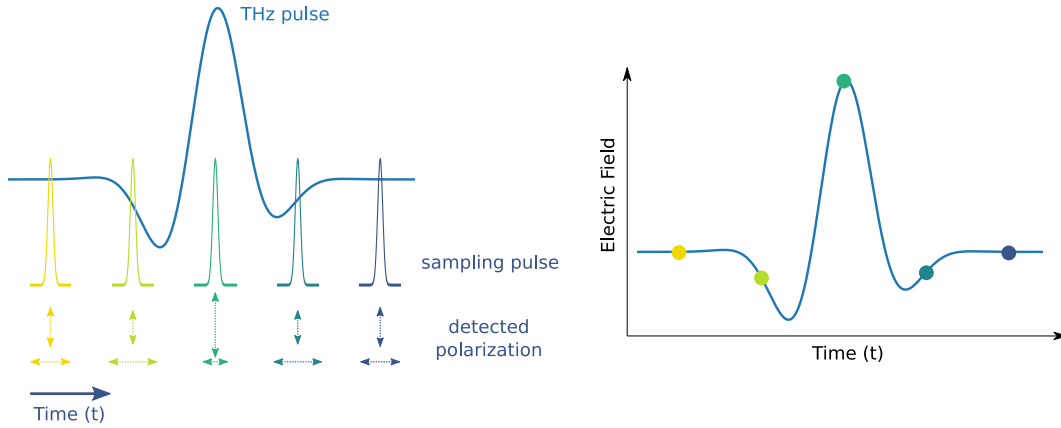


**Figure 2.8:** Reconstruction of the electric field of a THz pulse using EOS. The sampling pulse is shifted in time relative to the THz pulse to detect the THz pulse’s electric field in the time domain. If the sampling pulse duration is much shorter than the picosecond THz pulse duration, the measured changes in polarization are directly proportional to the electric field.

### The setup

In a THz-TDS setup, a femtosecond laser pulse is split into two parts of unequal intensity. The high-intensity beam is used for THz generation *via* optical rectification. The THz beam is collimated by a first off-axis parabolic mirror (OAP) and then focused onto the sample by a second OAP. A third OAP collimates the THz beam again before it is focused onto the detection crystal by a fourth OAP. The weaker part of the femtosecond laser beam acts as a sampling pulse and is therefore temporarily and spatially overlaid with the THz beam in the detection crystal to reconstruct the electric field of the THz pulse using EOS. The high-intensity beam travels over a computer-controlled mechanical delay stage to set the time delay between THz and sampling pulse and through a chopper operating at half the laser repetition rate.<sup>65</sup>

### Fourier transformation to the frequency domain and data analysis

The time-dependent electric fields  $E(t)$  measured by THz-TDS can be converted to THz spectra  $\tilde{E}(\omega)$  by a Fourier transformation  $\mathcal{F}$  (and *vice versa*).<sup>59</sup> Herein lies the advantage of measuring the electric field over most other spectroscopic methods that measure intensities: The Fourier transformation yields both amplitude and phase of each frequency component.<sup>2</sup>

<sup>2</sup>Note that the sign of the exponent in Equation (2.12) and (2.13) is chosen by convention and could also be swapped. In literature, both definitions are common.

$$\tilde{E}(\omega) = \frac{1}{2\pi} \int_{-\infty}^{\infty} E(t) e^{-i\omega t} dt \quad (2.12)$$

$$E(t) = \int_{-\infty}^{\infty} \tilde{E}(\omega) e^{i\omega t} d\omega \quad (2.13)$$

To obtain information about the complex conductivity, the permittivity or the refractive index of a sample, the electric field of the THz pulse propagating through the sample and free space (or an empty reference substrate) are measured. Both are converted to a spectrum

$$E_{ref}(t) \xrightarrow{\mathcal{F}} S_{ref}(\omega), \quad (2.14)$$

$$E_{sample}(t) \xrightarrow{\mathcal{F}} S_{sample}(\omega). \quad (2.15)$$

The transfer function  $H(\omega)$  of the sample is defined as the relation of those two spectra.<sup>63</sup> It describes the effect of the sample on the electric THz field.<sup>3</sup>

$$H(\omega) = \frac{S_{sample}(\omega)}{S_{ref}(\omega)} \quad (2.16)$$

By comparing this experimentally determined transfer function to a theoretical transfer function, the complex refractive index of the sample can be obtained. The derivation of the theoretical transfer function for the simplest case of a single-layer system is shown here exemplarily. After passing through air, the incoming beam  $S_{in}$  is transmitted through the interface between air and the sample. The beam travels through the sample of thickness  $d$ , where absorption and dispersion of the beam might occur, and passes the interface between the sample and air. This leads to

$$S_{sample} = P_0 T_{0,1} P_{1,d} T_{1,0} P_0 S_{in}, \quad (2.17)$$

where  $P$  and  $T$  describe absorption and transmission, 0 denotes air and 1 denotes the sample. The reference measurement (*i.e.* without sample) can be described as

$$S_{ref} = P_0 P_{0,d} P_0 S_{in}. \quad (2.18)$$

The theoretical transfer function can thus be written as

$$H = \frac{S_{sample}}{S_{ref}} = \frac{T_{0,1} P_{1,d} T_{1,0}}{P_{0,d}}. \quad (2.19)$$

Transmission  $T$  (and reflection  $R$ ) can be described using the Fresnel equations, which give

$$T_{a,b} = \frac{2n_b}{n_a + n_b} \quad (2.20)$$

in the case of plane waves at normal incident at the sample, where  $n$  is the refractive index of the respective material  $a$  or  $b$ .<sup>67</sup> Absorption  $P$  can be described as<sup>68</sup>

$$P_{a,d} = \exp\left(-\frac{in_a \omega d}{c}\right), \quad (2.21)$$

---

<sup>3</sup>The concept of transfer functions is borrowed from electrical engineering, where it describes the relation of the input, that is given into a system, and its output.<sup>66</sup>

where  $c$  is the speed of light. If the thickness  $d$  of the sample is precisely known, Equations (2.20) and (2.21) can be inserted into Equation (2.19) to calculate the complex refractive index of the sample from the measured spectra  $S_{sample}$  and  $S_{ref}$ .

Taking single or even multiple reflections into account, the transfer function already gets much more complicated. Numerical approaches as well as approximations have been developed for more complex systems such as thin films on substrates. As the experiments presented in this work focus on OPTP spectroscopy, those are not discussed in detail here. Several reviews have been published that discuss data analysis of THz-TDS in more detail.<sup>60,61,64</sup>

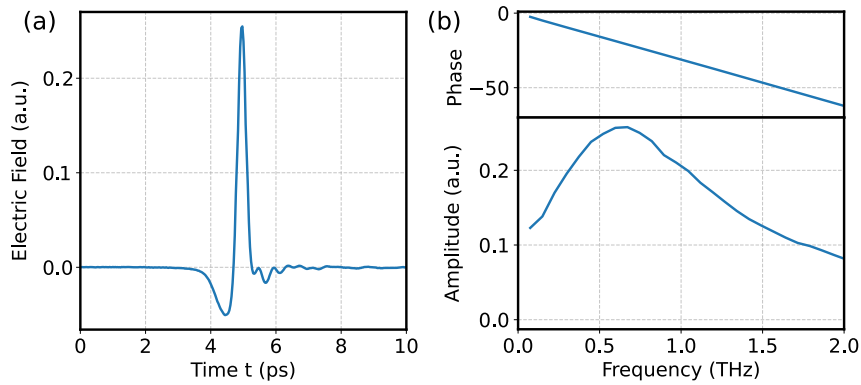


**Figure 2.9:** (a) Exemplary THz-TDS timetrace. (b) Amplitude and phase after Fourier transformation.

### 2.3.2 Optical-pump-terahertz-probe spectroscopy

To study the electrical properties of excited charge carriers, OPTP is used. THz-TDS setups can be extended to OPTP setups by adding an optical pump beam path. In such OPTP experiments, a second delay stage is installed to control the delay between the optical pump and the THz probe beam. The chopper is removed from the THz generation beam path and placed into the optical pump beam path. Therefore, the measured signal  $\Delta T$  is the difference between the electric THz field transmitted through the photoexcited sample ( $T_{on}$ ) and through the unexcited sample ( $T_{off}$ ) and can be used to gain information about the photoconductivity of the sample. Figure 2.10 shows the OPTP setup as used in this work.

#### Data shape and data evaluation

OPTP measures the changes in transmission of a THz pulse through the sample at certain delay times after photoexcitation. This differential transmission of the THz pulse is measured in the time domain. Thus, to measure a complete data set in OPTP both the THz delay  $\Delta t$  as well as the optical-pump delay  $\Delta \tau$  need to be scanned, which usually is very time-consuming. In many cases, only one of the two delays is scanned. So-called THz scans measure the complete differential THz waveform at a fixed optical-pump delay time and allow to calculate the THz photoconductivity at this delay time, but do not provide

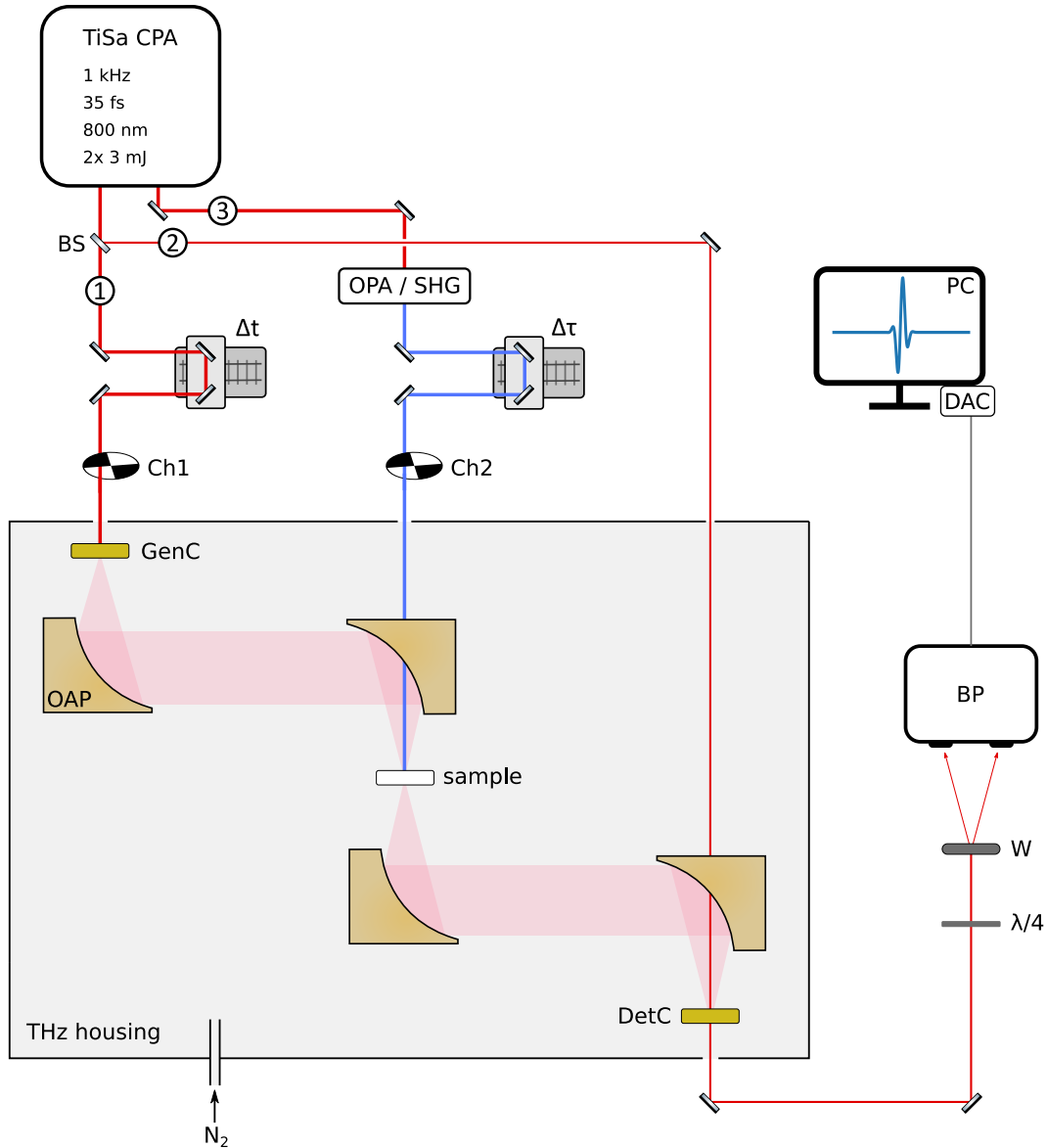


**Figure 2.10:** Schematic representation of a THz-TDS and OPTP-setup. TiSa CPA: titanium sapphire chirped-pulse amplifier, 1: THz generation beam path, 2: THz detection beam path, 3: optical pump beam path (only in OPTP configuration), BS: beamsplitter,  $\Delta t$ : THz delay stage,  $\Delta \tau$ : optical pump delay stage, Ch1: THz chopper (used in TDS-configuration), Ch2: optical pump chopper (used in OPTP configuration), GenC: THz generation crystal, OAP: off-axis parabolic mirror, DetC: THz detection crystal,  $\lambda/4$ : quarter-wave plate, W: Wollaston prism, BP: balanced photodiodes, DAC: data acquisition card,  $N_2$ : continuous nitrogen flow.

information about the relaxation behaviour of excited charge carriers. Pump scans probe a fixed point on the THz waveform and monitor the decay of the photoresponse of the sample with pump-probe delay time. Note that the terminology is not used consistently in literature. Here, the terms pump scan and THz scan are used to clarify that they are two modes of operation of the same experiment, namely *Optical-Pump-Terahertz-Probe Spectroscopy*. Some authors refer to pump scans as *Optical-Pump-Terahertz-Probe Spectroscopy* and to THz scans as *Time-Resolved Terahertz Spectroscopy*. Pump scans performed at the maximum of the undisturbed THz waveform approximately give the time evolution of the real part of the photoinduced conductivity, whereas pump scans conducted at the zero crossing of the THz waveform yield the time evolution of the imaginary part.<sup>69,70</sup> Complete 2D data sets allow for a detailed study of the development of the THz photoconductivity with pump-probe delay time. Vertical and horizontal cuts through a complete 2D data set yield pump scans and THz scans, respectively, as shown in Figure 2.11.

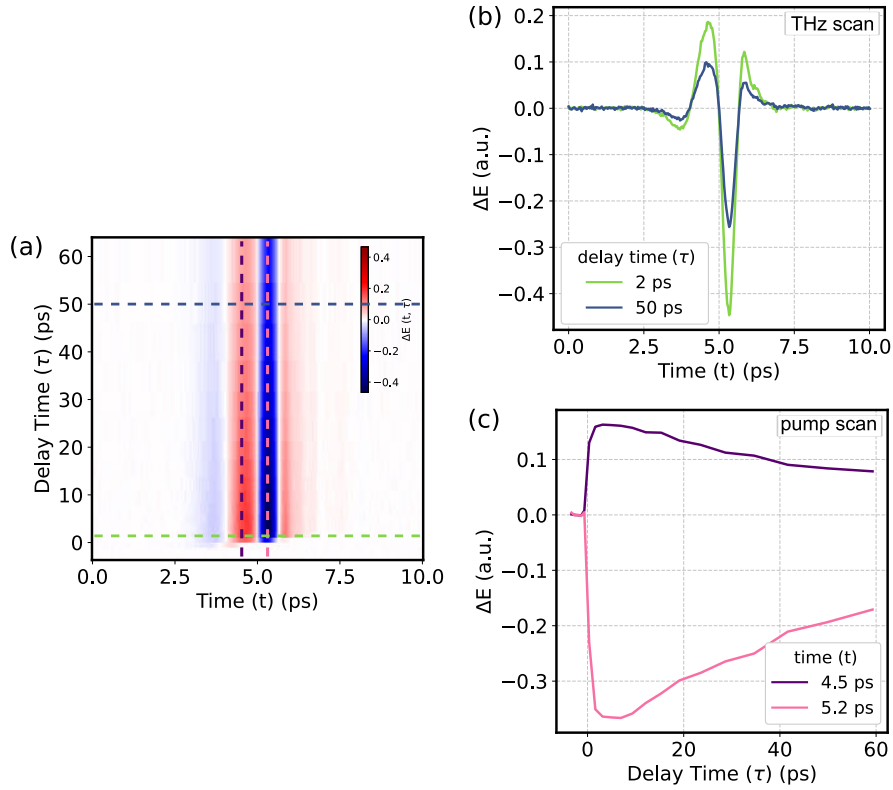


**Figure 2.11:** Exemplary OPTP data. (a) 2D OPTP data map. (b) Differential THz fields (THz scans) at two different optical pump delay times generated from horizontal cuts through the 2D data map. (c) Optical pump scans at two fixed THz delay times generated from vertical cuts through the 2D data map.

For low excitation densities, where the differential THz field is much weaker than the initial THz field, the frequency-dependent complex photoconductivity  $\sigma(\omega)$  can be calculated using the thin-film approximation<sup>71,72</sup>

$$\sigma(\omega) = -\frac{\epsilon_0 c (1 + n_{\text{substrate}})}{d} \frac{\Delta T(\omega)}{T(\omega)}, \quad (2.22)$$

where  $\epsilon_0$  is the vacuum permittivity,  $c$  is the speed of light,  $n_{\text{substrate}}$  is the refractive index of the substrate,  $d$  is the thickness of the sample,  $T(\omega)$  and  $\Delta T(\omega)$  are the Fourier-transform of the THz pulse transmitted through the unperturbed sample and the differential THz pulse. This approximation, also known as the Tinkham-Glover formula, was first developed to describe the conductivity of thin superconducting materials<sup>73</sup> and is nowadays widely used in OPTP. A derivation of Equation (2.22) can be found in the reviews of Joyce<sup>71</sup> or Neu.<sup>72</sup> If the thickness of the sample is not known with sufficient accuracy, the so-called sheet-photoconductivity  $\sigma_d(\omega)$  is often calculated.

$$\sigma_d(\omega) = \sigma(\omega)d = -\epsilon_0 c (1 + n_{\text{substrate}}) \frac{\Delta T(\omega)}{T(\omega)} \quad (2.23)$$

If the thin-film approximation does not apply, the transfer function needs to be evaluated and solved numerically.<sup>74,75</sup> Open-source software packages are available for this purpose.<sup>76</sup>

Figure 2.12 exemplarily shows a simulated THz pulse that experiences absorption and shift in a photoexcited sample and both amplitude and phase of the unperturbed and the differential THz pulse.<sup>4</sup>

### 2.3.3 Physical models of terahertz conductivity

Applying the thin-film approximation to the measured data yields the frequency-dependent complex photoconductivity  $\sigma(\omega)$  of the sample. Physical models can be fitted to these spectra to obtain detailed information about the mechanisms of charge transport. Here, the Drude model and Lorentz-Drude model are exemplarily discussed. Many other descriptions of conductivity in the THz spectral region were reported in literature, such as effective medium theories<sup>77</sup> or quantum-mechanical conductivity models.<sup>78</sup> Reviews by Lloyd-Hughes<sup>79</sup> and Kuzel<sup>80</sup> provide an extensive overview.

#### Drude model

The Drude model describes charge carriers in solid state materials as an ideal electron gas.<sup>81,82</sup> The core electrons are bound to the nuclei and screen the charge, hence valence electrons can be regarded as freely moving, without any interactions with the nuclei. When applying an external electric field  $E(t)$ , the equation of motion of a free electron is<sup>83</sup>

$$\frac{d}{dt}v + \frac{1}{\tau}v = -\frac{e}{m}E(t), \quad (2.24)$$

where  $\tau$  is the charge carrier scattering time,  $e$  and  $m$  are the elementary charge and the mass of the electron and  $v$  is its velocity. Assuming a time-dependent electric field  $E(t) = E_0 e^{-i\omega t}$ , which implies that  $v$  is also time-dependent in  $v = v_0 e^{-i\omega t}$ , and using the definition of the current density  $j = -env$  and the conductivity  $\sigma = j/E$  the Drude conductivity can be described as

---

<sup>4</sup>Note that the sign of the imaginary part of the photoconductivity depends on the chosen Fourier convention (*cf.* Chapter 2.3.1). Since Fourier conventions are not used consistently in literature, both positive and negative imaginary photoconductivities are reported for comparable experiments.

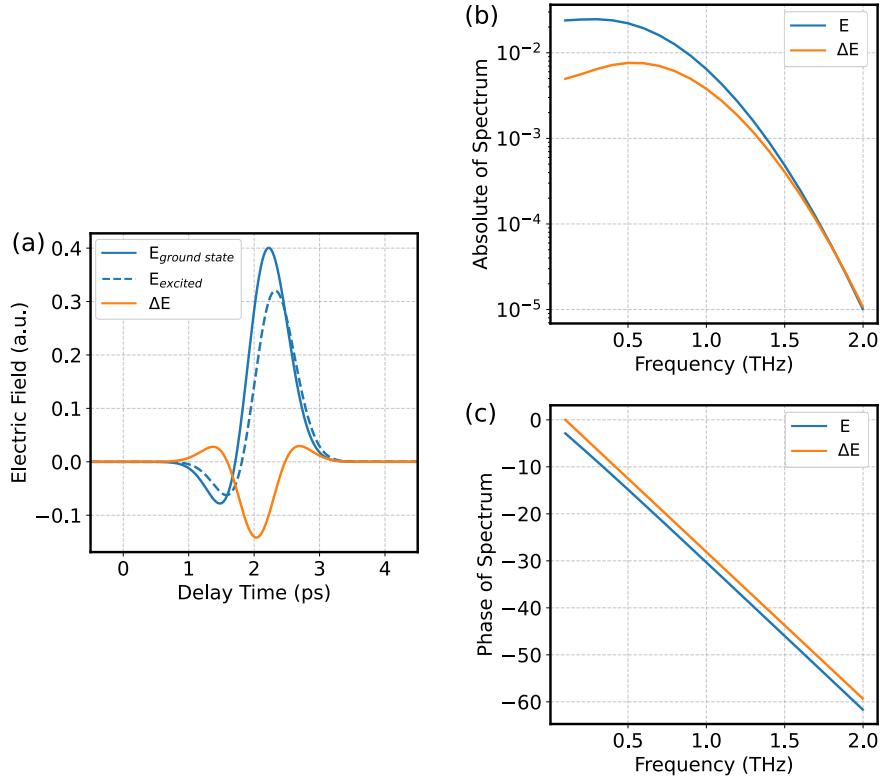


**Figure 2.12:** (a) Simulated OPTP data. The THz pulse transmitted through the optically excited sample is partly absorbed and shifted as compared to the THz pulse transmitted through the sample in its ground state. (b) Amplitude of spectrum of the THz pulse and the differential THz pulse. (c) Phase of THz pulse and the differential THz pulse.

$$\sigma_{\text{Drude}}(\omega) = \frac{ne^2\tau}{m} \frac{1}{1 - i\omega\tau}. \quad (2.25)$$

In the stationary case, *i.e.*  $\frac{d}{dt}v = 0$ , the Drude DC conductivity  $\sigma_{DC}$  is obtained.

$$\sigma_{DC} = \frac{ne^2\tau}{m} \quad (2.26)$$

Thus, the Drude conductivity can also be described as

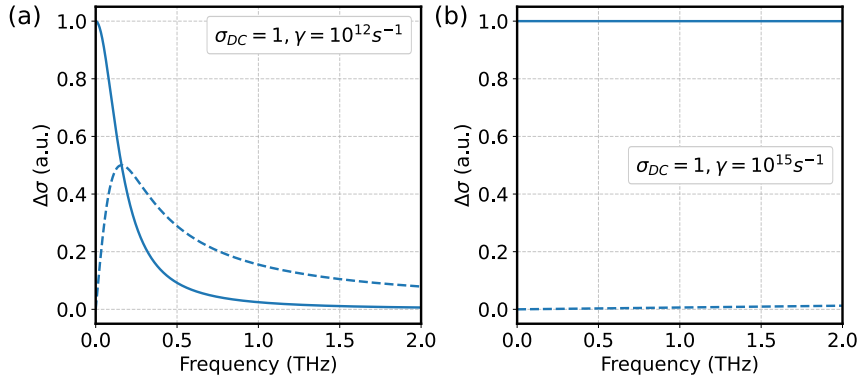
$$\sigma_{\text{Drude}}(\omega) = \sigma_{DC} \frac{1}{1 - i\omega\tau}. \quad (2.27)$$

Figure 2.13 shows the complex Drude conductivity for scattering rates  $\gamma = 1/\tau$  both within and above the probed THz frequencies. The former results in a nonzero real and imaginary conductivity, while the latter shows approximately zero imaginary conductivity and a spectrally flat real conductivity that equals  $\sigma_{DC}$ .<sup>84</sup>

### Lorentz-Drude model

The Lorentz-Drude model expands the Drude model by additionally taking a restoring force into account, which results in a resonance at a finite frequency that follows a Lorentzian





**Figure 2.13:** Real (solid line) and imaginary (dashed line) part of the photoconductivity of a Drude response. (a) The scattering rate ( $1/\tau$ ) lies within the THz probe window. (b) The scattering rate is much higher than the probed THz frequencies. Reproduced with permission from Ulbricht.<sup>84</sup>

function. In solid state material, resonances that fall into the THz spectral regime could be phonons, low-energy electronic transitions or collective modes such as plasmons (which is why the Lorentz-Drude model is also referred to as the plasmon model). The restoring force  $\omega_0 x$  is added to the equation of motion<sup>85</sup>

$$\frac{d}{dt}v + \frac{1}{\tau}v + \omega_0^2 x = -\frac{e}{m}E(t), \quad (2.28)$$

where  $\omega_0$  is the resonance or plasmon frequency. The frequency-dependent complex conductivity for the Lorentz-Drude model  $\sigma_{LD}(\omega)$  can be described by<sup>79</sup>

$$\sigma_{LD}(\omega) = \frac{ne^2}{m} \frac{\tau}{(1 - (i\tau(\omega - \omega_0^2/\omega)))}. \quad (2.29)$$

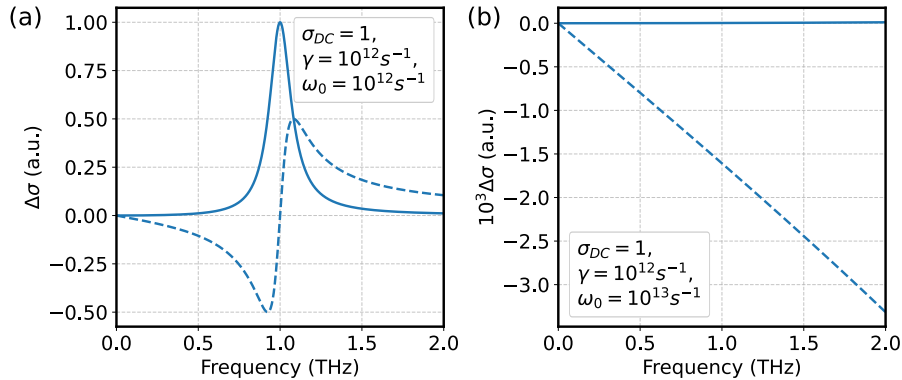


**Figure 2.14:** Real (solid line) and imaginary (dashed line) part of the photoconductivity of a Drude-Lorentz response. (a) The resonance frequency lies within the THz probe window. (b) The resonance frequency is much higher than the probed THz frequencies. Reproduced with permission from Ulbricht.<sup>84</sup>

In Figure 2.14, the Lorentz-Drude conductivity is shown for both a resonant and an off-resonant response.<sup>84</sup>

### 2.3.4 Terahertz-pump-optical-probe spectroscopy

Strong electric fields can induce changes in the optical properties of materials, *e.g.* via the Stark-Effect in semiconductors. Terahertz-pump-optical-probe experiments (TPOP) can be used to measure such changes with sub-picosecond time resolution. OPTP setups can easily be converted to TPOP setups. In OPTP, the optical pump pulse is dumped after passing through the sample. In TPOP, the optical pulse serves as a probe, hence it has to be detected using a spectrometer or photodiodes. As the THz-induced changes in absorption are usually rather weak, strong THz fields, as well as sensitive optical detection, are required for this kind of experiment. The measured quantity is, just as in TA, the differential absorption  $\Delta A$ , *i.e.* the difference in absorption between the THz<sub>on</sub> and THz<sub>off</sub> state (*cf.* Equation (2.8)). Chapter 6.1 discusses TPOP measurements on CdSe nanoplatelets.

# 3. Hot electron dynamics in gold nanoparticles

The following chapter on AuNPs is split into two parts: First, the optical properties of gold and the LSPR resonances of AuNPs are explained. Second, the current understanding of the dynamic processes following plasmon excitation and how they can be investigated by pump-probe spectroscopy is discussed.

## 3.1 Optical properties of bulk metals

To understand the optical properties of bulk and nanoscopic gold, the dielectric constant  $\varepsilon$  of the bulk metal is required, as it connects the applied electric field of the light  $E$  with the induced polarisation of the material  $P$ <sup>86</sup>

$$P = \varepsilon_0(\varepsilon - 1)E, \quad (3.1)$$

where  $\varepsilon_0$  is the vacuum permittivity. The dielectric constant (or dielectric function) is generally frequency-dependent, *i.e.*  $\varepsilon = \varepsilon(\omega)$  and is given by<sup>86</sup>

$$\varepsilon(\omega) = 1 + \frac{i\sigma(\omega)}{\omega\varepsilon_0}, \quad (3.2)$$

where  $\sigma(\omega)$  is the frequency-dependent conductivity. The easiest model to explain the conductivity of bulk metals is the Drude model, which was already discussed in Chapter 2.3.3. Inserting the Drude conductivity from Equation (2.27) into Equation (3.2) yields the dielectric function of a metal<sup>87</sup>

$$\varepsilon(\omega) = 1 - \frac{\omega_p^2}{(\omega^2 + i\omega\gamma)}. \quad (3.3)$$

The damping rate  $\gamma$  summarizes all electron scattering processes *i*<sup>88</sup>

$$\gamma = \sum_i \tau_i^{-1} \quad (3.4)$$

and will be discussed later in more detail. The plasma frequency  $\omega_p$  is the resonance frequency of the oscillation of the Drude free electron gas against the atomic lattice and is defined as<sup>88</sup>

$$\omega_p = \sqrt{\frac{ne^2}{\epsilon_0 m}}. \quad (3.5)$$

Below the plasma frequency, light cannot enter the metal, *i.e.* the material is reflective. Above the plasma frequency, the metal is transparent.<sup>88</sup>

In the case of gold, the dielectric function has to be modified to take into account the contribution of interband electronic transitions  $\epsilon_{ib}$

$$\epsilon(\omega) = \epsilon_{ib} - \frac{\omega_p^2}{(\omega^2 + i\omega\gamma)}, \quad (3.6)$$

as the interband absorption from  $5d$  to  $6sp$  falls into the optical frequency range, giving gold its unique color.<sup>89</sup> Figure 3.1 compares the calculated dielectric function of a Drude free electron gas with the measured dielectric function of gold. As the Drude free electron gas neglects interband transitions, significant deviations from the experimental results occur at high energies.

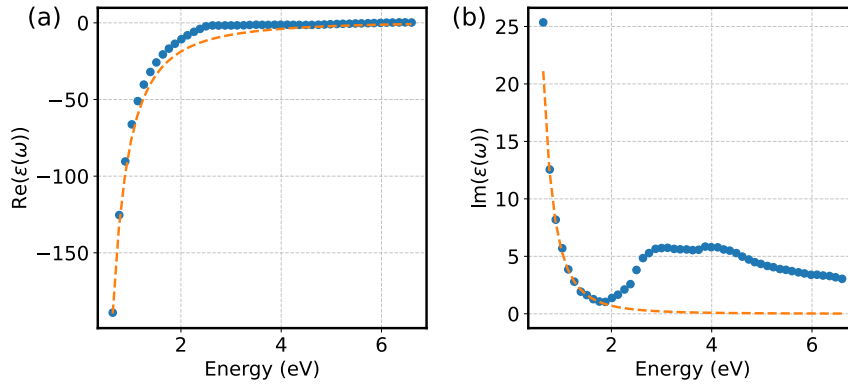


**Figure 3.1:** (a) Real and (b) imaginary part of the dielectric function of gold. Blue dots are measured values from Johnson and Christy.<sup>90</sup> Orange dashed line is the dielectric function of the Drude free electron gas calculated using values for  $\omega_p = 8.89$  eV and  $\gamma = 70.88$  meV from Zeman and Schatz.<sup>91</sup> Deviations at high frequencies are due to interband transitions. Adapted with permission from Maier.<sup>87</sup>

Oscillations of the free electron gas at its resonance frequency  $\omega_p$  are called plasma oscillations and behave like harmonic oscillators. As the energy of the plasma oscillations is quantized in units of  $\hbar\omega_p$ , they are referred to as plasmons.<sup>83</sup> Light is a transversal wave that can not excite volume plasmons in bulk metals, which are longitudinal oscillations. Volume plasmons are thus studied by inelastic scattering techniques such as electron energy loss spectroscopy.<sup>92</sup> At the surface of a metal, a second class of plasmons can be excited, the so-called surface plasmons. These charge density oscillations travel along the surface and can be excited by light under certain configurations (such as an attenuated total reflection geometry).<sup>93</sup> As there is a strong interaction between the photon and the plasmon, surface plasmons are also referred to as propagating surface plasmon polaritons.<sup>83</sup> Metal nanoparticles exhibit surface plasmons that do not propagate along the surface, hence they are called localized surface plasmons. As they are the type of plasmon of main interest for this thesis, they will be discussed in more detail in the next section.

### 3.2. Localized surface plasmon resonance in gold nanoparticles

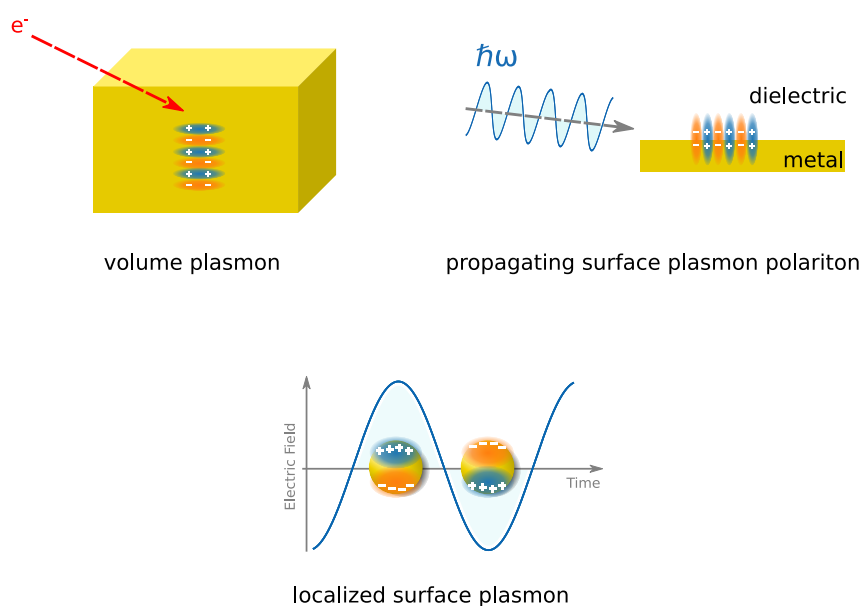


**Figure 3.2:** Schematic depiction of the three main types of plasmons in metal and their excitation mechanisms: Volume plasmons can not be excited by light but by inelastic scattering of electrons. Propagating surface plasmon polaritons can be excited by light under certain conditions such as under an attenuated total reflection geometry. Localized surface plasmons of metal particles that are smaller than the wavelength of the light are excited very effectively.

## 3.2 Localized surface plasmon resonance in gold nanoparticles

The metal skin depth of gold in the visible is in the nanometer size regime.<sup>94</sup> Hence, incident optical light can penetrate a nanometer-sized gold particle and polarize its conduction band electrons. This displacement of the electrons against the positively charged crystal lattice generates a restoring force that pulls the electrons back to the lattice, which can be described as a mass-spring harmonic oscillator. The oscillation, the LSPR of the AuNPs, can be driven by resonant incident light waves and dictates the optical properties of AuNPs. The LSPR amplifies the electromagnetic field of the incident light near the particle's surface, which effectively acts as a nano-lens.<sup>95</sup> The high local fields are exploited in surface-enhanced Raman scattering<sup>96</sup> or surface-enhanced infrared absorption spectroscopy.<sup>97</sup>

Wet-chemical procedures allow the synthesis of AuNPs of various shapes.<sup>7</sup> As the LSPR is a surface effect, its properties depend strongly on the shape of the particles. For example, elongated particles show two distinct resonances that depend heavily on the aspect ratio of the particle, corresponding to plasmon vibrations along and perpendicular to the elongated axis, whereas spherical AuNPs possess only one LSPR. This thesis focuses on spherical AuNPs synthesized *via* seeded-growth approaches.<sup>98</sup> Figure 3.3 shows an exemplary transmission electron microscopy (TEM) image of the AuNPs employed in the study presented in Chapter 5.2.

Already in 1908, Gustav Mie explained the red color of dispersions of AuNPs by solving Maxwell's equations for the interaction of light with a homogeneous spherical particle in a non-absorbing medium.<sup>44</sup> He used the dielectric function of the bulk material and set

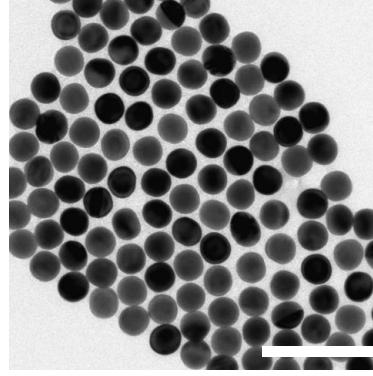


**Figure 3.3:** TEM image of 26 nm monocrystalline AuNPs studied in Chapter 5.2.<sup>99</sup> The scale bar corresponds to 100 nm.

boundary conditions for a spherical particle.<sup>100</sup> Using multipole extension of the fields, he was able to explain the optical properties of any sphere in a homogeneous medium without requiring any approximations. His calculations yield a complex result including an infinite series of Riccarti-Bessel functions. Bohren and Hoffman discuss Mie's theory in detail and state that those who work through the derivation of Mie's solution will have "acquired virtue through suffering".<sup>86</sup> However, for nanoparticles that are much smaller than the wavelength of the incident light ( $d \ll \lambda$ ), only the dipole plasmon resonance needs to be considered, as the phase of the electric field of the light is approximately constant throughout the particle (quasi-static approximation or dipole approximation). This approximation yields reasonable results for a particle size below 100 nm. Absorption and scattering properties are determined by the particles polarizability  $\alpha$ , which can be described as<sup>87</sup>

$$\alpha = 4\pi a^3 \frac{\varepsilon(\omega) - \varepsilon_m}{\varepsilon(\omega) + 2\varepsilon_m}, \quad (3.7)$$

where  $a$  is the particle radius,  $\varepsilon$  and  $\varepsilon_m$  are the metal's and medium's dielectric functions, respectively. It can be seen that the polarization is resonantly enhanced when the so-called Fröhlich condition

$$\varepsilon(\omega) = -2\varepsilon_m \quad (3.8)$$

is fulfilled. Strictly, this is never the case, since the dielectric function of the metal is complex ( $\varepsilon(\omega) = \varepsilon'(\omega) + i\varepsilon''(\omega)$ ). It can however be approximately fulfilled when  $\varepsilon'(\omega) = -2\varepsilon_m$ .<sup>101</sup> When the Fröhlich condition is met, the conduction band electrons oscillate in resonance with the incident light field, *i.e.* the dipole localized surface plasmon is excited. For gold, this is the case in the visible frequency regime. The scattering and absorption cross sections of the sphere can be calculated from the polarizability as<sup>87</sup>

$$C_{sca} = \frac{k^4}{6\pi} |\alpha|^2 = \frac{8\pi}{3} k^4 a^6 \left| \frac{\varepsilon(\omega) - \varepsilon_m}{\varepsilon(\omega) + 2\varepsilon_m} \right|^2 \quad (3.9)$$

$$C_{abs} = k \text{Im}(\alpha) = 4\pi k a^3 \text{Im} \left( \frac{\varepsilon(\omega) - \varepsilon_m}{\varepsilon(\omega) + 2\varepsilon_m} \right) \quad (3.10)$$

### 3.2. Localized surface plasmon resonance in gold nanoparticles

with  $k = 2\pi/\lambda$ . Figure 3.4 compares the simulated absorption spectra for 10 nm and 45 nm AuNPs in water. As the absorption and scattering cross sections scale with  $a^3$  and  $a^6$ , respectively, absorption dominates for small particles. At larger particle sizes, scattering becomes more important.

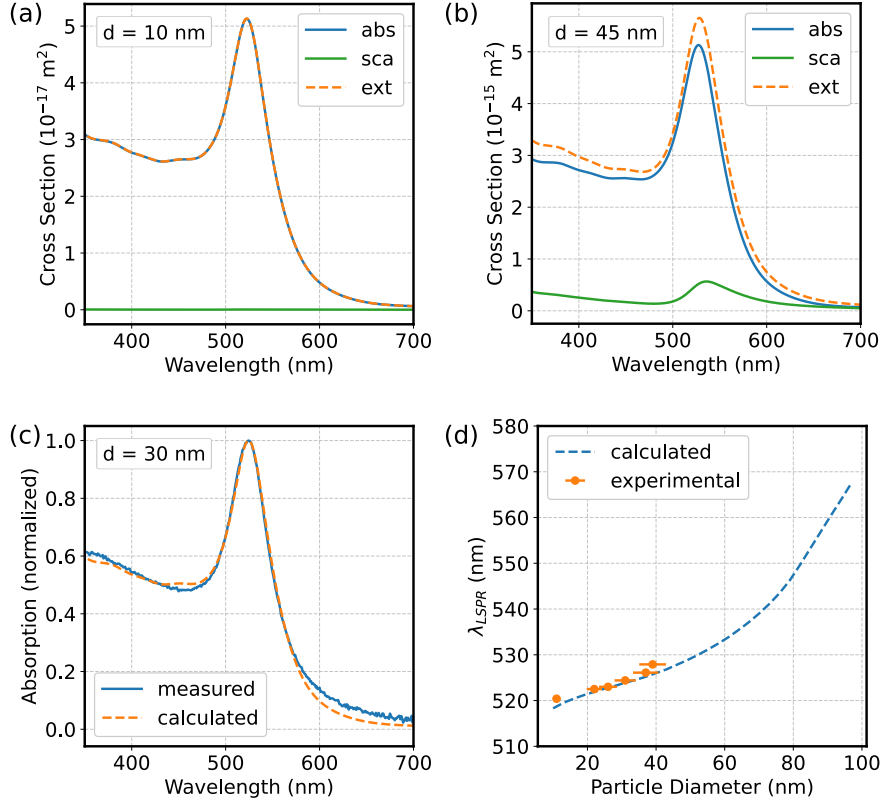


**Figure 3.4:** (a) Simulated absorption, scattering and extinction spectra for 10 nm and (b) 45 nm AuNPs in water. (c) Simulated and experimental absorption spectrum for 30 nm AuNPs in water. The absorption spectra of AuNPs show absorption of interband transitions on the blue side of the LSPR absorption peak. (d) The LSPR maximum red shifts with increasing particle diameter. Simulated data was calculated using PyMieScatt.<sup>102,103</sup> The dielectric function of gold was taken from Johnson and Christy<sup>90</sup> and size-corrected according to Haiss *et al.*<sup>104</sup> The refractive index of the surrounding medium was set to 1.33 for water. Experimental data was taken from the study presented in Chapter 5.2.<sup>99</sup>

For particle sizes smaller than the mean free path of electrons in the bulk material (around 50 nm in gold)<sup>105</sup>, the dielectric function of the particle no longer equals the bulk dielectric function from Equation (3.6). Scattering of electrons at the particle surface can be taken into account by adjusting the damping rate  $\gamma$ . The so-called Kreibig damping  $\gamma(R)$  can be described as<sup>106</sup>

$$\gamma = \gamma_{bulk} + \frac{v_F}{R}, \quad (3.11)$$

where  $\gamma_{bulk}$  is the bulk damping rate and  $v_F$  is the Fermi velocity ( $v_F = 1.4 \cdot 10^6$  m/s for gold<sup>88</sup>). The size dependency of the dielectric function  $\epsilon(\omega, R)$  also alters the Fröhlich condition and is considered an intrinsic size effect. For larger particle sizes, the dipole

approximation breaks down and higher-order modes become more important. This extrinsic size effect leads to a red-shift of the plasmon resonance with increasing particle size, as the higher-order modes are lower in energy.<sup>107</sup>

### Effect of the dielectric environment on the plasmon resonance

The LSPR occurs when the Fröhlich condition is met. As in the visible and NIR region, the damping constant  $\gamma$  is much smaller than the plasma frequency  $\omega_p$ , following the Drude model,  $\varepsilon'(\omega)$  can be written as<sup>108</sup>

$$\varepsilon'(\omega) = 1 - \frac{\omega_p^2}{\omega^2}. \quad (3.12)$$

Inserting the Fröhlich condition into Equation (3.12) yields the LSPR frequency  $\omega_{LSPR}$  as<sup>109</sup>

$$\omega_{LSPR} = \frac{\omega_p}{\sqrt{2\varepsilon_m + 1}}. \quad (3.13)$$

Equation (3.13) shows that the spectral position of the LSPR maximum can be tuned by changing the dielectric environment. An increase in refractive index thereby leads to a redshift.<sup>95</sup>

### Plasmonic coupling

Placing AuNPs near each other enables interaction between their plasmon resonances. The simplest exemplary structures for plasmonic interaction are plasmonic dimers. The interaction of their plasmon modes can be described by hybridization leading to a bonding and an antibonding plasmon mode. The antibonding plasmon mode is dark, *i.e.* it can not be excited by light. The bonding mode is lower in energy than the individual plasmon modes of the particles, effectively leading to a red shift of the coupled mode with decreasing inter-particle distance.<sup>110,111</sup> Ordered multi-layer structures of AuNPs, synthesized employing a self-assembly approach, exhibit even stronger interaction between the plasmonic modes and incident light. It was shown that by employing such structures, the deep strong light-matter coupling regime can be reached.<sup>24</sup>

### Temperature effects

Static heating of the sample leads to a thermal dilatation of the AuNPs, which effectively decreases the electron density. The LSPR frequency depends on the plasma frequency, which in turn depends on the electron density. Hence, a decreasing electron density due to static heating leads to a red shift of the LSPR.<sup>112</sup> Chapter 3.3 will discuss how transient heating alters the LSPR in more detail, as the temperature-dependence of the LSPR is exploited in TA measurements to study the charge carrier dynamics in AuNPs after optical excitation of the plasmon resonance.



### 3.3 Hot electron dynamics

The excitation of the LSPR in AuNPs is followed by a cascade of events that eventually lead to the dissipation of the input energy. The plasmon dephases rapidly on a ten femtosecond time scale and transfers its energy onto a few charge carriers. This leads to a so-called non-thermal electron distribution, *i.e.* an electron distribution that can not be assigned a temperature according to the Fermi-Dirac distribution. *Via* electron-electron scattering, the energy is distributed over the whole electron gas on a hundred femtosecond timescale, yielding a hot, thermal electron distribution. The hot electron distribution thermalizes with the crystal lattice *via* electron-phonon coupling within a few picoseconds. Eventually, heat transfer to the environment occurs on a hundred to thousand picoseconds timescale. The separation of timescales allows to study the individual processes separately. However, in some cases the processes are more entangled and the timescales can not be separated as clearly. Here, TA is discussed as an important tool to study electron-phonon coupling and heat dissipation to the environment, followed by a literature overview of the four main steps in plasmon dynamics in order of increasing time scales.

#### 3.3.1 Transient absorption experiments on gold nanoparticles

TA is often used to study plasmon dynamics in AuNPs. However, as the time resolution of the experiment is too low to study plasmon dephasing (and in most cases also electron-electron scattering), mostly electron-phonon coupling and phonon-phonon coupling are studied *via* TA. In the experiment, the pump pulse establishes an elevated electronic temperature. As the dielectric function of gold depends on the electronic temperature, the plasmon absorption changes. Brown *et al.* provided values for the temperature-dependent dielectric function of gold from *ab initio* calculations.<sup>105</sup> The contribution of direct interband excitations to the dielectric function (*cf.* Equation (3.6)) depends on the electron occupation numbers, which in turn depend on the electronic temperature. Also, electron-electron scattering rates increase with electron temperature. The combination of these two factors leads to a broadening and shift of the plasmon absorption. Figure 3.6(a) and (b) exemplarily shows the absorption spectra of 16 nm AuNPs in toluene with and without prior optical excitation as well as the differential TA spectrum. An optical pump pulse established an electronic temperature of 1400 K. PyMieScatt was used to solve the Mie equations with the dielectric function provided by Brown *et al.* at 300 K and 1400 K. The calculated absorption spectra and differential absorption spectra resemble the measured data quite well. Figure 3.6(c) shows calculated TA spectra for different electronic temperatures. It can be shown that the change in absorption linearly depends on the difference between the electronic temperature of the ground and the excited state. Hence, the establishment of a hot, thermal electron distribution (if time resolution allows) and its cooling *via* energy transfer to the lattice can be directly followed by TA spectroscopy. How to calculate the initial rise in electronic temperature induced by the pump pulse will be discussed later.

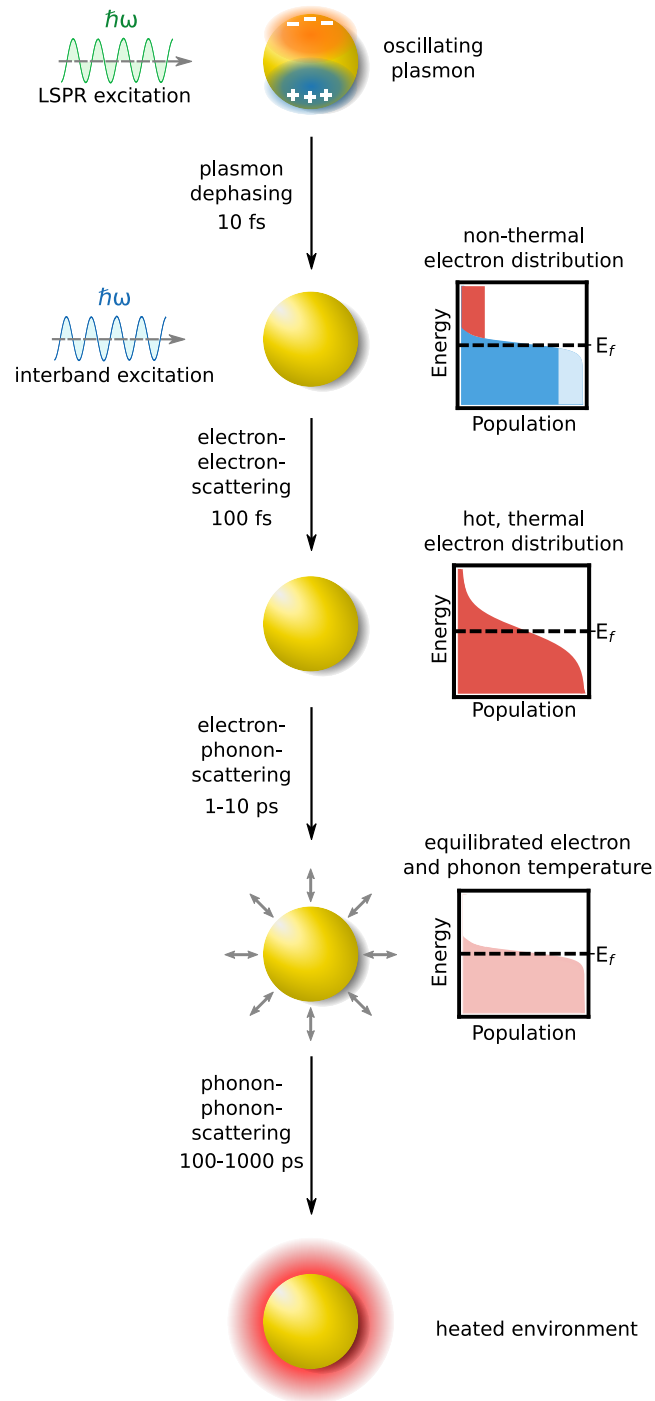


**Figure 3.5:** Schematic depiction of the processes following LSPR excitation. The LSPR dephases within a few femtoseconds *via* Landau damping, resulting in a non-thermal electron distribution. Electron-electron scattering, taking place on a timescale of hundreds of femtoseconds results in a hot, thermal electron distribution. The electrons transfer their energy to the lattice within a few picoseconds *via* electron-phonon scattering. Finally, *via* phonon-phonon scattering, the heat dissipates to the environment.

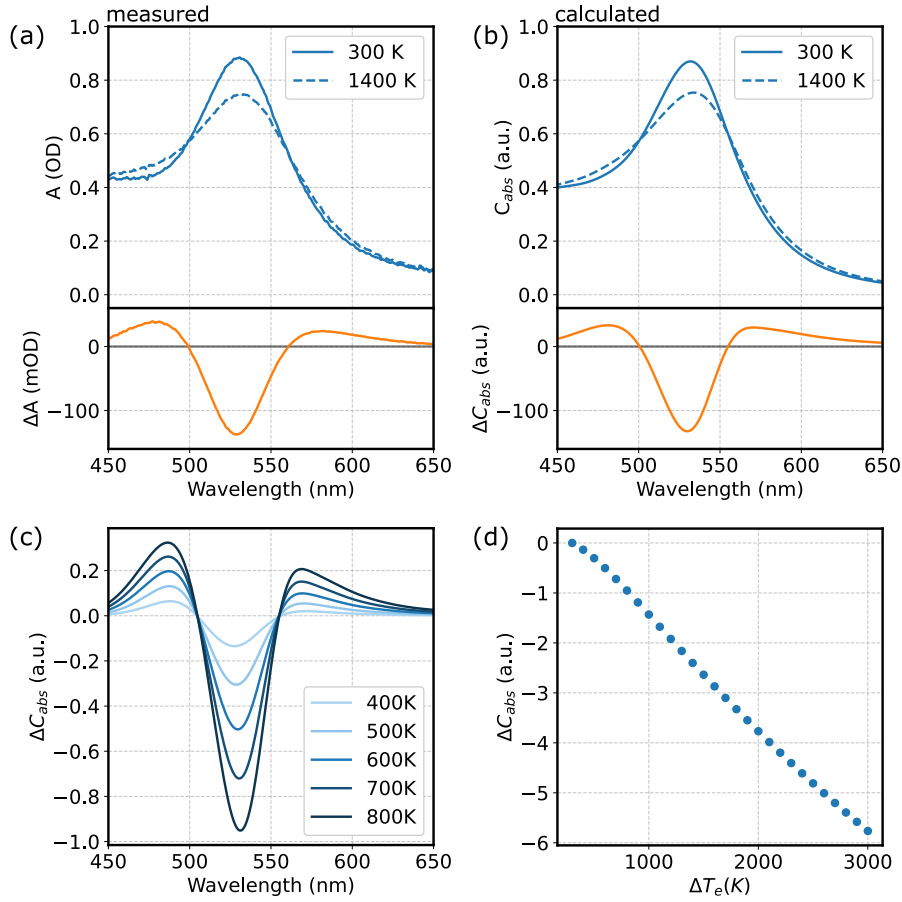


**Figure 3.6:** (a) Measured absorption and differential absorption spectra for 16 nm AuNPs in toluene. A 400 nm pump pulse was employed to establish an electronic temperature of 1400 K. (b) Calculated absorption and differential absorption spectra for the same initial conditions. The calculated spectra resemble the experimental data very well. (c) Calculated differential absorption spectra for several electronic temperatures relative to a ground-state temperature of 300 K. (d) Calculated temperature-dependent maximum differential absorption relative to a ground-state temperature of 300 K, proving that the differential absorption linearly depends on the electronic temperature difference. All calculations were performed using PyMieScatt<sup>102,103</sup> and the temperature-dependent dielectric function provided by Brown *et al.*<sup>105</sup>

### 3.3.2 Plasmon dephasing and hot electron generation

Dephasing (or damping) of the plasmon oscillation can occur *via* radiative (*i.e.* scattering) and non-radiative mechanisms. The damping rate  $\gamma$  was already discussed briefly in Section 3.1 and 3.2. The plasmon lifetime  $\tau$  is the inverse of the damping rate,  $\tau = 1/\gamma$ . In bulk metals, plasmons dephase due to electrons scattering on other electrons, phonons, and lattice defects

$$\gamma_{bulk} = \gamma_{el-el} + \gamma_{el-ph} + \gamma_{defects}. \quad (3.14)$$

However, in AuNPs, plasmon dephasing is dominated by an additional process, the so-called Landau damping. Direct transitions between two states with different wave vectors by absorption of a photon are forbidden due to momentum conservation. However, electron-surface scattering enables such a transition, as momentum can be transferred to phonons or

defects.<sup>113,114</sup> Hence, it is also referred to as surface-enhanced Landau damping.<sup>115</sup> Hartland *et al.* refer to Landau damping as the "quantum effect of surface scattering".<sup>46</sup> Landau damping results in the direct interband excitation of relatively few electron-hole pairs in the metal by the electric field of the LSPR.<sup>116,117</sup> The excited electron-hole pairs carry the plasmon energy  $\hbar\omega_p$  and are called *hot charge carriers*.<sup>118</sup> The electron distribution can at this point not be described by a Fermi-Dirac distribution and is hence referred to as a non-thermal electron distribution. It is described as a step-like function.<sup>119</sup> The hot electrons can be transferred to molecules adsorbed to the AuNPs surface and are thus available for photocatalytic applications.<sup>120–122</sup>

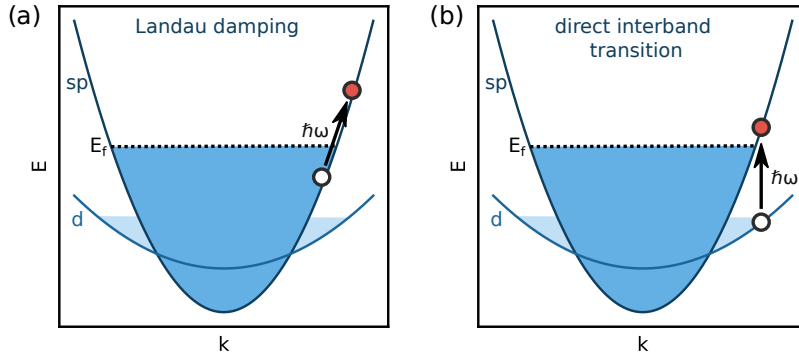


**Figure 3.7:** Schematic illustration of the generation of electron-hole pairs in AuNPs. (a) Landau damping. Momentum can be transferred to phonons, therefore the absorption does not have to be vertical. (b) Direct interband absorption from the *d* band to the *sp* band. Adapted with permission from Kim and Yoon.<sup>113</sup>

As the damping rate  $\Gamma$  determines the bandwidth of the plasmon absorption, dephasing times can be calculated from the absorption spectra. Dephasing times on the single-digit femtosecond timescale were reported.<sup>123–125</sup>

### 3.3.3 Electron-electron scattering

The hot carriers generated by Landau damping of the LSPR thermalize with the electron bath *via* electron-electron scattering, resulting in a hot, thermal electron distribution.<sup>126,127</sup> The process is usually explained using the Fermi liquid theory.<sup>88</sup> An initial hot electron scatters with an electron below the Fermi level and thus shares its energy, whereby a single scattering event takes place on the timescale of 10 fs.<sup>128</sup> The electron-electron scattering rate is proportional to the energy difference of the electron to the Fermi level,<sup>129</sup>

$$\frac{1}{\tau_{e-e}} \propto (E - E_f)^2 \quad (3.15)$$

*i.e.* low energy carriers close to the Fermi level have the longest lifetime and mean free path.<sup>130,131</sup> Note that single events of electron-phonon scattering occur on comparable timescales. However, as the typical phonon energy is many times smaller than  $\hbar\omega_p$ , it takes many more scattering events to transfer a certain amount of energy from electrons to phonons. Hence, energy transfer to phonons, although already starting instantly after Landau excitation of electrons, is much slower than electron thermalization and the two

processes can be regarded as disentangled.<sup>45</sup> As described in Chapter 3.3.1, the LSPR resonance depends on the electronic temperature. The rise time of the TA signal can therefore in principle be used to study the electron thermalization. However, as the thermalization takes place on a timescale of hundreds of femtoseconds,<sup>132,133</sup> the process may not be resolvable due to limited time resolution.

The rise in electronic temperature  $\Delta T_e^{initial}$  established after electron thermalization can be calculated from the amount of energy  $U$  deposited *via* absorption of the pump pulse<sup>134</sup>

$$\Delta T_e^{initial} = -T_0 + \sqrt{T_0^2 + \frac{2}{\gamma_e} U}, \quad (3.16)$$

where  $\gamma_e$  is the electronic heat capacity coefficient ( $\gamma = 68 \text{ Jm}^{-3}\text{K}^{-2}$  for gold<sup>135</sup>) and  $T_0$  is the ambient temperature. In TA experiments,  $\Delta T_e^{initial}$  can therefore be controlled by the employed pump pulse fluence and easily reach thousands of Kelvins.<sup>99</sup>

In silver nanoparticles, slower electron thermalization was observed for larger particles for diameters up to 12 nm.<sup>136</sup> For AuNPs of 9, 22 and 48 nm diameter, similar electron thermalization times were found.<sup>137</sup> Electron thermalization in thin films occurs similarly fast than in nanoparticles.<sup>132</sup> Recently, Karaman *et al.* reported longer electron thermalization times in monocrystalline Au films as compared to polycrystalline films, which they attributed to the contribution of electron scattering at grain boundaries and lattice defects.<sup>138</sup> Heilpern *et al.* directly determined electron distributions from pump-probe reflectivity measurements on gold films and could in fact show the evolution of a thermalized Fermi-Dirac distribution from a step-like distribution (containing hot, non-thermalized electrons) within a few hundred femtoseconds.<sup>133</sup> O’Keeffe *et al.* managed to disentangle the contribution of non-thermal and thermalized electrons to the change in absorption in TA experiments of gold nanoellipsoids and ascribed a blue-shift at short delay times to the contribution of non-thermal electrons.<sup>139</sup> To do so, the contribution of the non-thermal electrons to the change in dielectric function was modeled using an approach based on the energy distribution of the joint density of states of the respective optical transition.<sup>132</sup>

### 3.3.4 Electron-phonon scattering

Both non-thermal and thermalized electrons lose their energy to the lattice *via* electron-phonon coupling on a single-digit picosecond timescale.<sup>123,129,134,140–143</sup> This process has been intensely studied by TA spectroscopy, as it is well observable as a fast decay component of the bleach.

The energy transfer from the electrons to the lattice can be simulated by the so-called two-temperature model (TTM). Electrons and lattice are described as two interchanging heat baths, the coupling between which is determined by the electron-phonon coupling constant  $G$ . Two coupled differential equations describe the interplay between the electron temperature  $T_e$  and the lattice temperature  $T_l$  with time  $t$ .<sup>144</sup>

$$C_e(T_e) \frac{dT_e}{dt} = -G(T_e - T_l) \quad (3.17)$$

$$C_l \frac{dT_l}{dt} = G(T_e - T_l) \quad (3.18)$$

The electronic heat capacity of gold is linearly dependent on the temperature ( $C_e(T_e) = \gamma_e T_e$ ) up to above 3000 K,<sup>105</sup> with the electronic heat capacity coefficient  $\gamma_e$  as the proportionality constant. The lattice heat capacity  $C_l$  of gold is  $24 \cdot 10^5 \text{ Jm}^{-3}\text{K}^{-1}$ .<sup>105</sup> From Equation (3.17) and (3.18) it can be seen that a higher difference of electron and lattice temperatures leads to slower equilibration of temperatures, *i.e.* longer electron-phonon coupling times. In TA experiments, the initial electron temperature can be controlled *via* the pump pulse fluence as described in Chapter 3.3.3. Increasing the pump fluence leads to higher initial electron temperatures, which in turn leads to longer electron-phonon coupling times. As the bleach signal in TA scales linearly with electronic temperature (*cf.* Figure 3.6(c)), electron cooling as calculated from the TTM and the bleach recovery dynamics from TA measurements can be directly correlated (*cf.* Figure 3.8(a) and (b)). The electron-phonon coupling time  $\tau_{el-ph}$  can be derived from the data by fitting an exponential decay function.

As the electron-phonon coupling time depends on the initial electron temperature, pump fluence-dependent measurement series are often conducted to ensure the comparability of measurements. The electron-phonon coupling constant  $G$  can be extracted as the slope of the linear function fitted to the electron-phonon coupling times vs. the initial rise in electronic temperature. Figure 3.8(c) exemplarily shows the linear relation between the electron-phonon coupling time and the initial rise in electron temperature for 16 nm AuNPs.

$$\tau_{el-ph} = \frac{\gamma_e}{G} \cdot \Delta T_e^{initial} \quad (3.19)$$

As the electronic heat capacity at room temperature is much smaller than the lattice heat capacity, the initial electron temperature is much higher than the temperature of electrons and lattice after equilibration, which is usually on the order of a few tens of Kelvins. However, at very high excitation powers, the nanoparticles can be melted or fragmented.<sup>145</sup>

The size-dependency of the electron-phonon coupling constant in AuNPs has been extensively studied. However, contradictory reports exist. Chapter 5.2 discusses the size- and crystallinity dependency of electron-phonon coupling in AuNPs in detail.

On timescales of tens of picoseconds, oscillations of the diameter of the AuNPs, so-called breathing oscillations, have been observed.<sup>146</sup> As described above, the LSPR frequency depends on the electron density of the AuNP. Hence, oscillations of the particle diameter can be observed in TA as oscillations of the LSPR frequency, usually probed at the long-wavelength side of the LSPR bleach.<sup>147</sup> Figure 3.9(a) exemplarily shows the breathing oscillation of 16 nm AuNPs after optical excitation. Within the first few picoseconds after excitation, the TA dynamics are dominated by electron-phonon coupling, which makes it difficult to assess the onset of the breathing oscillation. The fast heating of the lattice due to electron-phonon coupling leads to an expansion of the particle. If this heating is faster

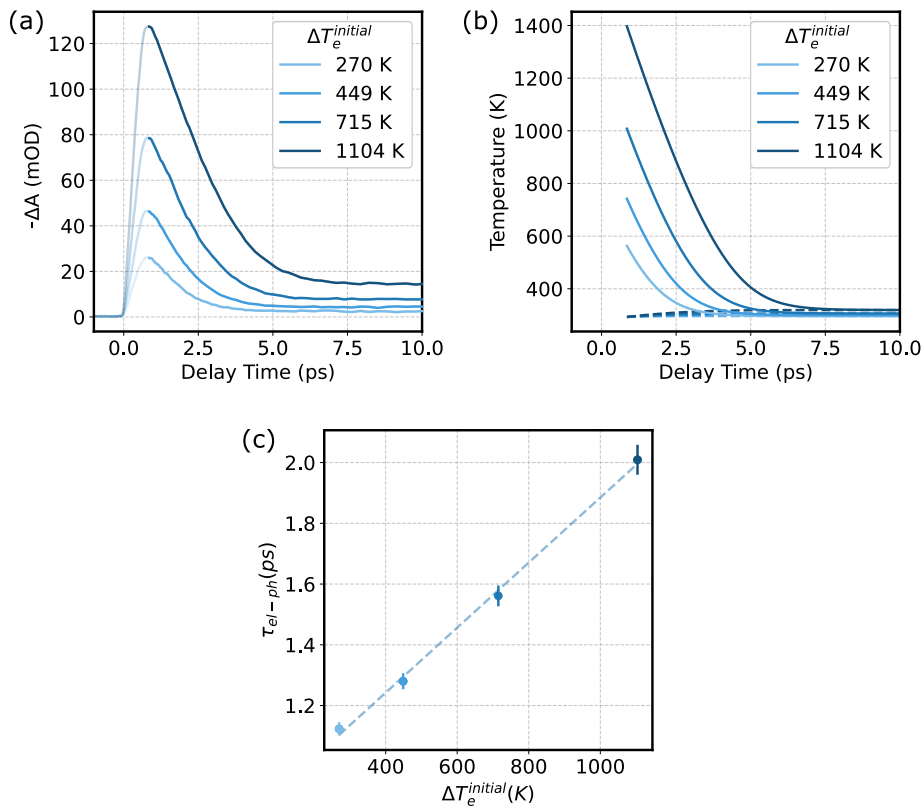


**Figure 3.8:** (a) Bleach recovery dynamics of 16 nm AuNPs after excitation with a 400 nm pump pulse and four different pump fluences that were translated into a rise in electronic temperature. The bleach is plotted with a positive  $\Delta A$  to provide better comparability with the data shown in (b). (b) Electronic (solid line) and lattice (dashed line) temperatures as obtained from the TTM starting with the electronic temperatures established in the measurements displayed in (a). The curves are shifted from zero on the x-axis to match the bleach recovery curves in (a). (c) Electron-phonon coupling times obtained from exponential fitting of the measured data vs. the initial rise in electronic temperature. A linear dependency is observed.

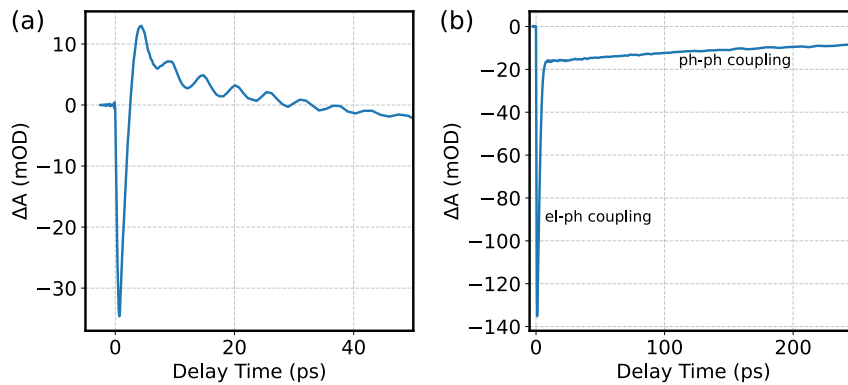


**Figure 3.9:** Breathing oscillation of 16 nm AuNPs after 400 nm excitation with a pump fluence of  $400 \mu\text{J}/\text{cm}^2$  probed at the long wavelength side of the LSPR bleach. In the first few picoseconds, electron-phonon coupling dominates the signal. (b) Bleach recovery dynamics of the same measurement probed at the maximum of the LSPR bleach. Phonon-phonon coupling takes place within hundreds of picoseconds to nanoseconds.

than the period of the vibration, the heating can impulsively excite the vibrational modes correlated with expansion.<sup>119,146</sup> However, the thermal expansion alone can not describe the onset and phase of the oscillation. Recently, Hoening *et al.* reported time-resolved X-ray scattering experiments on AuNPs that prove that the breathing oscillations onset is faster than the electron-phonon coupling time. Including optically induced electron density gradients as an additional driving force for breathing oscillations, they were able to describe the phase of oscillation appropriately.<sup>148,149</sup>

The breathing oscillation is damped by energy transfer to the environment. Furthermore, in ensemble measurements such as TA spectroscopy, an additional dephasing contribution is observed. As the oscillation time of the breathing mode depends on the particle's size, the size distribution naturally occurring in wet-chemically produced AuNPs leads to the dephasing of the oscillation.<sup>119</sup>

*Interband excitation:* Spectral overlap of the pump pulse with the spectral region of interest of the probe pulse can render TA data unusable if the measured signal cannot be properly corrected for scattered photons incident on the detector. Hence, in many studies reported in literature as well as in the project presented in Chapter 5.2 of this thesis, off-resonant interband excitation is used to study electron-phonon coupling in AuNPs. The created d-band holes (*cf.* Figure 3.7) recombine by transferring their energy to the conduction electrons *via* an Auger<sup>1</sup> process.<sup>150</sup> Subsequently, rapid thermalization of excited electrons with the electron bath renders electron-phonon coupling in AuNPs independent of the employed pump wavelength. Hence, resonant excitation (and subsequent Landau damping) of the LSPR and excitation of interband transitions (*cf.* Figure 3.7) yield the same electron-phonon coupling behavior given that the same amount of energy was deposited into the AuNPs,<sup>151</sup> as in this case the same initial rise in electron temperature is established.<sup>2</sup>

### 3.3.5 Phonon coupling to the environment

On a timescale of hundreds of picoseconds to some nanoseconds, the energy is transferred from the AuNPs to the environment *via* phonon-phonon coupling, effectively heating the environment (*cf.* Figure 3.9(b)). The interplay of the interface conductance and the heat dissipation in the environment leads to a complicated size dependency with accelerated phonon-phonon coupling for decreasing particle sizes.<sup>146,152</sup>

---

<sup>1</sup>See Chapter 4.3.2 for a more detailed explanation of Auger processes.

<sup>2</sup>To ensure comparable induced changes in the initial electron temperature for different pump wavelengths, the pump fluence has to be adjusted according to the absorption of the sample at the respective wavelength.



# 4. Charge carrier dynamics in semiconductor nanocrystals

In this chapter a description of the optical properties of semiconductor NCs and the processes occurring after absorption of optical light is given. The chapter focuses on Cd-chalcogenide-based NCs as the main semiconducting material class studied in this thesis.

## 4.1 Optical properties of bulk and nanoscale semiconductors

### Bulk semiconductors

The electronic structure of bulk semiconductors consists of a fully occupied valence band (VB) and an empty conduction band (CB) that are energetically separated by the band gap energy ( $E_g$ ). The absorption of a photon carrying a photon energy  $h\nu$  larger than  $E_g$  leads to the excitation of an electron from the VB to the CB, leaving behind a positively charged hole in the VB. As electrons and holes have opposite charges, they feel a Coulomb attraction. This Coulomb attraction can lead to the formation of a bound electron-hole pair, a so-called exciton, that can be described in analogy to the Bohr hydrogen model. The Bohr exciton radius  $a_0$  can be calculated from<sup>83</sup>

$$a_0 = \frac{4\pi\hbar^2\varepsilon}{e^2} \left( \frac{1}{m_e} + \frac{1}{m_h} \right), \quad (4.1)$$

where  $e$  is the electron charge,  $\hbar$  is the reduced Planck's constant,  $\varepsilon$  is the dielectric constant of the semiconductor and  $m_e$ ,  $m_h$  are the effective masses of electron and hole, respectively. The Bohr exciton radius is material-dependent and usually on the order of a few nanometers ( $a_0 = 2.8$  nm for CdS,  $a_0 = 5.8$  nm for CdSe).<sup>1</sup> Generally, the larger  $E_g$ , the smaller  $a_0$ .<sup>153</sup> In bulk semiconductors, the excitonic binding energy is usually on the order of the thermal energy, hence excitons are not stable at room temperature and dissociate into unbound electrons and holes.<sup>154</sup>

### Nanoscale semiconductors

For semiconductors in the size regime of the Bohr exciton radius, charge carriers are affected by the particle boundaries. This so-called quantum confinement leads to an increase in band gap with decreasing particle size. Furthermore, nanometer-sized semiconductors exhibit

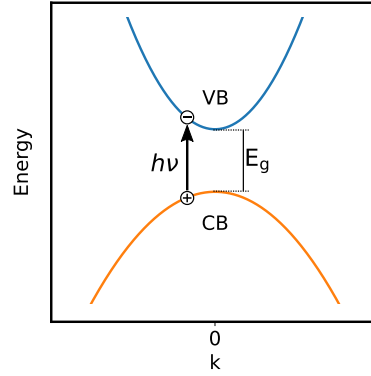


**Figure 4.1:** Absorption in bulk direct-band-gap semiconductors.

discrete, atom-like electronic energy levels rather than a continuum of electronic states. Electrons and holes can be described by the well-known particle-in-a-box model. The energy states of electron  $E_e$  and hole  $E_h$  as a function of the QDs radius  $R$  can be calculated as<sup>1,18</sup>

$$E_{e,n,L}(R) = \frac{\hbar^2 \phi_{n,L}^2}{2m_e R^2}, \quad (4.2)$$

$$E_{h,n,L}(R) = \frac{\hbar^2 \phi_{n,L}^2}{2m_h R^2}. \quad (4.3)$$

$n$  and  $L$  are the two quantum numbers that classify the envelope wave functions.  $L$  describes the wave function orbital momentum. The naming convention for  $L$  is borrowed from atomic physics (S, P, D, F for  $L=0,1,2,3$ ).  $n$  is the state number in a series of states with the same  $L$  ( $n=1,2,3,\dots$ ).  $\phi_{n,L}$  is the  $n^{\text{th}}$  root of the spherical Bessel function of the  $L^{\text{th}}$  order. For  $L=0$  and  $n=1$ , *i.e.* the 1S band edge state,  $\phi_{1S} = \pi$ . The sum of the energies of the lowest electron and hole state is the confinement energy  $E_{conf}$ <sup>18</sup>

$$E_{conf}(R) = E_{e,1S} + E_{h,1S} = \frac{\hbar^2 \pi^2}{2R^2} \left( \frac{1}{m_e} + \frac{1}{m_h} \right). \quad (4.4)$$

Summation of the bulk band gap  $E_g^{bulk}$  with the confinement energy  $E_{conf}$  yields the QDs band gap, whereby also the Coulomb-attraction between electron and hole  $E_C$  has to be taken into account:<sup>155,156</sup>

$$E_g(R) = E_g^{bulk} + E_{conf}(R) - E_C(R) \quad (4.5)$$

Equation (4.5) is the so-called Brus formula.  $E_C$  can be calculated as

$$E_C(R) = \frac{1.8e^2}{\epsilon R}. \quad (4.6)$$

A decreasing particle radius leads to the confinement term in Equation (4.5) increasing, while the Coulomb term decreases. For small radii, the confinement term dominates, effectively leading to an increase in band gap for decreasing particle sizes.<sup>157</sup> Therefore, the confinement energy allows to tune the emission of QDs across the whole optical frequency

## 4.2. Different types of colloidal semiconductor nanocrystals

range. Figure 4.2 schematically shows the absorption between the discrete energy levels in a QD. In real QD samples, size distribution, as well as thermal effects, lead to an inhomogeneous broadening of the absorption resonances. The absorption spectra can therefore best be described by multiple Gaussian components with a polynomial background.<sup>158</sup>

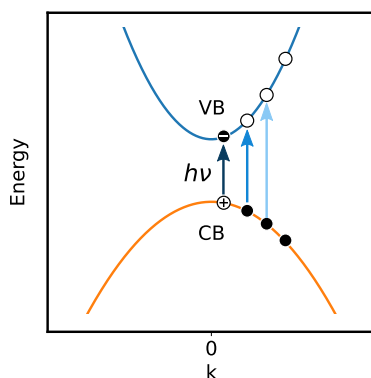


**Figure 4.2:** Schematic depiction of optical transition in QDs that exhibit quantized energy levels.

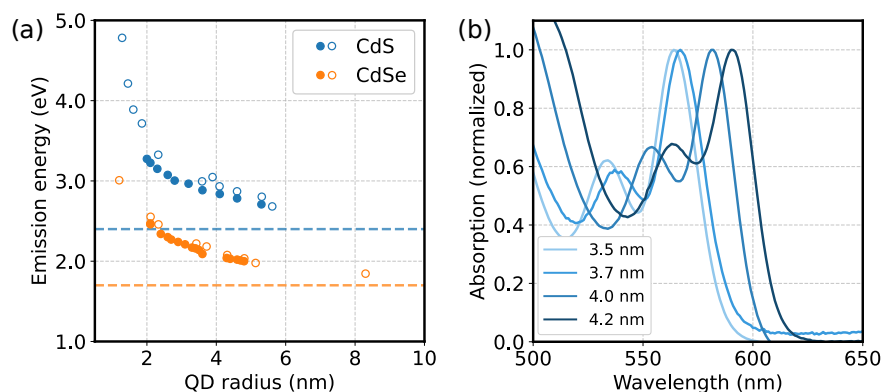


**Figure 4.3:** (a) Emission energy vs. QD radius for CdSe and CdS QDs. Dashed lines show the bulk band gap energies of the corresponding semiconductor.<sup>159</sup> Values taken from literature: CdS: blue dots<sup>160</sup>, blue open circles<sup>161</sup>. CdSe: orange dots<sup>162</sup>, orange open circles<sup>35</sup>. (b) Exemplary absorption spectra of CdSe QDs of different diameters that show inhomogeneously broadened discrete optical transitions and the size-dependency of the lowest transition.

## 4.2 Different types of colloidal semiconductor nanocrystals

Chapter 4.1 explains quantum confinement on the example of spherical NCs. However, wet-chemical approaches allow to synthesize colloidal NCs with a plethora of shapes. The physical properties of NCs, and hence their possible applications, do significantly depend on their dimensionality. Besides the zero-dimensional QDs, one-dimensional nanorods, two-dimensional nanoplatelets, and more complicated shapes are nowadays readily available.<sup>163</sup> The following chapter briefly discusses the properties of non-spherical NCs as well as heteronanostructures.

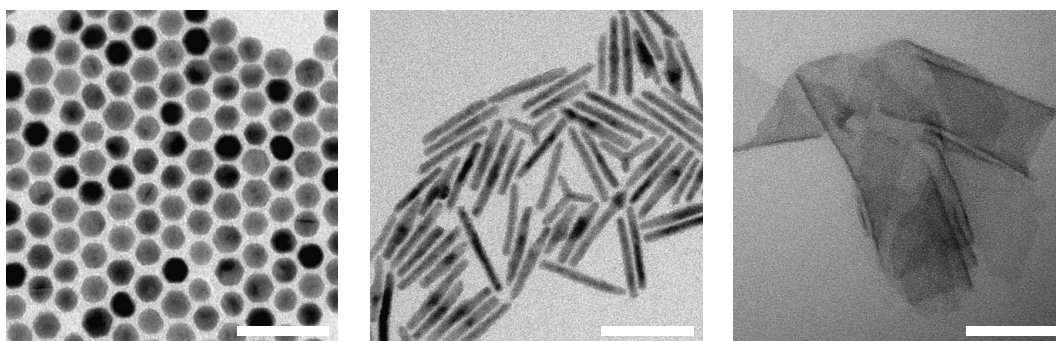


**Figure 4.4:** Exemplary TEM images of the samples studied in this thesis. Left: 0D-QDs (see Chapter 5.3). Middle: 1D-Nanorods (see Chapter 5.3). Right: 2D-Nanoplatelets (see Chapter 6.1). All scale bars correspond to 50 nm.

### Nanorods

Nanorods (or quantum rods) are elongated semiconductor nanomaterials that exhibit quantum confinement in two directions. The optical properties therefore depend much more on the lateral thickness of the rod than its length.<sup>164</sup> The physical anisotropy leads to an optical anisotropy: light emitted perpendicular to the long axis is linearly polarized along this axis.<sup>165</sup> Nanorods (and heterostructures thereof<sup>166</sup>) are heavily studied for their photocatalytical properties,<sup>11,167–169</sup> since they are in many cases catalytically more active than their spherical counterparts.<sup>170</sup>

### Nanoplatelets

Two-dimensional nanoplatelets have a large lateral size but are only a few monolayers thick, hence quantum confinement is limited to their z-axis. Nanoplatelets can be synthesized with atomically precise thickness, *i.e.* near-perfect monodispersity along the quantum-confined dimension.<sup>171</sup> Therefore, ensembles of colloidal nanoplatelets do not suffer from inhomogeneous broadening, which results in optical features much narrower than observed in QDs or NRs. The absorption spectra of Cd-based nanoplatelets usually show two distinct absorption maxima, which can be attributed to heavy hole (lower energy) and light hole transitions (higher energy), as the valence band energy levels are split in nanoplatelets.<sup>172</sup> Exciton binding energies and oscillator strengths are usually higher than in QDs.<sup>173</sup> The narrow optical features make nanoplatelets an interesting candidate for various applications.<sup>174</sup> In lasing, low threshold and high gain values were observed for nanoplatelets.<sup>175</sup>

### Heteronanostructures

Heteronanocrystals (or hybrid NCs) consist of two or more different semiconductor material domains. Modern wet-chemical synthesis allows to control size and shape of each domain and therefore offers a whole library of NCs (*e.g.* spherical core-shell particles, dot-in-rod particles, rod-in-rod particles, core-shell platelets, core-crown platelets, Janus particles).<sup>9,10</sup> In this thesis, core-shell NCs are studied, in which the core-material is fully enclosed by

## 4.2. Different types of colloidal semiconductor nanocrystals

the shell-material. The optical properties of a heteronanocrystal are dictated by the relative energies of the valence and conduction bands of its components. Figure 4.5 shows three types of possible band alignment in core-shell NCs. In type I particles, the band gap of the shell material encloses the band gap of the core material. After optical excitation, both electrons in the conduction band and holes in the valence band do therefore localize in the core material. In type II materials, electrons and holes are spatially separated into the two domains due to the staggered band alignment. Finally, in so-called quasi type II structures, one charge carrier is localized in one material, whereas the other charge carrier is delocalized over both materials due to a small band offset.

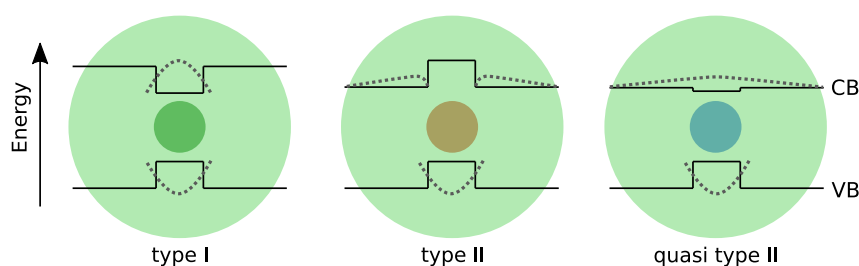


**Figure 4.5:** Three types of heterostructures and their band alignment (dotted lines schematically represent the electron and hole wavefunction): In type I structures, electron and hole are located in the same material. In type II structures, the charge carriers are separated into the two materials, due to the staggered band alignment. In quasi type II structures, as the band offset is small, one of the charge carriers is delocalized over both materials.

By carefully selecting the employed materials, NCs with specific band alignment can be synthesized. However, as the band gap in NCs depends on the particle size, a certain combination of materials does not necessarily lead to a certain band alignment.<sup>176,177</sup> Due to the large valence band offset and the small conduction band offset of CdSe and CdS,<sup>178</sup> CdSe-CdS core-shell NCs can be type I or quasi type II, depending on the CdSe core size,<sup>179,180</sup> CdS shell size and shape.<sup>181,182</sup> Shelling of NCs with a larger-band gap material generally improves photoluminescence quantum yield due to the saturating of dangling bonds, which can act as trap states.<sup>183,184</sup> Also, large shells can prevent blinking,<sup>185,186</sup> as will be further discussed in Chapter 4.3.2.

### Metal-semiconductor nanohybrids

Besides heteronanocrystals consisting of multiple semiconductor materials, metal-semiconductor hybrids are a second well-researched class of nanohybrids. Such hybrids are especially interesting for catalytic applications, as they combine the functionalities of their components.<sup>187</sup> The semiconductor domain can function as a light-collecting antenna and transfer excited electrons to the metal domain, which can then serve as a catalytic surface for redox reactions. With the electron in the metal domain and the hole remaining in the semiconductor domain, long-lived charge separation can be established, which is crucial for chemical reactions taking place on the NC's surface.<sup>188</sup> Metal-tipped CdSe/CdS dot-in-rod particles (DRs) serve as a model system for photocatalytic hydrogen generation.<sup>11,12,168</sup> Several parameters have been optimized for photocatalysis, such as seed size,<sup>189</sup> rod length,<sup>190</sup> tip size,<sup>191,192</sup> tip number<sup>193</sup> and material<sup>194,195</sup> and chemical environment.<sup>196</sup> In this struc-

ture, the photogenerated holes localize into the CdSe core. Removal of these holes turned out to be a crucial step for efficient hydrogen generation.<sup>196–198</sup> Electron donating agents are added to extract the holes,<sup>197,198</sup> effectively preventing charge recombination and photo-oxidation of the semiconductor domain.<sup>199</sup> Kalisman *et al.* reported near unity hydrogen evolution quantum yields on Pt-tipped CdSe/CdS DRs at high pH values.<sup>200</sup> Furthermore, full water splitting was achieved by introducing a molecular co-catalyst for the oxygen evolution reaction.<sup>201</sup>

### 4.3 Charge carrier dynamics

This chapter describes the relaxation of charge carriers in semiconductor NCs after optical excitation. As TA is the main tool to unravel the relaxation processes, the first part of the chapter focuses on the mechanisms leading to contrast in a TA experiment of semiconductor NCs, followed by a description of the processes leading to charge carrier relaxation in order of increasing time scales. OPTP is discussed as a second means to study photoexcited charge carriers in semiconductor NCs. The chapter concludes with a literature overview of OPTP experiments on NC samples.

#### 4.3.1 Transient absorption experiments on semiconductor nanocrystals

In TA experiments of semiconductor NCs, the pump pulse photon energy is usually set so it can excite electrons above the band gap. The three main contributions yielding contrast in the experiment (*i.e.* different absorption properties of the sample in its excited state as compared to its ground state) are schematically shown in Figure 4.6.

*Ground state bleach:* After optical excitation, electrons occupy the quantized states at the conduction band edge in the excited sample, which leads to a weaker absorption of the probe pulse due to the Pauli exclusion principle (*cf.* Figure 4.7). This results in negative differential absorption, the so-called ground state bleach (GSB). It can be investigated for quantitative analysis of the number of excited charge carriers per particle, which follows a Poisson statistic (see below).<sup>202–205</sup> In Cd-based NCs, GSB is dominated by electrons (*i.e.* state filling of the conduction band) with only a minor contribution of holes (state filling of the valence band) due to a high degeneracy of band edge hole states.<sup>206</sup> Literature reports suggest that the exact relative amounts of electron and hole contribution depend on surface passivation,<sup>207</sup> probe spectral region<sup>208</sup> and shape of the investigated particles.<sup>209</sup> GSB features usually spectrally coincide with the linear absorption features (*cf.* Figure 4.7).

*Photoinduced absorption:* The probe pulse can induce transitions of the pump-excited charge carriers into even higher energy levels. This photoinduced absorption (PIA) results in a positive differential absorption. In Cd-based NCs, a broad PIA feature can often be observed at long probe wavelengths due to surface-trapped holes being excited deeper into the valence band (*cf.* Figure 4.11).<sup>210–212</sup>

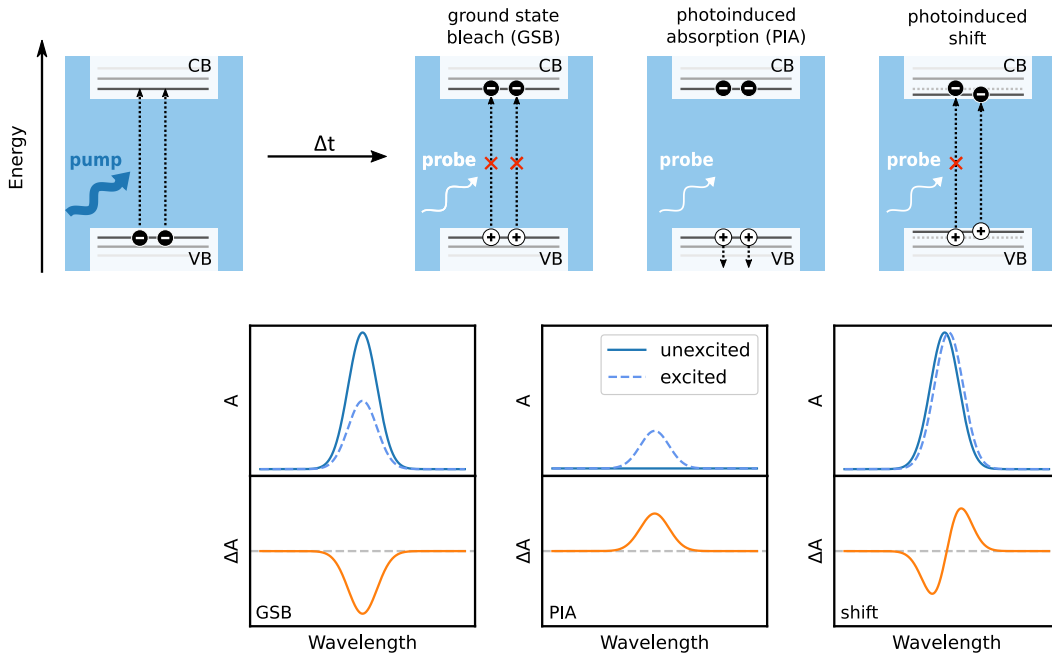


**Figure 4.6:** Contrast giving mechanisms in TA experiments of semiconductor NCs: The pump pulse excites electrons above the band gap into the conduction band, leaving holes inside the valence band. After a certain delay time, the probe pulse arrives at the sample. Due to state filling, the excited NCs absorb less light from the probe pulse than the unexcited NCs, resulting in negative differential absorption (ground state bleach). Photoinduced absorption occurs when absorption from the excited state into higher excited states is possible, yielding positive differential absorption. A spectral shift of an optical transition leads to a derivative-like differential absorption.

*Photoinduced shift:* The presence of excited charge carriers can shift energy levels within the NC due to Coulomb interactions, which results in a derivative-like differential absorption with both negative and positive components. An exciton created by the pump pulse leads to a shift of the excitonic absorption wavelength for the probe pulse. This can be used to study biexcitonic binding energies in NCs.<sup>213</sup>

### Quantifying the number of excitons per nanocrystal

In TA experiments of semiconductor NCs,<sup>1</sup> the number of excitons  $N$  initially created in each NC is essentially determined by the pump fluence  $J$  and the absorption cross-section of the NCs  $\sigma_{abs}$ . The excitation is governed by Poisson statistics, hence at a certain excitation fluence, not every NC contains the same number of excitons. Rather, a distribution of NCs containing different exciton numbers with a certain average exciton number  $\langle N \rangle$  is established. The probability  $P(\langle N \rangle, N)$  of a NC containing  $N$  excitons is given by

$$P(\langle N \rangle, N) = \frac{\langle N \rangle^N}{N!} e^{-\langle N \rangle}. \quad (4.7)$$

<sup>1</sup>The following derivation was reproduced from Gramlich *et al.*, who provided an excellent explanation on the Poisson excitation statistics in colloidal NCs.<sup>202</sup>

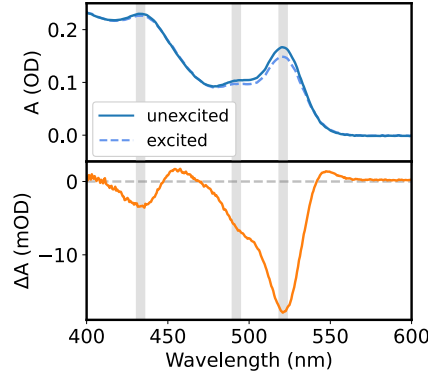


**Figure 4.7:** Exemplary absorption spectrum and differential absorption spectrum after excitation with above band gap photons (350 nm pump wavelength, 10 ps after excitation) of 3 nm CdSe QDs. The bleach features in the differential spectrum resemble the excitonic absorption features.

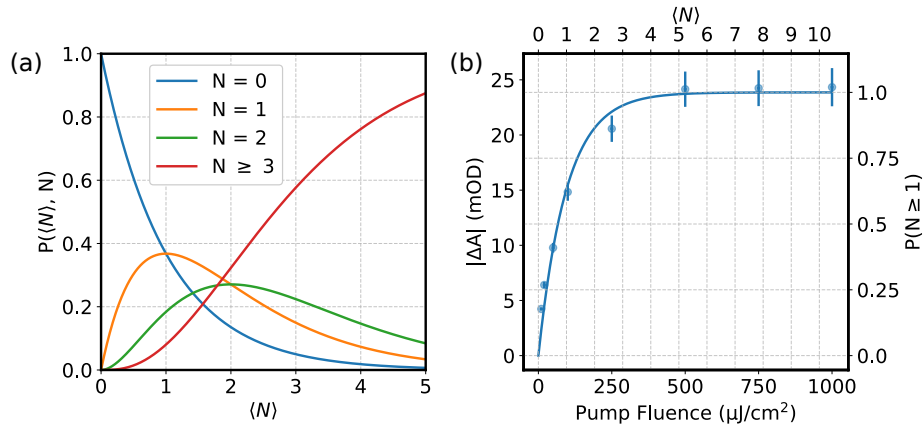


**Figure 4.8:** (a) Probability of a NC containing a certain number of excitons  $N$  at a certain average number of excitons per particle  $\langle N \rangle$ . Reproduced with permission from Gramlich *et al.*<sup>202</sup> (b) Absolute of mean bleach of the CdS shell bleach averaged from 3 to 5 ns for CdSe-CdS giant-shell QDs versus pump fluence.

Figure 4.8 shows the probability of a NC containing zero, one, two or more excitons depending on the average number of excitons per NC  $\langle N \rangle$ . In an ensemble measurement such as TA, the probability that a NC contains exactly  $N$  excitons  $P(\langle N \rangle, N)$  corresponds to the fraction of NCs containing  $N$  excitons.

If multiple excitons per NC are created, they interact *via* Auger recombination (see below) until eventually only one exciton per NC remains. Auger recombination usually occurs within tens to hundreds of picoseconds, single exciton decay due to radiative recombination on timescales of tens to hundreds of nanoseconds.<sup>18</sup> Hence, at single-digit nanosecond delay times, multi-excitons have been diminished due to Auger recombination, but little exciton decay due to radiative recombination has taken place. Therefore, all NCs that initially carried one or more excitons carry exactly one exciton at these delay times. The fraction of NCs containing one exciton can be described as

$$P(\langle N \rangle, N \geq 1) = 1 - P(\langle N \rangle, N = 0) = 1 - e^{-\langle N \rangle}. \quad (4.8)$$



This means that the GSB at such delay times in the TA experiment can be regarded as a measure of how many NCs initially contained one or more excitons. At high pump fluences, every NC initially contains at least one exciton, hence the mean GSB at such delay times saturates. The mean GSB at single-digit nanosecond delay times versus pump fluence can be described as

$$|\Delta A| = A_{max} \cdot (1 - e^{(-C_{ex} \cdot J)}), \quad (4.9)$$

where  $A_{max}$  is the saturation value.  $C_{ex}$  is a constant that relates the pump fluence  $J$  with the mean number of excitons  $\langle N \rangle$

$$\langle N \rangle = C_{ex} \cdot J. \quad (4.10)$$

The NC's absorption cross section  $\sigma_{abs}$  can be calculated using the photon energy  $E_{ph}$  as

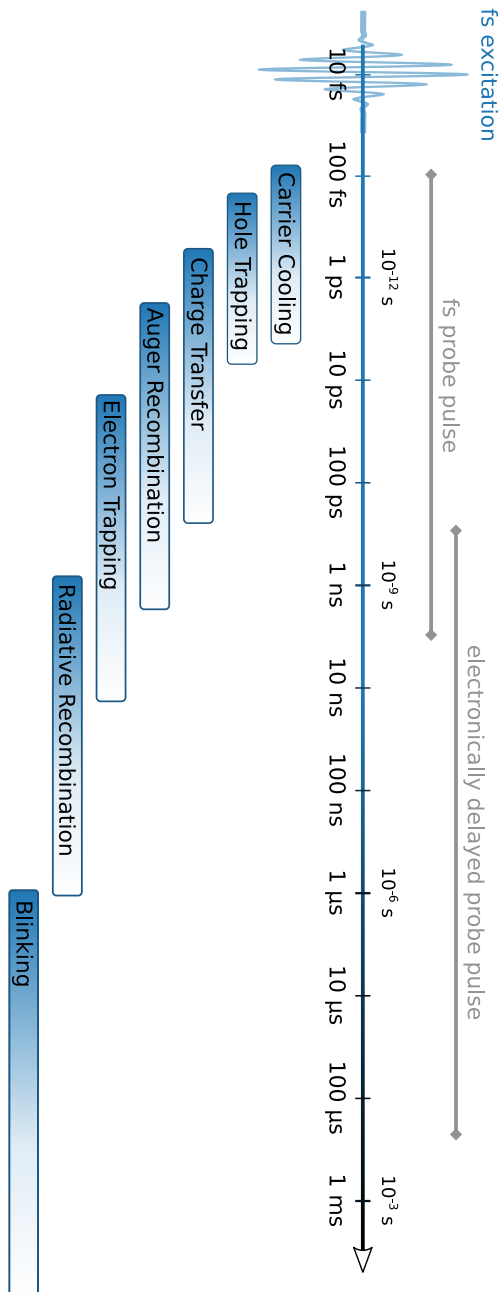
$$\sigma_{abs} = E_{ph} \cdot C_{ex}. \quad (4.11)$$

Figure 4.8(b) exemplarily shows the mean bleach at single nanosecond delay times for the CdS GSB of the giant-shell CdSe-CdS QDs employed in Chapter 6.2 versus pump fluence. As the mean exciton number  $\langle N \rangle$  linearly depends on the pump fluence, it can be plotted as a second x-axis. The fraction of NCs initially containing one or more excitons is plotted as a second y-axis.

### 4.3.2 Relaxation processes

#### Carrier cooling

After excitation with above band gap photon energies, electrons and holes carry excess energy. These so-called "hot carriers" relax to the band edge on the femtosecond to picosecond timescale, a process that is referred to as carrier cooling or carrier thermalization.<sup>157,214</sup> In bulk semiconductors, charge carriers can cool *via* electron-phonon coupling due to the continuous electronic DOS. In NCs, due to the quantized nature of the electronic energy states, carrier cooling due to interaction with phonons was expected to be much slower, an effect termed the "phonon bottleneck".<sup>215,216</sup> It was shown that due to the valence band energy states being denser than the conduction band states, the phonon bottleneck is less strongly developed for holes than for electrons.<sup>217</sup> Energy can be transferred from electrons to holes *via* an Auger-type interaction. Subsequently, the holes can cool to the band edge, effectively circumventing the electronic phonon bottleneck.<sup>218</sup> Surface-ligands vibrations can also contribute to carrier cooling in NCs.<sup>219,220</sup> In TA measurements, carrier cooling can be observed as a rise of the band edge bleach feature.<sup>221,222</sup> Figure 4.10 exemplarily shows the rise of the lowest exciton bleach feature for 3 nm CdSe QDs after excitation with different photon energies above the band gap. A higher excess energy leads to a longer rise time in the experiment, *i.e.* slower carrier cooling. Furthermore, hot carriers broaden the GSB feature. Analysis of the high-energy tail of that feature was used to assess carrier temperatures in NCs.<sup>223,224</sup>



**Figure 4.9:** Schematic overview over the processes happening in semiconductor NCs after light absorption. TA experiments with femtosecond probe pulses and electronically delayed picosecond probe pulses allow gap-less probing of delay times from the hundred femtoseconds to the hundred microseconds regime, hence covering nine orders of magnitude.

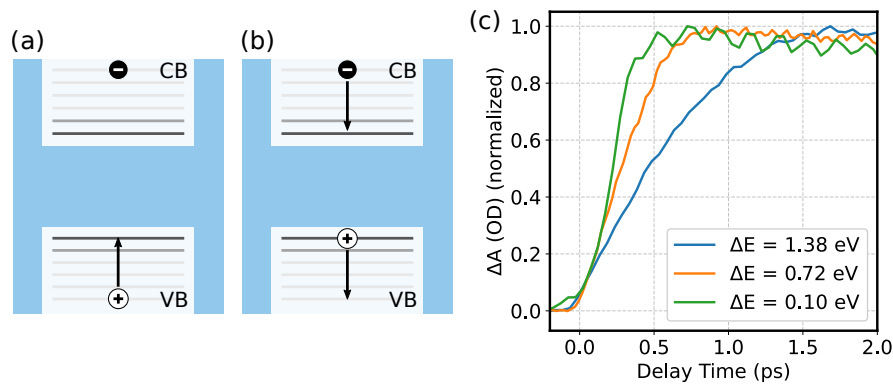


**Figure 4.10:** (a) Holes cool to the band edge *via* phonon-coupling. (b) Electrons cool to the band edge by transferring their energy onto holes in an Auger-like interaction. The thereby excited hole subsequently cools to the band edge as shown in (a). (c) Rise of the band edge excitonic bleach feature in 3 nm CdSe QDs for three pump pulses with varying photon energy above the band gap. The more excess energy electrons and holes carry, the slower the cooling to the band edge.

### Carrier trapping

Due to their high surface-to-volume ratio, NCs possess many surface states. Surface defects or dangling bonds can form states within the band gap, which can act as trap states for charge carriers. Hole trap states arise from unpassivated chalcogenide atoms in the NCs surface, electron traps from undercoordinated Cd-atoms, respectively.<sup>225,226</sup>

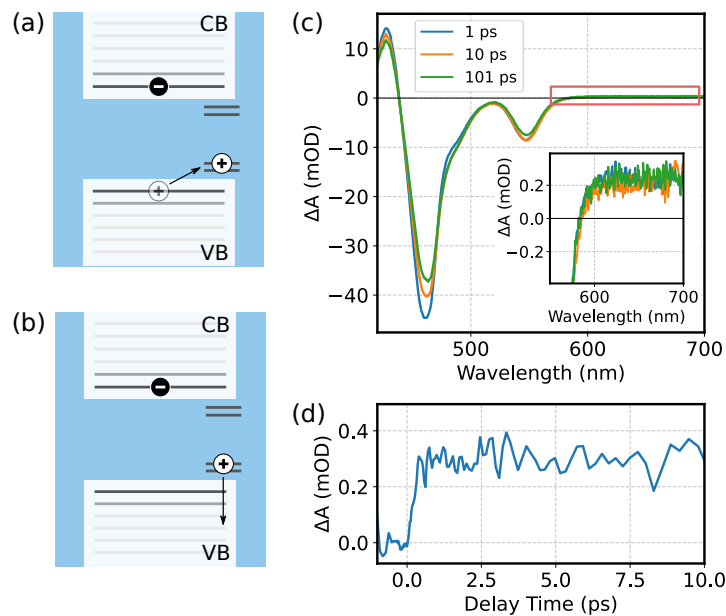


**Figure 4.11:** (a) Localization of holes into surface trap states. (b) Excitation of trapped holes into the VB which can be observed as a PIA in TA. (c) TA spectra of CdSe-CdS DRs. Inset: Zoom on long probe wavelengths. A broad PIA of trapped holes is observable. (d) TA dynamics of PIA of trapped holes (averaged over the probe wavelength range from 600 to 700 nm). From the fast rise of the PIA feature, it can be inferred that hole trapping takes place on below-picosecond timescales.

In the TA spectra of Cd-based QDs<sup>212</sup> and NRs,<sup>188</sup> a broad PIA feature in the red spectral region is observed, which is ascribed to trapped holes being excited deeper into the valence band. This assignment was confirmed by the addition of hole-accepting ligands, which accelerate the decay of the PIA feature, whereas the addition of electron-accepting species does not alter the observed dynamics.<sup>227</sup> Atomistic calculations further support the assignment.<sup>211</sup> The PIA feature arises within less than a picosecond in the measurement on CdSe-CdS DRs exemplarily shown in Figure 4.11, which is in agreement with fast hole trapping times reported in literature.<sup>188,228,229</sup>

Earlier, trapped holes were thought to be localized at one trap site until their recombination.<sup>230</sup> However, Dukovic *et al.* reported that trapped holes on the surface of Cd-chalcogenide NRs are not localized, but rather hop from one trap site to another. They describe the motion of trapped holes as a 1D diffusive random walk along the NR's z-axis.<sup>231–234</sup>

As commonly used ligands bind to Cd<sup>2+</sup>, electron traps are often well passivated and therefore less important for the properties of the NCs.<sup>235,236</sup> It was shown that for CdS NRs, there is on average less than one electron trap per NC.<sup>237,238</sup> Electron trapping times ranging from tens of picoseconds to nanoseconds were reported.<sup>236,239</sup>

### Charge transfer

In hybrid systems, charge carriers localize into the lower-band gap material on a timescale of hundreds of femtoseconds to a few picoseconds.<sup>240–242</sup> In CdSe-CdS DRs that can exhibit either type I or quasi type II band alignment, charge carriers that are excited in the CdS shell material localize into the CdSe core material (in type I systems) or delocalized over core and shell (electrons in quasi type II systems). This charge transfer from shell to core can be observed in TA measurements, where the bleach features of core and shell are spectrally separated. As shown in Figure 4.12, the fast decay component observed in the shell bleach coincides with the rise time of the core bleach feature.<sup>243</sup>

NRs and DRs are usually synthesized by growing an elongated shell onto a spherical seed.<sup>9,10</sup> This often results in the final rod being not perfectly cylindrical, but having a higher diameter around the rod position.<sup>244</sup> The thicker part of the rod is usually termed the bulb region and exhibits decreased quantum confinement as compared to the thinner part of the rod. This leads to lower CB and higher VB levels in the bulb region, which can result in type I band alignment in single-material rods.<sup>231</sup> Due to the smaller band gap energy, the bulb region can be observed as a shoulder in the TA data and charge transfer from rod to bulb can be observed (*cf.* Figure 4.12).<sup>231–234</sup>

In semiconductor-metal hybrids, electron transfer from the semiconductor domain to the metal domain can also be observed as a fast decay component of the semiconductor bleach signal in TA.<sup>188,196</sup> In both metal-tipped CdS NRs and CdSe-CdS DRs, charge separation of the electron in the metal tip and the hole in the semiconductor domain leads to a Stark

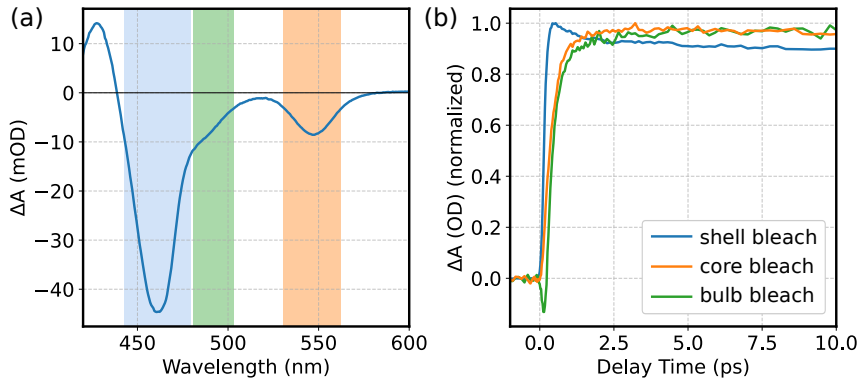


**Figure 4.12:** (a) TA spectra at 1 ps delay time after shell excitation in CdSe-CdS DRs. Shell, bulb and core bleach are highlighted in blue, green and orange, respectively. (b) Normalized bleach dynamics of the three features. The shell bleach rises within the time resolution of the experiment and shows a fast decay component in the single-digit picosecond time range. Bulb and core bleach show rise times comparable with this fast decay component of the shell bleach, indicating charge transfer from shell to both core and bulb.

effect induced red-shift of the CdS absorption. A positive shift signal can be observed in TA, revealing lifetimes of the charge-separated state in the microsecond regime.<sup>188,192,195</sup>

### Auger recombination

At sufficiently high photon densities, more than one electron-hole pair can be created in a single NC. The interaction of multiple excitons in a NC can lead to the relaxation of an exciton without the emission of a photon. The energy of the relaxing exciton is transferred onto a charge carrier of the other exciton, effectively sending either the electron or the hole deeper into the CB or VB, respectively.<sup>205,245</sup> This so-called Auger recombination is schematically shown in Figure 4.13(a) and (b). As the Auger-excited charge carrier thermalizes to the band edge, Auger recombination effectively results in an energy loss as heat. The Auger recombination time  $\tau_{XX}$  is usually measured in TA by comparing the bleach recovery dynamics of NCs after excitation with several excitation fluences. At low excitation fluence, zero or one exciton per particle are created, *i.e.* Auger recombination is not observable. As at higher fluences, multiple excitons per particle are created, an additional component is observed in the bleach recovery dynamics. Subtracting the single exciton dynamics from the multiple exciton dynamics allows to isolate the Auger recombination dynamics. Note that at too high excitation fluences, there will be NCs containing more than two electron-hole pairs, which again alters the bleach recovery dynamics.<sup>246</sup> Gramlich *et al.* comprehensively showed how to choose appropriate pump photon densities to isolate bi-excitonic Auger recombination from higher-order Auger recombination.<sup>202</sup> Figure 4.13(c) and (d) show the bleach recovery dynamics after excitation with several fluences in 4 nm CdSe NCs as well as the difference in single exciton dynamics and biexciton dynamics.

It was shown that in NCs of several materials, the Auger recombination time  $\tau_{XX}$  scales with the NCs volume (so-called volume scaling law or "V-scaling"),  $\tau_{XX} = \chi V$ .<sup>247</sup> In Cd-based NCs, scaling constant  $\chi$  is usually around  $1 \text{ ps nm}^{-3}$ .<sup>18,204</sup> The exemplary data shown in Figure 4.13 for 4 nm CdSe NCs ( $V = 33.5 \text{ nm}^3$ ) is in agreement with this value, as the Auger recombination time is 28 ps.

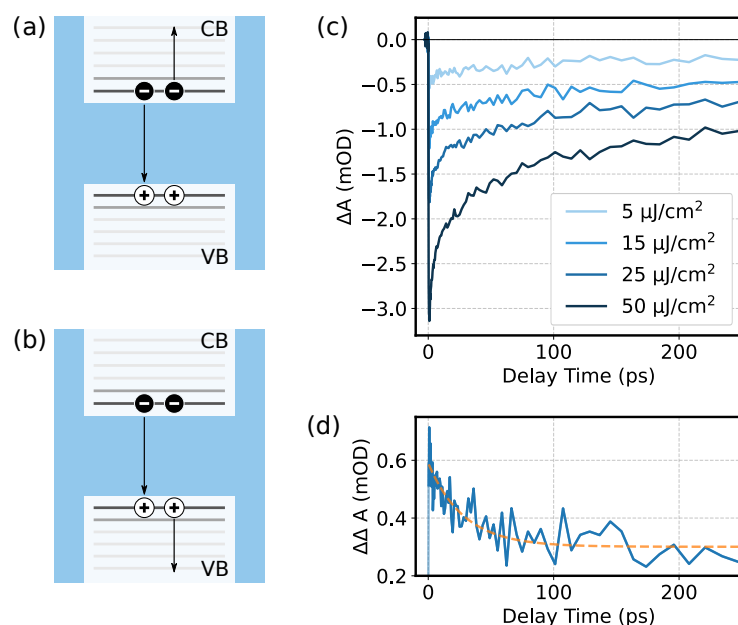


**Figure 4.13:** (a),(b) Schematic illustration of the Auger recombination mechanism. The energy of one exciton is transferred to either electron or hole of the other exciton, whereby the former relaxes non-radiatively and the latter is excited into the CB or VB, respectively. (c) Bleach recovery dynamics of 4 nm CdSe QDs after excitation with several pump fluences. (d) The difference in the bleach recovery dynamics of the  $5 \mu\text{J}/\text{cm}^2$  measurement (none or one exciton per particle) and the  $15 \mu\text{J}/\text{cm}^2$  measurement (none, one or two excitons per particle) (blue line). A single-exponential fit (dashed orange line) yields an Auger recombination time  $\tau_{XX}$  of 28 ps.

Auger recombination is detrimental for NC lasing applications, as optical gain from NCs requires the presence of biexcitons or higher multiexcitons.<sup>248</sup> Auger recombination limits gain lifetimes and leads to a high gain threshold.<sup>17</sup> To overcome this issue, giant core-shell QDs were developed, which exhibit longer biexciton lifetimes.<sup>185,249</sup> Furthermore, compositionally graded shells with smoothed band alignment relax the carrier confinement and hinder Auger recombination.<sup>250,251</sup> By employing giant core-shell QDs with graded shells, Auger lifetimes in the single-digit nanosecond regime could be reached.<sup>252,253</sup>

### Radiative recombination

Radiative recombination of an electron at the band edge of the CB and a hole at the band edge of the VB by emission of a photon is the desired recombination pathway for applications like light-emitting diodes (LEDs),<sup>254</sup> displays<sup>14</sup> or lasing.<sup>18</sup> Time-resolved photoluminescence techniques like time-correlated single photon counting are used to study radiative recombination.<sup>255</sup> Radiative lifetimes are usually in the nanosecond regime for Cd-based NCs, depending on shape and composition. Type II systems usually show long radiative lifetimes, as they possess small electron-hole overlap.<sup>256</sup>

The quantum efficiency  $\eta$  of radiative recombination can be written as<sup>255</sup>

$$\eta = \frac{\gamma_{rad}}{\gamma_{rad} + \gamma_{non-rad}}, \quad (4.12)$$

where  $\gamma_{rad}$  and  $\gamma_{non-rad}$  are the radiative and non-radiative decay rates, respectively. Passivation of surface trap states by shelling with a second semiconducting material (*i.e.* in type I systems) improves quantum efficiency by reducing the non-radiative decay rate.<sup>183,184</sup>

### Blinking

In PL measurements of single NCs, it is observed that their fluorescence intermittently turns on and off on timescales of microseconds to seconds.<sup>257,258</sup> This so-called blinking (or fluorescence intermittency) is not observable in ensemble measurements, where it averages out over the entirety of the ensemble. The exact origins and mechanisms of blinking are manifold and still under debate.<sup>259,260</sup> However, blinking is generally explained by charge carriers located in long-lived trap states. Auger recombination of excitons with these trapped charge carriers provides an efficient, non-radiative recombination channel, effectively turning the emission of the NC off.<sup>261</sup> Several strategies to suppress blinking have been developed, such as passivating trap states and suppressing Auger recombination.<sup>250,262</sup>

### 4.3.3 Optical-pump-terahertz-probe experiments on semiconductor nanocrystals

While TA mainly probes the occupation of electronic states after optical excitation, OPTP probes the electrical properties of the excited charge carriers. OPTP has several advantages over classical electrical measurements. Nanomaterials are difficult to contact electrically, causing classical electrical measurement techniques to fail. Even in case electrical contact can be made, the interface between the nanomaterial and the contact might dominate the measurement over the nanomaterials' internal electrical properties.<sup>263</sup> OPTP allows to gain knowledge on the nature of excited charge carriers in nanomaterials *via* an optical experiment, circumventing those difficulties. As OPTP probes a broad spectral range, it is capable of studying electrical properties within individual NCs as well as transport between them. Within individual NCs, OPTP is used to distinguish bound excitons from free charge carriers<sup>264</sup> and to study charge carrier localization.<sup>265,266</sup> Transport between NCs is governed by hopping, where OPTP is useful to differentiate between various hopping mechanisms.<sup>267</sup> The pump-probe character of the experiment further allows to study processes on ultrafast timescales.<sup>80</sup>

### Individual nanocrystals

THz spectroscopy can be employed to study excitons in QDs. The excitonic energy levels are separated by tens of meV<sup>268</sup> and transitions between such can therefore be resonantly probed by THz spectroscopy at high THz frequencies.<sup>269–272</sup> However, optical rectification, which is used by most laboratories to generate THz radiation, does not deliver such high THz frequencies, leaving transitions between excitonic states often experimentally inaccessible.

In such experimental configurations, only the low-frequency end of the Lorentz-Drude resonance can be observed (*cf.* Figure 2.14). In this case, the interaction of the THz radiation with the exciton is non-resonant. As electrons and holes in excitons are bound in a neutral quasiparticle, they do not follow the electric field. The THz electric field is rather polarizing the exciton. This results in a photoinduced change of the dielectric function that is purely real, *i.e.* a zero real conductivity and linearly rising imaginary conductivity. The change in the dielectric function allows to determine the exciton polarizability  $\alpha$ , which is a measure of how strong the electron and hole wave function are deformed under an applied electric field.<sup>84</sup> It was shown that the exciton polarizability grows with the fourth-power of the QDs radius for different QD materials (*cf.* Figure 4.14).<sup>273–275</sup> For CdSe NCs, exciton polarizabilities on the order of  $10 \text{ nm}^3$  were observed.<sup>273</sup> Bergren *et al.* studied the exciton formation in silicon QDs and reported slower exciton formation for smaller QDs, which they attributed to decreased electron-phonon coupling in small QDs.<sup>264</sup>

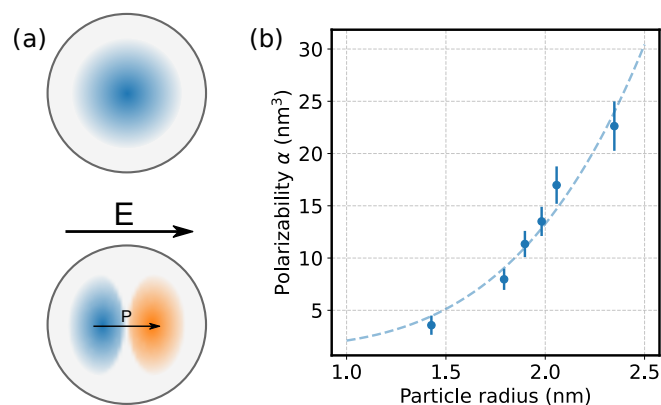


**Figure 4.14:** (a) Schematic representation of the excitonic polarizability by an electric field  $E$ . In the ground-state exciton, electron and hole wave functions are centered in the particle. The exciton is polarized under an applied electric field, effectively leading to a dipole moment  $P$ . (b) Exciton polarizability as a function of the particle radius for CdSe NCs. The dotted line shows the  $r^4$ -scaling. Data taken from Wang *et al.*<sup>273</sup> Reproduced with permission from Springer Nature.

Fast exciton formation (within a few picoseconds) was also observed in CdS nanorods<sup>276</sup> and CdSe nanoplatelets.<sup>277</sup> THz spectroscopic measurements on CdSe-CdS DRs show the existence of mobile electrons due to the fast localization of holes. Kunneman *et al.* could reproduce the measured photoconductivity with a classical model that takes the Coulomb interaction with the core-localized hole into account.<sup>278</sup> Larger nanorods exhibit higher charge carrier mobility.<sup>279</sup>

### Assemblies of nanocrystals

When NCs are assembled into larger structures, where they are arranged close to each other (*e.g.* by drop casting or more elaborate self-assembly techniques), higher conductivities can be observed than for NCs at high interparticle distances. THz spectroscopy can then be used to study the hopping of charge carriers between the NCs. Strong electronic coupling between the NCs is required to enable efficient hopping.<sup>280</sup> Native ligands that are attached



to the NCs surface after synthesis are usually electrically insulating and therefore not suited to allow for hopping between NCs in assemblies. In an earlier study, Beard *et al.* showed that the interparticle charge transport strongly depends on the interparticle distance, which was tuned using ligands of different lengths. They found a sixfold increase in photoconductivity when decreasing the interparticle distance of 3.2 nm InP NCs from 1.8 nm to 0.9 nm (*cf.* Figure 4.15(a)).<sup>281</sup> Gorris *et al.* were able to increase the conductivity of a film of CuInSe<sub>2</sub> NCs by orders of magnitude by altering the electronic structure of the ligand molecule. They employed fully conjugated molecules as bridging ligands and used OPTP to show that the charge transport is most likely hole-dominated (*cf.* Figure 4.15(c)).<sup>267</sup> Momper *et al.* observed purely imaginary photoconductivity in dispersed CdSe nanoplatelets (*i.e.* excitonic behavior) and real photoconductivity in assemblies thereof, whereby the direction of assembly strongly altered the charge transport properties (*cf.* Figure 4.15(d)).<sup>277</sup> High conductivities alone are not necessarily beneficial for application. Guglietta *et al.* measured both OPTP pump scans and THz scans on films of PbSe treated with either organic or inorganic ligands. They showed that even though the samples treated with inorganic ligands showed higher conductivity than the samples treated with organic ligands, they still exhibited shorter charge carrier diffusion lengths due to a faster decay of the transient photocurrent (*cf.* Figure 4.15(b)).<sup>282</sup> By removing the ligands of CsPbI<sub>3</sub> NCs, Sarkar *et al.* increased the interparticle conductivity, while at the same time enabling faster trapping at dangling bonds on the particles surface.<sup>283</sup> Under specific circumstances, band-like transport can dominate over hopping transport in nanoparticle solids.<sup>284</sup>

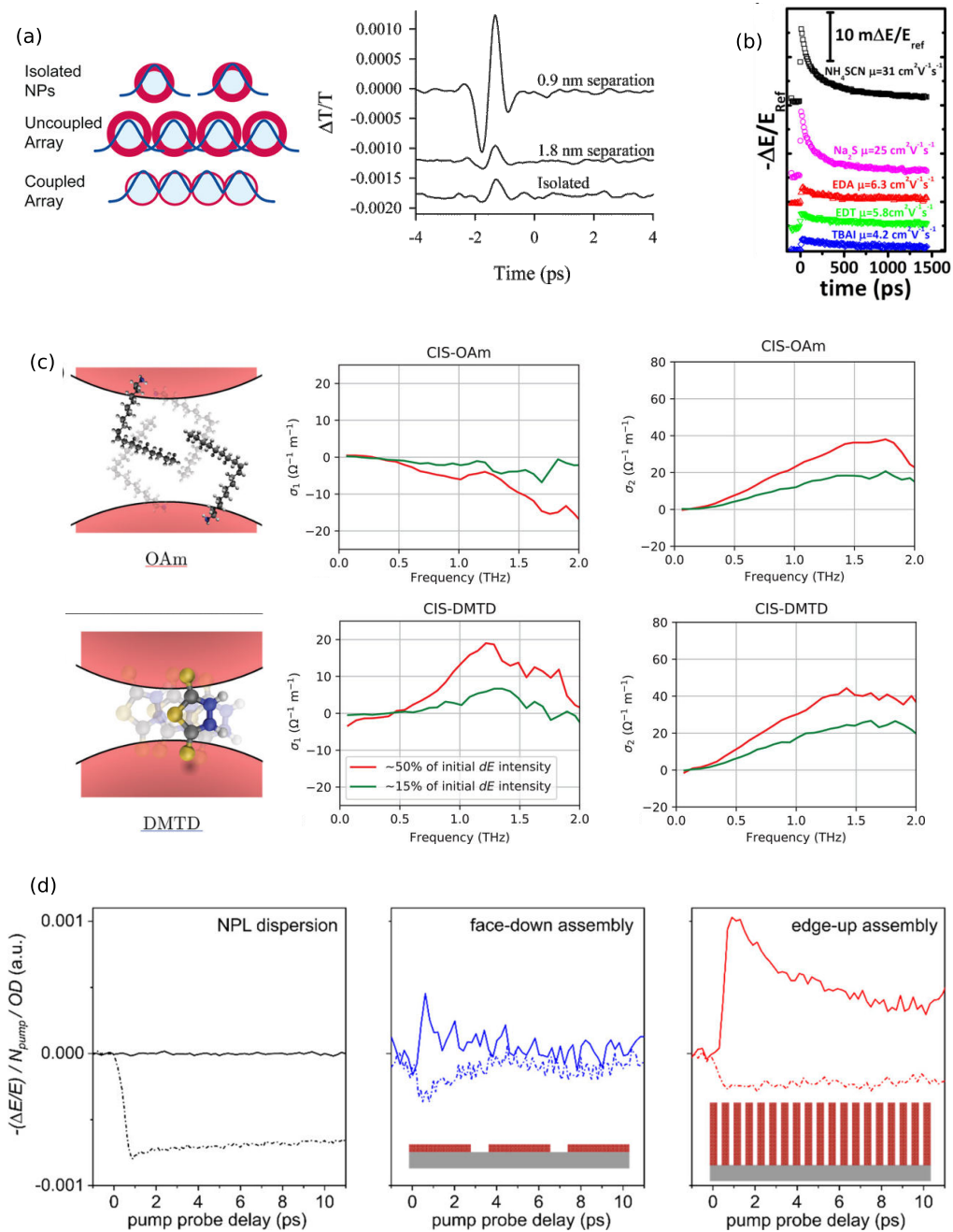


**Figure 4.15:** (a) Left: Schematic depiction of isolated NCs and dense arrays of NCs. Right: Densely packed NC assemblies show larger differential THz fields. Reprinted with permission from Beard *et al.*,<sup>281</sup> Copyright 2003 American Chemical Society. (b) OPTP pump scans of PbSe NC films with different ligands. Reprinted with permission from Guglietta *et al.*,<sup>282</sup> Copyright 2015 American Chemical Society. (c) Oleylamine (OAm) is electronically insulating and does therefore not allow efficient charge transport between CuInSe<sub>2</sub> NCs. Ligand exchange to the fully conjugated 2,5-dimercapto-1,3,4-thiadiazole (DMTD) leads to a significant increase in photoconductivity. Reprinted from Gorris *et al.*,<sup>267</sup> published under CC BY-NC 4.0 Deed. (d) Real (solid lines) and imaginary (dashed lines) photoconductivity of CdSe nanoplatelets. Reprinted from Momper *et al.*,<sup>277</sup> published under CC-BY.

# 5. Synopsis

## 5.1 Motivation

The suitability of a NC sample for certain optical applications often depends on the charge carrier relaxation processes after optical excitation. These relaxation processes are essentially determined by the structural properties of the NCs, such as size, shape, composition or crystallinity. Therefore, an in-depth understanding of the relation between structure and charge carrier relaxation is crucial for a targeted design of new materials for applications such as photocatalysis or photovoltaics. This thesis aims to contribute to the understanding of charge carrier dynamics in metal and semiconductor NCs as well as hybrids thereof. Furthermore, one of the presented projects deals with experimental uncertainties in OPTP.

## 5.2 Size-dependent electron-phonon coupling in monocrystalline gold nanoparticles

This publication is reprinted with permission from Yannic U. Staechelin, Dominik Hoening, Florian Schulz and Holger Lange, *ACS Photonics* **2021**, 8, 752-757 - published by the American Chemical Society (ACS).<sup>99</sup> The related supporting information is reprinted in Chapter A.2.

DOI: [10.1021/acsphotonics.1c00078](https://doi.org/10.1021/acsphotonics.1c00078)

In this work, a systematic study of the size-dependent electron-phonon coupling behavior in AuNPs is presented. Spherical mono- and polycrystalline AuNPs of different diameters were synthesized using two different wet-chemical approaches and characterized using TEM and X-ray diffraction (XRD). Electron-phonon coupling is studied using TA. It is shown that in monocrystalline AuNPs, the electron-phonon coupling constant is size-dependent and decreases with increasing particle size, effectively approaching the values reported for bulk gold. This behavior is attributed to size-dependent electron-surface scattering. In polycrystalline AuNPs, this size-dependency is blurred due to electron-surface scattering at internal grain boundaries.

*The author of this thesis contributed to the conceptualization of the project, partly synthesized the samples, conducted all TA measurements, analyzed the data and wrote the manuscript with the help of the co-authors.*

## Size-Dependent Electron–Phonon Coupling in Monocrystalline Gold Nanoparticles

Yannic U. Staechelin,\* Dominik Hoeng, Florian Schulz, and Holger Lange

Cite This: *ACS Photonics* 2021, 8, 752–757

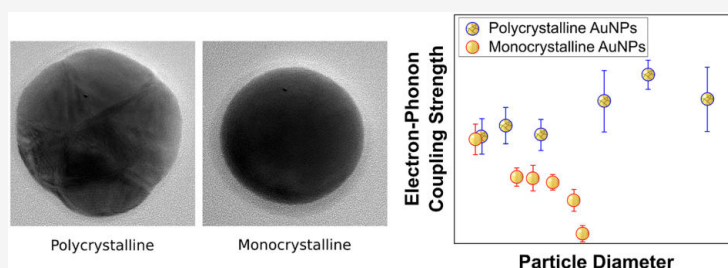
Read Online

ACCESS |

Metrics &amp; More

Article Recommendations

Supporting Information



**ABSTRACT:** Hot electrons in metal nanoparticles thermalize with the lattice via electron–phonon coupling. Size dependency is controversially discussed in literature. Here we investigate poly- and monocrystalline gold nanoparticles via transient absorption spectroscopy. As reported earlier, electron–phonon coupling in polycrystalline particles is not size-dependent. However, we clearly observe a size-dependent electron–phonon coupling in monocrystalline particles. Larger monocrystalline particles show slower electron–phonon coupling due to the decreasing effect of electron–surface scattering, with electron–phonon coupling constants approaching the values reported for bulk gold. In polycrystalline particles, size dependencies are outweighed by effective electron scattering at grain boundaries. Linear absorption spectra indicate that plasmon damping is also enhanced in polycrystalline particles by grain boundaries.

**KEYWORDS:** gold nanoparticles, plasmonics, transient absorption spectroscopy, hot electron dynamics, electron–phonon coupling

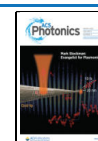
The damping of localized plasmons in gold nanoparticles (AuNPs) results in a nonequilibrium electron distribution that equilibrates into a hot electron gas. Damping of plasmons occurs via several competing processes, namely, Landau damping, electron–electron, electron–phonon, and electron–surface scattering. Landau damping is responsible for the generation of nonequilibrium electrons.<sup>1</sup> Electron–electron scattering then results in an equilibrated hot electron gas. Subsequent electron–phonon coupling and heat dissipation lead to a hot nanoparticle and environment.<sup>2,3</sup> A vast body of research explores the possibilities resulting from the different stages of the plasmon dynamics for applications such as photocatalysis<sup>4–7</sup> and solar energy conversion,<sup>8–10</sup> sometimes summarized under the term “hot-electron science”. For the lifetime of hot electrons, meaning feasibility of applications, electron–phonon coupling is the most relevant energy-loss mechanism.<sup>1,11</sup> Hot-electron relaxation processes in AuNPs after plasmon damping are therefore studied extensively.<sup>12,13</sup> However, there is disagreement about whether and how surfaces contribute to electron–phonon coupling and whether this leads to a size dependency.

Numerous studies about size effects on electron–phonon coupling in nanoparticles have been reported. Most commonly, experiments addressing the electron relaxation extract the

electron–phonon coupling time  $\tau_{\text{el-ph}}$ , that is, the time required for the electrons to thermally equilibrate with the lattice. Most experiments conducted on gold and silver nanoparticles showed no size-dependent electron–phonon coupling for particles larger than 10 nm. Hodak et al. found size-independent electron–phonon coupling times in silver nanoparticles with diameters ranging from 10 to 50 nm,<sup>14</sup> as well as in AuNPs ranging from 2 to 8 nm.<sup>15</sup> Link et al. observed nearly identical electron–phonon coupling times in AuNPs in the size range of 9 to 48 nm.<sup>16</sup> In our previous study, we also reported the absence of a size dependency for AuNPs from 12 to 56 nm diameter.<sup>17</sup> Experiments on smaller particles indicate a size dependency for particle sizes below 10 nm. Recently, Guzelturk et al. observed increasing electron–phonon coupling with decreasing particle size in the range of 6 to 13 nm via ultrafast electron diffraction.<sup>18</sup> Arbouet et al.

Received: January 14, 2021

Published: March 8, 2021



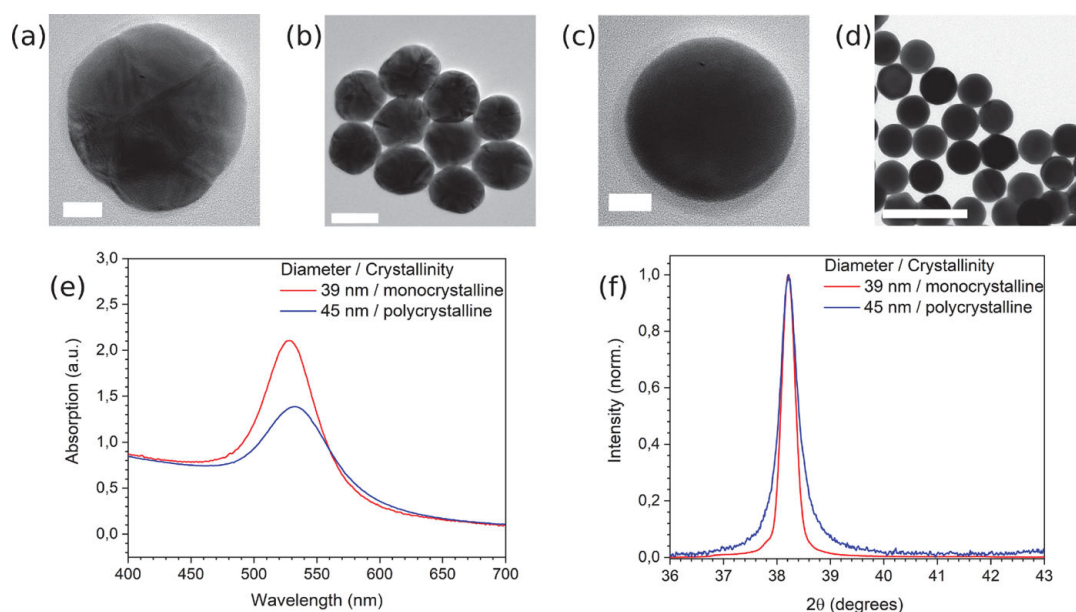


**Figure 1.** (a, b) TEM images of polycrystalline AuNPs with 45 nm diameter. (c, d) TEM images of monocrystalline AuNPs with 39 nm diameter. The scale bars in (a) and (c) correspond to 10 nm, the scalebar in (b) corresponds to 40 nm, and the scalebar in (d) corresponds to 100 nm. (e) UV-vis absorption spectra of the samples shown in (a)–(d). (f) X-ray diffractogram of the samples shown in (a)–(d) showing the (111) reflection of fcc-gold.

reported a size dependency of the electron–phonon coupling time in AuNPs in the weak excitation regime for particles smaller than 10 nm.<sup>19</sup> Aruda et al. found the electron–phonon coupling constant to be dependent on the passivating ligands for small AuNPs of 3.5 nm diameter, which indicates surface contributions in this size regime.<sup>20</sup> Master equation based calculations by Saavedra et al. show now size-dependent electron–phonon coupling for small nanoparticles, in agreement with first principle calculations by Brown et al.<sup>21,22</sup> Hogen et al. used Raman spectroscopy to study electron–phonon coupling in lithographically designed gold nanostructures in the size range of 100 to 500 nm. They reported decreasing electron–phonon coupling constants with decreasing size.<sup>23</sup> Other studies indicate that grain boundaries provide hot electrons an effective way to couple to phonons. Huang et al. experimentally addressed this issue by comparing lithographically fabricated polycrystalline prismatic AuNPs with nearly monocrystalline spherical AuNPs. Although they observed similar electron–phonon coupling constants for their mono- and polycrystalline samples, they found faster electron–phonon coupling in the polycrystalline prismatic AuNPs and explained this with the electron–surface scattering at grain boundaries.<sup>24</sup> Elsayed-Ali et al. also observed faster electron–phonon coupling in polycrystalline gold film as compared to monocrystalline.<sup>25</sup> Tang et al. observed a similar trend when comparing poly- and monocrystalline silver nanoparticles.<sup>26</sup>

Owing to the routine outcome of established synthesis routes, most experimental studies of the electron–phonon coupling to date have employed polycrystalline AuNPs. In the case of grain boundaries being of importance, past discussions of size and shape dependencies might be blurred. Recent developments in synthesis have led to a significant improve-

ment in the crystalline quality. Ensembles of nearly exclusively monocrystalline, spherical AuNPs with small size distributions can be obtained.<sup>27</sup> In the present work, we employ mono- and polycrystalline AuNPs to revisit the topic of a size-dependent electron–phonon coupling for particles ranging from 10 to 70 nm in diameter, which is the size range where line widths and light–matter interactions are optimal for application.<sup>28</sup> We use transient absorption (TA) spectroscopy to follow the electron–phonon coupling times and resolve clear surface contributions. Polycrystalline AuNPs show no size dependency of the electron–phonon coupling constant, which agrees with earlier experimental studies. However, monocrystalline AuNPs show a clear size-dependent electron–phonon coupling. Surfaces are an important factor for electron relaxation. A comparison of the spectral widths points toward a reduced importance of Landau damping for polycrystalline AuNPs due to surface scattering contributing to the plasmon damping. Surfaces and grain boundaries seem to be of importance for all stages of the plasmon damping.

Polycrystalline spherical AuNPs with diameters ranging from 12 to 72 nm were synthesized via the citrate synthesis described by Bastús et al.<sup>29</sup> Nearly monocrystalline spherical AuNPs with diameters ranging from 11 to 39 nm were synthesized via a modified approach of Zheng et al.<sup>27</sup> Further details regarding the syntheses can be found in the [Supporting Information](#).

**Figure 1a,b** shows transmission electron microscopy (TEM) images of polycrystalline AuNPs of 45 nm diameter. Grain boundaries can be discerned as contrast variations in the TEM images. Stacking faults lead to differently sized crystal domains within the particles. **Figure 1c,d** shows TEM images of nearly monocrystalline AuNPs of 39 nm diameter. Most of the particles are comprised of a single crystal domain, while there

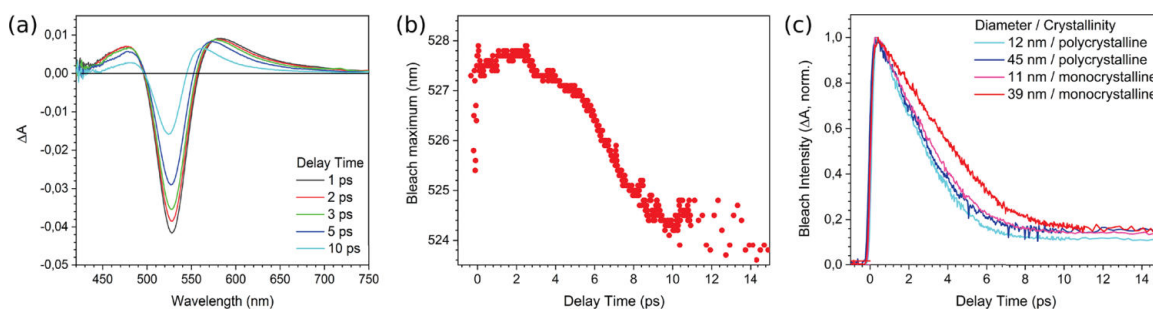


**Figure 2.** (a) TA spectra of 39 nm monocrystalline AuNPs at different delay times after excitation with  $250 \mu\text{J}/\text{cm}^2$  and  $\lambda_{\text{pump}} = 330 \text{ nm}$  pulses. (b) Dynamics of the bleach maximum for the same excitation conditions as in (a). (c) Dynamics of the TA bleach recovery of different AuNPs after excitation with  $100 \mu\text{J}/\text{cm}^2$  pulses.

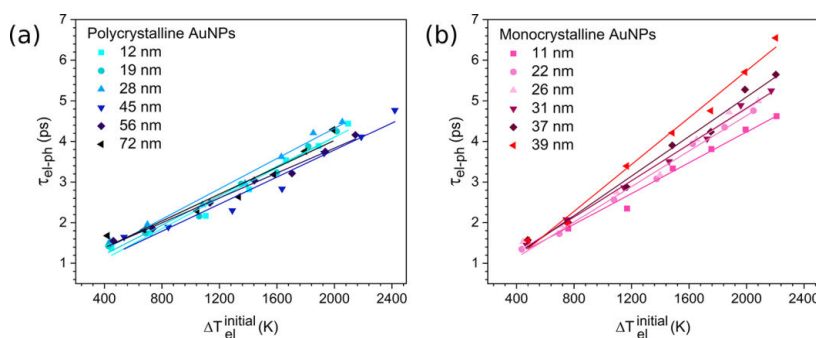


**Figure 3.** Electron–phonon coupling times vs initial electron temperature for (a) polycrystalline and (b) monocrystalline AuNPs.

are only a few bicrystalline and polycrystalline particles in the sample.

Powder X-ray diffraction (XRD) was used for a quantification of the domain sizes. For crystallite sizes up to 200 nm, the broadening of the reflections in XRD is size-dependent (cf. Figure 1f) and can be used for an estimate of the mean crystallite size via the Scherrer equation.<sup>30</sup> The data confirms the monocrystallinity of the AuNPs synthesized via the Zheng approach and estimates the domain sizes of the polycrystalline AuNPs to 10 nm (see Supporting Information).

The time-dependent electron temperature can be assessed via TA spectroscopy.<sup>2,16</sup> The change in electron temperature induced by the pump pulse leads to a change of the dielectric constant and a broadening of the plasmon resonance.<sup>14,31</sup> This leads to a bleach at the spectral position of the plasmon resonance and two positive sidebands in the TA spectra of AuNPs. The temporal dynamic of the TA response is directly related to the temporal evolution of the electronic temperature of the particles.<sup>32</sup> As the spectral position of the plasmon resonance is temperature-dependent,<sup>33</sup> a spectral shift of the bleach maximum occurs with cooling of the electron gas.<sup>14</sup> Figure 2a shows exemplary TA spectra of 39 nm monocrystalline AuNPs at different time delays after excitation. To account for the spectral shift, the TA spectra were fitted with Gaussian functions and their maxima were evaluated versus delay time in order to receive the temporal evolution of the bleach maximum. The temporal evolution of the spectral position of the bleach maximum is shown in Figure 2b. Exemplary bleach dynamics are shown in Figure 2c for two different sizes of mono- and polycrystalline AuNPs. A biexponential decay is observed, whose two components stem from electron–phonon

and phonon–phonon coupling. The electron–phonon coupling time can be extracted from this data via fitting the fast dynamics (refer to the Supporting Information for further details). Phonon–phonon coupling occurs on the longer time scale. The diameter-dependent behavior seems to differ between mono- and polycrystalline AuNPs.

The interplay of electron and lattice dynamics can be discussed within the framework of a two-temperature model (TTM). The temperatures of the electron gas and the lattice are described by two coupled differential equations

$$\begin{aligned} C_e(T_e) \frac{dT_e}{dt} &= -G(T_e - T_l); \\ C_l \frac{dT_l}{dt} &= G(T_e - T_l) \end{aligned} \quad (1)$$

where  $C_e$  and  $C_l$  are the electron and lattice heat capacity.  $T_e$  and  $T_l$  are the electron and lattice temperature, respectively, and  $G$  is the electron–phonon coupling constant mediating between electrons and lattice. Electron–phonon coupling times depend on the initial electronic temperature (and therefore the pump laser fluence in laser spectroscopic experiments). For an assumed temperature-independent electron–phonon coupling constant in the investigated temperature range, pump-fluence-dependent measurements allow extracting the electron–phonon coupling characteristics.<sup>14,15,34</sup>

The experiment-related unit pump fluence can be related with the initial jump in electron temperature  $\Delta T_{\text{el}}^{\text{initial}}$  by<sup>18,20</sup>

$$U = \frac{1}{2}\gamma((\Delta T_{\text{el}}^{\text{initial}} + T_{\text{RT}})^2 - (T_{\text{RT}})^2) \quad (2)$$

where  $U$  is the absorbed energy per pulse and unit volume of Au,  $T_{\text{RT}}$  is the room temperature and  $\gamma$  is the electron heat capacity coefficient for bulk gold ( $\gamma = 68 \text{ J m}^{-3} \text{ K}^{-2}$ ).<sup>35</sup>  $U$  can be evaluated from

$$U = \frac{I_{\text{abs}}}{N_{\text{AuNP}} \cdot V_{\text{AuNP}}} \quad (3)$$

with the absorbed energy from the pump pulse  $I_{\text{abs}}$ , which can be derived from the optical density at the pump wavelength by Beer–Lambert's Law, the number of particles in the pump beam  $N_{\text{AuNP}}$  and the volume of a single AuNP  $V_{\text{AuNP}}$ . Values for the electron–phonon coupling times as a function of the initial electron temperature are shown in Figure 3. At high pump fluences (or high initial electron temperatures, respectively), we observe differences in electron–phonon coupling times between mono- and polycrystalline AuNPs. At an initial electron temperature of about 2000 K, all polycrystalline samples have an electron–phonon coupling time of about 4.4 ps, whereas electron–phonon coupling times in monocrystalline samples range from 4.6 ps for the smallest particles (11 nm diameter) to 6.5 ps for the largest particles (39 nm diameter). For the lowest initial electron temperature of about 450 K, all poly- and monocrystalline samples have an electron–phonon coupling time of about 1.5 ps. Electron–phonon coupling time and initial electron temperature are connected via

$$\tau_{\text{el-ph}} = \frac{\gamma}{G} \cdot \Delta T_{\text{el}}^{\text{initial}} \quad (4)$$

The observed linear dependency of electron–phonon coupling times versus initial electron temperature (Figure 3) confirms that the electron–phonon coupling constant is temperature-independent in the investigated range of electron temperatures up to 2000 K, in agreement with literature.<sup>22,36</sup> Fitting a linear function gives the electron cooling rate in ps/K as the slope. The resulting electron–phonon coupling constants for all employed samples are shown in Figure 4.

The electron–phonon coupling constant in polycrystalline AuNPs shows no distinct size dependence, with values around  $4 \times 10^{16} \text{ W/m}^3 \text{ K}$ . However, we observe a clear size-dependent electron–phonon coupling constant in monocrystalline

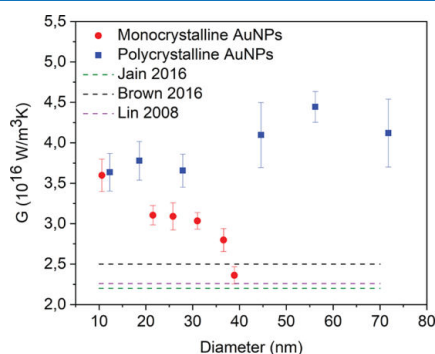


**Figure 4.** Electron–phonon coupling constants as a function of particle diameter. Literature bulk gold values are plotted as dashed lines for comparison.

AuNPs. The smallest investigated monocrystalline AuNPs (11 nm diameter) show an electron–phonon coupling constant of  $3.6 \times 10^{16} \text{ W/m}^3 \text{ K}$ . Their size agrees with the average domain sizes of polycrystalline AuNPs, which share a similar coupling constant. With increasing particle size, the electron–phonon coupling constant in monocrystalline AuNPs decreases, with a value of  $2.4 \times 10^{16} \text{ W/m}^3 \text{ K}$  for 39 nm AuNPs. Comparison with literature values shows that, as the particle diameter approaches the electron mean free path ( $\sim 50 \text{ nm}$  in gold<sup>37</sup>), the electron–phonon coupling constant of the monocrystalline AuNPs approaches the reported bulk values of  $2.2 \times 10^{16}$  to  $2.5 \times 10^{16} \text{ W/m}^3 \text{ K}$ .<sup>22,36,38</sup>

We attribute this behavior to electron–surface scattering having a large influence on electron–phonon coupling. In monocrystalline AuNPs, electrons scatter at the surface or with bulk phonons. Decreasing the surface-to-volume ratio for larger particles makes scattering at the particles' surfaces less probable and, therefore, the electron–phonon coupling slows down. In polycrystalline metals, electrons can scatter at the particles' surface, grain boundaries and with bulk phonons. Scattering at grain boundaries is known to play an important role in polycrystalline metal films in which the crystallite size is smaller than the electron mean free path.<sup>39,40</sup> As the polycrystalline AuNPs' crystallite sizes are significantly smaller than the electron mean free path, scattering at grain boundaries is quite effective. Scattering at the particles' outer surface becomes negligible and therefore the size of the particle does not alter the electron–phonon coupling significantly. While electron–phonon coupling in polycrystalline AuNPs is faster than in monocrystalline AuNPs, this does not significantly affect the lattice temperature after electron–phonon temperature equilibration. Compared to the electron and phonon dynamics, heat dissipation is slow. The obtained maximum lattice temperature thus only depends on the initial electron temperature. For applications based on heat generation by AuNPs, crystallinity therefore plays a minor role. Differences in electron–phonon coupling times in poly- and monocrystalline AuNPs being larger at higher pump fluences leads to the assumption that scattering at grain boundaries is more important at higher electron temperature. A higher kinetic energy within the electron gas increases the frequency and importance of scattering events at grain boundaries.

Plasmon damping can be assessed by comparing the widths of the linear absorption spectra of mono- and polycrystalline AuNPs. Several processes contribute to the damping of plasmons. Landau damping occurs when the particles size is comparable to the Debye length, which is generally the case for nanoparticles. Scattering with electrons, phonons, and surfaces also contributes to plasmon damping. Increased damping leads to a shorter plasmon lifetime and therefore a broader absorption. Figure 5 shows the experimental linear absorption spectra of the 28 nm polycrystalline AuNPs and the 31 nm monocrystalline AuNPs compared to spectra calculated using Mie theory. The width of the plasmon absorption for monocrystalline AuNPs is well described by the simulation, which assumes a homogeneous (i.e., monocrystalline) gold sphere. For polycrystalline AuNPs, the measured absorption is broader than the simulated. Scattering at grain boundaries acts as an additional damping mechanism. This results in additional damping channels and a shorter plasmon lifetime. Therefore, the relative contribution of Landau damping, which is supposed to result in the application-relevant nonequilibrium electrons,<sup>41</sup> decreases in polycrystalline AuNPs. Moreover, the



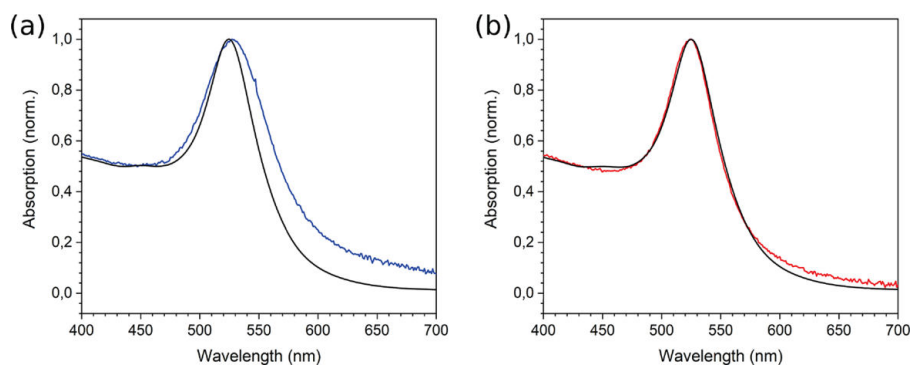


**Figure 5.** Comparison of measured linear absorption spectra of (a) 28 nm polycrystalline AuNPs (blue) and (b) 31 nm monocrystalline AuNPs (red) and simulated spectra (black).

additional channels can be expected to decrease the probability of hot electron generation at the particle's surface in polycrystalline AuNPs as compared to monocrystalline AuNPs. Hot electrons near the particle's surface are advantageous for catalysis since they are more probable to be transferred to surface-bound molecules.<sup>42,43</sup> In this regard, monocrystalline AuNPs will be beneficial beyond an increased hot electron lifetime.

In conclusion, we investigated electron–phonon coupling of AuNPs in the size regime of 10 to 70 nm diameters. We showed that electron–phonon coupling depends on the particle size in the case of monocrystalline AuNPs. Particles with larger diameters show slower electron–phonon coupling, which indicates that electron–surface scattering plays a vital role in the process. The absence of a size dependency in polycrystalline particles, which was reported earlier, can therefore be related to electron scattering at grain boundaries. Also, plasmon damping is accelerated in polycrystalline AuNPs due to scattering at grain boundaries.

## ■ ASSOCIATED CONTENT

### SI Supporting Information

The Supporting Information is available free of charge at <https://pubs.acs.org/doi/10.1021/acsp Photonics.1c00078>.

Material and synthesis details, methods, XRD data, experimental and simulated linear absorption spectra, TA fitting details and dynamics, and additional TEM images (PDF)

## ■ AUTHOR INFORMATION

### Corresponding Author

**Yannic U. Staechelin** – Institute of Physical Chemistry, Universität Hamburg, 20146 Hamburg, Germany; [orcid.org/0000-0001-8588-9117](https://orcid.org/0000-0001-8588-9117); Email: [yannic.staechelin@chemie.uni-hamburg.de](mailto:yannic.staechelin@chemie.uni-hamburg.de)

### Authors

**Dominik Hoening** – Institute of Physical Chemistry, Universität Hamburg, 20146 Hamburg, Germany; CUI: Advanced Imaging of Matter, 22761 Hamburg, Germany; [orcid.org/0000-0002-3965-0903](https://orcid.org/0000-0002-3965-0903)

**Florian Schulz** – Institute of Physical Chemistry, Universität Hamburg, 20146 Hamburg, Germany; [orcid.org/0000-0003-4440-3680](https://orcid.org/0000-0003-4440-3680)

**Holger Lange** – Institute of Physical Chemistry, Universität Hamburg, 20146 Hamburg, Germany; CUI: Advanced Imaging of Matter, 22761 Hamburg, Germany; [orcid.org/0000-0002-4236-2806](https://orcid.org/0000-0002-4236-2806)

Complete contact information is available at: <https://pubs.acs.org/10.1021/acsp Photonics.1c00078>

### Notes

The authors declare no competing financial interest.

## ■ ACKNOWLEDGMENTS

We thank the EM division of the Department of Chemistry, University of Hamburg, the XRD division of the Department of Chemistry, University of Hamburg, and Kai-Fu Wong for support with initial test experiments and Lukas Mielke for support with syntheses. We acknowledge financial support from the German Research Foundation (DFG) via the Graduate School “Nanohybrid” (GRK 2536) and the Cluster of Excellence “CUI: Advanced Imaging of Matter” (EXC 2056 - Project No. 390715994).

## ■ REFERENCES

- (1) Boriskina, S. V.; Cooper, T. A.; Zeng, L.; Ni, G.; Tong, J. K.; Tsurimaki, Y.; Huang, Y.; Meroueh, L.; Mahan, G.; Chen, G. Losses in plasmonics: from mitigating energy dissipation to embracing loss-enabled functionalities. *Adv. Opt. Photonics* **2017**, *9*, 775.
- (2) Hartland, G. V. Optical studies of dynamics in noble metal nanostructures. *Chem. Rev.* **2011**, *111*, 3858–3887.
- (3) Besteiro, L. V.; Yu, P.; Wang, Z.; Holleitner, A. W.; Hartland, G. V.; Wiederrecht, G. P.; Govorov, A. O. The fast and the furious: Ultrafast hot electrons in plasmonic metastructures. Size and structure matter. *Nano Today* **2019**, *27*, 120–145.
- (4) Clavero, C. Plasmon-induced hot-electron generation at nanoparticle/metal-oxide interfaces for photovoltaic and photocatalytic devices. *Nat. Photonics* **2014**, *8*, 95–103.
- (5) Yang, J.; Guo, Y.; Lu, W.; Jiang, R.; Wang, J. Emerging Applications of Plasmons in Driving CO<sub>2</sub> Reduction and N<sub>2</sub> Fixation. *Adv. Mater.* **2018**, *30*, 1802227.
- (6) Rodio, M.; Graf, M.; Schulz, F.; Mueller, N. S.; Eich, M.; Lange, H. Experimental Evidence for Nonthermal Contributions to Plasmon-Enhanced Electrochemical Oxidation Reactions. *ACS Catal.* **2020**, *10*, 2345–2353.
- (7) Zhang, Y.; He, S.; Guo, W.; Hu, Y.; Huang, J.; Mulcahy, J. R.; Wei, W. D. Surface-Plasmon-Driven Hot Electron Photochemistry. *Chem. Rev.* **2018**, *118*, 2927–2954.

- (8) Kamat, P. V. Meeting the Clean Energy Demand: Nanostructure Architectures for Solar Energy Conversion. *J. Phys. Chem. C* **2007**, *111*, 2834–2860.
- (9) Wu, X.; Chen, G. Y.; Owens, G.; Chu, D.; Xu, H. Photothermal materials: A key platform enabling highly efficient water evaporation driven by solar energy. *Mater. Today Energy* **2019**, *12*, 277–296.
- (10) Linic, S.; Christopher, P.; Ingram, D. B. Plasmonic-metal nanostructures for efficient conversion of solar to chemical energy. *Nat. Mater.* **2011**, *10*, 911–921.
- (11) Khurgin, J. B. How to deal with the loss in plasmonics and metamaterials. *Nat. Nanotechnol.* **2015**, *10*, 2–6.
- (12) Hattori, Y.; Meng, J.; Zheng, K.; Meier de Andrade, A.; Kullgren, J.; Broqvist, P.; Nordlander, P.; Sá, J. Phonon-Assisted Hot Carrier Generation in Plasmonic Semiconductor Systems. *Nano Lett.* **2021**, *21*, 1083–1089.
- (13) Kuppe, C.; Rusimova, K. R.; Ohnoutek, L.; Slavov, D.; Valev, V. K. Hot\* in Plasmonics: Temperature-Related Concepts and Applications of Metal Nanostructures. *Adv. Opt. Mater.* **2020**, *8*, 1901166.
- (14) Hodak, J. H.; Martini, I.; Hartland, G. V. Spectroscopy and Dynamics of Nanometer-Sized Noble Metal Particles. *J. Phys. Chem. B* **1998**, *102*, 6958–6967.
- (15) Hodak, J. H.; Henglein, A.; Hartland, G. V. Electron-phonon coupling dynamics in very small (between 2 and 8 nm diameter) Au nanoparticles. *J. Chem. Phys.* **2000**, *112*, 5942–5947.
- (16) Link, S.; Burda, C.; Wang, Z. L.; El-Sayed, M. A. Electron dynamics in gold and gold–silver alloy nanoparticles: The influence of a nonequilibrium electron distribution and the size dependence of the electron–phonon relaxation. *J. Chem. Phys.* **1999**, *111*, 1255–1264.
- (17) Minutella, E.; Schulz, F.; Lange, H. Excitation-Dependence of Plasmon-Induced Hot Electrons in Gold Nanoparticles. *J. Phys. Chem. Lett.* **2017**, *8*, 4925–4929.
- (18) Guzelturk, B.; et al. Nonequilibrium Thermodynamics of Colloidal Gold Nanocrystals Monitored by Ultrafast Electron Diffraction and Optical Scattering Microscopy. *ACS Nano* **2020**, *14*, 4792–4804.
- (19) Arbouet, A.; Voisin, C.; Christofilos, D.; Langot, P.; Fatti, N. D.; Vallée, F.; Lermé, J.; Celep, G.; Cottancin, E.; Gaudry, M.; Pellarin, M.; Broyer, M.; Maillard, M.; Pileni, M. P.; Treguer, M. Electron-phonon scattering in metal clusters. *Phys. Rev. Lett.* **2003**, *90*, 177401.
- (20) Aruda, K. O.; Tagliazucchi, M.; Sweeney, C. M.; Hannah, D. C.; Schatz, G. C.; Weiss, E. A. Identification of parameters through which surface chemistry determines the lifetimes of hot electrons in small Au nanoparticles. *Proc. Natl. Acad. Sci. U. S. A.* **2013**, *110*, 4212–4217.
- (21) Saavedra, J. R. M.; Asenjo-García, A.; García de Abajo, F. J. Hot-Electron Dynamics and Thermalization in Small Metallic Nanoparticles. *ACS Photonics* **2016**, *3*, 1637–1646.
- (22) Brown, A. M.; Sundararaman, R.; Narang, P.; Goddard, W. A.; Atwater, H. A. Nonradiative Plasmon Decay and Hot Carrier Dynamics: Effects of Phonons, Surfaces, and Geometry. *ACS Nano* **2016**, *10*, 957–966.
- (23) Hogan, N.; Wu, S.; Sheldon, M. Photothermalization and Hot Electron Dynamics in the Steady State. *J. Phys. Chem. C* **2020**, *124*, 4931–4945.
- (24) Huang, W.; Qian, W.; El-Sayed, M. A.; Ding, Y.; Wang, Z. L. Effect of the Lattice Crystallinity on the Electron–Phonon Relaxation Rates in Gold Nanoparticles. *J. Phys. Chem. C* **2007**, *111*, 10751–10757.
- (25) Elsayed-Ali, H. E.; Juhasz, T.; Smith, G. O.; Bron, W. E. Femtosecond thermorefectivity and thermotransmissivity of polycrystalline and single-crystalline gold films. *Phys. Rev. B: Condens. Matter Mater. Phys.* **1991**, *43*, 4488–4491.
- (26) Tang, Y.; Ouyang, M. Tailoring properties and functionalities of metal nanoparticles through crystallinity engineering. *Nat. Mater.* **2007**, *6*, 754–759.
- (27) Zheng, Y.; Zhong, X.; Li, Z.; Xia, Y. Successive, Seed-Mediated Growth for the Synthesis of Single-Crystal Gold Nanospheres with Uniform Diameters Controlled in the Range of 5–150 nm. *Part. Part. Syst. Charact.* **2014**, *31*, 266–273.
- (28) Jain, P. K.; Lee, K. S.; El-Sayed, I. H.; El-Sayed, M. A. Calculated absorption and scattering properties of gold nanoparticles of different size, shape, and composition: applications in biological imaging and biomedicine. *J. Phys. Chem. B* **2006**, *110*, 7238–7248.
- (29) Bastús, N. G.; Comenge, J.; Puntès, V. Kinetically controlled seeded growth synthesis of citrate-stabilized gold nanoparticles of up to 200 nm: size focusing versus Ostwald ripening. *Langmuir* **2011**, *27*, 11098–11105.
- (30) Scherrer, P. Bestimmung der Größe und der inneren Struktur von Kolloidteilchen mittels Röntgenstrahlen. *Nachr. Ges. Wiss. Göttingen* **1918**, 98–100.
- (31) Del Fatti, N.; Vallée, F. Ultrafast optical nonlinear properties of metal nanoparticles. *Appl. Phys. B: Lasers Opt.* **2001**, *73*, 383–390.
- (32) Hartland, G. V. Measurements of the material properties of metal nanoparticles by time-resolved spectroscopy. *Phys. Chem. Chem. Phys.* **2004**, *6*, 5263.
- (33) Link, S.; El-Sayed, M. A. Size and Temperature Dependence of the Plasmon Absorption of Colloidal Gold Nanoparticles. *J. Phys. Chem. B* **1999**, *103*, 4212–4217.
- (34) Shabaninezhad, M.; Abuhagr, A.; Sakthivel, N. A.; Kumara, C.; Dass, A.; Kwak, K.; Pyo, K.; Lee, D.; Ramakrishna, G. Ultrafast Electron Dynamics in Thiolate-Protected Plasmonic Gold Clusters: Size and Ligand Effect. *J. Phys. Chem. C* **2019**, *123*, 13344–13353.
- (35) Ortolani, M.; Mancini, A.; Budweg, A.; Garoli, D.; Brida, D.; de Angelis, F. Pump-probe spectroscopy study of ultrafast temperature dynamics in nanoporous gold. *Phys. Rev. B* **2019**, *99*, 776.
- (36) Lin, Z.; Zhigilei, L. V.; Celli, V. Electron-phonon coupling and electron heat capacity of metals under conditions of strong electron-phonon nonequilibrium. *Phys. Rev. B* **2008**, *77*, 776.
- (37) Brown, A. M.; Sundararaman, R.; Narang, P.; Goddard, W. A.; Atwater, H. A. Ab initio phonon coupling and optical response of hot electrons in plasmonic metals. *Phys. Rev. B: Condens. Matter Mater. Phys.* **2016**, *94*, 075120.
- (38) Jain, A.; McGaughey, A. J. H. Thermal transport by phonons and electrons in aluminum, silver, and gold from first principles. *Phys. Rev. B* **2016**, *93*, 776.
- (39) Zhu, L.; Jin, K.; Zheng, X. Effect of quantum transport on the resistivity of metal nanocrystalline materials in an electric field. *Appl. Phys. Lett.* **2007**, *91*, 103108.
- (40) Zhang, Q. G.; Cao, B. Y.; Zhang, X.; Fujii, M.; Takahashi, K. Influence of grain boundary scattering on the electrical and thermal conductivities of polycrystalline gold nanofilms. *Phys. Rev. B: Condens. Matter Mater. Phys.* **2006**, *74*, 134109.
- (41) Hartland, G. V.; Besteiro, L. V.; Johns, P.; Govorov, A. O. What's so Hot about Electrons in Metal Nanoparticles? *ACS Energy Lett.* **2017**, *2*, 1641–1653.
- (42) Khurgin, J. B. Fundamental limits of hot carrier injection from metal in nanoplasmonics. *Nanophotonics* **2020**, *9*, 453–471.
- (43) Cortés, E.; Besteiro, L. V.; Alabastri, A.; Baldi, A.; Tagliabue, G.; Demetriadou, A.; Narang, P. Challenges in Plasmonic Catalysis. *ACS Nano* **2020**, *14*, 16202.



### 5.3 Carrier localization in zero-dimensional and one-dimensional CdSe-CdS heterostructures

This publication is reprinted with permission from Yannic U. Staechelin, Michael Deffner, Sonja Krohn, Christian Castillo Delgadillo, Jan Steffen Niehaus and Holger Lange, *The Journal of Chemical Physics* **2022**, 156, 061102 - published by the American Institute of Physics (AIP Publishing).<sup>285</sup>

DOI: [10.1063/5.0079619](https://doi.org/10.1063/5.0079619)

This study compares the charge-carrier relaxation in spherical CdSe-CdS QDs and elongated CdSe-CdS DRs. TA and OPTP measurements were conducted under identical excitation conditions to directly correlate the obtained dynamics. It was shown that for the spherical QDs, exciton formation occurs in under 2 ps for both core and shell excitation. The elongated DRs show real photoinduced THz conductivity after shell excitation, indicating mobile charge carriers. The THz signal decays with similar dynamics as the shell bleach in the TA dynamics, suggesting that shell-located electrons remain mobile until they localize into the core to form a bound exciton with the holes.

*The author of this thesis contributed to the conceptualization of the project, carried out TA and OPTP measurements, analyzed the data and wrote the manuscript with the help of the co-authors.*

# Carrier localization in zero-dimensional and one-dimensional CdSe–CdS heterostructures

Cite as: J. Chem. Phys. **156**, 061102 (2022); <https://doi.org/10.1063/5.0079619>

Submitted: 23 November 2021 • Accepted: 24 January 2022 • Published Online: 09 February 2022

 Yannic U. Staechelin, Michael Deffner, Sonja Krohn, et al.

## COLLECTIONS

Paper published as part of the special topic on [Transport of Charge and Energy in Low-Dimensional Materials](#)



View Online



Export Citation



CrossMark

## ARTICLES YOU MAY BE INTERESTED IN

[Electronic excitations through the prism of mean-field decomposition techniques](#)

The Journal of Chemical Physics **156**, 061101 (2022); <https://doi.org/10.1063/5.0082938>

[Critical assessment of machine-learned repulsive potentials for the density functional based tight-binding method: A case study for pure silicon](#)

The Journal of Chemical Physics **156**, 064101 (2022); <https://doi.org/10.1063/5.0081159>

[Path integral description of semiflexible active Brownian polymers](#)

The Journal of Chemical Physics **156**, 064105 (2022); <https://doi.org/10.1063/5.0081020>



Chemical Physics Reviews

First Articles Now Online!

READ NOW >>>

# Carrier localization in zero-dimensional and one-dimensional CdSe–CdS heterostructures

Cite as: J. Chem. Phys. 156, 061102 (2022); doi: 10.1063/5.0079619

Submitted: 23 November 2021 • Accepted: 24 January 2022 •

Published Online: 9 February 2022



Yannic U. Staechelin,<sup>1</sup> Michael Deffner,<sup>2,3</sup> Sonja Krohn,<sup>4</sup> Christian Castillo Delgadillo,<sup>4</sup> Jan Steffen Niehaus,<sup>4</sup> and Holger Lange<sup>1,3,a)</sup>

## AFFILIATIONS

<sup>1</sup>Institut für Physikalische Chemie, Universität Hamburg, Hamburg, Germany

<sup>2</sup>Institut für Anorganische und Angewandte Chemie, Universität Hamburg, Hamburg, Germany

<sup>3</sup>The Hamburg Centre for Ultrafast Imaging, Hamburg, Germany

<sup>4</sup>Fraunhofer IAP-CAN, Hamburg, Germany

**Note:** This paper is part of the JCP Special Topic on Transport of Charge and Energy in Low-Dimensional Materials.

**a)** Author to whom correspondence should be addressed: [Holger.Lange@chemie.uni-hamburg.de](mailto:Holger.Lange@chemie.uni-hamburg.de)

## ABSTRACT

Mobile charge carriers in heterostructured nanoparticles are relevant for applications requiring charge separation and extraction. We investigate the benchmark systems CdSe–CdS core–shell quantum dots and quantum dots in quantum rods by optical and THz pump–probe spectroscopy. We relate photoconductivity and carrier location and observe that only shell-located electrons in quantum rods contribute to an observable photoconductivity. Despite the shallow electron confinement in the quasi-type II heterostructures, core-located carriers are bound into immobile excitons that respond on external electrical fields by polarization.

Published under an exclusive license by AIP Publishing. <https://doi.org/10.1063/5.0079619>

## I. INTRODUCTION

Heterostructured colloidal semiconductor nanoparticles, for instance, spherical core–shell quantum dots (QDs) or elongated quantum dots in quantum rods (QRs), are presently entering commercial markets and discussed for different applications, such as lasing or photocatalysis.<sup>1–3</sup> These applications have in common that they require low-defect nanoparticles but differ in their requirements regarding the movement of charge and energy within the materials. While light emission is favored by well-confined electron–hole pairs, the conversion of optical to chemical or electrical energy typically requires the extraction of excited carriers. QDs show outstanding photoluminescence properties, such as a size-dependent and narrow emission band. While QDs consisting of only one material exhibit many trap states on the particles surface, growing an inorganic shell onto QDs passivates the traps, which leads to high quantum yields. CdSe–CdS core–giant-shell QDs are nowadays readily available with near-unity photoluminescence quantum yields (PLQYs), which makes them interesting candidates for lasing or display applications.<sup>1,4</sup> QRs show especially promising photocatalytic properties.<sup>5–7</sup> While fast exciton formation was observed in CdS

QRs,<sup>8</sup> heterostructured CdSe–CdS core–shell QRs exhibit mobile electrons.<sup>9</sup> Holes are strongly confined in the core (valence band offset  $>0.5$  eV) in these structures, whereas they feature a shallow confinement for the electrons (conduction band offset  $<0.2$  eV).<sup>10</sup> Fast hole localization in the core leads to a partial charge separation. The conduction band electrons within the shell, therefore, have a macroscopic mobility and contribute to an observable photoconductivity.<sup>9</sup> The shallow confinement might also allow core electrons to retain some mobility within the shell and to be extracted into surface-adsorbed molecules, for example. Knowledge of which carriers in which states are mobile within the nanostructure would be of benefit for design considerations for heteronanostructure-based photonic and photocatalytic applications.

In this context, we exemplarily investigate state-of-the-art CdSe–CdS core–shell QDs and CdSe–CdS core–shell QRs. By applying a combination of optical and THz pump–probe experiments, we can resolve the dynamics following selective carrier excitation in the shell (CdS) and core material (CdSe). The QDs show a uniform behavior, independent of the excitation. Carriers quickly condense into excitons. In QRs, electrons within the shell contribute to a

significant photoconductivity, which is reduced after electron localization within the core, followed by exciton condensation. Despite the modest localization, core electrons show a negligible contribution to the QR photoconductivity.

## II. RESULTS AND DISCUSSION

To resolve differences in the charge carrier mobility within CdSe–CdS core–shell QDs and QRs, we performed optical transient absorption (TA) and optical-pump THz-probe (OPTP) experiments. States populated by excited carriers lead to a reduced optical absorption by Pauli blocking. A TA experiment then allows following the excited state dynamics, for instance, carrier cooling and transfer.<sup>11,12</sup> THz-electric fields oscillate at frequencies small enough to drive mobile carriers into macroscopic movement. When a THz pulse passes through a sample with mobile carriers, the pulse is damped and the analysis of the differential pulse allows to conclude on the properties of the mobile carriers.<sup>13,14</sup> For the optical experiments, carriers were selectively excited in either core or shell of the QDs and QRs by appropriate optical pulses of 400 nm wavelength for shell excitation and 570 nm for core excitation [cf. absorption spectra in Figs. 1(b) and 3(b)].

### A. Exciton formation in quantum dots

CdSe/CdS core-giant-shell quantum dots were synthesized following the protocol of Chen *et al.*<sup>15</sup> The QDs are composed of a CdSe core with a diameter of 4.0 nm and giant CdS-shell accumulating to an average total diameter of 13 nm ( $\pm 1.5$  nm) as determined by transmission electron microscopy [cf. Fig. 1(a)]. Due to the large shell volume, the absorption of the CdS-shell dominates the UV–vis spectrum [Fig. 1(b)], whereas the absorption of the CdSe core is much weaker. Two core related absorption features can be resolved at 558 and 623 nm, which can be assigned to the  $1S_e-2S_h$  and  $1S_e-1S_h$  transitions, respectively.<sup>16</sup> The low defect density and good surface passivation within the heterostructured QDs result in a near-unity photoluminescence quantum yield (PLQY) (98%) after shell excitation, a radiative charge recombination time of 96.9 ns, and a non-radiative recombination time of 4750 ns [cf. Fig. 1(c)]. Figure 1(d) schematically shows the band alignment in spherical CdSe–CdS core–shell QDs, with a large conduction band offset and a small valence band offset.

Figure 2(a) compares the obtained TA spectra of QDs after excitation of shell and core. Photoinduced absorption bleaches are observed at 622 and 490 nm. These wavelengths coincide with the core and shell absorption features in the UV–vis spectra, and the

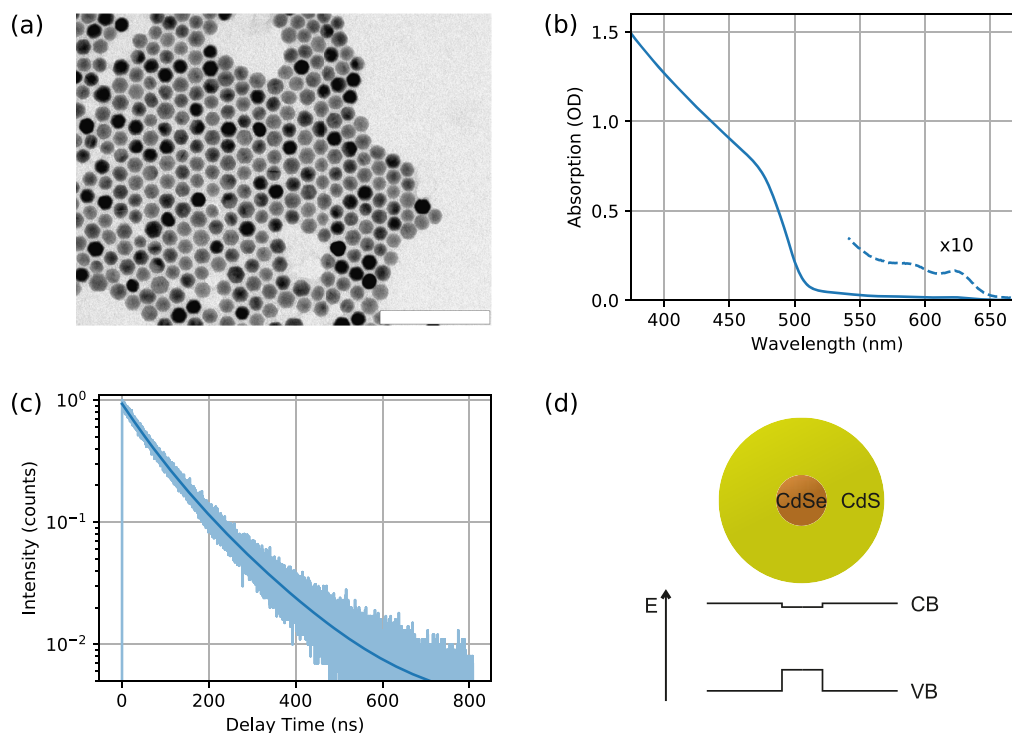


**FIG. 1.** Characterization of the investigated QDs. (a) Transmission electron microscopy image. The scale bar corresponds to 100 nm. (b) UV–vis absorption spectrum. (c) Time-resolved photoluminescence decay curves after shell excitation. (d) Schematic representation of band alignment.

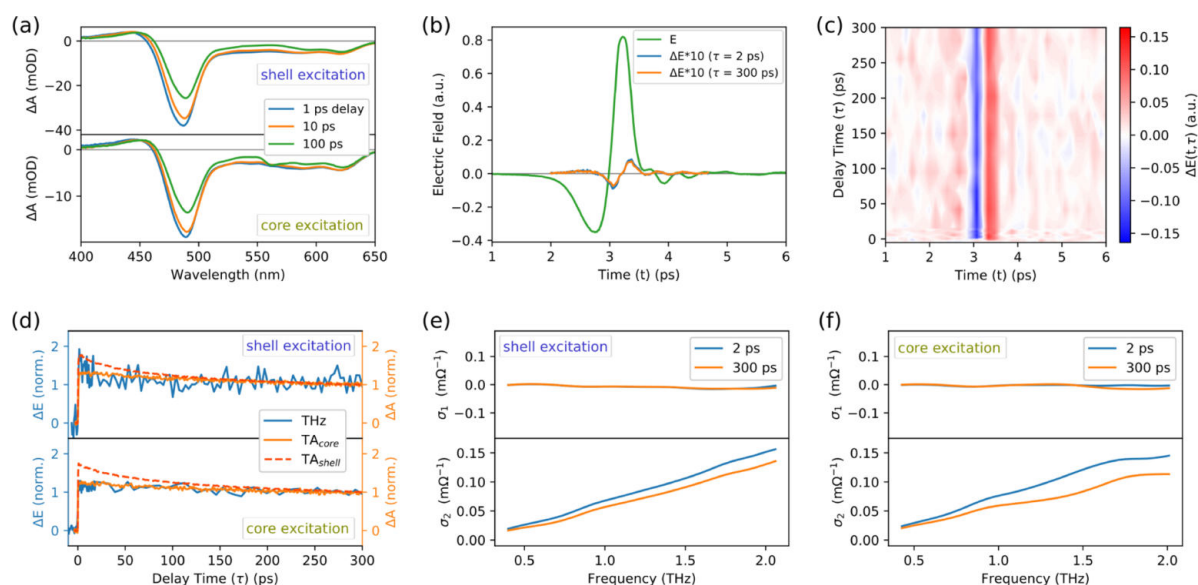


**FIG. 2.** TA and OPTP data for the QDs. (a) TA spectra at different delay times after shell and core excitation. (b) Exemplary THz waveform  $E$  transmitted through the unexcited QR sample and the photoinduced changes in the THz transmittance  $\Delta E$  of the QR sample at 2 and 300 ps delay after shell excitation. (c) Exemplary OPTP map of QDs following shell excitation. (d) Comparison of OPTP and TA dynamics following shell and core excitation, normalized at 300 ps delay time.  $TA_{\text{core}}$  and  $TA_{\text{shell}}$  refer to the TA dynamics probed at core and shell bleach, respectively. OPTP dynamics were measured at the maximum of differential THz pulse. [(e) and (f)] Frequency-dependent complex sheet-photoconductivities of the QDs at two representative delay times after shell and core excitation.  $\sigma_1$  corresponds to the real part and  $\sigma_2$  corresponds to the imaginary part of the complex photoconductivity.

bleach features can be assigned to the  $1S_c-1S_h$  transition in the core and shell material. Due to the quasi-type II band alignment, core and shell transitions share the same  $1S_c$  level. Therefore, excitation of the CdSe core leads to a bleach at the shell resonance.<sup>17</sup> Besides that, two-photon absorption might excite charge carriers in the shell material. The ratio of TA bleach in core and shell material is nearly identical for both excitations, suggesting similar carrier distributions. For OPTP, the pulse dampening by transmission through an optically excited sample is especially prominent at the peak field [Figs. 2(b) and 2(c)], and the relative field strength change can be related to the amount and mobility of the photo-generated carriers. Performing a Fourier analysis of the differential THz waveform of excited and unexcited sample allows for a more detailed discussion of the photoconductivity.<sup>13,18</sup> Figure 2(d) compares the carrier dynamics obtained by TA with the OPTP peak field dynamics. TA and OPTP share the same dynamics, which follows the long-lived exciton dynamics [cf. Fig. 1(c)]. To obtain complex conductivity spectra, the sheet-photoconductivities can be calculated by evaluating<sup>19</sup>

$$\sigma(\omega) = -\epsilon_0 c (1 + n_{\text{substrate}}) \frac{\Delta T(\omega)}{T(\omega)}, \quad (1)$$

where  $\Delta T(\omega)$  and  $T(\omega)$  are the Fourier transform of the differential THz waveform after photoexcitation and the THz waveform transmitted through the unexcited sample,  $\epsilon_0$  is the vacuum permittivity,

$c$  is the speed of light, and  $n_{\text{substrate}}$  is the refractive index of the substrate [ $1.44 + 0.00i$  for polytetrafluoroethylene (PTFE)].<sup>19</sup> Further details on the data extraction procedure can be found in the work of Gorris *et al.*<sup>20</sup> QD complex photoconductivities shortly after photoexcitation and for longer delays are shown in Figs. 2(e) and 2(f). Independent of excitation wavelength and delay, QDs show zero real photoconductivity and linearly increasing imaginary photoconductivity. The response of bound electron-hole pairs, excitons, to THz-electric fields differs from that of free carriers.<sup>21,22</sup> The exciton is polarized by the oscillating field and reacts depending on the exciton-polarizability. As example, Wang *et al.* reported zero imaginary photoinduced susceptibility and a frequency-independent real photoinduced susceptibility as a signature of exciton polarization in CdSe QDs.<sup>23</sup> These reported susceptibility features correspond to the observed zero real and linearly rising imaginary photoconductivity. It should be noted that the sign of the imaginary part of a Fourier transformation depends on the used Fourier convention. Therefore, positive and negative imaginary photoconductivities of excitonic systems are found in the literature.<sup>8,9</sup> In the QDs, carriers condense into excitons on sub-picosecond timescales, independent of core or shell excitation. Such systems represent optimal systems for light-emission applications.

## B. Charge carrier dynamics in quantum rods

CdSe-CdS quantum dots in quantum rods were synthesized according to the procedure described by Jochum *et al.*<sup>24</sup> CdSe-cores



with an average diameter of 3.3 nm were used. After growth of an elongated CdS-shell, the particles had an average length of 40 nm ( $\pm 5$  nm) with a width of 4.5 nm ( $\pm 0.5$  nm) [cf. Fig. 3(a)]. The CdS absorption onset is at shorter wavelengths for the QRs ( $\sim 480$  nm) as compared to the QDs since charge carriers exhibit a stronger confinement in the two directions perpendicular to the rod axis. As observed for the QDs, absorption of the CdSe core is relatively weak, showing a well-defined  $1S_e-1S_h$  transition at 600 nm [cf. Fig. 3(b)]. The measured PLQY after shell excitation was 73%. The radiative and non-radiative charge recombination rates were determined to be 15.6 and 42.2 ns [cf. Fig. 3(c)]. A schematic depiction of the band alignment in CdSe-CdS QRs is shown in Fig. 3(d).

TA and OPTP measurements of QRs are summarized in Fig. 4. As for the QDs, the main TA bleach features around 600 and 467 nm originate from Pauli blocking within the core and shell  $1S_e-1S_h$  transitions [cf. Fig. 3(b)]. For the QR geometry, shell excitation results in an increased relative carrier concentration within the shell compared to QDs [Fig. 4(a)]. Lupo *et al.* measured TA on CdSe-CdS QRs with similar dimensions and assigned the shell bleach after core excitation to electron delocalization into the shell,<sup>12</sup> as expected from the band alignment of quasi-type II structures. Two-photon absorption of the shell material might also contribute to the shell bleach in the QRs.<sup>25</sup> A comparison of the core and shell TA bleach dynamics [Figs. 4(b)-4(d)] shows a fast decay of the carrier population in the shell and a rise of the carrier population in the core within a

few picoseconds. This can partly be reasoned by a fast carrier transfer from the shell to core, evidenced by the relative timescales of the TA contrast rise [Fig. 4(d)]. Core-localized carriers then show a long lifetime decay in similar means as for the QDs. However, shell bleach shows an additional decay component, not resembled by the rise of the core bleach. This might probably be due to multiexcitonic Auger-type processes in some particles or trapping of electrons at the CdS-shell.<sup>26</sup> Interestingly, the OPTP contrast follows the carrier dynamics of shell-localized carriers (TA bleach of the shell). When carriers are localized within the core, a reduction of mobile carriers leads to decreasing OPTP contrast and a reduction of Pauli blocking of shell states. After 150 ps, TA dynamics of the core and shell and OPTP dynamics resemble. In contrast to QDs, shell-excited carriers are mobile within the QRs. The complex sheet-photoconductivities of the QRs following shell excitation [Fig. 5(a)] show a significant real photoconductivity when carriers are present in the shell (cf. Fig. 4). This can be explained by the fact that holes are quickly localized in the core. This leads to a partial charge carrier separation, leaving mobile electrons in the conduction band of the shell. Hole-trapping at the surface of the CdS-shell may also contribute to a charge separation. However, we do not observe a photoinduced absorption at wavelengths to the red of the bleach in our TA measurements, which is usually ascribed to trapped holes.<sup>27,28</sup> After electron localization at the core or after direct core excitation, sheet conductivities show an excitonic

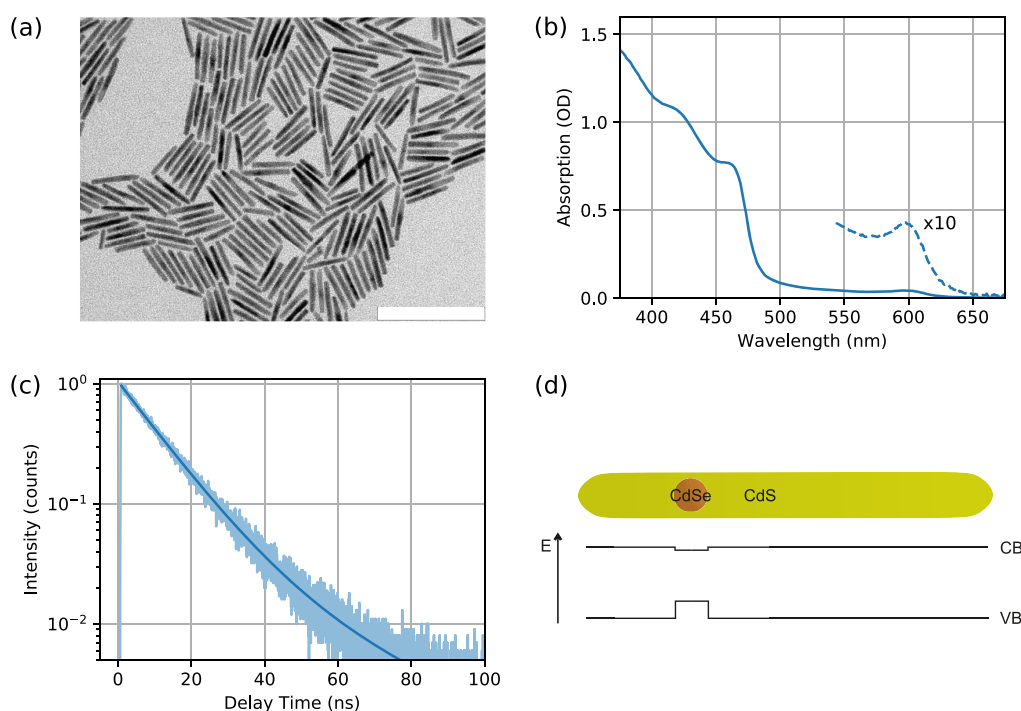


**FIG. 3.** Characterization of the investigated QRs. (a) Transmission electron microscopy image. The scale bar corresponds to 100 nm. (b) UV-vis absorption spectrum. (c) Time-resolved photoluminescence decay curves after shell excitation. (d) Schematic representation of band alignment.

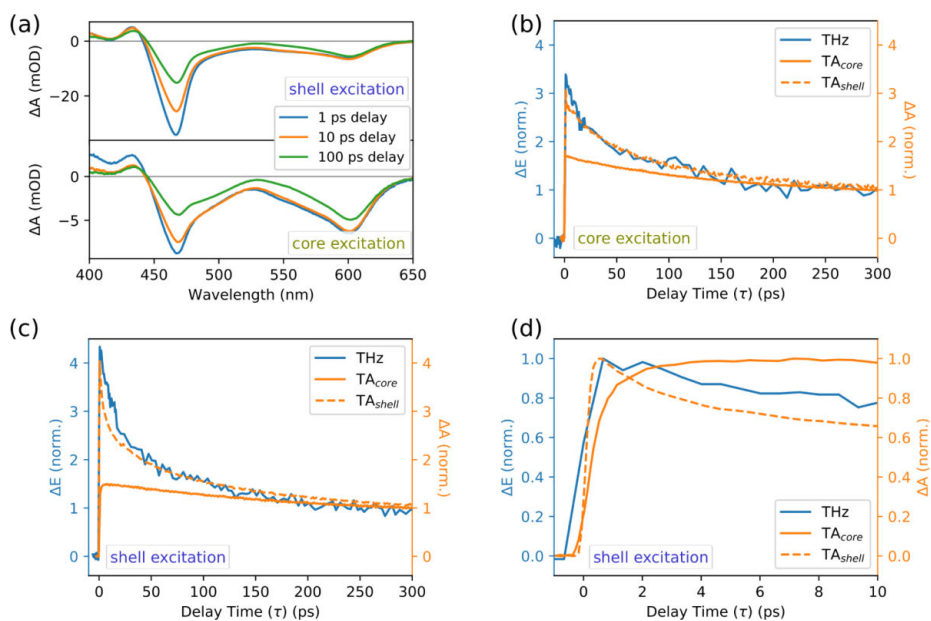


**FIG. 4.** TA and OPTP data for the QRs. (a) TA spectra at different delay times after shell and core excitation. [(b) and (c)] Comparison of OPTP and TA dynamics after core and shell excitation, normalized at 300 ps delay time.  $TA_{core}$  and  $TA_{shell}$  refer to the TA dynamics probed at core and shell bleach, respectively. OPTP dynamics were measured at the maximum of the differential THz pulse. (d) Same data as in (c) for short delay times after shell excitation, normalized to maximum signal.

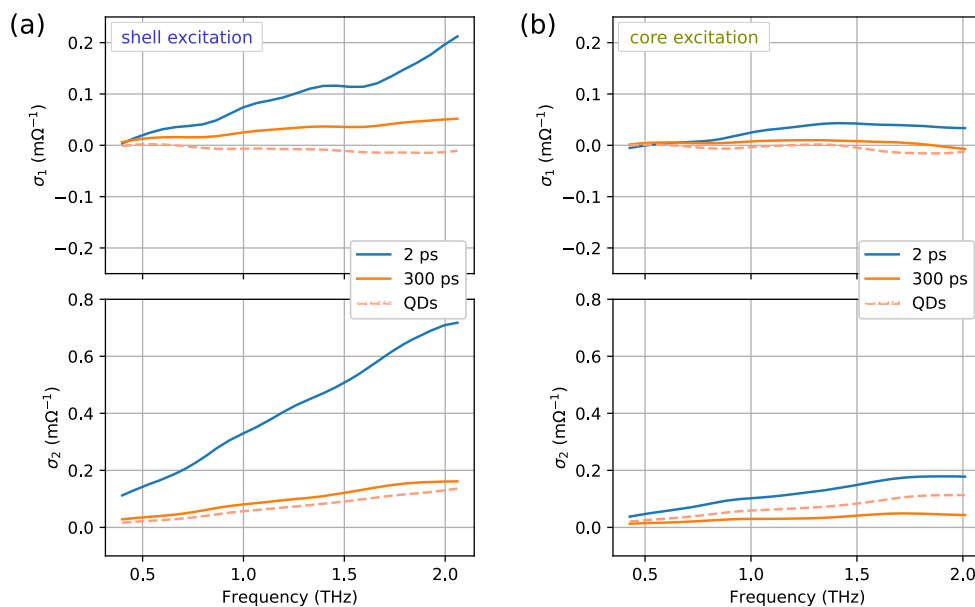


**FIG. 5.** Real ( $\sigma_1$ ) and imaginary ( $\sigma_2$ ) part of the complex sheet-photoconductivity of the QR sample at two representative delay times after (a) shell and (b) core excitation. The excitonic response of the QD sample (300 ps delay) is plotted for comparison.

character [cf. Fig. 5(b)]. This demonstrates that only electrons populating conduction band states of the shell are mobile within the QR, while electron localization within the core results in immobile excitons. The latter occurs by charge transfer or direct core excitation.

### III. CONCLUSIONS

In summary, we investigated CdSe/CdS core-shell nanocrystals of spherical and elongated shape with high monodispersity and photoluminescence quantum yields. We studied carrier relaxation and localization by TA and OOTP spectroscopy. In QDs, charge carriers condense into excitons on sub-picosecond timescales, independent of core or shell excitation. In QRs, fast hole localization in the core leads to partial charge separation, resulting in electrons within the shell, which are mobile on macroscopic scales. Core-localized carriers form excitons and do not contribute to a photoconductivity. For light-emitting applications, the excitonic properties of charge carriers in QDs are beneficial and reflected in high QYs. For applications such as photocatalysis, which require charge separation and mobile carriers, QRs are the geometry of choice. However, despite the shallow confinement in CdSe-CdS QRs, core-localized carriers do not significantly contribute to a real photoconductivity, which has to be considered in the material design.

### IV. EXPERIMENTAL METHODS

#### A. Optical characterization

Linear absorption spectra were recorded using a Varian Cary 50 spectrometer. TEM images were analyzed to determine size distributions of the samples. A Joel JEM-1011 instrument was used, operating at 100 kV. Time-resolved photoluminescence was measured employing a FluoTime300 PicoQuant with an excitation wavelength of 450 nm.

#### B. Pump-probe spectroscopy

OOTP and TA setups were described previously.<sup>20,29</sup> Excitation pulses of 400 and 570 nm wavelength were generated by second-harmonic generation of the 800 nm laser fundamental in a BBO-crystal and in an optical parametric amplifier, respectively. For the OOTP experiments, the samples were dropcasted onto a PTFE substrate and the experiments were carried out under a dry nitrogen atmosphere. PTFE has a constant refractive index of  $1.44 + 0.0i$  in the THz frequency range. TA experiments were conducted on samples in solution. Pump fluences were 80 and 600  $\mu\text{J}/\text{cm}^2$  for excitation at 400 nm (shell excitation) and 570 nm (core excitation), respectively.

### ACKNOWLEDGMENTS

This work was supported by the Cluster of Excellence "Advanced Imaging of Matter" (EXC 2056-Project ID 390715994) and the Graduate School "Nanohybrid" (Grant No. GRK 2536) of the Deutsche Forschungsgemeinschaft (DFG).

### AUTHOR DECLARATIONS

#### Conflict of Interest

The authors have no conflicts to disclose.

#### DATA AVAILABILITY

The data that support the findings of this study are available from the corresponding author upon reasonable request.

### REFERENCES

- H. Jung, N. Ahn, and V. I. Klimov, "Prospects and challenges of colloidal quantum dot laser diodes," *Nat. Photonics* **15**(9), 643 (2021).
- F. Pelayo García de Arquer, D. V. Talapin, V. I. Klimov, Y. Arakawa, M. Bayer, and E. H. Sargent, "Semiconductor quantum dots: Technological progress and future challenges," *Science* **373**(6555), eaaz8541 (2021).
- R. Burke, K. L. Bren, and T. D. Krauss, "Semiconductor nanocrystal photocatalysis for the production of solar fuels," *J. Chem. Phys.* **154**(3), 030901 (2021).
- Y. E. Panfil, M. Oded, and U. Banin, "Colloidal quantum nanostructures: Emerging materials for display applications," *Angew. Chem., Int. Ed.* **57**(16), 4274–4295 (2018).
- L. Amirav and A. P. Alivisatos, "Photocatalytic hydrogen production with tunable nanorod heterostructures," *J. Phys. Chem. Lett.* **1**(7), 1051–1054 (2010).
- C. M. Wolff, P. D. Frischmann, M. Schulze, and B. J. Bohn, R. Wein, P. Livadas, M. T. Carlson, F. Jäckel, J. Feldmann, F. Würthner, and J. K. Stolarczyk, "All-in-one visible-light-driven water splitting by combining nanoparticulate and molecular co-catalysts on CdS nanorods," *Nat. Energy* **3**(10), 862–869 (2018).
- K. Wu and T. Lian, "Quantum confined colloidal nanorod heterostructures for solar-to-fuel conversion," *Chem. Soc. Rev.* **45**(14), 3781–3810 (2016).
- Y. Yang, K. Wu, A. Shabaev, A. L. Efros, T. Lian, and M. C. Beard, "Direct observation of photoexcited hole localization in CdSe nanorods," *ACS Energy Lett.* **1**(1), 76–81 (2016).
- L. T. Kunneman, M. Zanella, L. Manna, L. D. A. Siebbeles, and J. M. Schins, "Mobility and spatial distribution of photoexcited electrons in CdSe/CdS nanorods," *J. Phys. Chem. C* **117**(6), 3146–3151 (2013).
- P. Maity, T. Debnath, and H. N. Ghosh, "Ultrafast charge carrier delocalization in CdSe/CdS quasi-type II and CdS/CdSe inverted type I core-shell: A structural analysis through carrier-quenching study," *J. Phys. Chem. C* **119**(46), 26202–26211 (2015).
- V. I. Klimov, "Optical nonlinearities and ultrafast carrier dynamics in semiconductor nanocrystals," *J. Phys. Chem. B* **104**(26), 6112–6123 (2000).
- M. G. Lupo, F. Della Sala, L. Carbone, M. Zavelani-Rossi, A. Fiore, L. Lüer, D. Polli, R. Cingolani, L. Manna, and G. Lanzani, "Ultrafast electron-hole dynamics in core/shell CdSe/CdS dot/rod nanocrystals," *Nano Lett.* **8**(12), 4582–4587 (2008).
- R. Ulbricht, E. Hendry, J. Shan, T. F. Heinz, and M. Bonn, "Carrier dynamics in semiconductors studied with time-resolved terahertz spectroscopy," *Rev. Mod. Phys.* **83**(2), 543–586 (2011).
- P. Kužel and N. Hynek, "Terahertz spectroscopy of nanomaterials: A close look at charge-carrier transport," *Adv. Opt. Mater.* **8**(3), 1900623 (2020).
- Y. Chen, J. Vela, H. Htoon, J. L. Casson, D. J. Werder, D. A. Bussian, V. I. Klimov, and J. A. Hollingsworth, "Giant multishell CdSe nanocrystal quantum dots with suppressed blinking," *J. Am. Chem. Soc.* **130**(15), 5026–5027 (2008).
- G. Grimaldi, J. J. Geuchies, W. van der Stam, I. du Fossé, B. Brynjarsson, N. Kirkwood, S. Kinge, L. D. A. Siebbeles, and A. J. Houtepen, "Spectroscopic evidence for the contribution of holes to the bleach of Cd-chalcogenide quantum dots," *Nano Lett.* **19**(5), 3002–3010 (2019).
- H. Zhu, N. Song, W. Rodríguez-Córdoba, and T. Lian, "Wave function engineering for efficient extraction of up to nineteen electrons from one CdSe/CdS quasi-type II quantum dot," *J. Am. Chem. Soc.* **134**(9), 4250–4257 (2012).
- A. Nahata, A. S. Weling, and T. F. Heinz, "A wideband coherent terahertz spectroscopy system using optical rectification and electro-optic sampling," *Appl. Phys. Lett.* **69**(16), 2321–2323 (1996).

- <sup>19</sup>H. J. Joyce, J. L. Boland, C. L. Davies, S. A. Baig, and M. B. Johnston, "A review of the electrical properties of semiconductor nanowires: Insights gained from terahertz conductivity spectroscopy," *Semicond. Sci. Technol.* **31**(10), 103003 (2016).
- <sup>20</sup>F. E. S. Gorris, M. Deffner, S. Priyadarshi, C. Klinke, H. Weller, and H. Lange, "Postdeposition ligand exchange allows tuning the transport properties of large-scale CuInSe<sub>2</sub> quantum dot solids," *Adv. Opt. Mater.* **8**(1), 1901058 (2020).
- <sup>21</sup>G. L. Dakovski, S. Lan, C. Xia, and J. Shan, "Terahertz electric polarizability of excitons in PbSe and CdSe quantum dots," *J. Phys. Chem. C* **111**(16), 5904–5908 (2007).
- <sup>22</sup>M. R. Bergren, P. K. B. Palomaki, N. R. Neale, T. E. Furtak, and M. C. Beard, "Size-dependent exciton formation dynamics in colloidal silicon quantum dots," *ACS Nano* **10**(2), 2316–2323 (2016).
- <sup>23</sup>F. Wang, J. Shan, M. A. Islam, I. P. Herman, M. Bonn, and T. F. Heinz, "Exciton polarizability in semiconductor nanocrystals," *Nat. Mater.* **5**(11), 861–864 (2006).
- <sup>24</sup>T. Jochum, J. Niehaus, and H. Weller, "Elongated semiconductor nanorods—Emitter of polarized light in red and green," *SID Symp. Dig. Tech. Pap.* **48**(1), 2091 (2017).
- <sup>25</sup>G. Xing, S. Chakraborty, K. L. Chou, N. Mishra, C. H. A. Huan, Y. Chan, and T. C. Sum, "Enhanced tunability of the multiphoton absorption cross-section in seeded CdSe/CdS nanorod heterostructures," *Appl. Phys. Lett.* **97**(6), 061112 (2010).
- <sup>26</sup>H. Htoon, J. A. Hollingsworth, R. Dickerson, and V. I. Klimov, "Effect of zero- to one-dimensional transformation on multiparticle auger recombination in semiconductor quantum rods," *Phys. Rev. Lett.* **91**(22), 227401 (2003).
- <sup>27</sup>A. N. Grennell, J. K. Utterback, O. M. Pearce, M. B. Wilker, and G. Dukovic, "Relationships between exciton dissociation and slow recombination within ZnSe/CdS and CdSe/CdS dot-in-rod heterostructures," *Nano Lett.* **17**(6), 3764–3774 (2017).
- <sup>28</sup>K. Wu, Y. Du, H. Tang, Z. Chen, and T. Lian, "Efficient extraction of trapped holes from colloidal CdS nanorods," *J. Am. Chem. Soc.* **137**(32), 10224–10230 (2015).
- <sup>29</sup>E. Minutella, F. Schulz, and H. Lange, "Excitation-dependence of plasmon-induced hot electrons in gold nanoparticles," *J. Phys. Chem. Lett.* **8**(19), 4925–4929 (2017).



## 5.4 Impact of pump beam spot size on semiconductor carrier dynamics in optical-pump-terahertz-probe spectroscopy

The accepted manuscript of this publication is reprinted with permission from Yannic U. Staechelin, Tobias Kroh, Franz X. Kärtner and Holger Lange, *Journal of the Optical Society of America B* **2023**, 40 (8), 2058-2063 - published by Optica.<sup>286</sup> The related supporting information is reprinted in Chapter A.3.

DOI: [10.1364/JOSAB.496228](https://doi.org/10.1364/JOSAB.496228)

This study focuses on an experimental error that frequently occurs in OPTP measurements. Due to the long-wavelength nature of the THz radiation, the probe pulse can only be focused to a certain, frequency-dependent spot size. The pump pulse spot size should be considerably larger to ensure homogeneous excitation of the probed sample area. However, the pump pulse spot size can be experimentally limited. It was shown that inhomogeneous excitation can lead to distortions in the measured differential THz spectrum. A model was established to estimate the deviations. It was studied how the deviations depend on the employed experimental configurations.

*The author of this thesis conceptualized the project, carried out all measurements, analyzed the data, developed the presented models and wrote the manuscript with the help of the co-authors.*

# Impact of Pump Beam Spot Size on Semiconductor Carrier Dynamics in Optical-Pump-THz-Probe Spectroscopy

YANNIC U. STAECHELIN<sup>1,\*</sup>, TOBIAS KROH<sup>2,3</sup>, FRANZ X. KÄRTNER<sup>2,3</sup>,  
HOLGER LANGE<sup>3,4</sup>

<sup>1</sup>*Institute of Physical Chemistry, Universität Hamburg, Martin-Luther-King-Platz 6, 20146 Hamburg, Germany*

<sup>2</sup>*Center for Free-Electron Laser Science CFEL, Deutsches Elektronen-Synchrotron DESY, Germany*

<sup>3</sup>*The Hamburg Centre for Ultrafast Imaging, Luruper Chaussee 149, 22761 Hamburg, Germany*

<sup>4</sup>*University of Potsdam, Institute of Physics and Astronomy, Karl-Liebknecht-Straße 24, Potsdam, Germany*  
<sup>\*</sup>[yannic.staechelin@uni-hamburg.de](mailto:yannic.staechelin@uni-hamburg.de)

**Abstract:** Optical-Pump-Terahertz-Probe experiments (OPTP) are widely employed to study the dynamics of photoexcited carriers in semiconductors. In these experiments, due to the long wavelength nature of the Terahertz (THz) probe radiation, the probe beam can only be focused to a spot size in the mm range. To ensure homogeneous excitation of the probed sample region, a significantly larger optical pump beam spot size must be used, which is often difficult to implement in the experiment. Frequently used experimental geometries employ beam paths which result in small pump beam spot sizes, leading to spectral distortions of the sample response, translating to uncertainties in calculated THz conductivities and fitted Drude conductivity models, for example. We investigate the influence of the pump beam spot size on benchmark OPTP experiments and evaluate model calculations to estimate the induced deviations. We demonstrate the impact of this effect on the acquired data with different dependencies on the investigated sample and the employed experimental configuration. We can provide guidelines for optimal configurations for the most commonly employed experiments.

## 1. Introduction

Optical-Pump-THz-Probe spectroscopy (OPTP) is a powerful technique to study the electrical properties of photoexcited semiconductors. As a non-contact technique, it is especially useful for nanomaterials, which are inherently difficult to make electrical contact to [1–4]. In OPTP, a femtosecond optical laser pulse is used to photoexcite the sample of interest. After a variable delay time  $\tau$ , a THz pulse probes the photoinduced changes in THz transmittance of the sample. The measurement of the differential THz transmittance of excited and unexcited sample leads to the photoconductivity in the THz frequency range. Experimentally, the THz probe pulse is commonly generated by optical rectification and spans a frequency range from 0.1 to 2 THz, which corresponds to wavelengths of about 3 to 0.15 mm [5–7]. Off-axis parabolic mirrors (OAPs) are used to collimate and focus the THz radiation onto the sample. As the relative bandwidth of the THz probe pulse is very large, higher frequencies (i.e. shorter wavelengths) are focused more tightly than lower frequencies (i.e. longer wavelengths). In most cases, the optical pump beam is transmitted through a hole in the focusing OAP for collinear beam propagation (cf. Figure 1(a)). The size of the hole is typically in the millimeter range and limits the spot size of the optical pump beam. Large holes would lead to distortions in the THz beam profile as well as loss of THz intensity. Comparably small pump beam spot sizes result in the lower THz probe frequencies, which have a larger spot size, propagating through relatively less excited parts of the sample than the higher THz frequencies, that are focused to smaller spot sizes. This leads to an attenuation of the measured differential THz-electric field at low THz frequencies, effectively shifting the differential THz spectrum to higher frequencies. When evaluating the

46 differential data, for example for calculating the complex photoconductivity and fitting e.g. a  
47 Drude conductivity model, the frequency-dependence has to be weighted accordingly.  
48 Beard *et al.* demonstrated the problem experimentally in OPTP measurements on GaAs. They  
49 concluded that for a homogeneous excitation, the pump beam spot size should be at least two  
50 times larger than the probe beam spot size [8]. Dakovski *et al.* modelled the pump-beam-spot-  
51 size-dependent THz response as radiation from a pump-induced current driven by the THz  
52 electric field and suggested the use of metallic apertures for the THz radiation to reduce the  
53 probed area of the sample [9]. Strait *et al.* defined an overlap factor to account for the mismatch  
54 in pump and THz spot sizes and correct the differential spectra [10].  
55 Depending on the discussed quantities and varied parameters, the uncertainties resulting from  
56 insufficient overlap might not be too problematic. For example, discussing differences in the  
57 high-frequency part of the complex conductivity could be robust. In similar ways, time-constants  
58 of photoinduced changes or excitation-power dependencies might be unperturbed by spot-size  
59 problems as they might lack significant frequency dependencies. In the present work, we try to  
60 deliver a comprehensive picture of how spot size-related problems occur in the most common  
61 OPTP experiments on semiconductors. We investigate how they reflect in typically discussed  
62 data and which part of the data can be regarded as unproblematic. For this purpose, we performed  
63 OPTP with a setup geometry found often across the literature. We investigated two reference  
64 semiconductor materials, silicon and CdS nanostructures and we show where focus-related errors  
65 occur. We model the problem using plain, accessible calculations in order to explain how errors  
66 evolve and under which experimental conditions reliable data can be recorded. We consider the  
67 influence of the investigated sample as well as the experimental setup, aimed to serve as primer  
68 for carefully designing experiments.

## 69 2. Experimental setup

70 For our pump-beam-spot-size study, we employed the most widely used OPTP setup geometry  
71 (Fig. 1(a)) [5, 6]. An amplified Ti-sapphire laser system (Spitfire-Ace, 800 nm, 1 kHz, 35 fs;  
72 Spectra Physics) was employed as excitation source. The laser beam was split into three arms for  
73 the optical pump beam, the THz generation and the THz detection beam. For the optical pump  
74 beam, the 800 nm laser fundamental was frequency-doubled to obtain 400 nm using a BBO  
75 crystal. The THz radiation was generated in a ZnTe crystal by optical rectification. A weak part  
76 of the 800 nm fundamental was retained for electro-optical sampling (EOS) of the THz electric  
77 field in another ZnTe crystal. Fig. 1(b) shows the THz probe spectrum as measured with THz  
78 time domain spectroscopy (TDS). OPTP spectra of the two reference materials (CdS nanowires  
79 and Si) were measured with three different optical pump beam spot sizes (0.54 mm, 1.16 mm  
80 and 3.02 mm beam radius). To assess size-dependencies, the pump-beam-spot sizes were set  
81 by using different lenses to focus the optical pump beam onto the samples. For the collinear  
82 pump-probe geometry, the focus points were placed inside the through-hole of the OAP so that  
83 the beam diverged before impinging onto the sample. Since the diameter of the through-hole in  
84 the OAP (1.5 mm diameter at the OAPs front surface and 5 mm diameter at its backside) sets an  
85 upper limit to the pump beam spot size, we switched to a non-collinear pump-probe geometry  
86 for experiments with the largest pump beam spot size. There, the pump hits the sample at an  
87 angle, which leads to a distortion of the spherical pump beam profile into an elliptical profile  
88 and adds a temporal delay between opposite sides of the pump beam. The pump beam radii  
89 ( $1/e^2$  intensity) were measured by knife-edge scans. In the measurements under non-collinear  
90 geometry, the elliptical beam profile impinging onto the sample was calculated using the known  
91 angle of incidence. We treated the elliptical beam profile as an effective spherical beam of the  
92 same area. Beam radii of collinearly propagating pump beams were 0.54 mm and 1.16 mm. The  
93 effective beam radius of the non-collinear pump beam was 3.02 mm, which corresponds to an  
94 ellipse with radii of 2.71 mm and 3.36 mm. The pump fluence was ensured to be the same in



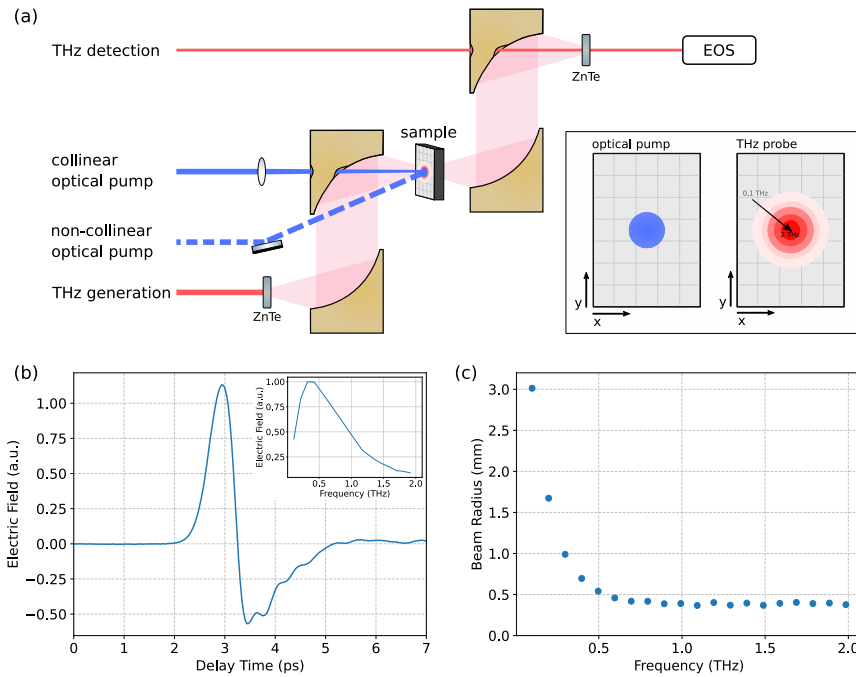


Fig. 1. (a) Experimental setup of the Optical-Pump-THz-Probe experiment and schematic representation of the spot-size problem: The optical pump beam spot size is typically smaller than the THz probe beam spot size to measure undistorted OPTP data. However, the probe beam can only be focused to a certain spot size due to its long wavelength nature. Additionally, the THz frequencies in the probe beam spot are inhomogeneously distributed (frequency-dependent focus). (b) THz-electric field of the probe beam as measured by THz-TDS. The corresponding spectrum is displayed as inset. (c) Frequency-dependent beam radii ( $1/e^2$ ) of the THz probe beam as measured using the knife-edge technique at the sample position.

95 all experiments and set to  $60 \mu\text{J}/\text{cm}^2$ . The spatial distribution of the different frequencies of  
 96 the THz probe pulses at the focus spot was obtained by combining the knife-edge technique  
 97 with THz-TDS. By recording spectra vs the insertion of the blade into the focused beam, the  
 98 THz radii of each frequency component were obtained (Fig. 1(c)). As expected, we find that  
 99 longer wavelengths are focused to larger spot sizes. The beam radii do not perfectly follow the  
 100 expected  $1/\lambda$  behavior for high THz frequencies. For the focusing conditions in our experiment,  
 101 all frequencies above 1 THz are focused to the same spot size. The knife-edge data is shown in  
 102 more detail in Figure S1.

### 103 3. Discussion

#### 104 3.1. Spectral distortions in the differential THz field

105 Fig. 2(a) shows the photoinduced changes in the THz waveform transmitted through a Si wafer  
 106 after excitation with different pump beam spot sizes. Fourier-transformation of this data yields  
 107 the differential THz spectra, shown in Fig. 2(b). As expected, we observe a shift towards higher

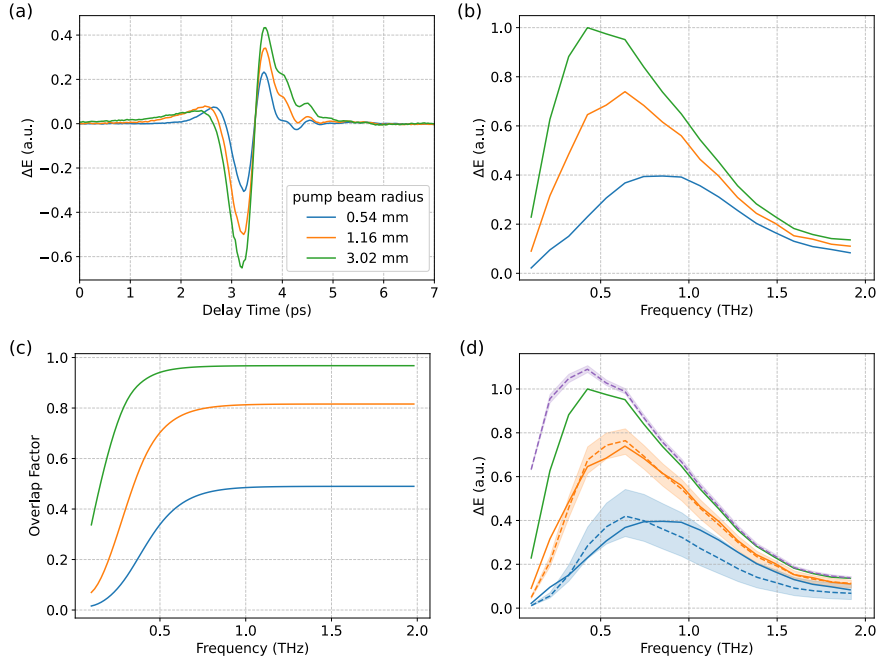


Fig. 2. (a) Photoinduced changes in the THz waveform  $\Delta E$  transmitted through a 1" Si Wafer 30 ps after excitation with  $\lambda = 400$  nm and three different pump beam spot sizes. (b), (c) and (d) use the same colour code. (b) Fourier-transform of the data shown in (a). For larger pump beam spot sizes, higher differential fields are measured at equal excitation fluences. Also, a shift towards lower frequencies is observed. (c) Frequency-dependent pump-probe beam spot overlap factor for the three different pump beam spot sizes. (d) The solid lines show the same data as in (b) and the dashed lines show simulated differential fields. The shaded areas present the uncertainty due to the errors in the characterization of the pump and probe beam radii. Using the overlap factors plotted in (c), the purple dashed line shows the differential electric field for an infinite large pump beam spot size, calculated from the data measured with a pump beam radius of 3.02 mm. From this, we can calculate the differential electric field for the pump beam spot sizes of 0.54 mm and 1.16 mm (dashed orange and green lines).

108 THz frequencies when employing smaller pump beam spot sizes. We define an overlap factor  
 109 that scales with the carrier density within the sample material through which the THz radiation  
 110 propagates. A value of 0 means that the THz radiation traverses an unexcited region of the  
 111 sample, whereas a value of 1 means that the THz radiation traverses the sample area subject  
 112 to maximum excitation given the specific excitation conditions employed. This plain model  
 113 calculation allows analyzing the distortions in the differential THz spectra depending on the  
 114 pump beam spot size for thin films or thin photoexcited layers. In the first step, the spatial charge  
 115 carrier distribution in the sample after excitation is modelled, assuming an excitation density, at  
 116 which the spatial charge carrier density is proportional to the excitation beam intensity, i.e. no  
 117 non-linear effects. In the second step, the spatial THz electric field distribution is calculated for  
 118 every frequency component of the THz pulse, using the frequency-dependent THz beam spot  
 119 sizes shown in Figure 1(c). Both the spatial charge carrier distribution as well as the spatial THz

120 electric field distribution are modelled as two-dimensional Gaussians. Since in less excited parts  
 121 of the samples there will be less interaction of the THz probe pulse with photoexcited charge  
 122 carriers, the THz electric field profiles are now weighted with the charge carrier distribution  
 123 profile; again assuming interaction in the linear regime. Integration of the THz electric fields  
 124 over the entire sample area yields an effective THz spectrum that can be compared with the initial  
 125 THz spectrum to calculate a frequency-dependent pump-probe overlap factor  $OF$ . The overlap  
 126 factor is described by

$$OF(\nu) = \frac{1}{2} \left( \frac{w_{pump}^2}{w_0(\nu)^2 + \frac{1}{2}w_{pump}^2} \right), \quad (1)$$

127 where  $\nu$  is the THz frequency,  $w_{pump}$  is the pump beam spot size and  $w_0(\nu)$  is the frequency-  
 128 dependent THz probe beam spot size (the derivation for this expression is provided in the SI).  
 129 Figure 2(c) shows this overlap factor for the three pump beam spot sizes employed in this work.  
 130 As expected, the overlap factor is higher for larger pump beam spot sizes. Also, at low THz  
 131 frequencies, i.e. long wavelengths, the overlap factor drops significantly. The smaller the pump  
 132 beam, the higher the THz frequency at which this drop occurs. This means, the spectral distortion  
 133 in the measured differential THz E-field increases. Using the overlap factors from Figure 2(c),  
 134 we can calculate the actual differential THz spectrum that would be measured with infinitely  
 135 large pump spot size from the measured differential THz spectra. For this calculation, we use  
 136 the spectrum obtained with the largest pump spot and, therefore, best SNR. The dashed purple  
 137 line in Fig. 2(d) shows this undistorted differential THz spectrum. From there, we can calculate  
 138 the differential THz spectra at the two smaller pump beam spot sizes and find good agreement  
 139 with the measured data, validating our overlap factors. Similar experiments were performed  
 140 on CdS nanowires and show the same trends (cf. Fig. S2). Our results show that for our THz  
 141 focusing conditions, for THz frequencies larger than 1 THz, the differential THz electric field is  
 142 not distorted spectrally even with pump beam spot sizes as small as 0.54 mm.

### 143 3.2. Influence on estimated conductivities

144 From the measured differential THz spectra, the complex photoconductivities of thin photoexcited  
 145 films are commonly calculated employing the Tinkham-Glover formula [2]

$$\sigma(\omega) = -\epsilon_0 c (1 + n_{\text{substrate}}) \frac{\Delta T(\omega)}{T(\omega)}, \quad (2)$$

146 where  $\epsilon_0$  is the vacuum permittivity,  $c$  is the speed of light and  $n_{\text{substrate}}$  is the refractive index of the  
 147 substrate and  $\Delta T(\omega)$  and  $T(\omega)$  are the Fourier-transform of the differential THz waveform after  
 148 photoexcitation and the THz waveform transmitted through the unexcited sample, respectively.  
 149 Thus, the distortion in the measured differential THz spectrum linearly transforms on to the  
 150 calculated complex photoconductivities. Fig. 3 exemplarily shows simulated distortions in  
 151 the real and imaginary photoconductivity of a sample exhibiting (a) Drude response and (b)  
 152 Lorentz-Drude response when pumped with a beam radius of 1.16 mm and probed with the THz  
 153 focusing conditions that we found in our setup. Especially when aiming at discussing the dc limit,  
 154 discrepancies can be strong.

### 155 3.3. Influence on dynamics

#### 156 3.3.1. Temporal evolution of photoconductivity

157 The main advantage of OPTP is the possibility to study the temporal evolution of the real and  
 158 imaginary photoconductivity with the pump-probe delay time [4, 11, 12]. There, measuring  
 159 the differential electric field at the THz delay of the peak electric field of the undisturbed  
 160 THz pulse yields approximately the frequency averaged real photoconductivity, whereas the  
 161 same measurement at the THz delay of the zero-crossing of the undisturbed THz pulse yields

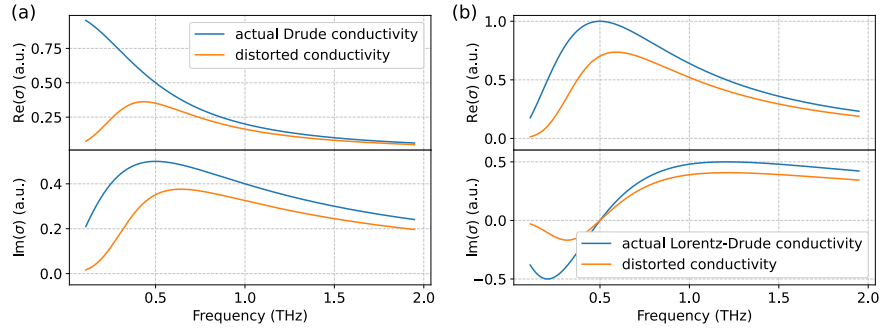


Fig. 3. Simulated perfect (a) Drude response and (b) Lorentz-Drude response and its distortion when a pump beam radius of 1.16 mm is employed and the THz beam is focused as in our setup.

162 approximately the frequency averaged imaginary photoconductivity [13, 14]. To assess the pump  
 163 beam spot size influence on such quantities that do not require a Fourier-transformation to the  
 164 frequency space, we used CdS nanowires as benchmark material and measured pump-probe  
 165 scans at the THz delay of the maximum of the undisturbed THz pulse. Fig. 4(a) shows that after  
 166 normalization, the frequency averaged real photoconductivity of CdS nanowires after excitation  
 167 with  $\lambda = 400$  nm, decays independent of the pump beam spot size. Preconditioned sufficient  
 168 contrast, the frequency averaged quantities can be considered robust. However, we observe  
 169 that for the largest pump beam radius of 3.02 mm, where the experiment was conducted in a  
 170 non-collinear fashion, the rise time of the signal is 2.3 ps, when it is only 1.2 ps for the pump beam  
 171 radius of 1.16 mm with a collinear experimental setup. Excitation at an angle results in a relative  
 172 delay between opposite transverse sides of the beam such that one side of the sample is excited  
 173 earlier than the other, effectively lowering the experiments temporal resolution. Thus, in such  
 174 non-collinear geometry it is important to keep the angle of incidence minimum to not degrade  
 175 the temporal resolution when using large pump beams. Pulse front tilting can be used to mitigate  
 176 this issue and improve the temporal resolution in non-collinear setups. In this application case,  
 177 the collinear arrangement is beneficial. Another approach to reduce errors is using beam-splitters  
 178 to unite the beam path of pump and probe beam for collinear excitation with large pump beam  
 179 spot sizes [15].

### 180 3.3.2. Charge Diffusion in highly conductive samples

181 In highly conductive extended samples, photoinduced charge carriers quickly diffuse after  
 182 excitation. With longer delay times between optical pump and THz probe, the spatial charge carrier  
 183 distribution widens, effectively changing the THz frequency range probing the photoinduced  
 184 changes. The diffusivity of charge carriers in silicon after photoexcitation with a fs-laser can be  
 185 as much as 1000 times higher than the room temperature diffusivity of  $30 \text{ cm}^2/\text{s}$  [16, 17]. From  
 186 this, we estimate a diffusion length of 0.04 mm within 600 ps after excitation. Employing optical  
 187 excitation with a beam radius of 0.54 mm on a silicon wafer, this corresponds to an expansion  
 188 of the spatial charge carrier distribution of 15 %. The influence of this broadening can be  
 189 demonstrated experimentally. Fig. 5(a) shows the differential THz spectrum transmitted through  
 190 a Si wafer at several delay times after optical excitation with a beam radius of 0.54 mm. For  
 191 frequencies larger than 1 THz, the differential THz spectrum does not change on the timescales  
 192 investigated here. The pump beam spot size is large enough to homogeneously excite the part of  
 193 the sample, to which the high THz frequencies are focused. However, for smaller THz frequencies,

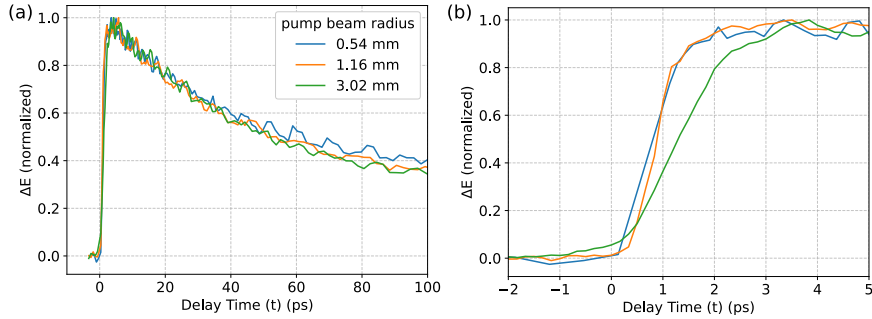


Fig. 4. (a) OPTP dynamics measured on CdS nanowires after excitation with  $\lambda = 400$  nm at the maximum of the undisturbed THz pulse for different pump beam radii. No differences in the decay dynamics are observed. (b) Same data as in (a), but zoomed to shorter pump-probe delay times. For the non-collinearly pumped experiment (3.02 mm pump beam radius), the rise time is longer than for the collinearly pumped experiments (1.16 mm and 0.54 mm).

194 which are focused to larger spot sizes, a rise in signal is observed, as charge carriers diffuse away  
 195 from the initially excited spot of the sample into the wider low-frequency probe beam spot. This  
 196 leads to a time-dependent change of the transmitted spectrum in addition to the one caused by the  
 197 dynamics of interest. Therefore, for investigations of high-conductivity samples, a large pump  
 198 spot size, realized using a non-collinear geometry or beam-splitters, is generally required. It  
 199 should be noted that charges do not only diffuse in plane but also along the excitation direction  
 200 into the material, effectively thickening the excited layer, which may also lead to a change of the  
 201 transmitted THz spectrum.

#### 202 4. Conclusion

203 We discussed the distortions induced by too small pump beam spot sizes on OPTP and described  
 204 them by a simple weighting of the frequency-resolved probe beam spot profiles with the spatial  
 205 charge carrier distribution induced by the pump pulse. In case of frequency-dependent quantities  
 206 such as the Drude model are to be discussed, a large enough pump beam spot size should be  
 207 ensured. In most employed OPTP configurations, this requires a non-collinear pump-probe  
 208 arrangement, which come with the downside of a reduction of temporal resolution. However, if  
 209 the THz focus is characterized carefully, the distortions can also be corrected for using the overlap  
 210 factor we describe. In case the OPTP dynamics are of central interest, a collinear geometry,  
 211 where the optical pump pulse is overlaid with the THz probe pulse through a hole in a OAP, is  
 212 beneficial. For highly conductive samples, diffusion of charge carriers away from the pump beam  
 213 spot leads to larger excited areas, which yields spectral shifts in the measured differential electric  
 214 field if too small pump beam spot sizes are employed.

#### 215 5. Funding

216 This work is supported by the Cluster of Excellence ‘Advanced Imaging of Matter’ of the Deutsche  
 217 Forschungsgemeinschaft (DFG) – EXC 2056 – project ID 390715994 and via the Graduate  
 218 School ‘Nanohybrid’ (GRK 2536). H.L. and F.X.K. acknowledge support within the DFG project  
 219 No. 432266622.

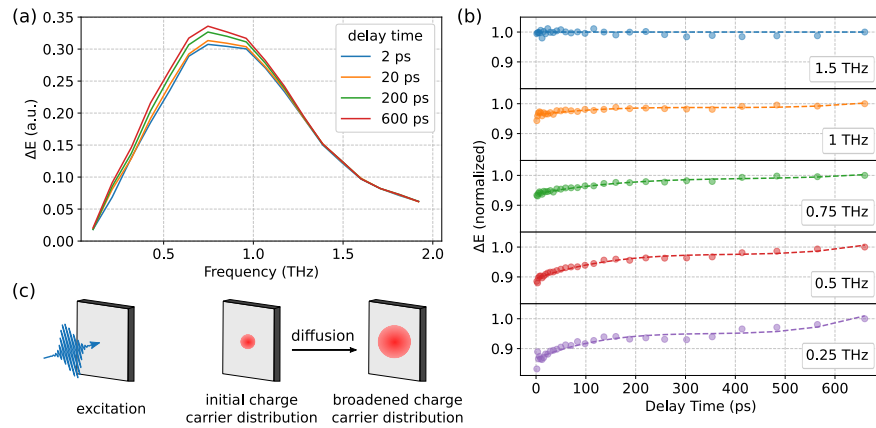


Fig. 5. (a) Measured differential THz spectrum transmitted through a Si wafer at different delay times after excitation with  $\lambda = 400$  nm at an excitation fluence of  $220 \mu\text{J}/\text{cm}^2$  with a pump beam radius of 0.54 mm. (b) Normalized differential electric fields of the measurement displayed in (a) over pump-probe delay. The initial rise in signal at short delay times is omitted for clarity. (c) Schematic representation of the observed spatial broadening in the charge carrier distribution, that leads to better overlap with low THz frequencies at later delay times.

## 220 6. Acknowledgments

221 The authors thank Daniel Lengle for providing the CdS nanowire sample.

## 222 7. Disclosures

223 The authors declare no conflicts of interest.

## 224 8. Data availability

225 Data underlying the results presented in this paper are not publicly available at this time but may  
226 be obtained from the authors upon reasonable request.

## 227 9. Supplemental document

228 See Supplement 1 for supporting content.

## 229 References

- 230 1. U. Banin, N. Waiskopf, L. Hammarström, G. Boschloo, M. Freitag, E. M. J. Johansson, J. Sá, H. Tian, M. B. Johnston,  
231 L. M. Herz, R. L. Milot, M. G. Kanatzidis, W. Ke, I. Spanopoulos, K. L. Kohlstedt, G. C. Schatz, N. Lewis, T. Meyer,  
232 A. J. Nozik, M. C. Beard, F. Armstrong, C. F. Megarity, C. A. Schmuttenmaer, V. S. Batista, and G. W. Brudvig,  
233 "Nanotechnology for catalysis and solar energy conversion," *Nanotechnology* **32**, 042003 (2021).
- 234 2. H. J. Joyce, J. L. Boland, C. L. Davies, S. A. Baig, and M. B. Johnston, "A review of the electrical properties of  
235 semiconductor nanowires: insights gained from terahertz conductivity spectroscopy," *Semicond. Sci. Technol.* **31**,  
236 103003 (2016).
- 237 3. P. Kužel and H. Němec, "Terahertz Spectroscopy of Nanomaterials: a Close Look at Charge-Carrier Transport," *Adv.*  
238 *Opt. Mater.* **8**, 1900623 (2020).
- 239 4. Y. U. Staechelin, M. Deffner, S. Krohn, C. Castillo Delgado, J. S. Niehaus, and H. Lange, "Carrier localization in  
240 zero-dimensional and one-dimensional CdSe–CdS heterostructures," *The J. Chem. Phys.* **156**, 061102 (2022).
- 241 5. R. Ulbricht, E. Hendry, J. Shan, T. F. Heinz, and M. Bonn, "Carrier dynamics in semiconductors studied with  
242 time-resolved terahertz spectroscopy," *Rev. Mod. Phys.* **83**, 543–586 (2011).

- 243 6. P. Jepsen, D. Cooke, and M. Koch, "Terahertz spectroscopy and imaging - Modern techniques and applications: THz  
244 spectroscopy and imaging - Modern techniques and applications," *Laser & Photonics Rev.* **5**, 124–166 (2011).
- 245 7. S. L. Dexheimer, ed., *Terahertz Spectroscopy: Principles and Applications* (CRC Press, Boca Raton, 2008).
- 246 8. M. C. Beard, G. M. Turner, and C. A. Schmuttenmaer, "Transient photoconductivity in GaAs as measured by  
247 time-resolved terahertz spectroscopy," *Phys. Rev. B* **62**, 15764–15777 (2000).
- 248 9. G. L. Dakovski, B. Kubera, S. Lan, and J. Shan, "Finite pump-beam-size effects in optical pump-terahertz probe  
249 spectroscopy," *J. Opt. Soc. Am. B* **23**, 139 (2006).
- 250 10. J. H. Strait, P. A. George, M. Levendorf, M. Blood-Forsythe, F. Rana, and J. Park, "Measurements of the  
251 Carrier Dynamics and Terahertz Response of Oriented Germanium Nanowires using Optical-Pump Terahertz-Probe  
252 Spectroscopy," *Nano Lett.* **9**, 2967–2972 (2009).
- 253 11. L. T. Kunnenan, M. Zanella, L. Manna, L. D. A. Siebbeles, and J. M. Schins, "Mobility and Spatial Distribution of  
254 Photoexcited Electrons in CdSe/CdS Nanorods," *The J. Phys. Chem. C* **117**, 3146–3151 (2013).
- 255 12. A. Burgos-Caminal, E. Socie, M. E. F. Bouduban, and J.-E. Moser, "Exciton and Carrier Dynamics in Two-Dimensional  
256 Perovskites," *The J. Phys. Chem. Lett.* **11**, 7692–7701 (2020).
- 257 13. P. D. Cunningham, "Accessing Terahertz Complex Conductivity Dynamics in the Time-Domain," *IEEE Trans. on  
258 Terahertz Sci. Technol.* **3**, 494–498 (2013).
- 259 14. X. Xing, L. Zhao, Z. Zhang, X. Liu, K. Zhang, Y. Yu, X. Lin, H. Y. Chen, J. Q. Chen, Z. Jin, J. Xu, and G.-h. Ma,  
260 "Role of Photoinduced Exciton in the Transient Terahertz Conductivity of Few-Layer WS<sub>2</sub> Laminates," *The J. Phys.  
261 Chem. C* **121**, 20451–20457 (2017).
- 262 15. L. Fekete, P. Kužel, H. Němec, F. Kadlec, A. Dejneka, J. Stuchlík, and A. Fejfar, "Ultrafast carrier dynamics in  
263 microcrystalline silicon probed by time-resolved terahertz spectroscopy," *Phys. Rev. B* **79**, 115306 (2009).
- 264 16. E. Najafi, V. Ivanov, A. Zewail, and M. Bernardi, "Super-diffusion of excited carriers in semiconductors," *Nat.  
265 Commun.* **8**, 15177 (2017).
- 266 17. R. Brunetti, C. Jacoboni, F. Nava, L. Reggiani, G. Bosman, and R. J. J. Zijlstra, "Diffusion coefficient of electrons in  
267 silicon," *J. Appl. Phys.* **52**, 6713–6722 (1981).

## 5.5 Cation exchange during the synthesis of colloidal type-II ZnSe-dot/CdS-rod nanocrystals

This publication is reprinted from Jannik Rebmann, Hans Werners, Florian Johst, Marcel Dohrmann, Yannic U. Staechelin, Christian Strelow, Alf Mews and Tobias Kipp, *Chemistry of Materials* **2023**, 35, 1238-1248, CC BY-NC-ND 4.0 - published by the American Chemical Society (ACS).<sup>287</sup>

DOI: [10.1021/acs.chemmater.2c03278](https://doi.org/10.1021/acs.chemmater.2c03278)

In this work, cation exchange during the growth of an elongated CdS shell onto a ZnSe core is studied. TA measurements were conducted on aliquots taken from the growth reaction and an exchange-only reaction to investigate spectral shifts of excitonic resonances as well as charge carrier thermalization and Auger lifetimes. It was shown that during the initial stages of the reaction, cation exchange dominates over shell growth, resulting in up to 50 % cation exchange in the ZnSe core.

*The author of this thesis carried out the TA measurements together with Hans Werners and helped with the discussion of the data.*



# Cation Exchange during the Synthesis of Colloidal Type-II ZnSe-Dot/CdS-Rod Nanocrystals

Jannik Rebmann, Hans Werners, Florian Johst, Marcel Dohrmann, Yannic U. Staechelin, Christian Strelow, Alf Mews,\* and Tobias Kipp\*

Cite This: *Chem. Mater.* 2023, 35, 1238–1248

Read Online

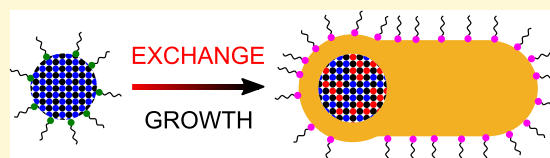
ACCESS |

Metrics & More

Article Recommendations

Supporting Information

**ABSTRACT:** Cation exchange is known to occur during the synthesis of colloidal semiconductor heteronanoparticles, affecting their band gap and thus altering their optoelectronic properties. It is often neglected, especially when anisotropic heterostructures are discussed. We present a study on the role of cation exchange inevitably occurring during the growth of anisotropic dot-in-rod structures consisting of a spherical ZnSe core enclosed by a rod-shaped CdS shell. The material combination exhibits a type-II band alignment. Two reactions are compared: the shell-growth reaction of CdS on ZnSe and an exchange-only reaction of ZnSe cores to CdSe. Transmission electron microscopy and a comprehensive set of optical spectroscopy data, including linear and time-resolved absorption and fluorescence data, prove that cation exchange from ZnSe to CdSe is the dominant process in the initial stages of the shell-growth reaction. The degree of cation exchange before significant shell growth starts was determined to be about 50%, highlighting the importance of cation exchange during the heteronanostructure growth.



## INTRODUCTION

Colloidal semiconductor heteronanostructures have great potential for optoelectronic devices because of their high quantum yields (QYs), tunable emission wavelengths, and variable fluorescence lifetimes.<sup>1–7</sup> In a classical core/shell nanostructure with a type-I band alignment, the larger band gap of the shell encloses the smaller band gap of the core and thus passivates the core.<sup>8–10</sup> In a type-II nanostructure, the conduction band (CB) and valence band (VB) are staggered, which leads to a spatial separation of electrons and holes above the heterointerface. This results in large Stokes shifts,<sup>11–13</sup> long fluorescence lifetimes,<sup>14,15</sup> and the fluorescence switchability upon external stimuli like external fields.<sup>16–19</sup> Moreover, type-II heterostructures are of great interest for photocatalysis because of their intrinsic property to spatially separate photoexcited charge carriers.<sup>15,20,21</sup>

The material system ZnSe/CdS exhibits a type-II band alignment, as sketched in Figure 1a. It has been shown to be suitable for the synthesis of heteronanostructures of different shapes, like spherical core–shell nanocrystals,<sup>22,23</sup> tetrapods,<sup>24</sup> dumbbells,<sup>25</sup> or dot-in-rod structures.<sup>14,16</sup> Since in this system, both materials consist of different cations, cation exchange can occur during the nanostructure synthesis. In fact, ZnSe and CdSe are fully miscible and are known to be exchangeable.<sup>26–28</sup>

For spherical ZnSe-core/CdS-shell nanocrystals, Boldt et al. showed how the optical properties can be adjusted by controlled interdiffusion of cations across the heterointerface.<sup>22,23</sup> Compared to spherical structures, anisotropic ZnSe-dot/CdS-rod nanostructures exhibit additional degrees of

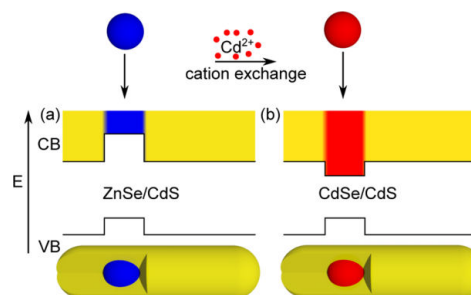


**Figure 1.** Schematic band alignment of (a) ZnSe/CdS and (b) CdSe/CdS dot-in-rod nanostructures. The offset of the conduction band is lowered when Zn<sup>2+</sup> ions are exchanged by Cd<sup>2+</sup> ions. This changes the band alignment from type-II to type-I.

freedom for designing their optical properties due to the expanded delocalization of charge carriers. Since the synthesis of a rod-like CdS shell around a ZnSe core is typically performed in an excess of Cd ions, these can partially exchange Zn ions such that Zn<sub>1-x</sub>Cd<sub>x</sub>Se cores are formed. Since CdSe/

Received: October 30, 2022

Revised: December 13, 2022

Published: January 31, 2023



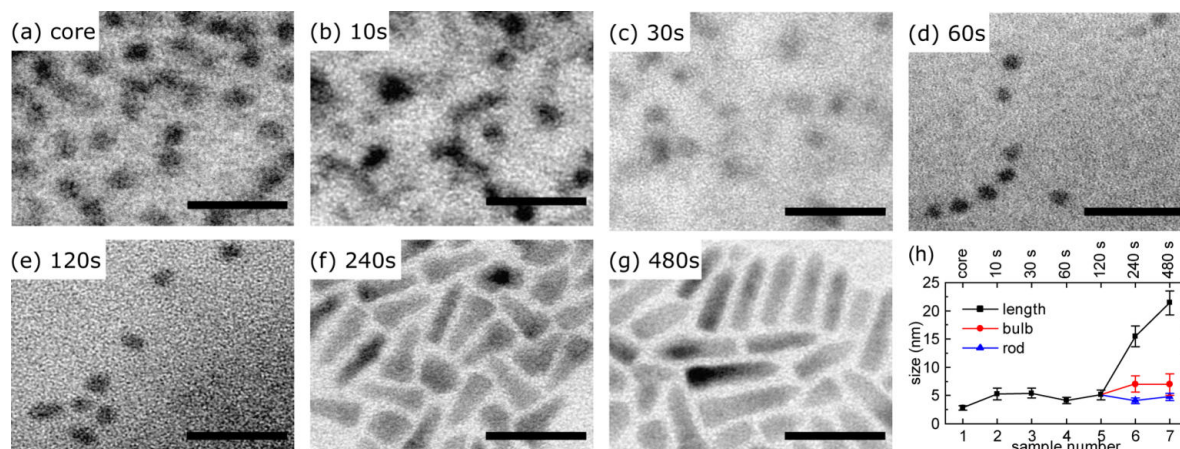


**Figure 2.** (a–g) Representative TEM images of (a) ZnSe core sample and (b–g) aliquots of the growth series, belonging to reaction times as noted. Scale bars: 25 nm. (h) Sizes of the length, rod diameter, and bulb diameter (if distinguishable) as determined by TEM vs the sample number. Lines connecting data points are guides to the eye.

CdS exhibits a type-I band alignment, as depicted in Figure 1b, the successive exchange of ZnSe to CdSe in the core material eventually leads to a transition from a type-II structure to a type-I structure. During cation exchange in particular, the conduction band edge is lowered, as sketched in Figure 1. Therefore, understanding the growth mechanism and the role of cation exchange in the synthesis of ZnSe/CdS dot-in-rod structures is not only of fundamental interest but also needed to tailor the optoelectronic properties of such heterostructures.

A major step in this direction was performed by Dorfs et al., who directly coated ZnSe cores with the anisotropic CdS shell. They observed that the shell growth is slow in the first 40 s of reaction time but increases thereafter so that the complete rod-shaped shell is formed after 120 s. The realization of type-II heterostructures was proven based on spectroscopic data, but the possibility of cation exchange in the core material was not taken into account.<sup>14,29</sup>

In a different work, Hewa-Kasakarage et al. first coated spherical ZnSe cores with two to three monolayers of a spherical CdS shell before an anisotropic CdS shell was grown. The growth process was monitored, but cation exchange or interdiffusion was not addressed.<sup>16</sup>

In this work, we investigate the synthesis of ZnSe/CdS dot-in-rod nanostructures in particular with respect to the cation exchange. We monitored the growth of an anisotropic CdS shell on spherical ZnSe cores by taking aliquots at different reaction times to perform transmission electron microscopy (TEM) as well as steady-state and time-resolved UV/vis absorption and photoluminescence (PL) measurements. In addition, we performed control experiments in which only cation exchange can occur but the shell growth is inhibited. We find that cation exchange is indeed the dominant process in the beginning of the shell-growth reaction: about 50% of the initial Zn ions in the core are exchanged by Cd ions before a significant CdS shell has been formed during the reaction.

## RESULTS AND DISCUSSION

Pairs of sample series are investigated, which consist of the so-called growth and exchange series, respectively. For each series, the starting point for the synthesis is pre-synthesized ZnSe core nanocrystals from the same batch dissolved and stored in

triethylphosphine (TOP). For the growth series, these ZnSe cores were dispersed in a mixture of sulfur and TOP (S/TOP) and hot-injected into a Cd precursor solution. The amount of the Cd precursor determines the CdS shell length. In our case, the ratio of Cd ions from the precursor to Zn ions from the ZnSe cores was 32:1. For the exchange series, the reaction conditions were absolutely identical except for using plain TOP instead of S/TOP. For both series, after certain reaction times between 10 s and 8 min, six samples were taken from the solutions for their later investigation. Thus, in the growth series, Cd and S were present in the reaction solution, allowing CdS to be formed, while in the exchange series, only Cd and no S was present.

### Investigation by Transmission Electron Microscopy.

Figure 2a–g shows representative TEM images of the original core sample and of aliquots of the growth series, from which changes in size and shape during the reaction time can be deduced. The ZnSe cores exhibit a spherical shape with a diameter of about 3 nm. The particles of the aliquots appear to be spherical in the early reaction, up to about 120 s of reaction time. After 240 s of reaction time, an anisotropic shape is evident. One end of the rod is thicker than the other and is presumably the location of the ZnSe core.<sup>14</sup>

Figure 2h summarizes the sizes of the particles at the different reaction stages as determined by TEM. Almost no increase of diameter occurs in the first 60 to 120 s of reaction time. The rod growth is observable only for longer reaction times, leading to a rod length of about 22 nm after 480 s of reaction time.

Even though the TEM images in Figure 2 are the best ones that were obtained during this study, the contrast is very weak. This is because of the organometallic cadmium phosphonate precursor, which is used as the cadmium source during the reaction. At early reaction stages, the unreacted cadmium precursor is still present in the samples. It is known that cadmium phosphonate forms polymeric layered structures.<sup>30–32</sup> This unreacted polymer precipitates in the cleaning procedure of the aliquots, when a polar solvent is added to precipitate the nanoparticles. Thus, the particles are trapped in the cadmium phosphonate polymer<sup>33</sup> and cannot be separated. The cadmium phosphonate complex shows low solubility and

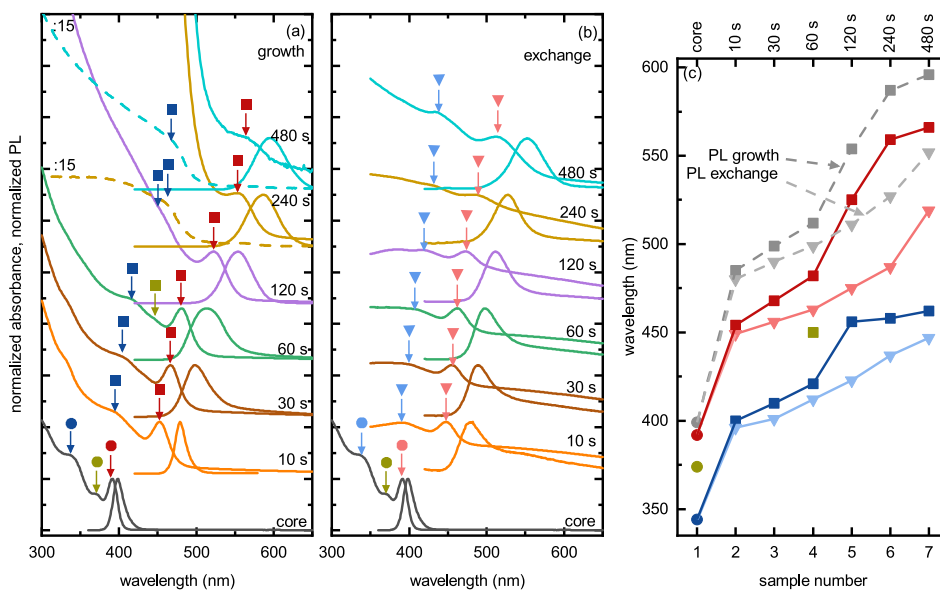


**Figure 3.** (a,b) Linear absorption and PL spectra of the (a) growth and (b) exchange sample series. Absorbance spectra are normalized to the first excitonic feature. Excitonic absorption maxima are marked with arrows and symbols. Dashed spectra correspond to the solid spectra of the same color divided by 15. (c) Position of all absorption and emission features marked in (a) for the growth series (squares) and (b) for the exchange series (triangles) vs the sample number. Lines connecting data points serve as guides to the eye.

melts only above 250 °C.<sup>31,34</sup> It produces high noise in TEM images and X-ray diffraction patterns, which hinders any further studies using high-resolution TEM, including high-resolution energy-dispersive X-ray spectroscopy, or X-ray diffraction.<sup>30–34</sup>

Hence, in the following, we present a detailed study of the changing optical properties of particles in solution to further investigate the different stages of the reaction.

**Linear Absorption and PL Measurements.** Figure 3 shows UV/vis absorption and PL spectra of all aliquots of (a) the growth series and (b) the exchange series. All spectra are normalized to their corresponding intensity of the low-energy transition.

The absorption spectrum of the core solution [given in panels (a) and (b)] shows the ground-state excitonic transition at a wavelength of about 392 nm (marked by a red arrow) as well as higher energy transitions at shorter wavelengths (marked by blue and dark yellow arrows). The PL emission is centered at about 399 nm; thus, the Stokes shift can be calculated to be 56 meV.

Regarding first the aliquots of the growth series (Figure 3a), the general shape of the UV/vis absorption spectra resembles that of the core spectrum with their features being continuously red-shifted until a reaction time of 60 s. After that, a strong absorption below 475 nm dominates the spectra, while the lowest excitonic transition at larger wavelengths (red arrows) remain visible as a shoulder. The PL emission is also shifting to the red with increasing reaction time. The Stokes shift abruptly increases already for the first aliquot to 175 meV and stays rather constant for longer reaction times. The red shift of the excitonic peaks both in absorption and emission cannot be explained by the growth of a CdS shell around the ZnSe core accompanied by a type-II band alignment between the core and shell material because according to TEM, no significant increase of particle diameter was observed for early

aliquots. Hence, this suggests that this initial red shift is not caused by CdS growth but by cation exchange from ZnSe to CdSe. The increase of absorption below 475 nm for long reaction times could then be explained by the formation of CdS during the reaction (bulk band gap of CdS: 2.44 eV, corresponding to 500 nm).

To validate the assumption of the cation exchange being responsible for the red shift at early stages, samples from the exchange series were taken at the same reaction intervals and investigated by UV/vis absorption spectroscopy and PL spectroscopy. Corresponding spectra are shown in Figure 3b. Similar to the growth series, the lowest excitonic transition (red arrows) continuously shifts to the red with increasing reaction time. In addition, the PL peak also shifts to longer wavelengths, while the Stokes shift again stays nearly constant over the reaction time.

Since for the exchange series no sulfur precursor is present during the reaction, a CdS shell growth can be ruled out. Here, the cation exchange reaction from the original ZnSe core nanocrystals (bulk band gap of ZnSe: 2.73 eV) to intermixed  $Zn_{1-x}Cd_xSe$  (bulk band gap of CdSe: 1.76 eV) can be the only reason for the observed red shift.

Figure 3c compares the position of all absorbance features marked by arrows in Figure 3a,b as well as the PL peaks of both the growth and exchange sample series. The horizontal axis gives the sample number, which is a non-linear representation of the reaction time. Noticeably, the excitonic ground-state absorption, a higher-state absorption, and the PL emission wavelength behave very similarly for both sample series up to a reaction time of about 60 s. Major differences of the absorption and emission wavelengths between growth and exchange series are only visible for reaction times longer than 60 s.

The similarity of absorption and emission wavelengths between the two series of samples for reaction times smaller 60

s suggests that similar processes take place during their reactions. Since cation exchange from Zn to Cd is the only possible process that explains the observed red shift for the exchange series, this process seems to be dominant also in the early stages for the growth series. The difference in absorption and emission wavelengths for reaction times longer than 60 s reveals that a fundamentally different process occurs for the growth series as compared to that for the exchange series. We attribute this to the growth of a CdS shell around the core nanocrystals that were originally ZnSe and were (partially) cation-exchanged to  $Zn_{1-x}Cd_xSe$  in the earlier course of the reaction.

**Estimating the Degree of Cation Exchange.** It is of importance to estimate the degree of cation exchange that occurred during the reactions as it determines the final CB and VB profiles. Hence, two independent methods were used to quantify the degree of cation exchange.

First, the composition of a final ZnSe-dot/CdS-rod sample after completed rod growth was determined by elemental analysis using inductively coupled plasma mass spectrometry (ICP–MS). Here, we determined the Zn to Se ratio since both ions are present in the initial ZnSe core and only Zn is partially exchanged to Cd. The ratio of Zn to Se in the final dot-in-rod structure was found to be 0.5:1. In comparison, pure ZnSe cores before rod growth show a ratio of Zn to Se of 1.2:1. Hence, about 50 to 60% of the Zn ions of the original ZnSe core nanocrystals are exchanged by Cd ions in the final dot-in-rod structure.

Second, the exciton energy for spherical  $Zn_{1-x}Cd_xSe$  nanocrystals was calculated in dependence of  $x$  within the effective mass approximation including the direct Coulomb interaction. The Schrödinger and Poisson equations were numerically solved in an iterative way using the commercial software COMSOL Multiphysics, following the procedure reported by Panfil and co-workers.<sup>35,36</sup> Importantly, for the calculations, we assumed a spatially homogeneous alloy within the nanocrystals. This assumption is justified by the work of Groeneveld et al., who reported on homogeneous alloying of even slightly larger ZnSe nanocrystals in a Cd cation exchange reaction already at much lower reaction temperatures of 240 °C within 60 s of reaction time. It was demonstrated that the rate-limiting steps in the exchange reaction are the processes on the nanocrystal surface and not the diffusion of Cd ions within the crystal, resulting in a fast homogeneous distribution of cadmium and zinc ions at high temperatures.<sup>26</sup> Homogeneous alloying in cation-exchanged  $Zn_{1-x}Cd_xSe$  nanocrystals has also been reported by Zhong and co-workers.<sup>37</sup> One might assume that lower temperatures during the synthesis lead to inhomogeneous alloying. However, we found that already at temperatures of 250 °C, no growth of the rod-like CdS shell occurs.

Figure 4 shows the calculated change in exciton energy  $\Delta E$  of alloyed  $Zn_{1-x}Cd_xSe$  nanocrystals for varying  $x$  compared to the exciton energy of pure ZnSe nanocrystals. For the calculation, a nanocrystal diameter of 3.16 nm was assumed, as estimated from the measured excitonic UV/vis absorption energy.<sup>38</sup> The calculations reveal that increasing the amount of Cd from pure ZnSe to pure CdSe in alloyed nanocrystals decreases the exciton energy by about 0.9 eV. This decrease would correspond to a red shift of the absorption and emission energies. The horizontal lines in Figure 4 represent experimental values of the red shifts after certain reaction times as determined from the emission spectra of the exchange

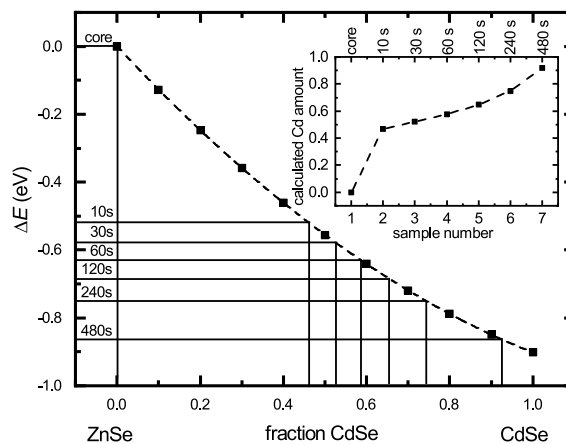


**Figure 4.** Calculated change in exciton energy of spherical  $Zn_{1-x}Cd_xSe$  nanocrystals with respect to that of pure ZnSe nanocrystals. The dashed line represents a continuous fit for the discrete data points. Horizontal lines represent energy shifts as measured in PL experiments of the exchange sample series (cf. Figure 3b). Points of intersection with the fit function give values of the estimated amount of Cd within the respective nanocrystal sample. In the inset, the  $x$  determined in this way is plotted against the corresponding sample number.

series shown in Figure 3b. From their intersections with the dashed line, which connects calculated data points, corresponding values of  $x$  can be estimated. As summarized in the inset of Figure 4,  $x$  increases rapidly within the first seconds of the reaction. After 10 s, already roughly 45% of Zn is exchanged by Cd. After 30 s of the exchange reaction,  $x$  has increased to approximately 50%.

Both the estimated degree of cation exchange in the readily prepared dot-in-rod sample and the calculated degree of cation exchange coincide well under the assumption that cation exchange is the dominant process in the early stages of the growth reaction before CdS shell growth starts.

**Growth Model for CdS on ZnSe Cores.** Figure 5a–d illustrates the proposed reaction progression for both the growth sample series and the exchange sample series. The starting point for both sample series is spherical ZnSe core nanocrystals covered with octadecylamine (ODA) ligands (cf. Figure 5a). A solution of ZnSe cores with (growth series) or without (exchange series) the sulfur precursor is injected into a hot Cd precursor solution containing octadecylphosphonic acid (ODPA) and hexylphosphonic acid (HPA). For both sample series, it is assumed that a surface modification such as ligand exchange takes place early after injection, where the amines are replaced by the phosphonic acids (cf. Figure 5a,b).<sup>27,39,40</sup> Experimental evidence for this ligand exchange will be discussed later using data from time-resolved optical spectroscopy.

For the exchange series, the only possible process that can explain the observed red shift of the excitonic features is cation exchange from Zn to Cd since here the reaction solution does not contain any extra anions that could lead to a further growth of the nanocrystals, which would be accompanied by a decrease in quantum confinement. Comparison of the experimentally determined excitonic energy shifts to theoretical modeling suggests that already after 10 s of reaction time, about 45% of the Zn ions are exchanged by Cd (cf. Figure 4).

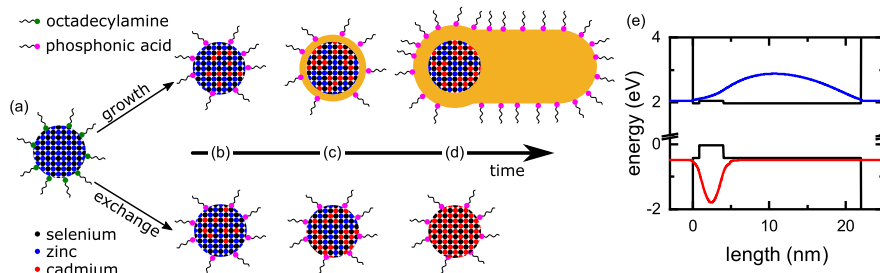


**Figure 5.** (a–d) Model for the comparison of growth of a CdS shell on ZnSe cores and exchange from ZnSe to CdSe. In the growth series, partial cation exchange from ZnSe to  $Zn_{1-x}Cd_xSe$  is followed by CdS shell growth. In the exchange series, exchange of Cd into the ZnSe core leads to a nearly fully exchanged CdSe core. (e) Potential landscape (black) and single-particle wave functions of the electron (blue) and the hole (red) in a dot-in-rod structure with a partially exchanged  $Zn_{1-x}Cd_xSe$  core with  $x = 0.5$ .

The degree of cation exchange is visualized in Figure 5 by partially changing the color representing the cations from blue to red. Since the ZnSe core nanocrystals are rather small and the reaction temperature is high, it is important to note that the exchanged Cd ions are expected to be homogeneously distributed even in the beginning of the reaction.<sup>26,37</sup>

In TEM images of the aliquots of the growth series at early reaction stages, no shell growth is evident. The great similarities in the linear absorption and PL spectra between the two sample series for early reaction times up to 60 s prove that in the beginning, cation exchange is the dominant process also for the growth series. Consequently, we assume that up to reaction times of 30 s to 60 s, the products of the growth series are essentially the same as those of the exchange series (cf. Figure 5b). The modeling for the exchange series delivered a degree of cation exchange of  $x = 0.5$  after about 30 s of reaction time. Subtle red shifts of the absorbance and PL maxima of the growth series compared to that of the exchange series suggest slight passivation of the partially exchanged  $Zn_{1-x}Cd_xSe$  core nanocrystals by CdS (cf. Figure 5c).

For reaction times of 60 s and larger, the positions of absorbance and PL features begin to diverge sharply between growth and exchange series. For the growth series, the pronounced red shifts of the lowest-energy excitonic features in PL and absorption are the result of CdS shell growth on partially exchanged  $Zn_{1-x}Cd_xSe$  cores, drastically altering the quantum confinement within the nanostructures (cf. Figure 5c,d). With the formation of the complete shell, further cation exchange should be slowed down because the thermodynamically preferred composition of  $Zn_{0.5}Cd_{0.5}Se$  has already been reached<sup>23</sup> and the higher stability of zinc phosphonate than that of cadmium phosphonate is not a driving force for exchange after shell deposition.<sup>26</sup> Results of the elemental analysis revealed a Zn/Se ratio of 0.5, which coincides well with the estimated  $x$  of the exchange series after about 30 s of reaction time. The growth of the CdS shell for long reaction times in the growth series is also evident by the increase of absorbance in the wavelength range of 475 nm (cf. Figure 3a), which corresponds to the CdS bulk band gap plus confinement energy, where the latter decreases for increasing reaction time.

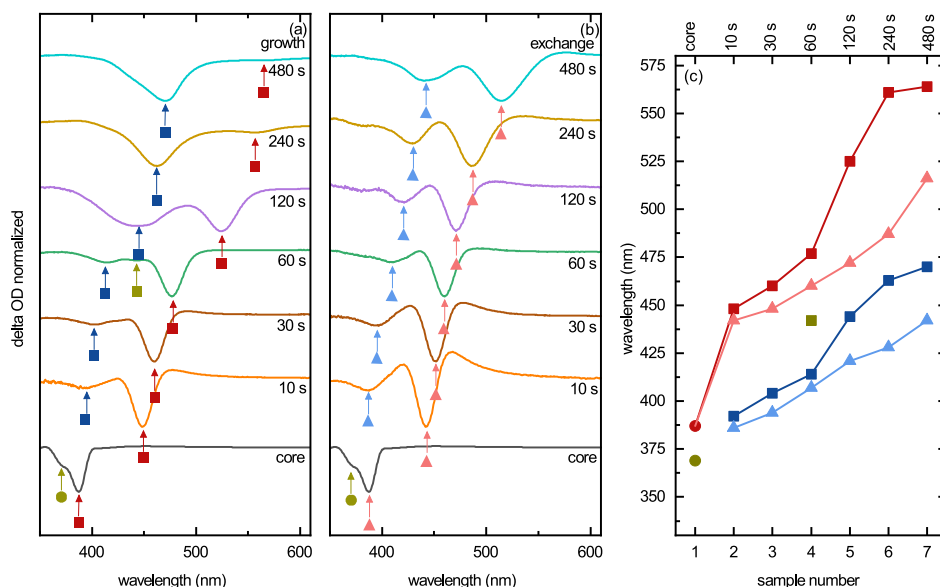
It is striking that the CdS shell growth does not start directly upon injection of the ZnSe cores into the precursors. We attribute this to the higher reaction speed of the cation exchange reaction in the beginning than that of the shell growth. Cd ions are initially consumed for exchange until the exchange rate decreases due to the higher cadmium amount in the  $Zn_{1-x}Cd_xSe$  core. Thus, the growth becomes more likely.

Anisotropic growth of the shell is promoted by high reaction temperatures, which lead to the growth of CdS in the wurtzite phase. It is further supported by the combination of phosphonic acids as ligands that passivate unpolar side facets better than polar basal facets.<sup>41</sup>

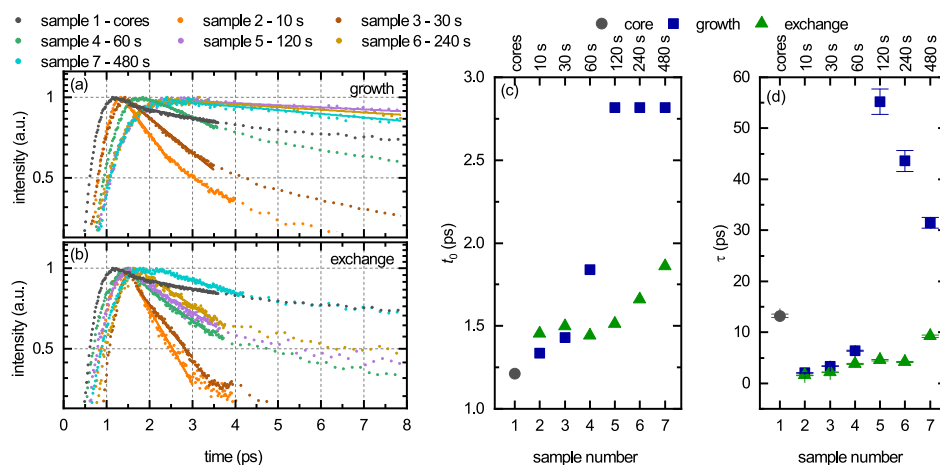
For the exchange series, for reaction times larger than 60 s, an ongoing cation exchange reaction is assumed until ultimately the former ZnSe core nanocrystals have completely transformed to CdSe (cf. Figure 5d). A complete exchange can be expected after reaction times of several minutes (cf. Figure 4). It is worth noting that we observed degradation in the exchange series of different sample pairs for long reaction times. We attribute this to the rapid exchange from smaller  $Zn^{2+}$  to bigger  $Cd^{2+}$ , which might introduce defects.<sup>26</sup> The details are beyond the scope of this study as it is not the main process in early reaction stages.

Figure 5e shows the CB and VB profiles along the rod axis for the final dot-in-rod sample. It has been calculated assuming a partially exchanged homogeneous  $Zn_{1-x}Cd_xSe$  core with  $x = 0.5$ , as determined by ICP–MS, surrounded by a CdS shell. The values for the effective masses, band gaps, and offsets were taken from refs 42 and 43. Further details can be found in Table S1. The potential landscape exhibits a clear type-II character with staggered bands. We calculated the single-particle electron and hole wave functions within such a potential assuming a core diameter of 3.16 nm, according to the initial ZnSe core size, and a shell geometry as obtained from TEM, that is, a length of 22 nm and a diameter of 4.77 nm (cf. Figure 2). Results are also shown in Figure 5e, illustrating the type-II-induced spatial charge separation, with the hole being localized in the core and the electron being delocalized within the shell. Calculations for dot-in-rod heterostructures with ZnSe and CdSe cores for comparison are shown in the Supporting Information.

In the following, we discriminate between type-II band alignment and type-II and quasi-type-II behavior. The band alignment is dependent on the composition of the core and shell materials, and the behavior is determined by the band alignment and the size of the core and shell. Particles with thin CdS shells exhibit type-II band alignment with the hole being confined in the core. The electron is being delocalized over the whole particle because it cannot be exclusively confined within a thin shell, which is ultimately referred to as quasi-type-II behavior. The type-II band alignment leads to a significantly decreased electron–hole overlap as soon as the shell thickness or length increases such that the electron effectively avoids the core region, which is called type-II behavior. As long as no



**Figure 6.** (a,b) TA spectra of the (a) growth and (b) exchange series. All spectra are normalized to their feature exhibiting the strongest bleach, respectively. The spectra correspond to pump–probe delay times between 1 and 3 ps, where the ground-state exciton transition reaches its maximum bleach. The absorption features are marked with arrows and symbols. All samples were excited with a wavelength of  $330 \text{ nm} \pm 20 \text{ nm}$ . (c) Position of TA bleach features marked in (a) for the growth series (squares) and (b) for the exchange series (triangles) vs the sample number. Connecting lines are guides to the eye.



**Figure 7.** (a,b) TA dynamics at the position of the ground-state exciton (red arrows Figure 6a,b for samples of the (a) growth and (b) exchange series. Symbols represent measured data, and solid lines represent the monoexponential fits. (c) Rise time  $t_0$  and (d) decay time  $\tau$  vs the sample number extracted from (a) and (b) for the growth (blue squares) and exchange (green triangles) series.

shell growth occurs, no kind of band alignment can be assigned to the alloyed core-only particles.

**Time-Dependent Optical Spectroscopy.** Time-dependent optical spectroscopy was performed to work out differences in the exciton dynamics during cation exchange and subsequent growth of the elongated CdS shell. It gives insights into the charge carrier separation due to the type-II band alignment of the final sample as well as of late reaction stages. Transient absorption (TA) spectroscopy is able to resolve ultrafast exciton dynamics in the picosecond regime, whereas exciton dynamics on the nano- to microsecond timescale are addressed by fluorescence lifetime measurements.

**Transient Absorption Spectroscopy.** TA measurements were performed with a pump wavelength of  $330 \text{ nm} \pm 20 \text{ nm}$ , which leads to an excitation far above the band gap of the core particles. We used a constant and rather high pump fluence to compensate for small absorption cross-sections of early particles and to achieve acceptable signal-to-noise ratios that are decreased by scattering on cadmium phosphonate polymeric impurities, as already mentioned above. Further details are given in the [Experimental Section](#).

Figure 6 shows normalized TA spectra of all samples of (a) the growth series and (b) the exchange series. The spectra correspond to pump–probe delay times between 1 and 3 ps,

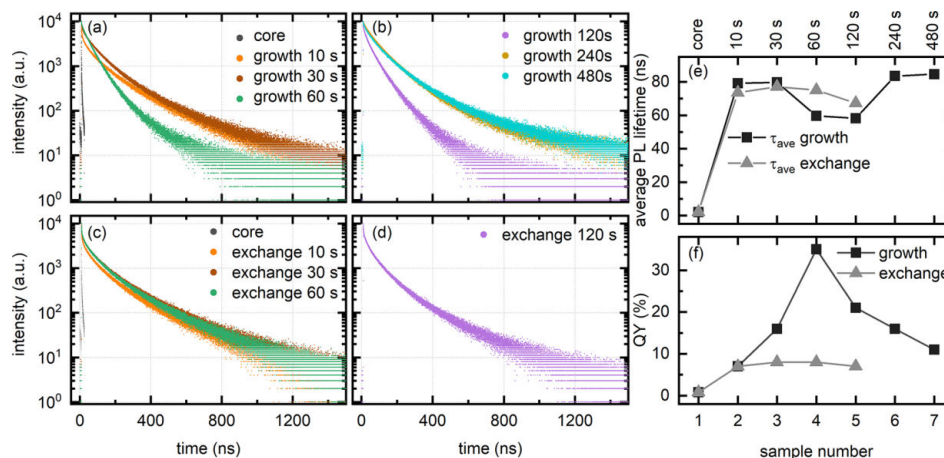


**Figure 8.** (a–d) Fluorescence decay curves of pure ZnSe cores, growth series (a,b), and exchange series (c,d). All samples were excited above the CdS band gap energy, with the repetition rates of 3.7 MHz (ZnSe cores) and 0.59 MHz (all aliquots), respectively. (e,f) Comparison of growth and exchange series regarding the (e) average lifetimes of the decay curves and (f) QY of each sample, measured in relation to the organic dye Coumarin 153. Lines are guides to the eye.

where the respective ground-state exciton transition (marked by red arrows) reaches its maximum bleach. All spectra are normalized to their feature exhibiting the strongest bleach, respectively.

Generally, the features that are observed in the linear absorption data in Figure 3a,b can also be seen in the TA spectra. The TA spectra better allow us to identify higher-state exciton transitions in particular for samples belonging to long reaction times, for which the UV/vis spectra are masked by scattering and detector saturation.

Figure 6c compares the position of all TA features marked by arrows in Figure 6a,b of both the growth and exchange sample series. Like in Figure 3c for the linear absorption, for reaction times up to 60 s, the TA bleaches occur at similar wavelengths for both sample series.

Starting at roughly 60 s, distinct differences occur. The energy needed to excite the ground-state exciton for the growth series shifts more strongly to the red than for the exchange series. Additionally, for the growth series, a more complex signature in the bleach signals of higher-state transitions occurs, best visible in the spectrum of the 60 s sample (marked dark blue and dark yellow).

In contrast, the exchange series exhibits only one higher-state transition bleach signal in the corresponding wavelength regime (light-blue triangles), which red-shifts similarly to the ground-state exciton transition bleach of the exchange series. Overall, also, the TA spectra reveal that the reaction processes in both sample series are similar for short reaction times, before the CdS shell growth starts after about 60 s of reaction time.

Figure 7a,b shows the picosecond TA dynamics at the position of the ground-state exciton (red arrows Figure 6a,b) for samples of the growth and exchange series, respectively.

In the following, two parameters that describe the transients are discussed: (i) the time required to reach the maximum bleach, here called the rise time  $t_0$  and (ii) the decay time  $\tau$  of the fastest dynamic, determined by fitting a monoexponential decay that starts shortly after the intensity maximum to avoid artifacts from the liquid-phase sample.<sup>44</sup> Details are given in the Supporting Information.

In Figure 7c,  $t_0$  values for the growth (blue squares) and exchange (green triangles) series are given versus the sample number. The rise time is the shortest for the core sample and tentatively increases with the sample number, that is, reaction time. For reaction times up to 60 s,  $t_0$  behaves similarly for both sample series. For a reaction time of 60 to 120 s,  $t_0$  drastically increases for the growth series, while it only slowly increases for the exchange series. The general increase in rise time with increasing reaction time seen in the exchange series and in early samples of the growth series is congruent to the previously discussed red shifts of the ground-state exciton transition energies during the cation exchange. Since the TA experiment was conducted with constant pump power and, more important, constant pump energy, the relaxation time to the probed ground-state increases for every sample.<sup>45</sup> The strong increase of  $t_0$  for the growth series can be explained with the growth of a shell during the reaction. Due to shell growth, type-II band alignment is achieved. With increasing shell thickness or length, the behavior changes from quasi-type-II to type-II. Photoexcited charge carriers need to separate across the interface of the core–shell structure and relax down to the ground-state exciton, which increases the rise time.

Figure 7d shows the decay times  $\tau$  versus the sample number, determined for the growth (blue squares) and the exchange (green triangles) series. The decay time  $\tau$  as analyzed here represents very fast multi-exciton decay channels, which are governed by Auger recombinations. There is a considerable shortening of  $\tau$  between the core sample and the first aliquots of both series, which is most likely caused by surface modification upon injection of the cores into an excess of phosphonic acid ligands and Cd ions<sup>46,47</sup> (cf. Figure 5a,b).

The most prominent feature of the data is the strong increase of  $\tau$  at a reaction time of 120 s only within the growth series. The increase can be explained with the initial growth of the CdS shell and its transitioning into a rod-like shape on the core nanocrystal. For nanoscaled systems it has been shown that the increase in volume reduces the Auger recombination rate.<sup>48–52</sup> Here in particular, the emerging type-II behavior results in a lower wave function overlap, additionally reducing the Auger rate. For longer reaction times, the decay time  $\tau$

slightly decreases. This might be explained by the fact that as the length of the rod-shaped shell of the nanocrystal increases, not only the absorption but also the possibility of charge carrier trapping at the rod surface increases.<sup>3,21,53</sup> Charge carrier trapping and trap-assisted Auger recombination have been shown to decrease the Auger lifetime of the ground-state bleach.<sup>47,54–57</sup>

**Fluorescence Lifetimes and Quantum Yield.** Figure 8a–d shows fluorescence decay curves, which were measured on a second pair of sample series with a slightly smaller core size (see the Supporting Information for details of the sample set and the Experimental section for details of the measurement).

The decay for the ZnSe core sample is much faster than for all other samples of both the growth and exchange series. The main reason for this must be the different surface composition of the ZnSe core nanocrystals compared to that of aliquot samples of the growth and exchange series upon injection of the cores into the mixture of Cd ions and phosphonic acids (cf. Figure 5a,b), leading to less non-radiative components and thus longer fluorescence lifetimes. Comparing the fluorescence decay curves of all aliquots with each other, it is noticeable that they are similar overall, and only in the growth series, the decay curves of the aliquots extracted after reaction times of 60 and 120 s reveal a considerably faster decay.

All fluorescence decay curves of the aliquots are strongly multi-exponential. A detailed analysis of the exact decay behavior is beyond the scope of this work. Here, we use a weighted average fluorescence lifetime as described in the Supporting Information to better compare the different decay dynamics.

Figure 8e shows the average fluorescence lifetime versus the sample number. Comparing the growth and the exchange series, differences in the lifetimes occur for reaction times of 60 and 120 s, where the lifetime significantly drops. The thin CdS shell leads to type-II band alignment with quasi-type-II behavior, in which the electron is delocalized over the whole particle. The decrease of the PL lifetime was reproducible between different, independent syntheses.

This behavior again suggests that the reaction processes in both sample series are similar for short reaction times, before the CdS shell growth starts at about 60 s of reaction time in the growth series. It is difficult to unambiguously assign the shortening of the average lifetime to its underlying physics. The decay curve reveals that fast processes lose their impact while medium-fast processes get faster and more dominant (cf. Table S3 for individual amplitudes and decay times). For the growth series, reaction times of 240 and 480 s lead to an increase of the average lifetime. This increase can be explained by an effective spatial charge carrier separation in the type-II heteronanostructure, with the hole trapped in the core and the electron localized within the elongated shell (cf. Figure 5e).

Figure 8f shows the fluorescence QY versus the sample number for the above discussed pair of sample series. Details of the experiments can be found in the Experimental section. The QY increases from below 1% for ZnSe cores to 7% after 10 s of reaction time in both the growth and the exchange series, which corresponds to less non-radiative decays compared to ZnSe cores. It increases further with increasing reaction time for the growth series, reaching a maximum of about 35% for the 60 s sample before decreasing again. The exchange series does not exhibit a strong change in the QY. Comparing both series, again, similar behaviors at small reaction times and

significant differences after about 60 s of reaction time can be seen, the latter of which can be explained by the formation of a shell in the growth series.

Remarkably, the maximum of the QY is already reached after 60 s of reaction time for the growth series, which coincides with the shortest average fluorescence lifetime. This can be rationalized by a suppression of fast non-radiative decay channels, but it also shows the complexity of underlying exciton dynamics. The decreasing QY for very long reaction times in the growth series can be explained by additional non-radiative decay channels introduced by an increasing surface area of the growing shell.<sup>3</sup> At the same time, the average PL lifetime increases, which might be explained by slow radiative decay channels due to the low wave function overlap because of the type-II band alignment. Long fluorescence lifetimes might also be explained by hole trapping after excitation at the large rod's surface, which also leads to a low wave function overlap.<sup>21</sup>

## CONCLUSIONS

In summary, we conducted a detailed study on the growth of an anisotropic CdS shell on spherical ZnSe-core nanocrystals. We performed TEM and linear and time-resolved absorption and PL spectroscopy analyses on aliquots taken during the synthesis as well as elemental analysis of a final dot-in-rod sample. The data were compared to results of a control experiment, in which the cadmium precursor but no sulfur was present during synthesis. In the control experiment, only cation exchange from ZnSe to Zn<sub>1-x</sub>Cd<sub>x</sub>Se and no shell growth can occur.

We found that the CdS shell growth is slow at early stages of the reaction. By comparing linear optical spectra of the growth and exchange series, it was proven that cation exchange is the dominant process in the beginning of the reaction even when the shell precursors are present. Before significant CdS shell growth starts, about 50% of the initial Zn ions in the core are exchanged by Cd ions, which was determined by elemental analysis as well as a combination of PL spectroscopy and theoretical calculations. Anisotropic growth of the CdS shell starts not before 120 s of reaction time. Modeling of a dot-in-rod heterostructure with an alloyed Zn<sub>1-x</sub>Cd<sub>x</sub>Se core showed a type-II band alignment with separated charge carriers.

Time-resolved optical measurements on the sample series fully support these findings. Increased rise times of the ground-state excitonic bleach measured in TA spectroscopy can be assigned to the formation of a type-II band alignment due to the development of the shell. A strong increase of the TA lifetime can be rationalized by the transition from spherical to rod-shaped shell growth, while a subsequent slight decrease in the lifetime can be attributed to charge carrier trapping, which becomes more important for larger shells. Drastic changes in the TA and fluorescence lifetimes in the very beginning of the syntheses is assigned to surface modifications. A decrease in the fluorescence lifetime, which coincides with the maximum PL QY, can be attributed to the full passivation of the core's surface by a complete CdS shell.

These findings highlight that cation exchange is inevitable in high-temperature reactions as used for rod growth on cores. This changes the band gap of the particles in the beginning and thus the band structure of the final particles. The reaction, usually referred to as the growth reaction, is an exchange of cations at early stages. The results can be transferred to other material combinations in which different cations and anions in



the core and shell are present. Changes in the band alignment because of cation exchange must be considered if optoelectronic properties of the heterostructure are explained based on their band structure. Tuning the degree of cation exchange and thus the extent of the band offset could be used to selectively adjust the optical properties of the heterostructure.

## EXPERIMENTAL SECTION

All chemicals were used as received. ODA ( $\geq 99\%$ ), trioctylphosphine oxide (TOPO, 99%), sulfur powder (S, 99.98%), and diethylzinc ( $\text{ZnEt}_2$ , 1.0 M in hexane) were purchased from Sigma-Aldrich; selenium (Se, 99.5% powder mesh 200) was purchased from Acros Organics; and TOP (97%) was purchased from ABCR. Cadmium oxide ( $\text{CdO}$ , 99.9999%) was purchased from ChemPur; ODPa ( $>99\%$ ) and HPA ( $>99\%$ ) were purchased from PCI Synthesis. Toluene ( $\geq 99.5\%$ ) was purchased from VWR, and methanol (99.5%) was purchased from Grüssing.

ZnSe core synthesis was adapted from Cozzoli et al.<sup>58</sup> Briefly, 7 g of ODA was degassed at 130 °C under vacuum. At 300 °C under a nitrogen flow, a mixture of 0.8 mL (1 M in hexane) of diethylzinc and 2.4 mL (0.33 M) of Se/TOP was injected, and the temperature was set to 265 °C. After 30 min, small ZnSe particles were formed, and further growth was achieved by adding 1 mL of the precursor solution within 5 min via a syringe pump followed by 30 min of reaction time. This cycle was repeated in total six times. The particles were cleaned by toluene/methanol extraction and centrifugation at 40 °C to avoid precipitation of ODA. Particles were stored in TOP in the glovebox.

The size was determined from the position of the first excitonic maximum, and the concentration was determined using size-dependent extinction coefficients from the literature.<sup>38</sup>

Anisotropic CdS shell growth was performed based on a method of Dorfs et al.<sup>14</sup> 3 g of TOPO, 290 mg of ODPa, 80 mg of HPA, and 60 mg of CdO were degassed at 150 °C under vacuum for 90 min and heated to 320 °C until it became optically clear and colorless. A mixture of 1.8 mL (2 M) of S/TOP and ZnSe cores ( $4 \times 10^{-8}$  mol) was rapidly injected. For the exchange control experiment, S/TOP was replaced by TOP. Samples were extracted using a syringe into cold toluene at different time steps and purified by toluene/methanol extraction and centrifugation at 11,000 rpm, 10 min. This cycle was repeated three times.

Absorbance spectra were recorded on a Varian Cary 5000 UV/vis/NIR spectrometer in the wavelength range between 300 and 800 nm using quartz cuvettes with a 10 mm path length. The preparation was carried out by dispersing the aliquots in toluene.

PL spectra were recorded on a Horiba Yvon FluoroMax 4 by excitation of the aliquots in quartz cuvettes with energies above the first absorbance maximum.

QYs were calculated in relation to the organic dye Coumarin 153. The samples were excited at the intersection of the absorbance spectra of the dye and sample.

Fluorescence lifetime measurements were performed using a PicoQuant FluoTime FT300 equipped with a NKT SuperK Fianium white light laser source. Samples were excited above the CdS band gap. The detection wavelength was set to the maximum of the PL spectrum with a 2.7 nm bandwidth, and repetition rates of 3.7 MHz for ZnSe cores and 0.59 MHz for all aliquots were used.

A quantitative elemental analysis of the final dot-in-rod sample was performed by ICP-MS on an Agilent Technologies series 7700. For the preparation, the samples were placed in a vial, the toluene was evaporated, and the resulting precipitate was dissolved in aqua regia [ $3:1$  (v/v)] HCl/ $\text{HNO}_3$ ] under stirring. After 16 h, the dissolved samples were diluted with 2% HCl.

TA spectroscopy was performed using an amplified Ti-sapphire laser (Spitfire-Ace, 800 nm, 1 kHz, 35 fs) as an excitation source seeding an optical parametric amplifier (TOPAS-Prime; Light Conversion) with a frequency mixer (NirUvis; Light Conversion) to reach the desired pump wavelength of  $330 \pm 20$  nm using a constant power of 300. Each sample was measured using a broadband white-light continuum with a spectral range of 310–900 nm generated

by a 2 mm thick sapphire crystal. The diameter of the pump beam covers around 500  $\mu\text{m}$ , while the focused diameter of the probe beam is approximately 100  $\mu\text{m}$ . The samples were diluted in toluene and filled in 2 mm thick quartz cuvettes (Hellma Analytics). A more detailed description of the TA setup can be found in the work of Minutella et al.<sup>59</sup>

The quantum mechanical calculations for the exciton energies of the  $\text{Zn}_{1-x}\text{Cd}_x\text{Se}$  dots were carried out within the effective mass approximation based on the procedure reported by Panfil et al.<sup>35,36</sup> All equations were solved numerically using the software COMSOL Multiphysics based on the finite element method. Further details can be found in the Supporting Information.

## ASSOCIATED CONTENT

### Supporting Information

The Supporting Information is available free of charge at <https://pubs.acs.org/doi/10.1021/acs.chemmater.2c03278>.

Details of the calculation for spherical particles and heterostructures, absorbance and PL spectra of the second sample set, details of the fitting procedure for the PL lifetime, individual decay times and amplitudes of the fit of the PL decay curves, and details of the fitting procedure for TA spectra (PDF)

## AUTHOR INFORMATION

### Corresponding Authors

Alf Mews – Institute of Physical Chemistry, University of Hamburg, 20146 Hamburg, Germany; [orcid.org/0000-0001-5739-8820](https://orcid.org/0000-0001-5739-8820); Email: [mews@chemie.uni-hamburg.de](mailto:mews@chemie.uni-hamburg.de)

Tobias Kipp – Institute of Physical Chemistry, University of Hamburg, 20146 Hamburg, Germany; [orcid.org/0000-0002-9663-7422](https://orcid.org/0000-0002-9663-7422); Email: [kipp@chemie.uni-hamburg.de](mailto:kipp@chemie.uni-hamburg.de)

### Authors

Jannik Rebmann – Institute of Physical Chemistry, University of Hamburg, 20146 Hamburg, Germany

Hans Werners – Institute of Physical Chemistry, University of Hamburg, 20146 Hamburg, Germany

Florian Johst – Institute of Physical Chemistry, University of Hamburg, 20146 Hamburg, Germany; [orcid.org/0000-0002-7594-8440](https://orcid.org/0000-0002-7594-8440)

Marcel Dohrmann – Institute of Physical Chemistry, University of Hamburg, 20146 Hamburg, Germany

Yannic U. Staechelin – Institute of Physical Chemistry, University of Hamburg, 20146 Hamburg, Germany; [orcid.org/0000-0001-8588-9117](https://orcid.org/0000-0001-8588-9117)

Christian Strelow – Institute of Physical Chemistry, University of Hamburg, 20146 Hamburg, Germany; [orcid.org/0000-0002-5989-1675](https://orcid.org/0000-0002-5989-1675)

Complete contact information is available at <https://pubs.acs.org/doi/10.1021/acs.chemmater.2c03278>

### Author Contributions

J.R., H.W., and A.M. conceived and designed the project. A.M. and T.K. supervised the project. J.R. synthesized and prepared all samples and performed TEM imaging and analysis and UV/vis absorption spectroscopy and (time-resolved) PL spectroscopy. H.W. performed all TA experiments (with the help of Y.U.S.), as well as analyzed and interpreted the TA data. F.J. performed the calculations (with the help of M.D. and C.S.). J.R., H.W., and T.K. prepared the manuscript with contributions from all co-authors.

## Notes

The authors declare no competing financial interest.

## ACKNOWLEDGMENTS

The authors thank Stefan Werner for TEM images, Yang Liu for ICP-MS, and Holger Lange for support with TA measurements. The authors thank the Deutsche Forschungsgemeinschaft (DFG, German Research Foundation) for financial support via the Research Training Group "Nanohybrid" (GRK 2536). H.W. acknowledges the financial support by the Horizon-2020 research and innovation program of the European Union (grant no. 952335, NanoQIQO project).

## REFERENCES

- (1) García-Santamaría, F.; Chen, Y.; Vela, J.; Schaller, R. D.; Hollingsworth, J. A.; Klimov, V. I. Suppressed Auger recombination in "Giant" nanocrystals boosts optical gain performance. *Nano Lett.* **2009**, *9*, 3482–8.
- (2) Acharya, K. P.; Nguyen, H. M.; Paulite, M.; Piryatinski, A.; Zhang, J.; Casson, J. L.; Xu, H.; Htoon, H.; Hollingsworth, J. A. Elucidation of Two Giants: Challenges to Thick-Shell Synthesis in CdSe/ZnSe and ZnSe/CdS Core/Shell Quantum Dots. *J. Am. Chem. Soc.* **2015**, *137*, 3755–3758.
- (3) Hinsch, A.; Lohmann, S. H.; Strelow, C.; Kipp, T.; Würth, C.; Geißler, D.; Kornowski, A.; Wolter, C.; Weller, H.; Resch-Genger, U.; Mews, A. Fluorescence Quantum Yield and Single-Particle Emission of CdSe Dot/CdS Rod Nanocrystals. *J. Phys. Chem. C* **2019**, *123*, 24338–24346.
- (4) Klimov, V. I.; Mikhailovsky, A. A.; Xu, S.; Malko, A.; Hollingsworth, J. A.; Leatherdale, C. A.; Eisler, H.-J.; Bawendi, M. G. Optical Gain and Stimulated Emission in Nanocrystal Quantum Dots. *Science* **2000**, *290*, 314–317.
- (5) Cunningham, P. D.; Souza, J. B.; Fedin, I.; She, C.; Lee, B.; Talapin, D. V. Assessment of Anisotropic Semiconductor Nanorod and Nanoplatelet Heterostructures with Polarized Emission for Liquid Crystal Display Technology. *ACS Nano* **2016**, *10*, 5769–5781.
- (6) Kim, T.; Kim, K. H.; Kim, S.; Choi, S. M.; Jang, H.; Seo, H. K.; Lee, H.; Chung, D. Y.; Jang, E. Efficient and stable blue quantum dot light-emitting diode. *Nature* **2020**, *586*, 385–389.
- (7) Shu, Y.; Lin, X.; Qin, H.; Hu, Z.; Jin, Y.; Peng, X. Quantum Dots for Display Applications. *Angew. Chem., Int. Ed.* **2020**, *59*, 22312–22323.
- (8) Reiss, P.; Protière, M.; Li, L. Core/Shell Semiconductor Nanocrystals. *Small* **2009**, *5*, 154–168.
- (9) Hines, M. A.; Guyot-Sionnest, P. Synthesis and Characterization of Strongly Luminescing ZnS-Capped CdSe Nanocrystals. *The Journal of Physical Chemistry* **1996**, *100*, 468–471.
- (10) Xie, R.; Kolb, U.; Li, J.; Basché, T.; Mews, A. Synthesis and Characterization of Highly Luminescent CdSe-Core CdS/Zn 0.5 Cd 0.5 S/ZnS Multishell Nanocrystals. *J. Am. Chem. Soc.* **2005**, *127*, 7480–7488.
- (11) Nemchinov, A.; Kirsanova, M.; Hewa-Kasakarage, N. N.; Zamkov, M. Synthesis and Characterization of Type II ZnSe/CdS Core/Shell Nanocrystals. *The Journal of Physical Chemistry C* **2008**, *112*, 9301–9307.
- (12) de Mello Donegá, C. Formation of nanoscale spatially indirect excitons: Evolution of the type-II optical character of CdTe/CdSe heteronanocrystals. *Phys. Rev. B* **2010**, *81*, 165303.
- (13) Lo, S. S.; Mirkovic, T.; Chuang, C.-H.; Burda, C.; Scholes, G. D. Emergent Properties Resulting from Type-II Band Alignment in Semiconductor Nanoheterostructures. *Adv. Mater.* **2011**, *23*, 180–197.
- (14) Dorfs, D.; Salant, A.; Popov, I.; Banin, U. ZnSe quantum dots within CdS nanorods: A seeded-growth type-II system. *Small* **2008**, *4*, 1319–1323.
- (15) Acharya, K. P.; Khnayzer, R. S.; O'Connor, T.; Diederich, G.; Kirsanova, M.; Klinkova, A.; Roth, D.; Kinder, E.; Imboden, M.; Zamkov, M. The role of hole localization in sacrificial hydrogen production by semiconductor-metal heterostructured nanocrystals. *Nano Lett.* **2011**, *11*, 2919–2926.
- (16) Hewa-Kasakarage, N. N.; Kirsanova, M.; Nemchinov, A.; Schmall, N.; El-Khoury, P. Z.; Tarnovsky, A. N.; Zamkov, M. Radiative recombination of spatially extended excitons in (ZnSe/CdS)/CdS heterostructured nanorods. *J. Am. Chem. Soc.* **2009**, *131*, 1328–1334.
- (17) Kuo, Y.; Li, J.; Michalet, X.; Chizhik, A.; Meir, N.; Bar-Elli, O.; Chan, E.; Oron, D.; Enderlein, J.; Weiss, S. Characterizing the Quantum-Confinement Stark Effect in Semiconductor Quantum Dots and Nanorods for Single-Molecule Electrophysiology. *ACS Photonics* **2018**, *5*, 4788–4800.
- (18) Bar-Elli, O.; Steinitz, D.; Yang, G.; Tenne, R.; Ludwig, A.; Kuo, Y.; Triller, A.; Weiss, S.; Oron, D. Rapid Voltage Sensing with Single Nanorods via the Quantum Confinement Stark Effect. *ACS Photonics* **2018**, *5*, 2860–2867.
- (19) Ghosh, S.; Chizhik, A. M.; Yang, G.; Karedla, N.; Gregor, I.; Oron, D.; Weiss, S.; Enderlein, J.; Chizhik, A. I. Excitation and Emission Transition Dipoles of Type-II Semiconductor Nanorods. *Nano Lett.* **2019**, *19*, 1695–1700.
- (20) O'Connor, T.; Panov, M. S.; Mereshchenko, A.; Tarnovsky, A. N.; Lorek, R.; Perera, D.; Diederich, G.; Lambright, S.; Moroz, P.; Zamkov, M. The effect of the charge-separating interface on exciton dynamics in photocatalytic colloidal heteronanocrystals. *ACS Nano* **2012**, *6*, 8156–65.
- (21) Grennell, A. N.; Utterback, J. K.; Pearce, O. M.; Wilker, M. B.; Dukovic, G. Relationships between Exciton Dissociation and Slow Recombination within ZnSe/CdS and CdSe/CdS Dot-in-Rod Heterostructures. *Nano Lett.* **2017**, *17*, 3764–3774.
- (22) Boldt, K.; Schwarz, K. N.; Kirkwood, N.; Smith, T. A.; Mulvaney, P. Electronic structure engineering in ZnSe/CdS type-II nanoparticles by interface alloying. *J. Phys. Chem. C* **2014**, *118*, 13276–13284.
- (23) Boldt, K.; Bartlett, S.; Kirkwood, N.; Johannessen, B. Quantification of Material Gradients in Core/Shell Nanocrystals Using EXAFS Spectroscopy. *Nano Lett.* **2020**, *20*, 1009–1017.
- (24) Huang, J.; Kovalenko, M. V.; Talapin, D. V. Alkyl chains of surface ligands affect polytypism of CdSe nanocrystals and play an important role in the synthesis of anisotropic nanoheterostructures. *J. Am. Chem. Soc.* **2010**, *132*, 15866–15868.
- (25) Hewa-Kasakarage, N. N.; El-Khoury, P. Z.; Tarnovsky, A. N.; Kirsanova, M.; Nemitz, I.; Nemchinov, A.; Zamkov, M. Ultrafast carrier dynamics in type II ZnSe/CdS/ZnSe nanobarbells. *ACS Nano* **2010**, *4*, 1837–1844.
- (26) Groeneveld, E.; Witteman, L.; Lefferts, M.; Ke, X.; Bals, S.; Van Tendeloo, G.; de Mello Donegá, C. Tailoring ZnSe-CdSe colloidal quantum dots via Cation Exchange: From core/shell to alloy nanocrystals. *ACS Nano* **2013**, *7*, 7913–7930.
- (27) Lee, S.; Yoon, D. E.; Kim, D.; Shin, D. J.; Jeong, B. G.; Lee, D.; Lim, J.; Bae, W. K.; Lim, H. K.; Lee, D. C. Direct cation exchange of CdSe nanocrystals into ZnSe enabled by controlled binding between guest cations and organic ligands. *Nanoscale* **2019**, *11*, 15072–15082.
- (28) Ohtani, H.; Kojima, K.; Ishida, K.; Nishizawa, T. Miscibility gap in II-VI alloy semiconductor systems. *J. Alloys Compd.* **1992**, *182*, 103–114.
- (29) Steiner, D.; Dorfs, D.; Banin, U.; Della Sala, F. D.; Manna, L.; Millo, O. Determination of band offsets in heterostructured colloidal nanorods using scanning tunneling spectroscopy. *Nano Lett.* **2008**, *8*, 2954–2958.
- (30) Cao, G.; Lynch, V. M.; Yacullo, L. N. Synthesis, Structural Characterization, and Intercalation Chemistry of Two Layered Cadmium Organophosphonates. *Chem. Mater.* **1993**, *5*, 1000–1006.
- (31) García-Rodríguez, R.; Hendricks, M. P.; Cossairt, B. M.; Liu, H.; Owen, J. S. Conversion reactions of cadmium chalcogenide nanocrystal precursors. *Chem. Mater.* **2013**, *25*, 1233–1249.
- (32) Qiao, F.; Xu, W.; Liu, M.; Yang, J.; Cui, X.; Wang, Q.; Bian, J.; Kim, D. H. Effect of Cd-phosphonate complex on the self-assembly structure of colloidal nanorods. *Mater. Lett.* **2016**, *180*, 85–88.

- (33) Wang, W.; Banerjee, S.; Jia, S.; Steigerwald, M. L.; Herman, I. P. Ligand control of growth, morphology, and capping structure of colloidal CdSe nanorods. *Chem. Mater.* **2007**, *19*, 2573–2580.
- (34) Fischli, D.; Enders, F.; Boldt, K. Kinetically Driven Cadmium Chalcogenide Nanorod Growth Fed by Local Cluster Aggregates. *J. Phys. Chem. C* **2020**, *124*, 12774–12783.
- (35) Panfil, Y. E.; Shamalia, D.; Cui, J.; Koley, S.; Banin, U. Electronic coupling in colloidal quantum dot molecules; the case of CdSe/CdS core/shell homodimers. *J. Chem. Phys.* **2019**, *151*. DOI: 10.1063/1.5128086
- (36) Panfil, Y. E.; Cui, J.; Koley, S.; Banin, U. Complete Mapping of Interacting Charging States in Single Coupled Colloidal Quantum Dot Molecules. *ACS Nano* **2022**, *16*, 5566–5576.
- (37) Zhong, X.; Feng, Y.; Zhang, Y.; Gu, Z.; Zou, L. A facile route to violet- to orange-emitting Cd x Zn 1-x Se alloy nanocrystals via cation exchange reaction. *Nanotechnology* **2007**, *18*, 385606.
- (38) Toufanian, R.; Zhong, X.; Kays, J. C.; Saeboe, A. M.; Dennis, A. M. Correlating ZnSe Quantum Dot Absorption with Particle Size and Concentration. *Chem. Mater.* **2021**, *33*, 7527–7536.
- (39) Reiss, P. ZnSe based colloidal nanocrystals: Synthesis, shape control, core/shell, alloy and doped systems. *New J. Chem.* **2007**, *31*, 1843–1852.
- (40) de Mello Donegá, C. Synthesis and properties of colloidal heteronanocrystals. *Chem. Soc. Rev.* **2011**, *40*, 1512–1546.
- (41) Puzder, A.; Williamson, A. J.; Zaitseva, N.; Galli, G.; Manna, L.; Alivisatos, A. P. The Effect of Organic Ligand Binding on the Growth of CdSe Nanoparticles Probed by Ab Initio Calculations. *Nano Lett.* **2004**, *4*, 2361–2365.
- (42) Adachi, S. *Paper Knowledge. Toward a Media History of Documents*; John Wiley & Sons, Ltd, 2015; p 406.
- (43) Wei, S. H.; Zunger, A. Calculated natural band offsets of all II-VI and III-V semiconductors: Chemical trends and the role of cation d orbitals. *Appl. Phys. Lett.* **1998**, *72*, 2011–2013.
- (44) Ekvall, K.; van der Meulen, P.; Dhollande, C.; Berg, L. E.; Pommeret, S.; Naskrecki, R.; Mialocq, J. C. Cross phase modulation artifact in liquid phase transient absorption spectroscopy. *J. Appl. Phys.* **2000**, *87*, 2340–2352.
- (45) El-Ballouli, A. O.; Alarousu, E.; Usman, A.; Pan, J.; Bakr, O. M.; Mohammed, O. F. Real-Time Observation of Ultrafast Intraband Relaxation and Exciton Multiplication in PbS Quantum Dots. *ACS Photonics* **2014**, *1*, 285–292.
- (46) Guyot-Sionnest, P.; Wehrenberg, B.; Yu, D. Intraband relaxation in CdSe nanocrystals and the strong influence of the surface ligands. *J. Chem. Phys.* **2005**, *123*. DOI: 10.1063/1.2004818
- (47) Kambhampati, P. Hot exciton relaxation dynamics in semiconductor quantum dots: Radiationless transitions on the nanoscale. *J. Phys. Chem. C* **2011**, *115*, 22089–22109.
- (48) Klimov, V. I.; Mikhailovsky, A. A.; McBranch, D. W.; Leatherdale, C. A.; Bawendi, M. G. Quantization of multiparticle Auger rates in semiconductor quantum dots. *Science* **2000**, *287*, 1011–1013.
- (49) Klimov, V. I. Spectral and dynamical properties of multiexcitons in semiconductor nanocrystals. *Annu. Rev. Phys. Chem.* **2007**, *58*, 635–673.
- (50) Califano, M.; Zunger, A.; Franceschetti, A. Direct carrier multiplication due to inverse auger scattering in CdSe quantum dots. *Appl. Phys. Lett.* **2004**, *84*, 2409–2411.
- (51) Schaller, R. D.; Klimov, V. I. High efficiency carrier multiplication in PbSe nanocrystals: Implications for solar energy conversion. *Phys. Rev. Lett.* **2004**, *92*, 1–4.
- (52) Xing, G.; Liao, Y.; Wu, X.; Chakraborty, S.; Liu, X.; Yeow, E. K. L.; Chan, Y.; Sum, T. C. Ultralow-Threshold Two-Photon Pumped Amplified Spontaneous Emission and Lasing from Seeded CdSe/CdS Nanorod Heterostructures. *ACS Nano* **2022**, *6*, 10835–10844.
- (53) Achtstein, A. W.; Hennig, J.; Prudnikau, A.; Artemyev, M. V.; Woggon, U. Linear and Two-Photon Absorption in Zero- and One-Dimensional CdS Nanocrystals: Influence of Size and Shape. *J. Phys. Chem. C* **2013**, *117*, 25756–25760.
- (54) Morgan, D. P.; Kelley, D. F. What Does the Transient Absorption Spectrum of CdSe Quantum Dots Measure? *J. Phys. Chem. C* **2020**, *124*, 8448–8455.
- (55) Cohn, A. W.; Schimpf, A. M.; Gunthardt, C. E.; Gamelin, D. R. Size-dependent trap-assisted auger recombination in semiconductor nanocrystals. *Nano Lett.* **2013**, *13*, 1810–1815.
- (56) Tyagi, P.; Kambhampati, P. False multiple exciton recombination and multiple exciton generation signals in semiconductor quantum dots arise from surface charge trapping. *J. Chem. Phys.* **2011**, *134*. DOI: 10.1063/1.3561063
- (57) Klimov, V. I. Optical nonlinearities and ultrafast carrier dynamics in semiconductor nanocrystals. *J. Phys. Chem. B* **2000**, *104*, 6112–6123.
- (58) Cozzoli, P. D.; Manna, L.; Curri, M. L.; Kudera, S.; Giannini, C.; Striccoli, M.; Agostiano, A. Shape and phase control of colloidal ZnSe nanocrystals. *Chem. Mater.* **2005**, *17*, 1296–1306.
- (59) Minutella, E.; Schulz, F.; Lange, H. Excitation-dependence of plasmon-induced hot electrons in gold nanoparticles. *J. Phys. Chem. Lett.* **2017**, *8*, 4925–4929.

## Recommended by ACS

### Wurtzite InAs Nanocrystals with Short-Wavelength Infrared Emission Synthesized through the Cation Exchange of Cu<sub>3</sub>As Nanocrystals

Xinyao Shan, Botao Ji, et al.

MARCH 06, 2023  
CHEMISTRY OF MATERIALS

READ 

### Thiol-Free Synthesis of Bright Near-Infrared-Emitting Ag<sub>2</sub>S Nanocrystals through Heterovalent-Metal Decoration for Ecofriendly Solar Cells

Jieyu Zhang, Botao Ji, et al.

FEBRUARY 02, 2023  
CHEMISTRY OF MATERIALS

READ 

### Trioctylphosphine- and Octanethiol-Induced Photoluminescence Recovery of CdSe/ZnS Quantum Dots after Dilution–Quenching: Implications for Quantum Dot...

Hao Hao, Feng-Lei Jiang, et al.

FEBRUARY 09, 2023  
ACS APPLIED NANO MATERIALS

READ 

### Charge Transport Dynamics of Quasi-Type II Perovskite Janus Nanocrystals in High-Performance Photoconductors

Lin Zhang, Weihai Fang, et al.

FEBRUARY 13, 2023  
THE JOURNAL OF PHYSICAL CHEMISTRY LETTERS

READ 

Get More Suggestions >

## 5.6 Electron donor-specific surface interactions promote the photocatalytic activity of metal-semiconductor nanohybrids

This publication is reprinted from Soenke Wengler-Rust, Yannic U. Staechelin, Holger Lange and Horst Weller, *Small*, **2024**, 20, 2401388, CC BY 4.0 Deed - published by Wiley-VCH GmbH.<sup>288</sup> The related supporting information is reprinted in Chapter A.4.

DOI: [10.1002/sml.202401388](https://doi.org/10.1002/sml.202401388)

This project studies the influence of the employed EDA on the photocatalytic hydrogen production rates of Pt-tipped CdSe-CdS DRs. It was shown that ionic EDAs are surface-active and replace the stabilizing ligand (11-mercaptoundecanoic acid, MUA) from the DRs surface, lowering the colloidal stability of the DRs. TA measurements show accelerated hole transfer onto ionic EDAs as compared to alcoholic EDAs, which function in a diffusion-limited way, *i.e.* the holes are first transferred onto the MUA ligand and subsequently to the alcoholic EDA. Efficient hole transfer is correlated with high hydrogen production rates.

*The author of this thesis contributed to the conceptualization of the project, carried out the TA measurements, analyzed the TA data and contributed to the writing and editing of the manuscript.*

# Electron Donor-Specific Surface Interactions Promote the Photocatalytic Activity of Metal-Semiconductor Nanohybrids

Soenke Wengler-Rust,\* Yannic U. Staechelin, Holger Lange, and Horst Weller\*

In the past two decades, the application of colloidal semiconductor-metal nanoparticles (NPs) as photocatalysts for the hydrogen generation from water has been extensively studied. The present body of literature studies agrees that the photocatalytic yield strongly depends on the electron donating agent (EDA) added for scavenging the photogenerated holes. The highest reported hydrogen production rates are obtained in the presence of ionic EDAs and at high pH. The large hydrogen production rates are attributed to fast hole transfer from the NP onto the EDAs. However, the present discussions do not treat the influence of EDA-specific surface interactions. This systematic study focuses on that aspect by combining steady-state hydrogen production measurements with time-resolved and static optical spectroscopy, employing 11-mercaptopundecanoic acid-capped, Pt-tipped CdSe/CdS dot-in-rods in the presence of a large set of EDAs. Based on the experimental results, two distinct EDA groups are identified: surface-active and diffusion-limited EDAs. The largest photocatalytic efficiencies are obtained in the presence of surface-active EDAs that induce an agglomeration of the NPs. This demonstrates that the introduction of surface-active EDAs can significantly enhance the photocatalytic activity of the NPs, despite reducing their colloidal stability and inducing the formation of NP networks.

## 1. Introduction

The use of photocatalytic systems holds particular promise for molecular hydrogen generation from water. This direct process generates hydrogen without the need for an intermediate step of electricity production. For understanding the general principles limiting the efficiency of photocatalytic systems in large-scale applications, simple but solid model systems are preferred. Colloidal nanoparticles (NPs) are particularly interesting in this context, since they have synthetically adjustable optoelectronic properties and can easily be dispersed in an aqueous suspension.<sup>[1,2]</sup> Well studied multi-step synthesis procedures allow for combining multiple functional components in one hybrid nanostructure, including a light absorber, as well as acceptors for the photogenerated holes and electrons, in combination with catalytically active surfaces. A major challenge in photosynthetic applications is to generate long-lived charge-separated states.<sup>[3,4]</sup> An exemplary material system are Pt-tipped CdSe/CdS dot-in-rods (DRs),<sup>[5–9]</sup> which are composed of a spherical CdSe core embedded in an elongated CdS shell.<sup>[10–14]</sup> A Pt domain is

deposited on the tip of the DR, opposing the core (cf. **Figure 1a**).<sup>[5,9,15,16]</sup> In this anisotropic heterostructure photogenerated electrons transfer to the Pt tip, while holes are confined in the CdSe core, spatially separated from the Pt by the CdS rod of adjustable length. This system is especially favorable for hydrogen production since the Pt tip additionally lowers the overpotential for water reduction, while functioning as a photocathode.<sup>[1,6,17,18]</sup> For transferring the NPs into water, the native, organic, hydrophobic ligands are typically exchanged by thiol-terminated, hydrophilic ligands like 11-mercaptopundecanoic acid (MUA), allowing for a fast and reliable phase transfer, obtaining individually dispersed NPs.<sup>[7,19]</sup> The dimensions and number of functional components within the individual nanophotocatalyst (CdSe seed size, CdS rod length, tip number, and size) were tuned in order to determine the ideal parameters for photocatalytic hydrogen production.<sup>[5,7–9,20–22]</sup> In addition to the physical parameters of the NPs, multiple studies reported the choice of the electron donating agent (EDA) in the suspension as a relevant parameter for the hydrogen production catalytic yield.<sup>[5,8,17,23,24]</sup> These EDAs are typically added to the suspension to extract the photogenerated holes from the

S. Wengler-Rust, Y. U. Staechelin, H. Weller  
Institut für Physikalische Chemie  
Universität Hamburg  
20146 Hamburg, Germany  
E-mail: [Soenke.Wengler-Rust@uni-hamburg.de](mailto:Soenke.Wengler-Rust@uni-hamburg.de);  
[Horst.Weller@uni-hamburg.de](mailto:Horst.Weller@uni-hamburg.de)

H. Lange, H. Weller  
The Hamburg Centre for Ultrafast Imaging  
22761 Hamburg, Germany

H. Lange  
Institut für Physik und Astronomie  
Universität Potsdam  
14476 Potsdam, Germany

H. Weller  
Fraunhofer IAP-CAN  
20146 Hamburg, Germany

 The ORCID identification number(s) for the author(s) of this article can be found under <https://doi.org/10.1002/sml.202401388>

© 2024 The Authors. Small published by Wiley-VCH GmbH. This is an open access article under the terms of the [Creative Commons Attribution License](https://creativecommons.org/licenses/by/4.0/), which permits use, distribution and reproduction in any medium, provided the original work is properly cited.

DOI: 10.1002/sml.202401388

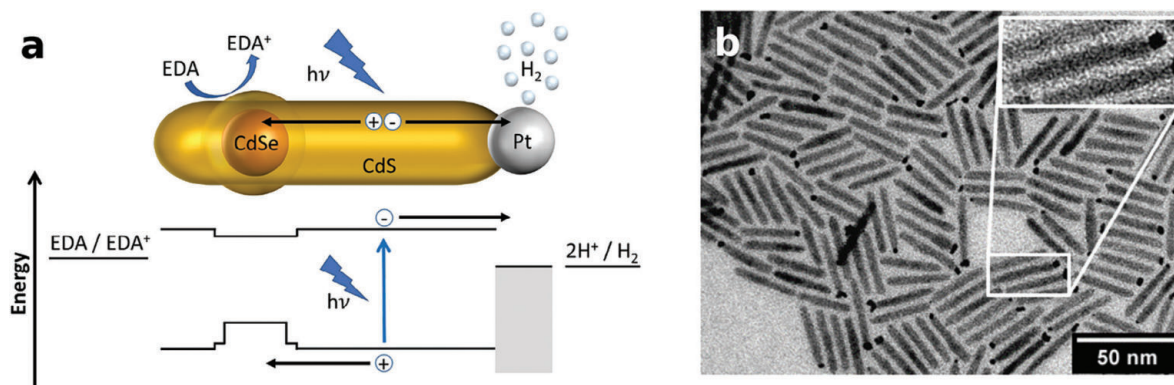


**Figure 1.** a) Scheme of a Pt-tipped CdSe/CdS DR and the related simplified energy level diagram, illustrating the separation of photogenerated charge carriers, hydrogen production, and hole scavenging by the EDA. The CdSe core is surrounded by a CdS bulb, while the Pt tip functions as a photocathode, catalyzing hydrogen production. b) Transmission electron micrograph of Pt-tipped CdSe/CdS DRs (inset shows a DR with a single Pt tip).

CdSe core of the NPs in order to prevent oxidation of the ligand or semiconducting domain, and additionally reduce the chance of charge recombination.<sup>[17,25–27]</sup> In various studies, the largest quantum efficiency in hydrogen production was obtained at very high pH, which was attributed to large hole transfer rates enabled by the high concentration of hydroxide anions that shuttle the holes from the NP's surface to the respective alcoholic EDA.<sup>[5,17]</sup> Based on the observed strong differences in quantum efficiency of hydrogen production in the presence of different EDAs, it was concluded that the hole transfer onto the EDA is the efficiency-limiting step in the overall hydrogen production process.<sup>[17,28,29]</sup> We assume that the respective hole transfer rate is highly dependent on the interaction of the EDA with the NPs' surface, which was not treated in the related studies.

We conducted a systematic study using steady-state hydrogen production measurements, dynamic light scattering (DLS), cryo-TEM, transient absorption (TA), time-resolved photoluminescence (PL), as well as static absorption and PL spectroscopy to relate the photocatalytic efficiencies with the charge carrier dynamics and the colloidal stability of MUA-capped, Pt-tipped CdSe/CdS DRs in the presence of different EDAs. Based on the observed carrier dynamics and static spectroscopy measurements, we divide the large set of investigated EDAs into the two groups of diffusion-limited and surface-active EDAs. While the alcoholic, diffusion-limited EDAs scavenge the holes from the oxidized thiol ligand, the ionic, surface-active EDAs scavenge the holes directly at the NP's surface. The largest efficiencies were observed in the presence of surface-active EDAs which also induce an agglomeration of the NPs. We assume that this agglomeration might increase the photocatalytic efficiency by enabling inter-particle charge transfer.<sup>[30–37]</sup> We investigated the assembly behavior of the anisotropic nanocatalysts using cryo-TEM and revealed that tip-to-tip attachment is preferred during assembly. This tip-to-tip attachment increases the photocatalytic efficiency by favoring the accumulation of electrons at combined Pt domains while maintaining charge separation from the holes at the CdSe cores.<sup>[30,31,34]</sup>

## 2. Results and Discussion

### 2.1. Optical Properties and Colloidal Stability of Pt-tipped CdSe/CdS Dot-in-Rods in the Presence of Electron Donating Agents

CdSe/CdS DRs were synthesized and the deposition of platinum tips was implemented following established synthesis procedures.<sup>[10,15]</sup> The DRs were prepared from CdSe seeds with a diameter of 2.3 nm, had an average length of  $29.3 \pm 3.4$  nm and a diameter of  $4.1 \pm 0.4$  nm. CdSe/CdS heterostructures with CdSe core sizes smaller than 2.8 nm were shown to have a quasi-type II band alignment.<sup>[38,39]</sup> The majority of the Pt-DRs had a single Pt tip (cf. Figure 1b and refer to Section S1 (Supporting Information) for further details on NP parameters, tip sizes, and numbers). For transferring the NPs to aqueous suspension, the native ligands were exchanged by MUA, following previous reports on ligand exchange.<sup>[7,19]</sup> The samples were prepared by adding the EDAs to the MUA-capped NPs in water, using typical concentrations.<sup>[5,17,23,24,29]</sup> In the case of methanol (MeOH), ethanol (EtOH), and isopropyl alcohol (IPA) the concentration of the EDA was 10 vol%, while for sodium sulfite and for the mixture of sodium sulfide and sodium sulfite it was 0.1 M each. Additionally, alcoholic EDAs were studied at increased pH value by dispersing the MUA-capped NPs in a 1 M KOH solution in water with 10 vol% MeOH and 10 vol% IPA, respectively (KOH & IPA and KOH & MeOH). Furthermore, as reference, the performance of the MUA-capped Pt-DRs without any additional EDA was investigated. In order to exclude any influence of deviating NP parameters, the same batch of Pt-tipped CdSe/CdS DRs was used for all displayed measurements unless otherwise stated (cf. Sections S5 and S6, Supporting Information).

Independent of the EDA introduced, the static absorption and absorbance spectra of the Pt-tipped CdSe/CdS DRs exhibit the characteristic features known for these metal-semiconductor heterostructures (Figure 2a,b). The weak absorption feature at 545 nm can be attributed to the excitonic transition in the CdSe core, while the more pronounced features at 460 and 415 nm can be assigned to the  $1\Sigma$  ( $1\sigma_e - 1\sigma_h$ ) and  $1\Pi$  ( $1\pi_e - 1\pi_h$ )

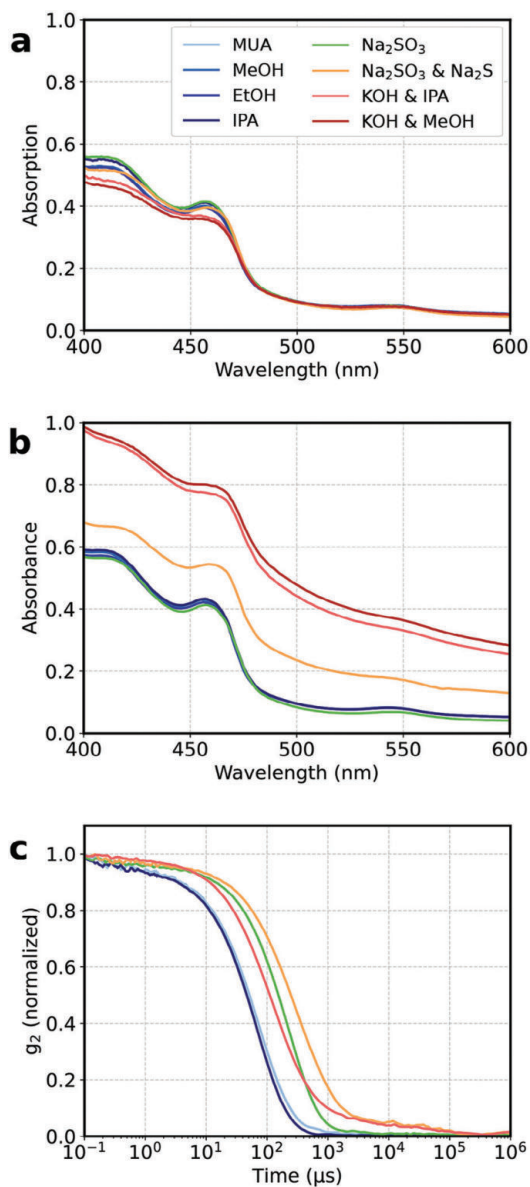


**Figure 2.** a) Static absorption and b) absorbance spectra, as well as c) normalized autocorrelation functions  $g_2(q, \tau)$  recorded from DLS measurements of MUA-capped, Pt-tipped CdSe/CdS DRs in water after adding different EDAs (see color code in a)).

excitonic transitions in the CdS rod domain, respectively (cf. Figure 1a).<sup>[1,6,20,40]</sup> The small shoulder at  $\approx 490$  nm can be assigned to the exciton transition in the so-called bulb region of CdS surrounding the CdSe core.<sup>[6,41–43]</sup> This bulb region is the area around the CdSe core, that has a slightly larger diameter than the rest of the rod and therefore a smaller exciton confinement energy (cf. Figure 1a).<sup>[42,44]</sup> The absorption features of the semi-conducting domain superimpose with the broad tail of the plat-

inum's surface plasmon (Figure S2, Supporting Information), spanning from the near-infrared to the ultraviolet region.<sup>[6,25,45]</sup> The Pt-tipping leads to a significant quenching of the DRs' PL (see Figure S2, Supporting Information). While the absorption spectra are similar in the presence of all EDAs (Figure 2a), the absorbance spectra are significantly increased over the whole spectral region after adding the sulfide and sulfite mixture, as well as the mixtures of KOH and alcohol as EDAs (Figure 2b). This increase in absorbance can be assigned to light scattering by the NPs in the presence of sulfide and hydroxide, which is also visible by eye (Figures S3 and S4, Supporting Information) and in TEM (Figure S5b, Supporting Information). Furthermore, we found that the NPs are colloidally stable in the presence of the alcoholic EDAs and sulfite for several days, while after adding the hydroxide and alcohol mixtures or the sulfide and sulfite mixture, the NPs precipitated within hours without stirring. These observations suggest that sulfide and hydroxide reduce the colloidal stability of the NPs and induce agglomeration. We conducted DLS measurements for a further analysis. To equalize the viscosity of the solvent for DLS measurements, the MUA-capped Pt-DRs were exposed to the different classes of EDAs for 15 min while stirring, followed by precipitation and redispersion of the NPs in water. The autocorrelation functions obtained from the DLS measurements reveal large differences in the hydrodynamic radii after the exposure to different EDAs (Figure 2c). The exposure to IPA did not change the hydrodynamic radii, whereas, after exposure to hydroxide and sulfide a second plateau formed at lag times larger 1 ms in the autocorrelation function, evidencing the presence of large agglomerates. Thus, large agglomerates form even after a short exposure to sulfide and hydroxide. This exposure seems to permanently reduce the colloidal stability of the NPs and hinders the dissolution of the agglomerates after precipitation and redispersion. This suggests that the hydroxide and sulfide interact with the NPs' surface, e.g. by attaching to it and displacing the MUA ligand. It was shown previously, that at high pH value hydroxides attach to CdS at the surface of NPs forming cadmium hydroxide.<sup>[46–48]</sup> Analogously, alkoxides forming from the alcoholic EDAs at pH 14, as well as the sulfide anions can attach to cadmium cations at the surface of the CdS crystal lattice, too.<sup>[49–53]</sup> Furthermore, after exposure to sulfite, sulfide, and hydroxide the hydrodynamic radii of the NPs increased, indicated by the shift of the autocorrelation function to larger lag times. Most likely, this shift of the autocorrelation function results mainly from the growth of the NPs' solvation shell by accumulation of salt ions, which also promotes electrostatic aggregation.<sup>[54–57]</sup>

Moreover, in the presence of hydroxide and sulfide a bathochromic shift occurs in the static absorption and absorbance spectra (see Figure 2a,b; Figure S7a, Supporting Information for magnified plot), as well as in the PL spectra (Figure S7b, Supporting Information). This shift is an additional indication of NP aggregation in the presence of these surface-active EDAs.

## 2.2. Steady-State Hydrogen Production Measurements

The effect of the various EDAs on the photocatalytic activity of the nanocatalysts was investigated by determining the quantum

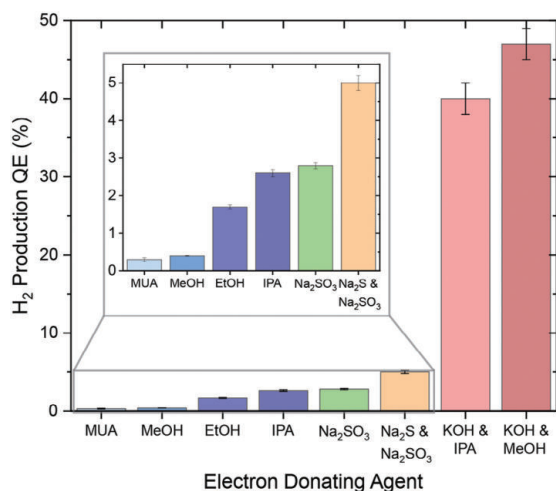


**Figure 3.** Hydrogen production quantum efficiencies for MUA-capped, Pt-tipped CdSe/CdS DRs in water, with no sacrificial EDA added (MUA,  $QE_{H_2} = 0.3 \pm 0.05\%$ ) and in the presence of different sacrificial EDAs: MeOH ( $0.4 \pm 0.01\%$ ), EtOH ( $1.7 \pm 0.06\%$ ), IPA ( $2.6 \pm 0.1\%$ ),  $Na_2SO_3$  ( $2.8 \pm 0.08\%$ ),  $Na_2S$  &  $Na_2SO_3$  ( $5 \pm 0.2\%$ ), KOH & IPA ( $40 \pm 2\%$ ), and KOH & MeOH ( $47 \pm 2\%$ ).

efficiency in hydrogen production ( $QE_{H_2}$ ; see Supporting Information for definition) in the presence of the different EDAs by conducting steady-state hydrogen production measurements (Figure 3). The experimental conditions were consistent for all measurements (see Experimental Section for details). As previously reported, the  $QE_{H_2}$  is strongly dependent on the choice of EDA.<sup>[5,17,23,24,29]</sup> Even though the introduction of hydroxide and sulfide induces agglomeration and thus reduces the overall accessible surface area, the photocatalysts still achieve by far the largest  $QE_{H_2}$  in the presence of these EDAs. In line with this observation, it was previously reported that the formation of extended 3D nanophotocatalyst networks in aqueous suspension could actually increase the  $QE_{H_2}$ .<sup>[30–37]</sup> According to these reports, the increase in  $QE_{H_2}$  results from the energetic coupling between the connected NPs, enabling photogenerated charge carriers to move within these networks. Thus, electrons generated in different particles could accumulate at one metal tip generating one specific reduction site with increased potential for hydrogen production.<sup>[31,34,36]</sup> This accumulation of electrons at one specific tip should yield a higher  $QE_{H_2}$  than distributing them across multiple tips.<sup>[8,9]</sup> This so-called “antenna mechanism” should be especially advantageous if the NPs within the networks have differently large Pt tips, or some have no tip, as it is always the case for the applied hot-injection synthesis of Pt domains (cf. Section S1, Supporting Information).<sup>[15,33,34]</sup> Therefore, within such a network, the individual NPs are not required to have uniformly sized Pt tips for achieving large  $QE_{H_2}$ , unlike the colloiddally stable nanophotocatalysts. Furthermore, the NPs assemble into chain-structures in suspension or form spherical “hedgehog”-agglomerates (cf. cryo-TEM measurements in Figure S6, Supporting Information).<sup>[34,58]</sup> Since tip-to-tip attachment is favored during NP assembly, it is also likely to be the predominant orientation within the large agglomerates observed in the presence of

hydroxide and sulfide. This results in multiple junctions of connected Pt domains within the forming particle network, favoring electron accumulation from multiple DRs in one combined Pt domain.

### 2.3. Time-Resolved Spectroscopy

To gain further insight into the underlying carrier dynamics, we employed TA spectroscopy at an excitation at 400 nm (Figure 4). The CdS shell bleach is located at  $\approx 460$  nm and the CdSe core bleach at 550 nm, in accordance with the UV-vis spectra (Figures 4a and 2a,b). Figure 4b,c displays the bleach recovery kinetics of the shell and core absorption features. As the spectral position of the shell and core absorption features slightly depend on the employed EDA (cf. Figure 4a), bleach recovery dynamics are not plotted for a single probe wavelength but rather for the wavelength of the maximum bleach amplitude of each respective EDA (therefore, the y-axes in Figure 4b,c are labeled as  $\Delta A_{max}$ ). The shift observed in the static absorption and PL spectra (see above) is present in the TA spectra, too. In Cd-chalcogenide NPs, the bleach feature is dominated by electrons.<sup>[59–61]</sup> Still, conclusions about the hole scavenging process can be drawn from the observed bleach recovery. Holes that have been removed from the DR by the EDA no longer exert a Coulomb attraction on the electrons, which are thus more mobile and localize into the metal tip faster (cf. Figure 4e).<sup>[17]</sup> We observe similar TA bleach recovery kinetics in both shell and core (Figure 4b,c) in the presence of the alcoholic EDAs (IPA, MeOH, EtOH) and without any added EDA (MUA). On the contrary, the TA kinetics in the presence of the ionic EDAs such as sulfite, the mixture of sulfide and sulfite and the mixtures of hydroxide and alcohol recover significantly faster than for the alcoholic EDAs.

Furthermore, the EDA-dependent differences regarding direct hole transfer are also visible at the so-called charge separated state (CSS) feature (Figure 4d). The CSS, with the electron located in the Pt tip and the hole located in the DR, can be observed as a photoinduced absorption in TA. The separated charges generate an electric field, which induces a Stark-shift of the CdS absorption.<sup>[1,6,16,20,25,62,63]</sup> Being red-shifted from the CdS shell bleach, the CSS feature (positive  $\Delta A$ ) spectrally overlaps with the bleach of the bulb region (negative  $\Delta A$ ). As the bulb regions absorption feature is highly dependent on the DRs shape and composition, which slightly varies between different batches, the relative contributions to the overall  $\Delta A$  in this spectral region varies between batches of DRs. In addition to the superposition with the bulb region, the formation of the CSS feature depends on the number and size of Pt tips.<sup>[20]</sup> For the Pt-DR batch used for the time-resolved and steady-state measurements above, the CSS feature did not occur as a discernable feature. Nevertheless, it emerged for another batch of Pt-DRs we studied (see Section S6, Supporting Information for sample parameters). Figure 4d shows the TA kinetics averaged over the CSS spectral region of 475 to 490 nm (for better signal-to-noise ratio) on long delay times. In case of the alcoholic EDAs, the CSS feature emerges and shows a lifetime in the  $\mu s$  regime, in agreement with literature.<sup>[6,20,62]</sup> For the ionic EDAs, the CSS feature is not observable and the corresponding spectral region is dominated by the bulb-bleach.



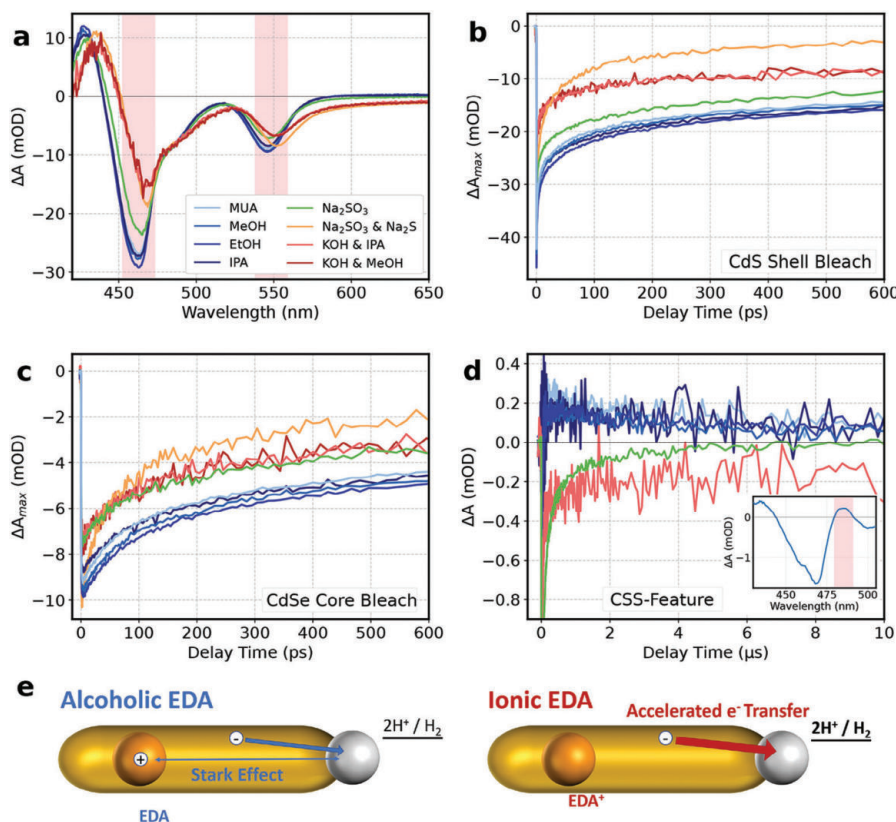


**Figure 4.** a) Transient absorption spectra at 10 ps delay time, bleach recovery kinetics of the b) CdS shell, and c) CdSe core feature at bleach maximum and d) averaged TA kinetics in the probe spectral range from 475 to 490 nm, showing the CSS-feature (see text), of MUA-capped, Pt-tipped CdSe/CdS DRs in the presence of different EDAs (see color code in a)), after excitation at 400 nm. The inset in d) shows the TA spectrum without added EDA (MUA) averaged from 0.01 to 1  $\mu$ s, displaying the CdS shell bleach and CSS feature. The spectral region of the CdS shell and CdSe core bleach, as well as of the CSS feature are highlighted in pink in a) and the inset of d), respectively. The kinetics in the presence of  $\text{Na}_2\text{S}$  &  $\text{Na}_2\text{SO}_3$  and KOH & MeOH are omitted in d) for clarity, as these measurements are very noisy in the displayed spectral region. The scheme in e) illustrates the Stark effect generated by the electric field between the spatially separated electron at the Pt tip and the hole at the core for the alcoholic EDAs, and the accelerated electron transfer into the Pt tip, resulting from likewise accelerated hole transfer for the ionic EDAs.

In the presence of the surface-active EDAs, the PL is strongly quenched (Figure S7b and Tables S1 and S2, Supporting Information) and the PL decay is accelerated (Figure S8, Supporting Information) compared to the diffusion-limited EDAs, similar to the TA kinetics.

### 2.3.1. Alcoholic Electron Donating Agents

In the case of no EDA added, the holes are exclusively scavenged by the MUA ligand.<sup>[16,25,29,64]</sup> Due to the unaltered TA bleach recovery kinetics (Figure 4b,c) and PL decay (Figure S8, Supporting Information) upon addition of the alcoholic EDAs, we conclude that the photogenerated holes do not transfer directly onto these EDAs. Instead, we assume, that the holes primarily transfer onto the MUA ligand before potentially being scavenged by the EDA (cf. Figure 5a). Since the photogenerated holes leave the semiconductor by transferring onto the MUA ligand, the eventual hole

transfer from the ligand onto the EDA can not be resolved in the TA measurement.

Initially, the MUA forms a stable protection layer on the NP's surface including a non-polar layer resulting from the interacting alkyl chains. This non-polar layer was shown to repel the aqueous solvent and therefore should not be penetrable by the alcoholic EDAs.<sup>[17,65–67]</sup> However, after being oxidized, the MUA forms a dithiol and detaches from the NP's surface.<sup>[17,25,26]</sup> The alcoholic EDAs can penetrate through the resulting holes in the ligand shell and reduce the oxidized MUA ligand diffusion-limited (cf. Figure 5a).

We attribute the differences in  $\text{QE}_{\text{H}_2}$  for the different alcoholic EDAs to the differences in redox potentials of the EDAs, enabling the scavenging of the trapped hole from the MUA ligand (-0.28 V for IPA forming acetone, -0.19 V for EtOH forming acetaldehyde, and -0.055 V for MeOH forming formaldehyde; actually, the hole transfer might not proceed via a two- but one-electron transfer process, generating a free radical intermediate, which is discussed later in more detail).<sup>[68,69]</sup>

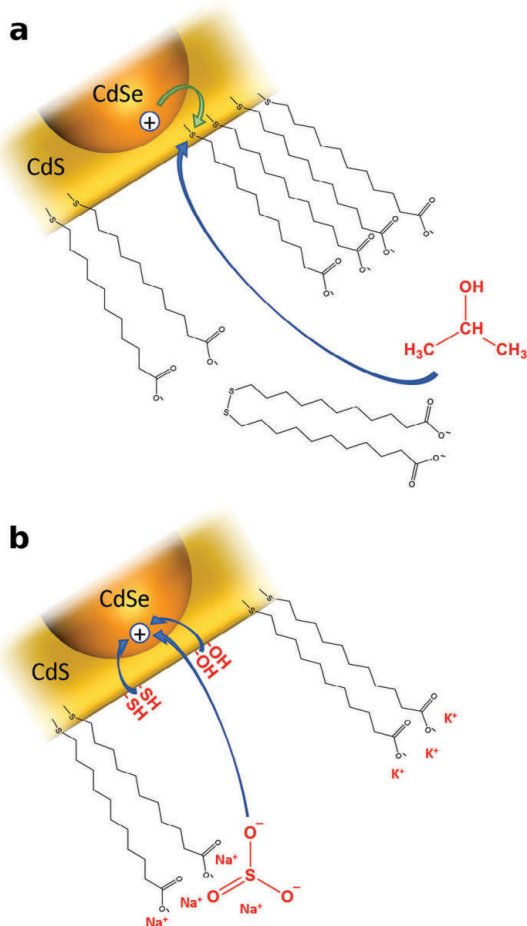


**Figure 5.** Schematic illustration of a) diffusion-limited and b) surface-active EDAs. The diffusion-limited, alcoholic EDA (IPA in this example) has to penetrate through gaps in the ligand shell for scavenging the photogenerated holes from the oxidized thiol ligand. In contrast, the surface-active EDAs (hydroxide, sulfide, and sulfite in this example) attach to the NP's surface, or locate in the solvation shell of the NPs resulting in a much faster hole transfer compared to the diffusion-limited EDAs. The blue arrows indicate movement of the EDA and electron transfer, the green arrow indicates hole transfer.

### 2.3.2. Ionic Electron Donating Agents

In the presence of the ionic EDAs, the TA bleach recovers and the PL decays significantly faster compared to the alcoholic EDAs, suggesting a direct transfer of the photogenerated holes onto the former EDAs, which is in line with the observed high  $QE_{H_2}$  for these systems. The direct hole transfer is enabled by the surface-activity of the ionic EDAs, which attach to the NPs surface (hydroxide and sulfide) or at least accumulate in the solvation shell of the NPs (sulfite) (cf. Figure 5b). The differences in hole transfer rates between the alcoholic and ionic EDAs is further evidenced by the differences in the occurrence of the CSS feature. In the presence of the diffusion-limited EDAs the CSS-feature occurs as

a positive absorption feature, indicating that the holes rest long enough at the CdSe core for the bulb bleach to recover sufficiently. Whereas, for the surface-active EDAs no observable positive CSS feature occurs, confirming the accelerated hole removal from the semiconducting domain.

The quenching of the NPs PL upon introduction of the ionic EDAs (Figure S7b and Tables S1 and S2, Supporting Information) additionally confirms the occurrence of alternative decay channels, like the direct hole transfer onto these surface-active EDAs.

**Sodium Sulfite:** The introduced sodium cations and therefore also the sulfite anions will locate into the solvation shell of the NPs, attracted by the deprotonated acid group of the MUA ligand (cf. Figure 5b). Furthermore, after some MUA detaches from the NP's surface due to oxidation, the sulfite anion as a polar species is likely to be in close proximity to the NP's surface. This surface activity of the sulfite anion favors a fast hole transfer, compared to the alcoholic EDAs (cf. Figure 5b). However, unlike the hydroxide, alkoxide, and sulfide anions, the sulfite anion does not bind to the CdS surface, but interacts only weakly with it.<sup>[70,71]</sup> Nevertheless, direct hole transfer is enabled for the sulfite anion, due to the small redox potential via the kinetically favored one-electron transfer, which generates a free radical intermediate ( $\approx 0.7$  V vs NHE at pH 10 for  $^*SO_3^- + e^- \rightarrow SO_3^{2-}$ ).<sup>[24,72–74]</sup> By comparison, the redox potential of the thiol ligand is roughly 0.8 V vs NHE,<sup>[25,29,75]</sup> explaining why for the sulfite a direct hole transfer onto the EDA is favored, while for the alcohols the hole is first transferred onto the ligand (e.g. for MeOH:  $\approx 1.2$  V vs NHE at pH 7 for  $^*CH_2OH + e^- + H^+ \rightarrow CH_3OH$ ).<sup>[24,69,76]</sup> Since sodium sulfite and sulfide function as bases, the increased concentration of hydroxide anions might additionally raise the hole transfer rate for both EDAs (pH = 10 for 0.1 M  $Na_2SO_3$  and pH = 13 for 0.1 M  $Na_2S$  &  $Na_2SO_3$ ; cf. Figure 5b).<sup>[8]</sup>

**Sodium Sulfide and Sodium Sulfite:** Interestingly, the fastest TA bleach recovery and PL decay was observed with the mixture of sulfide and sulfite, although this photocatalyst-EDA system achieves a significantly smaller  $QE_{H_2}$  than the hydroxide and alcohol system. Lian et al. argue that the fast decays in the presence of the sulfide and sulfite mixture result from the sulfide anion's ability to reduce redox-active mid-gap states of the semiconductor, creating "spectator" electrons at the NPs surface upon attachment.<sup>[51,77]</sup> These charges at the NP's surface enable recombination via the Auger mechanism.<sup>[51]</sup> However, as the sulfide anions predominantly exist as  $HS^-$  after hydrolysis in aqueous solution,<sup>[51,52]</sup> they do not necessarily charge the NP's surface negatively upon attachment. Most likely, these  $HS^-$  anions bind to the NP's surface similarly to the MUA ligand ( $RS^-$ ), but reduce the colloidal stability significantly due to the missing alkyl chain and carboxylic head group (cf. Figure 5b). Hence, the especially fast PL and TA kinetics might also indicate fast hole trapping and scavenging due to the surface-attached sulfide anions. Various factors might contribute to the comparably low  $QE_{H_2}$  in the presence of the sulfide and sulfite mixture. The disulfide anions, potentially forming after oxidation of the sulfide EDA, are an oxidative species that was reported to compete with the proton reduction at the Pt tip.<sup>[52,71]</sup> However, the addition of sulfite ions inhibits this process by forming thiosulfate instead of the reductive disulfide anions or polysulfide radicals.<sup>[24,52,71]</sup> Nevertheless, this process might contribute to the comparatively low  $QE_{H_2}$

measured while using sulfide and sulfite as a combined EDA system despite the rapid charge transfer. It was also reported that sulfur compounds tend to poison Pt electrodes by attaching to the surface and making it inaccessible.<sup>[78–82]</sup> This process should reduce the hydrogen production rates especially in the presence of sulfide anions.<sup>[80]</sup>

**Potassium Hydroxide and Alcohol:** By far the largest  $QE_{H_2}$  is obtained introducing a mixture of KOH and MeOH or IPA, respectively (Figure 3). The use of MeOH as an EDA at increased pH value has not been reported yet. Even though at neutral pH value the introduction of MeOH obtained the smallest  $QE_{H_2}$  of all alcoholic EDAs (6.5-times smaller  $QE_{H_2}$  than IPA), the  $QE_{H_2}$  was even larger than the one in the presence of IPA at pH 14. We assume that the larger  $QE_{H_2}$  in the presence of MeOH results from a larger concentration of alkoxides. Even though MeOH and IPA are weak acids, at pH 14 a fraction of the alcoholic EDAs dissociates, forming the respective alkoxide. Due to the smaller  $pK_a$  value of MeOH,<sup>[83]</sup> the concentration of methoxide at pH 14 is roughly two orders of magnitude larger than the concentration of the alkoxide formed from IPA ( $10^{-1} \frac{\text{mol}}{\text{L}}$  for MeOH and  $10^{-3} \frac{\text{mol}}{\text{L}}$  for IPA, see Section S7, Supporting Information for calculation). Since these alkoxides are highly reductive they can function as EDAs, additionally.

It was reported previously, that another reason for the significant increase in  $QE_{H_2}$  at high pH value is the high mobility of the hydroxide anion and radical, respectively.<sup>[5,17]</sup> Just a single electron transfer process is needed for oxidizing the hydroxide anion. Afterward, the formed hydroxide radical relays the hole to the respective alcoholic EDA present, thus functioning as a redox mediator.<sup>[17]</sup> In principle, this process of hole shuttling should also be possible after oxidation of the sulfide anion or the thiol group of the MUA ligand, creating an  $^*SH$  or  $^*SR$  radical, respectively. However, the reduction potentials of the sulfanyl and thyl radical are much smaller than for the hydroxide radical (1.2 V for sulfanyl and 1.9 V for hydroxide radical - potentials might differ for surface-bound species).<sup>[73,74]</sup> Therefore, the driving force for hole transfer from the oxidized MUA ligand onto the alcoholic EDA is much smaller than for the hydroxide, resulting in a much slower and less likely reaction. Due to its large reduction potential, the hydroxide radical is likely to oxidize any agent in its proximity diffusion-controlled. Therefore, we assume that the hydroxide radical will not only selectively shuttle the hole to the alcoholic EDA, but might also oxidize remaining MUA ligand at the NP's surface. This process would further promote a successive displacement of the MUA ligand from the NP's surface at high pH.

In addition, most of the radicals created by EDA oxidation are strong reducing agents (e.g.,  $\approx -2$  V at pH 10 vs NHE for  $SO_4^{2-} + H_2O + e^- \rightarrow ^*SO_3^- + 2 OH^-$  or  $-1.3$  V vs NHE at pH 7 for  $CH_2O + e^- + H^+ \rightarrow ^*CH_2OH$ ).<sup>[24,69,73,84,85]</sup> Therefore, in the absence of an alternative electron acceptor, like molecular oxygen, the radical is likely to inject an electron into the conduction band of the CdS or the Pt domain directly (e.g.  $^*CH_2OH \rightarrow CH_2O + H^+ + e^-_{CdS/Pt}$ ).<sup>[24,76,84]</sup> In the first case it might either be trapped within the semiconducting domain, favoring electron hole recombination or transfer into the Pt tip.<sup>[86]</sup> Thus, in the latter cases, the formation of molecular hydrogen is enabled after absorption of a single photon.<sup>[76]</sup> This so-

called “current doubling” effect was observed in many photocatalytic systems employing various alcoholic EDAs.<sup>[24,76,84,86–94]</sup> Bahnmann et al. point out that due to this effect, the yields obtained in molecular hydrogen formation should not be denoted as “water splitting efficiencies”.<sup>[24]</sup> To which extent this process occurs depends on the energetic position of the electronic bands of the semiconductor in relation to the redox potentials of the EDAs and the radicals forming after oxidation.<sup>[95]</sup> For the alcoholic EDAs, the IPA radical is most reductive, the EtOH radical second, and the MeOH radical the least reductive (correlating with the  $pK_a$  value of the radical: 12.2, 11.6, 10.7 for IPA, EtOH, and MeOH, respectively).<sup>[27,84,85,96]</sup> As a result, the current doubling effect is most likely to occur in the presence of IPA and least likely for MeOH, probably contributing to the differences in  $QE_{H_2}$  of the alcoholic EDAs. The reduction potential of the alcohols increases (more negative potential) with increasing pH value, favoring the current doubling effect.<sup>[84,85,96]</sup> While the reduction potentials of the conduction and valence bands of the CdS increase by  $-33$  mV  $pH^{-1}$ , the potentials of the EDAs follow a Nernstian behavior ( $-59$  mV  $pH^{-1}$ ).<sup>[17]</sup> Thus, this effect will contribute to the especially large  $QE_{H_2}$  in the presence of the alcohol and hydroxide EDA mixtures. For these mixtures, the current doubling effect might additionally occur upon oxidation of surface-attached alkoxides. As sulfide and sulfite radicals ( $^*S^-$ ,  $^*SO_3^-$ ) are highly reductive species, the current doubling effect may also occur for these inorganic EDAs.<sup>[24]</sup>

### 3. Conclusion

In conclusion, we observed EDA-dependent changes in the photocatalytic hydrogen production activity and colloidal stability of Pt-tipped CdSe/CdS DRs, investigating a large set of EDAs. We primarily attribute these changes to differing interactions of the EDAs with the NPs' surface and ligand shell. While the alcoholic EDAs (MeOH, EtOH, IPA) scavenge the holes diffusion-limited from the oxidized MUA ligand, the ionic EDAs (KOH & IPA, KOH & MeOH,  $Na_2SO_3$ , and  $Na_2S$  &  $Na_2SO_3$ ) are surface active, enabling direct hole transfer. The TA bleach recovery, the CSS-feature and PL decay validate significantly faster hole transfer and trapping for surface-active EDAs compared to diffusion-limited ones. Additionally, we found that the introduction of sulfide and hydroxide causes agglomeration of the NPs, conducting DLS and static absorption spectroscopy. We attribute the observed agglomeration to reduced colloidal stability due to the attachment of the ions to the NP's surface. Nevertheless, we obtained the largest  $QE_{H_2}$  in the presence of hydroxide, even though the nanophotocatalysts are not separately dispersed. Based on these observations, we conclude that NPs' agglomeration not necessarily reduces  $QE_{H_2}$  due to a loss of accessible surface area, but might increase it by enabling the accumulation of electrons at distinct metal domain junctions within the formed network. Thus, when designing NPs for photocatalysis by using surface-active EDAs, the former should not be considered as isolated photocatalysts, but building blocks within a network of these. This systematic study enhances our comprehension of the general EDA-dependent principles that impact hydrogen production activity by highlighting the interaction of the EDAs with the photocatalyst's surface and discussing the effect of EDA-induced agglomeration.

## 4. Experimental Section

**Materials:** Trioctylphosphine (TOP, 90%), selenium (>99%), sulfur (>99%), n-octylamine (99%), oleylamine (OAm, 70%), oleic acid (OA, 90%), 1,2-hexadecanediol (HDD, 90%) and diphenyl ether (DPE, 99%), 11-mercaptopundecanoic acid (MUA, 95%), and n-hexylphosphonic acid (HPA, 95%), sodium sulfide (95%) were purchased from Sigma-Aldrich. Trioctylphosphine oxide (TOPO, 98%), potassium hydroxide ( $\geq 85\%$ ) and sodium sulfite (98%) were obtained from Merck, while n-octadecylphosphonic acid (ODPA, 98%) was purchased from PCI Synthesis and Cadmium oxide (CdO, >99%) from ChemPur. Toluene ( $\geq 99.8\%$ ), acetone (>99%), methanol (MeOH,  $\geq 99.8\%$ ), ethanol (EtOH,  $\geq 99.8\%$ ), chloroform (>99%), isopropyl alcohol (IPA,  $\geq 99.7\%$ ) were obtained from VWR Chemicals. Nonanoic acid (97%), platinum(II) acetylacetonate (98%) were purchased from abcr and 1,2-dichlorobenzene (DCB, >99%) was purchased from Acros Organics. Hydrogen gas ( $\geq 99.999\%$ ) was obtained from Westfalen AG and nitrogen gas ( $\geq 99.999\%$ ) from SOL Group. Ultrapure water (18.2 M $\Omega$  cm, Millipore) was used in all experiments. All chemicals were used as received.

**Synthesis of CdSe Nanocrystals:** The CdSe seeds were prepared following the procedure reported by Manna et al.<sup>[10]</sup> In a 25 mL three-necked round-bottom quartz-glass flask (RBF), TOPO (3.0 g), ODPA (280 mg), and CdO (60 mg, 0.47 mmol) were introduced and degassed under vacuum at 150 °C for 1 h. Afterward, the solution was heated to 320 °C under nitrogen to dissolve the CdO until the solution turned optically clear and colorless. After 30 min, the temperature was set to 380 °C. At a temperature of 360 °C, TOP (1.5 g) was injected. Once the temperature recovered to 380 °C, a Se:TOP solution (Se (58 mg, 0.73 mmol) dissolved in TOP (360 mg)) was rapidly injected. The heating mantle was removed, and the suspension was rapidly cooled, using an ice bath. At 150 °C, the reaction was finally quenched by injecting toluene (5 mL). The nanocrystals were precipitated using centrifugation, after adding acetone and MeOH as anti-solvents. The precipitate was redispersed in toluene and the cleaning procedure was repeated several times. The product was stored in a glove box under nitrogen atmosphere.

**Synthesis of CdSe/CdS Dot-in-Rod Nanocrystals:** The procedure for seeded growth of the CdSe/CdS DRs was adopted from Manna and coauthors and was slightly modified.<sup>[10]</sup> In a 25 mL three-necked RBF, TOPO (3.0 g), ODPA (290 mg), HPA (90 mg), and CdO (90 mg, 0.70 mmol) were mixed and heated to 150 °C under vacuum for 1 h. The solution was heated to 300 °C under nitrogen for 30 min to form a clear and optically colorless solution. Subsequently, a second degassing step was conducted by lowering the temperature to 150 °C under vacuum for half an hour. Simultaneously, a CdSe injection solution was prepared by dissolving CdSe seeds (50 nmol) and sulfur (120 mg, 3.7 mmol) in TOP (2 mL). This injection solution was heated to 80 °C for 10 min to promote the dissolution of the sulfur. The main solution was heated to 330 °C under nitrogen and TOP (1.5 mL) was injected. The temperature was raised to 340 °C and the CdSe/S:TOP suspension was rapidly injected. After the temperature recovered, the reaction was allowed to proceed for 8 min. The reaction was quenched by removing the heating mantle and cooling the suspension, using an air blower. At 150 °C, toluene (12 mL) and octylamine (1.5 mL) were injected. After the synthesis, the product was washed by repeated size-selective precipitation using a mixture of acetone and MeOH and subsequent centrifugation. The precipitate was redispersed in toluene.

**Pt Tipping on CdSe/CdS Dot-in-Rods:** Pt tips were selectively deposited onto the CdSe/CdS DRs following the procedure by Mokari and coworkers.<sup>[15]</sup> First, OA (0.2 mL), OAm (0.2 mL), HDD (43.0 mg), and DPE (10 mL) were introduced into a 25 mL three-necked flask and were heated to 80 °C under vacuum for 45 min. Meanwhile, CdSe/CdS DRs ( $\approx 40$  nmol (concentration deduced from the absorbance spectrum, based on the calculations from Dorfs et al.)<sup>[97]</sup>) were concentrated by evaporating the solvent, combined with platinum(II) acetylacetonate (12 mg, 30.5  $\mu$ mol) and dissolved in DCB (2.5 mL). Afterward, the suspension was heated to 70 °C for 10 min. The solution in the RBF was heated to 200 °C under nitrogen and the mixture of DRs and Pt-precursor was injected. The reaction was allowed to proceed for 5 min and was quenched quickly by cooling the suspension using a water bath. The tipped DRs were washed

twice and separated from homonucleated Pt-NPs by precipitation via the addition of EtOH, centrifugation, and redispersion in toluene.

**Ligand Exchange on Pt-Tipped and Bare CdSe/CdS Dot-in-Rods:** For dispersing the Pt-tipped and bare CdSe/CdS DRs in aqueous suspension, the hydrophobic ligands on the NPs were exchanged to MUA following the procedure by Banin et al.<sup>[19]</sup> The NPs were dispersed in chloroform (10 mL), MUA (13 mg, 59.5  $\mu$ mol) was added ( $\approx 4000$  MUA molecules per NP), and the suspension was shaken and sonicated. Afterward, a KOH solution (2 mL,  $\approx 0.1$  M) was added to the NP suspension and shaken vigorously. After letting the milky mixture sit for roughly a minute, two phases formed. The upper, colored, aqueous phase, holding MUA-capped NPs, was separated. The procedure of adding the KOH solution (0.5 mL each) and separation of the upper phase was repeated four times. Finally, the NPs were precipitated with MeOH and centrifugation, followed by redispersion in water.

**Transmission Electron Microscopy (TEM):** Conventional TEM measurements were performed using a JEOL, JEM-1011 microscope operating at an accelerating voltage of 100 kV. High-resolution TEM (HRTEM) and high-angle annular dark field scanning transmission electron microscopy (HAADF STEM) measurements were carried out at a JEOL, JEM-2200FS microscope at 200 kV accelerating voltage. The samples for TEM imaging were prepared by drop-casting  $\approx 10$   $\mu$ L of diluted NP suspension onto a carbon-coated 400-mesh copper grid. Cryo-TEM measurements were conducted at a FEI Tecnai G2 Spirit Twin at an accelerating voltage of 120 kV. The samples for cryo-TEM imaging were prepared using a FEI Company, Vitrobot Mark IV for vitrification in liquid ethane. The micrographs were analyzed using the software ImageJ.

**Dynamic Light Scattering:** The DLS measurements were conducted after exposing MUA-capped Pt-DRs to the different classes of EDAs for 15 min while stirring, followed by precipitation and redispersion of the NPs in water. For the MUA-sample, we added the same volume of water instead of the EDA solution, in order to account for potential ligand loss by dilution, as well as during precipitation and redispersion. The DLS measurements were conducted using a different batch of Pt-tipped DRs than the one used for the hydrogen production measurements. A dynamic viscosity of 0.8872 mPa s (water at 25 °C) and a refractive index of 2.53 (CdSe/CdS NPs) was set for all measurements. The measurements were performed in a DLS instrument (Malvern Panalytical Ltd, Zetasizer Pro). The software ZS Xplorer was used for instrument control and data recording. The data was analyzed using OriginPro 2024 (OriginLab Corporation) and a self-written script in Python (Python Software Foundation).

**Steady-State Hydrogen Production Measurements:** The hydrogen generation measurements were performed in a cylindrical 50 mL quartz-glass cuvette with an optical path length of 2 cm. The optical density of all samples was adjusted to  $\approx 0.8$  at 445 nm inside the cuvette. The NP suspension was purged with nitrogen gas for roughly half an hour before starting the illumination. For illuminating the NPs a 445 nm LED (Thorlabs SOLIS-445C) was used, adjusted to 115 mW of total output power ( $\approx 6.3$  mW cm $^{-2}$ ), while the suspension was stirred. After every 15 min of irradiation, a gas aliquot of 500  $\mu$ L was taken from the cuvette using a gastight syringe (Hamilton, Gastight syringe) and injected into a gas chromatograph (GC) equipped with a thermal conductivity detector (Shimadzu, Nexis GC-2030). The GC was equipped with two columns, a 5 Å molecular sieve (SH-Rt-Msieve 5A, 30 m, 0.53 mm, 50  $\mu$ m) and a porous polymer Q-BOND column (SH-Rt-Q-BOND 30 m, 0.53 mm, 20  $\mu$ m) for separating permanent gases. Nitrogen was used as carrier gas. All EDA-dependent hydrogen production measurements were conducted using the same batch of Pt-tipped DRs, except for the MUA-sample, which was measured using a comparable batch of Pt-DRs (see Section S5 and Figure S11, Supporting Information). The software LabSolutions (Shimadzu) was used for instrument control, data recording, and analysis. For preventing a local accumulation of the evolved hydrogen gas, the cuvette was shaken before taking the gas aliquot. See Section S4 (Supporting Information) for details on data analysis, setup, and calibration.

**Transient Absorption Spectroscopy:** The femtosecond TA experiments were conducted using an amplified Ti:Sapphire laser system (Spitfire-Ace, 800 nm, 1 kHz, 35 fs, Spectra-Physics) in combination with a HELIOS TA spectrometer (Ultrafast Systems). The laser output was split into two

parts. One was used to generate the 400 nm pump beam via second-harmonic generation in a BBO crystal. The other passed a delay line and was used to generate whitelight in a CaF<sub>2</sub> crystal. The pump beam was sent through a chopper with a frequency of 500 Hz. For the nanosecond to microsecond TA experiments, an EOS spectrometer (Ultrafast Systems) was employed, which uses a 2 kHz probe whitelight generated by an electronically triggered whitelight laser source. The same 400 nm pump beam was used as for the femtosecond TA experiments. The excitation fluence was set to 30 μJ cm<sup>-2</sup> for all measurements. For both types of TA experiments, both pump and probe beam were focussed onto the sample, which was rapidly stirred in a 2 mm cuvette. The samples for the TA measurements were prepared by combining the MUA-capped DRs with the respective sacrificial EDA right before the measurement to avoid aging effects and were purged with nitrogen.

**Static Ultraviolet–Visible (UV–vis) Spectroscopy:** The absorption of the colloidal samples was determined using an UV–vis spectrometer (Agilent Technologies, Cary 5000), equipped with an integrating sphere (lampsphere, DRA-2500). Samples of 3 mL were transferred into a quartz-glass cuvette (Hellma Analytics) with an optical path length of 1 cm and placed in center position inside the integrating sphere. Absorbance measurements were conducted in a spectrometer with a linear beam path (Agilent Technologies, Applications was used for instrument control and data recording. The data was analyzed using OriginPro 2024 (OriginLab Corporation) and a self-written script in Python (Python Software Foundation).

**Time-Resolved Photoluminescence Spectroscopy:** The PL decay kinetics were recorded using a fluorescence lifetime spectrometer (PicoQuant GmbH, FluTime 300), equipped with a high power supercontinuum laser (NKT Photonics, SuperK Fianium), and a tunable high-contrast filter (NKT Photonics, LLTF Contrast), while the software EasyTau 2 (PicoQuant GmbH) and OriginPro 2024 (OriginLab Corporation) were used for instrument control, data recording and analysis. All samples were excited at 445 nm and the PL decay kinetic was recorded at the maximum of the PL peak of the respective sample.

**Static Photoluminescence Spectroscopy:** The PL spectra were recorded using a Spectrofluorometer system (Jobin Yvon HORIBA, Fluorolog-3), equipped with a photomultiplier (Jobin Yvon HORIBA, Spex DM302), using the software FluorEssence (HORIBA), OriginPro 2024 (OriginLab Corporation), and a self-written script in MATLAB (The MathWorks Inc.) for instrument control, data recording, and analysis, as well as for determining the PL quantum yields. All measurements were conducted using 445 nm excitation.

**pH Value Measurements:** The pH values of the solutions of the EDAs in water were determined using a pH meter (Mettler Toledo, FiveEasy), equipped with a pH electrode (InLab, pH electrode Micro).

## Supporting Information

Supporting Information is available from the Wiley Online Library or from the author.

## Acknowledgements

This work was supported by the Graduate School “Nanohybrid” (GRK 2536, No. 408076438) of the Deutsche Forschungsgemeinschaft (DFG). H. L. and H. W. acknowledge support within the DFG project Cluster of Excellence “CUI: Advanced Imaging of Matter” of the DFG (EXC 2056, No. 390715994). The authors gratefully thank A. Koeppen (Universität Hamburg (UHH)), S. Werner (UHH), and U. Koenig (UHH) for exciting HR- and cryo-TEM measurements.

Open access funding enabled and organized by Projekt DEAL.

## Conflict of Interest

The authors declare no conflict of interest.

## Data Availability Statement

The data that support the findings of this study are available from the corresponding author upon reasonable request.

## Keywords

catalysis, hole transfer, hybrid, metal, nanorod, photocatalysis, semiconductor

Received: February 21, 2024

Revised: March 25, 2024

Published online: April 18, 2024

- [1] K. Wu, H. Zhu, T. Lian, *Acc. Chem. Res.* **2015**, *48*, 851.
- [2] H. Weller, *Adv. Mater.* **1993**, *5*, 88.
- [3] P. Moroz, A. Boddy, M. Zamkov, *Front. Chem.* **2018**, *6*, 353.
- [4] K. Wu, T. Lian, *Chem. Soc. Rev.* **2016**, *45*, 3781.
- [5] P. Kalisman, Y. Nakibli, L. Amirav, *Nano Lett.* **2016**, *16*, 1776.
- [6] M. Wächtler, P. Kalisman, L. Amirav, *J. Phys. Chem. C* **2016**, *120*, 24491.
- [7] L. Amirav, A. P. Alivisatos, *J. Phys. Chem. Lett.* **2010**, *1*, 1051.
- [8] T. Simon, M. T. Carlson, J. K. Stolarczyk, J. Feldmann, *ACS Energy Lett.* **2016**, *1*, 1137.
- [9] Y. Nakibli, P. Kalisman, L. Amirav, *J. Phys. Chem. Lett.* **2015**, *6*, 2265.
- [10] L. Carbone, C. Nobile, M. De Giorgi, F. D. Sala, G. Morello, P. Pompa, M. Hytch, E. Snoeck, A. Fiore, I. R. Franchini, M. Nadasan, A. F. Silvestre, L. Chiodo, S. Kudera, R. Cingolani, R. Krahn, L. Manna, *Nano Lett.* **2007**, *7*, 2942.
- [11] J. Dimitrijevic, N. Krapf, C. Wolter, C. Schmidtke, J.-P. Merkl, T. Jochum, A. Kornowski, A. Schüth, A. Gebert, G. Hüttmann, T. Vossmeier, H. Weller, *Nanoscale* **2014**, *6*, 10413.
- [12] G. Menagen, J. E. Macdonald, Y. Shemesh, I. Popov, U. Banin, *J. Am. Chem. Soc.* **2009**, *131*, 17406.
- [13] S. Deka, A. Falqui, G. Bertoni, C. Sangregorio, G. Poneti, G. Morello, M. D. Giorgi, C. Giannini, R. Cingolani, L. Manna, P. D. Cozzoli, *J. Am. Chem. Soc.* **2009**, *131*, 12817.
- [14] B. T. Diroll, N. Gogotsi, C. B. Murray, *Chem. Mater.* **2016**, *28*, 3345.
- [15] S. E. Habas, P. Yang, T. Mokari, *J. Am. Chem. Soc.* **2008**, *130*, 3294.
- [16] T. O'Connor, M. S. Panov, A. Mereshchenko, A. N. Tarnovsky, R. Lorek, D. Perera, G. Diederich, S. Lambright, P. Moroz, M. Zamkov, *ACS Nano* **2012**, *6*, 8156.
- [17] T. Simon, N. Bouchonville, M. J. Berr, A. Vaneski, A. Adrović, D. Volbers, R. Wyrwich, M. Döblinger, A. S. Susha, A. L. Rogach, F. Jäckel, J. K. Stolarczyk, J. Feldmann, *Nat. Mater.* **2014**, *13*, 1013.
- [18] P. V. Kamat, *J. Phys. Chem. Lett.* **2012**, *3*, 663.
- [19] R. Costi, A. E. Saunders, E. Elmalem, A. Salant, U. Banin, *Nano Lett.* **2008**, *8*, 637.
- [20] Y. Nakibli, Y. Mazal, Y. Dubi, M. Wächtler, L. Amirav, *Nano Lett.* **2018**, *18*, 357.
- [21] Y. Ben-Shahar, F. Scotognella, I. Kriegel, L. Moretti, G. Cerullo, E. Rabani, U. Banin, *Nat. Commun.* **2016**, *7*, 10413.
- [22] L. Amirav, A. P. Alivisatos, *J. Am. Chem. Soc.* **2013**, *135*, 13049.
- [23] M. J. Berr, P. Wagner, S. Fischbach, A. Vaneski, J. Schneider, A. S. Susha, A. L. Rogach, F. Jäckel, J. Feldmann, *Appl. Phys. Lett.* **2012**, *100*, 223903.
- [24] J. Schneider, D. W. Bahnemann, *J. Phys. Chem. Lett.* **2013**, *4*, 3479.
- [25] Y. Liu, W. Yang, Q. Chen, D. A. Cullen, Z. Xie, T. Lian, *J. Am. Chem. Soc.* **2022**, *144*, 2705.
- [26] J. Aldana, Y. A. Wang, X. Peng, *J. Am. Chem. Soc.* **2001**, *123*, 8844.
- [27] K. Wenderich, G. Mul, *Chem. Rev.* **2016**, *116*, 14587.

- [28] K. P. Acharya, R. S. Khnayer, T. O'Connor, G. Diederich, M. Kirsanova, A. Klinkova, D. Roth, E. Kinder, M. Imboden, M. Zamkov, *Nano Lett.* **2011**, *11*, 2919.
- [29] K. Wu, Z. Chen, H. Lv, H. Zhu, C. L. Hill, T. Lian, *J. Am. Chem. Soc.* **2014**, *136*, 7708.
- [30] J. Schlenkrich, F. Lübke-Warwas, R. T. Graf, C. Wesemann, L. Schoske, M. Rosebrock, K. D. Hindricks, P. Behrens, D. W. Bahnemann, D. Dorfs, N. C. Bigall, *Small* **2023**, *91*, 2208108.
- [31] M. Rosebrock, D. Zámbo, P. Rusch, D. Pluta, F. Steinbach, P. Bessel, A. Schlosser, A. Feldhoff, K. D. Hindricks, P. Behrens, D. Dorfs, N. C. Bigall, *Adv. Funct. Mater.* **2021**, *31*, 2101628.
- [32] C.-Y. Wang, C. Böttcher, D. W. Bahnemann, J. K. Dohrmann, *J. Mater. Chem.* **2003**, *13*, 2322.
- [33] N. Lakshminarasimhan, W. Kim, W. Choi, *J. Phys. Chem. C* **2008**, *112*, 20451.
- [34] C.-Y. Wang, R. Pagel, J. K. Dohrmann, D. W. Bahnemann, *C. R. Chim.* **2006**, *9*, 761.
- [35] C.-Y. Wang, C. Böttcher, D. W. Bahnemann, J. K. Dohrmann, *J. Nanopart. Res.* **2004**, *6*, 119.
- [36] D. Friedmann, H. Hansing, D. Bahnemann, *Z. Phys. Chem.* **2007**, *221*, 329.
- [37] F. Sieland, J. Schneider, T. Lippmann, D. W. Bahnemann, in *Solar Hydrogen and Nanotechnology XI*, vol. 9935, SPIE, Bellingham, WA **2016**, pp. 21–30.
- [38] A. Sitt, F. D. Sala, G. Menagen, U. Banin, *Nano Lett.* **2009**, *9*, 3470.
- [39] G. Rainò, T. Stöferle, I. Moreels, R. Gomes, J. S. Kamal, Z. Hens, R. F. Mahr, *ACS Nano* **2011**, *5*, 4031.
- [40] J. Y. Choi, W.-W. Park, B. Park, S. Sul, O.-H. Kwon, H. Song, *ACS Catal.* **2021**, *11*, 13303.
- [41] N. J. Borys, M. J. Walter, J. Huang, D. V. Talapin, J. M. Lupton, *Science* **2010**, *330*, 1371.
- [42] K. Wu, W. E. Rodriguez-Cordoba, Z. Liu, H. Zhu, T. Lian, *ACS Nano* **2013**, *7*, 7173.
- [43] A. N. Grennell, J. K. Utterback, O. M. Pearce, M. B. Wilker, G. Dukovic, *Nano Lett.* **2017**, *17*, 3764.
- [44] L. Brus, *J. Phys. Chem.* **1986**, *90*, 2555.
- [45] G. Dukovic, M. G. Merkle, J. H. Nelson, S. M. Hughes, A. P. Alivisatos, *Adv. Mater.* **2008**, *20*, 4306.
- [46] L. Spanhel, M. Haase, H. Weller, A. Henglein, *J. Am. Chem. Soc.* **1987**, *109*, 5649.
- [47] H. Weller, M. Haase, L. Spanhel, A. Henglein, *Trends in Colloid and Interface Science II*, Springer, Berlin, Heidelberg **1988**, p. 24.
- [48] D. E. Westmoreland, R. J. Nap, F. Arcudi, I. Szeleifer, E. A. Weiss, *Chem. Commun.* **2019**, *55*, 5435.
- [49] T. J. Boyle, S. D. Bunge, T. M. Alam, G. P. Holland, T. J. Headley, G. Avilucea, *Inorg. Chem.* **2005**, *44*, 1309.
- [50] S. Jana, T. Pape, N. W. Mitzel, *Z. Naturforsch. B* **2007**, *62*, 1339.
- [51] H. Zhu, N. Song, T. Lian, *J. Am. Chem. Soc.* **2013**, *135*, 11461.
- [52] V. Chakrapani, D. Baker, P. V. Kamat, *J. Am. Chem. Soc.* **2011**, *133*, 9607.
- [53] M. C. Sekhar, K. Santhosh, J. Praveen Kumar, N. Mondal, S. Soumya, A. Samanta, *J. Phys. Chem. C* **2014**, *118*, 18481.
- [54] K. L. Chen, S. E. Mylon, M. Elimelech, *Environ. Sci. Technol.* **2006**, *40*, 1516.
- [55] J. Gregory, *Adv. Colloid Interface Sci.* **2009**, *147*, 109.
- [56] F. Otto, X. Sun, F. Schulz, C. Sanchez-Cano, N. Feliu, F. Westermeier, W. J. Parak, *Small* **2022**, *18*, 2201324.
- [57] M. J. Mulvihill, S. E. Habas, I. Jen-La Plante, J. Wan, T. Mokari, *Chem. Mater.* **2010**, *22*, 5251.
- [58] Y. Chen, L. Amirav, *Chem. Sci.* **2023**, *14*, 7512.
- [59] D. P. Morgan, D. F. Kelley, *J. Phys. Chem. C* **2020**, *124*, 8448.
- [60] G. Grimaldi, J. J. Geuchies, W. Van Der Stam, I. Du Fossé, B. Brynjarsson, N. Kirkwood, S. Kinge, L. D. Siebbeles, A. J. Houtepen, *Nano Lett.* **2019**, *19*, 3002.
- [61] M. M. Taheri, K. C. Elbert, S. Yang, B. T. Diroll, J. Park, C. B. Murray, J. B. Baxter, *J. Phys. Chem. C* **2021**, *125*, 31.
- [62] K. Wu, H. Zhu, Z. Liu, W. Rodriguez-Cordoba, T. Lian, *J. Am. Chem. Soc.* **2012**, *134*, 10337.
- [63] Y. Liu, D. A. Cullen, T. Lian, *J. Am. Chem. Soc.* **2021**, *143*, 20264.
- [64] J. H. Olshansky, T. X. Ding, Y. V. Lee, S. R. Leone, A. P. Alivisatos, *J. Am. Chem. Soc.* **2015**, *137*, 15567.
- [65] F. Schulz, G. T. Dahl, S. Besztejan, M. A. Schroer, F. Lehmkuhler, G. Grubel, T. Vossmeier, H. Lange, *Langmuir* **2016**, *32*, 7897.
- [66] F. Schulz, T. Vossmeier, N. G. Bastús, H. Weller, *Langmuir* **2013**, *29*, 9897.
- [67] F. Schulz, W. Friedrich, K. Hoppe, T. Vossmeier, H. Weller, H. Lange, *Nanoscale* **2016**, *8*, 7296.
- [68] W. M. Haynes, *CRC Handbook of Chemistry and Physics*, CRC Press, BocaRaton, FL **2014**.
- [69] W. Koppenol, J. Rush, *J. Phys. Chem.* **1987**, *91*, 4429.
- [70] W. Yao, X. Song, C. Huang, Q. Xu, Q. Wu, *Catal. Today* **2013**, *199*, 42.
- [71] N. Buehler, K. Meier, J. F. Reber, *J. Phys. Chem.* **1984**, *88*, 3261.
- [72] T. N. Das, R. E. Huie, P. Neta, *J. Phys. Chem. A* **1999**, *103*, 3581.
- [73] P. Wardman, *J. Phys. Chem. Ref. Data* **1989**, *18*, 1637.
- [74] D. A. Armstrong, R. E. Huie, W. H. Koppenol, S. V. Lymar, G. Merényi, P. Neta, B. Ruscic, D. M. Stanbury, S. Steenken, P. Wardman, *Pure Appl. Chem.* **2015**, *87*, 1139.
- [75] K. A. Brown, M. B. Wilker, M. Boehm, G. Dukovic, P. W. King, *J. Am. Chem. Soc.* **2012**, *134*, 5627.
- [76] T. A. Kandiell, R. Dillert, D. W. Bahnemann, *Photochem. Photobiol. Sci.* **2009**, *8*, 683.
- [77] A. Franceschetti, A. Zunger, *Phys. Rev. B* **2000**, *62*, R16287.
- [78] E. J. Radich, R. Dwyer, P. V. Kamat, *J. Phys. Chem. Lett.* **2011**, *2*, 2453.
- [79] T. Loučka, *J. Electroanal. Chem. Interfacial Electrochem.* **1972**, *36*, 355.
- [80] S. Chaveanghong, T. Nakamura, Y. Takagi, B. Cagnon, T. Uruga, M. Tada, Y. Iwasawa, T. Yokoyama, *Phys. Chem. Chem. Phys.* **2021**, *23*, 3866.
- [81] V. A. Sethuraman, J. W. Weidner, *Electrochim. Acta* **2010**, *55*, 5683.
- [82] M. Honkanen, M. Huuhtanen, M. Kärkkäinen, T. Kanerva, K. Lahtonen, A. Väliheikkilä, K. Kallinen, R. L. Keiski, M. Vippola, *J. Catal.* **2021**, *397*, 183.
- [83] E. P. Serjeant, B. Dempsey, *IUPAC Chemical Data Series* **1979**, *23*.
- [84] H. Nakamatsu, T. Kawai, A. Koreeda, S. Kawai, *J. Chem. Soc., Faraday Trans. 1* **1986**, *82*, 527.
- [85] P. Rao, E. Hayon, *J. Am. Chem. Soc.* **1974**, *96*, 1287.
- [86] E. Kalamaras, P. Lianos, *J. Electroanal. Chem.* **2015**, *751*, 37.
- [87] S. Morrison, T. Freund, *J. Chem. Phys.* **1967**, *47*, 1543.
- [88] Y. Maeda, A. Fujishima, K. Honda, *J. Electrochem. Soc.* **1981**, *128*, 1731.
- [89] J.-S. Lee, T. Kato, A. Fujishima, K. Honda, *Bull. Chem. Soc. Jpn.* **1984**, *57*, 1179.
- [90] P. Herrasti, L. Peter, *J. Electroanal. Chem. Interfacial Electrochem.* **1991**, *305*, 241.
- [91] R. Memming, in *Electron Transfer I*, Springer, Berlin **2005**, pp. 105–181.
- [92] R. Gao, A. Safrany, J. Rabani, *Radiat. Phys. Chem.* **2002**, *65*, 599.
- [93] Y. Nosaka, H. Sasaki, K. Norimatsu, H. Miyama, *Chem. Phys. Lett.* **1984**, *105*, 456.
- [94] N. Hykaway, W. Sears, H. Morisaki, S. R. Morrison, *J. Phys. Chem.* **1986**, *90*, 6663.
- [95] A. L. Linsebigler, G. Lu, J. T. Yates Jr, *Chem. Rev.* **1995**, *95*, 735.
- [96] J. Lilie, G. Beck, A. Henglein, *Ber. Bunsengesellsch. Phys. Chem.* **1971**, *75*, 458.
- [97] P. Adel, J. Bloh, D. Hinrichs, T. Kodanek, D. Dorfs, *Z. Phys. Chem.* **2017**, *231*, 93.



## 5.7 Incorporation strategy for organic dyes into gold nanoparticle superlattices

This publication is reprinted with permission from Shivani Kesarwani, Sabrina Juergensen, Yannic U. Staechelin, Stephanie Reich, Florian Schulz and Holger Lange, *The Journal of Chemical Physics* **2024**, 161, 044702 - published by the American Institute of Physics (AIP Publishing).<sup>289</sup> The related supporting information is reprinted in Chapter A.5.

DOI: [10.1063/5.0209021](https://doi.org/10.1063/5.0209021)

This project presents a synthesis strategy for AuNP-dye hybrids that can be assembled into superlattices. Cyanine7-amine was converted to cyanine isothiocyanate (ITC). AuNPs were ITC-functionalized before conducting a ligand exchange to thiol-terminated polystyrene (PSSH), which governs the supercrystal formation. TA measurements prove that carefully applying the dye to the AuNPs before ligand exchange is necessary to ensure strong optical interaction between AuNPs and dye molecules.

*The author of this thesis carried out the TA measurements, analyzed the TA data and contributed to the writing and editing of the manuscript.*



RESEARCH ARTICLE | JULY 22 2024

## Incorporation strategy for organic dyes into gold nanoparticle supercrystals

Special Collection: [Festschrift in honor of Louis E. Brus](#)

S. Kesarwani  ; S. Juergensen  ; Y. U. Staechelin  ; S. Reich  ; F. Schulz  ; H. Lange  



*J. Chem. Phys.* 161, 044702 (2024)

<https://doi.org/10.1063/5.0209021>



23 July 2024 07:36:22



Chemical Physics Reviews

Special Topic: Molecular Approaches  
for Spin-based Technologies

Submit Today!

# Incorporation strategy for organic dyes into gold nanoparticle supercrystals

Cite as: J. Chem. Phys. 161, 044702 (2024); doi: 10.1063/5.0209021

Submitted: 18 March 2024 • Accepted: 21 June 2024 •

Published Online: 22 July 2024



View Online



Export Citation



CrossMark

S. Kesarwani,<sup>1</sup>  S. Juergensen,<sup>2</sup>  Y. U. Staechelin,<sup>1</sup>  S. Reich,<sup>2</sup>  F. Schulz,<sup>3</sup>  and H. Lange<sup>4,5,a)</sup> 

## AFFILIATIONS

<sup>1</sup>Institut für Physikalische Chemie, Universität Hamburg, 20146 Hamburg, Germany

<sup>2</sup>Department of Physics, Freie Universität Berlin, 14195 Berlin, Germany

<sup>3</sup>Institute of Nanostructure and Solid State Physics, University of Hamburg, 22761 Hamburg, Germany

<sup>4</sup>The Hamburg Centre for Ultrafast Imaging, Universität Hamburg, 22761 Hamburg, Germany

<sup>5</sup>Department of Physics and Astronomy, Universität Potsdam, 14476 Potsdam, Germany

Note: This paper is part of the JCP Festschrift in honor of Louis E. Brus.

<sup>a)</sup>Author to whom correspondence should be addressed: [holger.lange@uni-hamburg.de](mailto:holger.lange@uni-hamburg.de)

## ABSTRACT

Ordered arrays of plasmonic nanoparticles, supercrystals can lead to the formation of plasmon-polaritons. Coupling light emitters with plasmon polaritons might allow the formation of exciton-plasmon polaritons with properties tuneable by the supercrystal design. To construct such optically active materials, the inclusion of emitters is imperative. The addition of organic dyes without affecting the periodic order of the nanocrystals is difficult, as post-formation protocols might dissolve the supercrystals, and pre-formation addition might affect the self-assembly process. Here, we present an exemplary strategy to functionalize gold nanoparticles prior to self-assembly with a cyanine isothiocyanate dye that was obtained by a straightforward reaction of the amine functionalized dye with carbon disulfide. In the second step, the nanoparticles are functionalized with a thiol-terminated polystyrene, which stabilizes the nanoparticles and governs the self-assembly process. The dye can be integrated in a quantitative fashion, and the nanoparticles can be self-assembled into supercrystals. The strategy should be applicable in general for amine functionalized dyes, which is a common modification.

Published under an exclusive license by AIP Publishing. <https://doi.org/10.1063/5.0209021>

## I. INTRODUCTION

Nanoparticle (NP) supercrystals are NP assemblies with crystalline order. The optical properties of such supercrystals are mostly determined by the interparticle interactions, which depend on the NP properties and their arrangement (interparticle distance, supercrystal geometry).<sup>1–5</sup> The assembly of plasmonic metal NPs results in the formation of plasmon polaritons, collective plasmon excitations of the entire supercrystal.<sup>6</sup> Interfacing light-emitting materials such as semiconductor NPs or fluorescent molecules with plasmon polaritons will have a strong impact on the emitter's optical states and can allow the supercrystal design tailor the emission characteristics of the entire system. The strongest interaction is expected for a guest–host configuration, where the embedded emitters share the periodicity of the plasmonic supercrystal.<sup>7</sup> However, current plasmonic supercrystals are synthesized by self-assembly from solution,

and uniform distribution of emitters into the supercrystal is not possible without a modification of the self-assembly protocol. Achieving control over the process is challenging as different parameters and forces operate across diverse lengths and time scales.<sup>8–11</sup> We developed robust protocols for a scalable and flexible plasmonic gold NP (AuNP) self-assembly.<sup>12</sup> This assembly on a liquid–liquid interface is governed by an interplay of polymer–ligand interactions and solvent evaporation kinetics. In our initial studies, we synthesized large-scale supercrystals and explored different dye solutions for potential infiltration with the molecules. We found such post-assembly infiltration to be ineffective as it dissolves the supercrystals or results in strong inhomogeneities in the dye concentration. In principle, pre-assembly functionalization of AuNPs is possible in multiple ways. Our AuNP self-assembly strategy requires polystyrene-thiol ligands (PSSH), bound to the AuNPs via the thiol end groups. Without the self-organization governing PSSH, supercrystal formation is not

possible. Substituting PSSH with dyes completely results in disordered structures or a loss of particle stability in solution. Partly functionalizing AuNPs with dyes is problematic too, as the strong affinity of the PSSH thiol endgroup to gold can drive competitive ligand replacement, removing the dye. Thus, a careful dye design and optimization of the mixed NP ligand shell are required in order to incorporate fluorescent dyes into NP supercrystals.

In this work, we present a flexible route to synthesize AuNP-dye supercrystals. We have chosen cyanine7-amine as an exemplary dye, which was converted to cyanine isothiocyanate (ITC) by reacting it with carbon disulfide. An appropriate concentration of ITC bound to AuNPs, subsequently functionalized with PSSH, allows for the assembly of the NPs in supercrystals with the ITC evenly distributed.

## II. EXPERIMENTAL SECTION

### A. Materials

Tetrachloroauric(III) acid ( $\geq 99.9\%$  trace metals basis), hexadecyltrimethylammonium bromide (CTAB,  $\geq 98\%$ ) and hexadecyltrimethylammonium chloride (CTAC,  $\geq 98\%$ ), L-ascorbic acid (reagent grade) and sodium borohydride ( $\geq 98\%$ ), and carbon disulfide ( $\text{CS}_2$ ,  $\geq 99.5\%$ ) were purchased from Sigma Aldrich (USA). Cyanine7-amine dye was purchased from Lumiprobe (Germany). Toluene ( $\geq 99.5\%$ ), tetrahydrofuran ( $\geq 99.5\%$ ), and ethanol (denat.,  $\geq 99.5\%$ ) were obtained from VWR (USA). Triethylamine ( $\text{Et}_3\text{N}$ ,  $\geq 99.5\%$ ) and diethylene glycol (DEG) (reagent grade) were obtained from Merck (Germany). Thiolated polystyrene PSSH12k:  $M_n = 11\,500\text{ g mol}^{-1}$  was purchased from Polymer Source (Canada). All reagents were used without further treatment.

### B. Synthesis

**AuNP@CTAC synthesis** AuNPs of 16, 32, and 49 nm in diameter were synthesized based on the protocol presented by Zheng *et al.*,<sup>13</sup> which was scaled up 10 times for high AuNP concentrations. The entire synthesis was carried out using ultrapure water (18.2  $\Omega$ ).

#### 1. CTAB-stabilized seeds

First, CTAB (200 mM, 5 ml) and tetrachloroauric(III) acid ( $\text{HAuCl}_4$ , 5 ml, 0.5 mM) were stirred at 27 °C. After complete mixing, sodium borohydride ( $\text{NaBH}_4$ , 600  $\mu\text{l}$ , 10 mM) was quickly injected into the mixture under rapid stirring (1000 rpm), and then the mixture was stirred at 400 rpm for 3 min. The solution turned brown and was left undisturbed for 3 h without agitation.

#### 2. First growth step

500  $\mu\text{l}$  of CTAB-stabilized seeds were mixed with a mixture of CTAC (20 ml, 200 mM) and ascorbic acid (15 ml, 100 mM) at 600 rpm, followed by a one shot injection of  $\text{HAuCl}_4$  (20 ml, 0.5 mM). After 15 min of stirring (400 rpm), the AuNPs were washed with water by centrifugation (20 000 g) three times, and the pellets were redispersed in CTAC (10 ml, 20 mM).

#### 3. Second growth step

CTAC (20 ml, 100 mM) and the desired volume of AuNP@CTAC (in 20 mM CTAC) from the first growth step were mixed. The mixture was then stirred (400 rpm) in a water bath at 30 °C, ascorbic acid (130  $\mu\text{l}$ , 100 mM) was added, and after 2 min,

the addition of  $\text{HAuCl}_4$  (20 ml, 0.5 mM) with a syringe pump at 20 ml  $\text{h}^{-1}$  was started. After the complete addition of the Au precursor, the mixture was stirred (400 rpm) for an additional 10 min at 30 °C and washed with water by centrifugation. The obtained particles were redispersed in CTAC (10 ml, 5 mM) for stability.

#### 4. Synthesis of the cyanine isothiocyanate derivative (ITC)

To synthesize the cyanine isothiocyanate derivative,  $\text{CS}_2$  (100  $\mu\text{l}$ ,  $16.5 \times 10^{-3}\text{ mol}$ ), cyanine7-amine in ethanol (2 ml, 1.4 mM), and triethylamine (40  $\mu\text{l}$ ,  $2.9 \times 10^{-4}\text{ mol}$ ) were mixed in a round bottom flask and stirred overnight at 300 rpm. Then the solvent and remaining  $\text{CS}_2$  were evaporated under reduced pressure, and the sample was dried under vacuum.

#### 5. Synthesis of ITC-bound AuNPs

1 ml of AuNPs, 16 nm ( $3.3 \times 10^{-9}\text{ M}$ ), 32 nm ( $0.29 \times 10^{-9}\text{ M}$ ), and 49 nm ( $0.12 \times 10^{-9}\text{ M}$ ) in diameter, were centrifuged (15 000 g, 20 min). Then, ITC (3 ml, 1  $\mu\text{M}$ ) in EtOH was added to the pellets, and the mixtures were stirred for 1 h. Later, ITC-bound AuNPs were centrifuged (15 000 g, 20 min), and the supernatant was used for the calculation of the number of ITC molecules per particle without any dilution.

#### 6. Self-assembly of ITC-bound AuNPs

To bind the self-assembly governing PSSH to the AuNP@ITC, ITC-bound AuNPs were mixed with 1  $\mu\text{M}$  PSSH12k in 6 ml THF and stirred for 2 h (400 rpm). The AuNP solution was then dried in a rotary evaporator, and the AuNPs (AuNP@ITC@PSSH12k) were redispersed in toluene. Afterward, the excess ligands were removed by centrifuging (15 000 g, 20 min) the AuNPs two times and washing in toluene. During each centrifugation step, 1 ml of toluene was removed. The method introduced by Dong *et al.* was used for the self-assembly of AuNP@ITC@PSSH12k.<sup>14</sup> In all experiments, 200  $\mu\text{l}$  of AuNP@ITC@PSSH12k in toluene were pipetted onto 600  $\mu\text{l}$  of diethylene glycol (DEG) in a Teflon well (an inner diameter of 1.1 cm) with a maximum volume of 1 ml. The Teflon well was covered with a glass slide to slow down the evaporation of toluene and left undisturbed overnight, after which a thin, golden film formed on the surface of the DEG phase.

### C. Instrumentation

Transmission electron microscopy (TEM) measurements were performed using a JEOL JEM-1011 microscope at an operating voltage of 100 kV.

Photoluminescence (PL) spectra were measured using an HORIBA FluoroMax-4 spectrometer. A fluorescence cuvette made of polymethyl methacrylate (PMMA) with a 1.0 cm path length was used for this purpose. The spectra were collected over a range of 680–900 nm (excitation, 680 nm; emission, 695 nm).

UV/vis measurements were carried out using a Varian Cary 50 spectrometer. Raman measurements were performed with a HORIBA XploRA with 600 gr/mm at 638 nm laser excitation. The spectra in solution were taken in a quartz cuvette (0.5 mm) at 3.1 mW laser power, the AuNP@ITC@PSSH12k crystals were measured at 0.31 mW laser power, and for the cyanine7-amine powder, 29  $\mu\text{W}$  laser power was used.

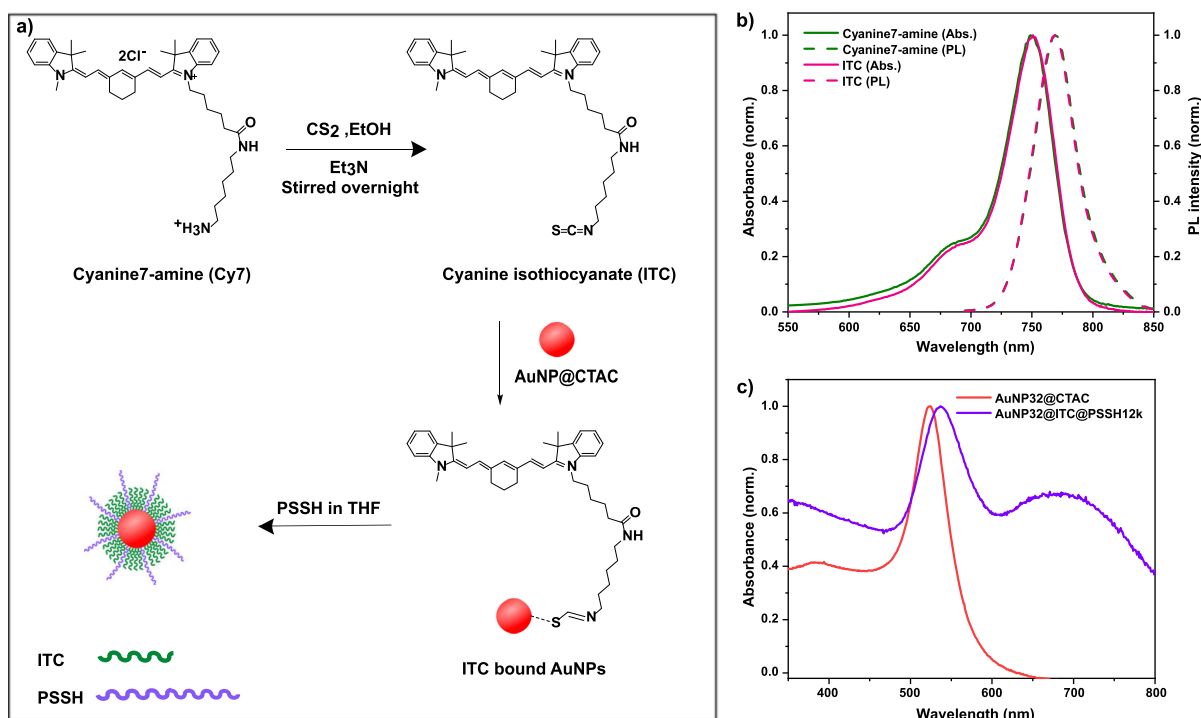


FIG. 1. (a) Schematic representation for preparing ITC-bound and PSSH-functionalized AuNPs. (b) Normalized absorption and emission spectra of cyanine7-amine and ITC, respectively. (c) Absorption spectra of 32 nm diameter AuNPs in CTAC (AuNP32@CTAC) and ITC-bound AuNPs functionalized with PSSH12k (AuNP32@ITC@PSSH12k).

Transient Absorption (TA) experiments were conducted employing a Ti:sapphire laser system (Spitfire-Ace, Spectra-Physics, 800 nm, 1 kHz, 35 fs) and a commercial TA spectrometer (HELIOS, Ultrafast Systems). The pump pulses of 715 and 400 nm were generated using an optical parametric amplifier (TOPAS Prime, Light Conversion) and second-harmonic generation in a BBO crystal, respectively. The probe pulse passed a delay stage, and the white-light continuum was generated in a CaF<sub>2</sub> crystal. The samples were placed in 2 mm cuvettes. All measurements were conducted at an excitation fluence of 150  $\mu\text{J}/\text{cm}^2$ .

### III. RESULT AND DISCUSSION

#### A. ITC-bound AuNPs synthesis

The general strategy for the synthesis of ITC-bound AuNPs, followed by further functionalization with PSSH, is displayed in Fig. 1(a). ITC is synthesized from cyanine7-amine by a straightforward reaction with carbon disulfide that converts the terminal amine to an isothiocyanate that binds much stronger to gold.<sup>15–17</sup> Since amine-functionalization of dyes is very common, this strategy can be adapted for a broad range of dyes depending on the desired optical properties (the characterization of the dye is provided as the [supplementary material](#); cf. Figs. S1–S3).

The optical properties of cyanine7-amine and ITC are summarized in Fig. 1(b). Both the absorption and PL spectra of cyanine7-amine and ITC coincide. The molecule's end group is well-separated from the part relevant for the transition dipole, and the modification of cyanine7-amine, therefore, does not alter the optical properties.

ITC then binds to AuNPs by the isothiocyanate group, thereby displacing some of the adsorbed CTAC ligands. This step was carried out in ethanol for two reasons: first, the photostability of the dye in ethanol is higher, which is important for the quantitation of bound dye. Second, the CTAC coating of the AuNP, a micellar bilayer that is hard to displace in water, is dissolved in ethanol, thus facilitating the binding of the ITC.<sup>18–21</sup> The AuNP@ITC was then centrifuged, and the supernatants were used for the quantitation of bound dye, as discussed in a later section. The pellets were reacted with PSSH in THF for stabilization and subsequent phase transfer to toluene. The PSSH coating is known to facilitate the well-ordered self-assembly of AuNPs from their dispersions in toluene.<sup>12,22</sup> With this sequential addition strategy, the maximum amount of dye was found to be bound to the AuNPs.

Figure 1(c) displays the absorption spectra of 32 nm diameter AuNPs with CTAC (AuNP32@CTAC) and the ITC-PSSH bound AuNP32 (AuNP32@ITC@PSSH12k) after washing. The strong

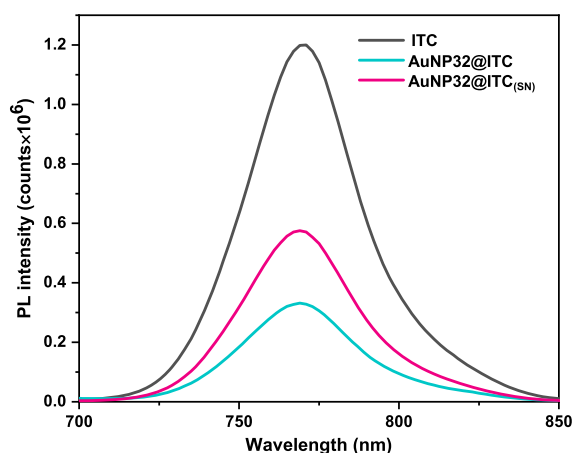


FIG. 2. PL spectra of the ITC ( $1 \times 10^{-6}$  M), AuNP32@CTAC ( $0.29 \times 10^{-9}$  M) mixed with ITC, and their respective supernatant (SN).

interaction between ITC and AuNPs broadens the ITC resonance around 700–750 nm.<sup>23</sup>

### B. ITC footprint

In the concentration range up to  $1 \times 10^{-6}$  M, the integrated ITC PL intensity scales linearly with concentration (supplementary material; cf. Fig. S4). Quantitative PL measurements thus allow the study of the ITC binding to AuNPs.<sup>24</sup> Figure 2 summarizes the general approach. When AuNP32@CTAC is added to the ITC solution, the PL is strongly quenched. To separate unbound ITC and ITC-bound AuNPs, the solutions were centrifuged, and the emission spectra of the supernatants were recorded. Then, the difference between the initial ITC PL intensity and the supernatant's PL intensity allows us to quantify the number of bound and unbound molecules. Accounting for the NP concentrations and sizes yielded the number of dye molecules per NP and the ITC footprints.

Figure 3 displays the ITC PL intensity vs the total surface area provided by the addition of different amounts of AuNPs (a) and for a constant number of AuNPs and increasing ITC concentrations (b). Different AuNP diameters were compared: 16, 32, and 49 nm. The maximum concentrations of the larger AuNPs were in a similar range (0.29 nM for 32 and 0.12 nM for 49 nm), whereas the concentration of the smaller AuNP (16 nm) was considerably higher (3.3 nM). In Fig. 3(a), it can be appreciated that the quenching behavior for the larger AuNP is very similar. The quenching of the 16 nm AuNP, however, seems to be less efficient. Based on the synthesis conditions, we assume that the stabilization of the AuNP in the intermediate steps plays a role. Because in ethanol, the CTAC molecules provide little colloidal stabilization, the stabilizing effect of dye adsorption becomes crucial. In the higher concentrated 16 nm AuNP sample, the number of dye/AuNP was lower (about 300 compared to  $\gg 3000$  for the larger AuNP). As a consequence, more agglomeration/aggregation of AuNP occurred in the ethanol phase, making the surface less available for the dye to be bound. Apart from

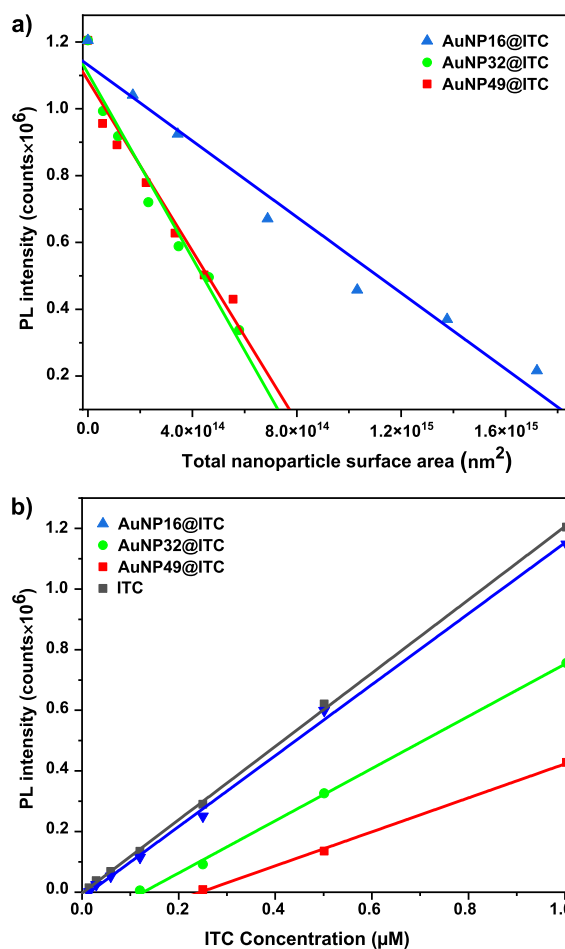


FIG. 3. SN PL intensity (measured at 773 nm) from a solution comprising (a)  $1 \times 10^{-6}$  M ITC vs provided total AuNP surface area to the solution. (b) ITC of varying concentrations from  $1 \times 10^{-6}$  M to  $0.02 \times 10^{-6}$  M and  $8.7 \times 10^{10}$  numbers of AuNPs.

this effect, a more efficient quenching/dye-AuNP interaction with increasing AuNP size might also play a role. In Fig. 3(b), the different quenching behaviors for different particle sizes are obvious. Since quenching is strongly distance dependent, the most efficient quenching takes place for bound dye. Since the surface area scales with particle size at a constant particle number, the quenching is more efficient for larger AuNPs. The observed linear dependencies indicate the binding of ITC to AuNPs. To quantify the number of bound ITC without possible quenching effects, we removed the AuNP@ITC by centrifugation and quantified the unbound ITC in the supernatants. For the different AuNP sizes and at different AuNP concentrations, we consistently obtain an ITC footprint of around  $1 \text{ nm}^{-2}$  (supplementary material; cf. Figs. S5–S8, cf. Tables T1 and T2).<sup>25</sup>

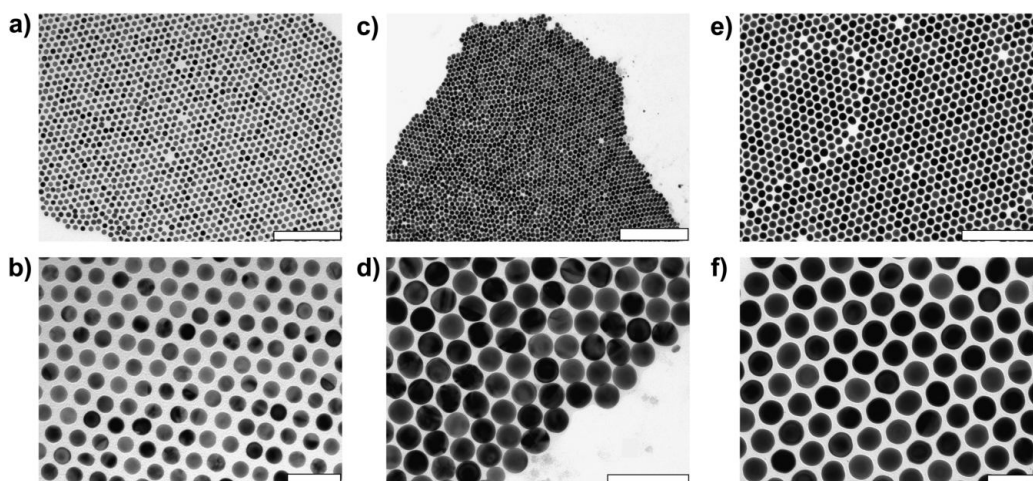


FIG. 4. Exemplary TEM images of self-assembled films: (a) and (b) AuNP16@ITC@PSSH12k with 200 and 50 nm scale bars. (c) and (d) AuNP32@ITC@PSSH12k with 500 and 100 nm scale bars. (e) and (f) AuNP49@ITC@PSSH12k with 500 and 100 nm scale bars, respectively.

### C. Supercrystal formation

The balance of ITC, PSSH, and AuNP concentrations is crucial for achieving well-defined AuNP supercrystal formation. An excessive amount of ITC may lead to overcrowding on the nanoparticle surface, hindering the assembly process by reducing the available binding sites for incoming PSSH, which might result in the agglomeration of the NPs. Low PSSH concentrations result in insufficient NP stabilization. Figures 4(a)–4(f) display exemplary TEM images of films assembled from AuNP@ITC@PSSH12k (16, 32, and 49 nm). For the employed identical amounts of ITC ( $1 \times 10^{-6}$  M) and PSSH12k ( $1 \times 10^{-6}$  M), varying film formation behaviors are observed. In the example images, AuNP32 demonstrates a relatively low far order, whereas AuNP16 and AuNP49 form larger ordered films with a higher density of defects. This variation in film formation highlights the importance of parameter optimization, where we recently presented guidelines for plain AuNPs.<sup>12,26</sup>

The potential of homogeneous film formation can be appreciated for all AuNP sizes. Periodic order is observed, yet the high density of defects and low long-range order in comparison to plain AuNP films imply that the utilized concentrations have to be further optimized.<sup>12,26</sup>

To further investigate the presence of ITC on the PSSH-functionalized AuNPs, we used the AuNP32@ITC@PSSH12k sample as an exemplary specimen for Raman spectroscopy experiments. Figure 5(a) displays the Raman spectra of cyanine7-amine and PSSH12k in powder form, as well as AuNP32@PSSH12k and AuNP32@ITC@PSSH12k in solution. Cyanine7-amine features vibrations that are not present in the polymer, as indicated by the green bars in Fig. 5(a). The presence of the corresponding Raman bands in the AuNP32@ITC@PSSH12k spectra and the absence of the Raman bands in the AuNP32@PSSH12k spectra confirm the presence of ITC after PSSH functionalization.

Exemplary Raman measurements on different positions of AuNP32@PSSH12k and AuNP32@ITC@PSSH12k supercrystals, with varying amounts of layer numbers, are shown in Figs. 5(b) and 5(c). As expected, the AuNP32@PSSH12k crystal in Fig. 5(b) shows, independent of the position (layer number), only the established PSSH vibrations with the aromatic ring-breathing ( $1000 \text{ cm}^{-1}$ ) and the in-plane CH deformation ( $1029 \text{ cm}^{-1}$ ) modes, as well as a broad fluorescence background that belongs to the AuNPs.<sup>27–29</sup> The Raman measurements on the AuNP32@ITC@PSSH12k supercrystal are depicted in Fig. 5(c). It shows across the film additional Raman modes between  $1100$  and  $1750 \text{ cm}^{-1}$ , which belong to the Raman signal of the cyanine7-amine. From these measurements, we can clearly confirm that the dye, equivalent to the measurements in solution, is present in the supercrystal. However, based on the Raman experiment, we cannot differentiate if the dye is bound to the gold nanoparticles or only physisorbed to the PSSH ligand brush. Thus, we extended the spectral range for the film assembled from AuNP32@ITC@PSSH12k up to  $5000 \text{ cm}^{-1}$  to monitor the PL of ITC, Fig. 5(d). Comparing the measurements of the AuNP32@ITC@PSSH12k supercrystal and the dye as powder shows a strong quenching of the PL of dye around  $3800 \text{ cm}^{-1}$  in the supercrystals, indicating that the ITC is bound to the AuNPs and, therefore, also incorporated into the supercrystal. If the dye was only absorbed to the crystal top, the PSSH prevented a quenching of the PL by AuNPs. Since the plasmonic properties of the AuNP-supercrystals depend strongly on the number of layers,<sup>6,29</sup> the incorporation and homogeneous distribution of the dye throughout the supercrystals are crucial. This is hard to achieve with post-assembly strategies.

### D. Dynamic studies

To explore the feasibility of the ITC-bound AuNPs for dynamic studies, we conducted TA experiments. Optical excitation of AuNPs

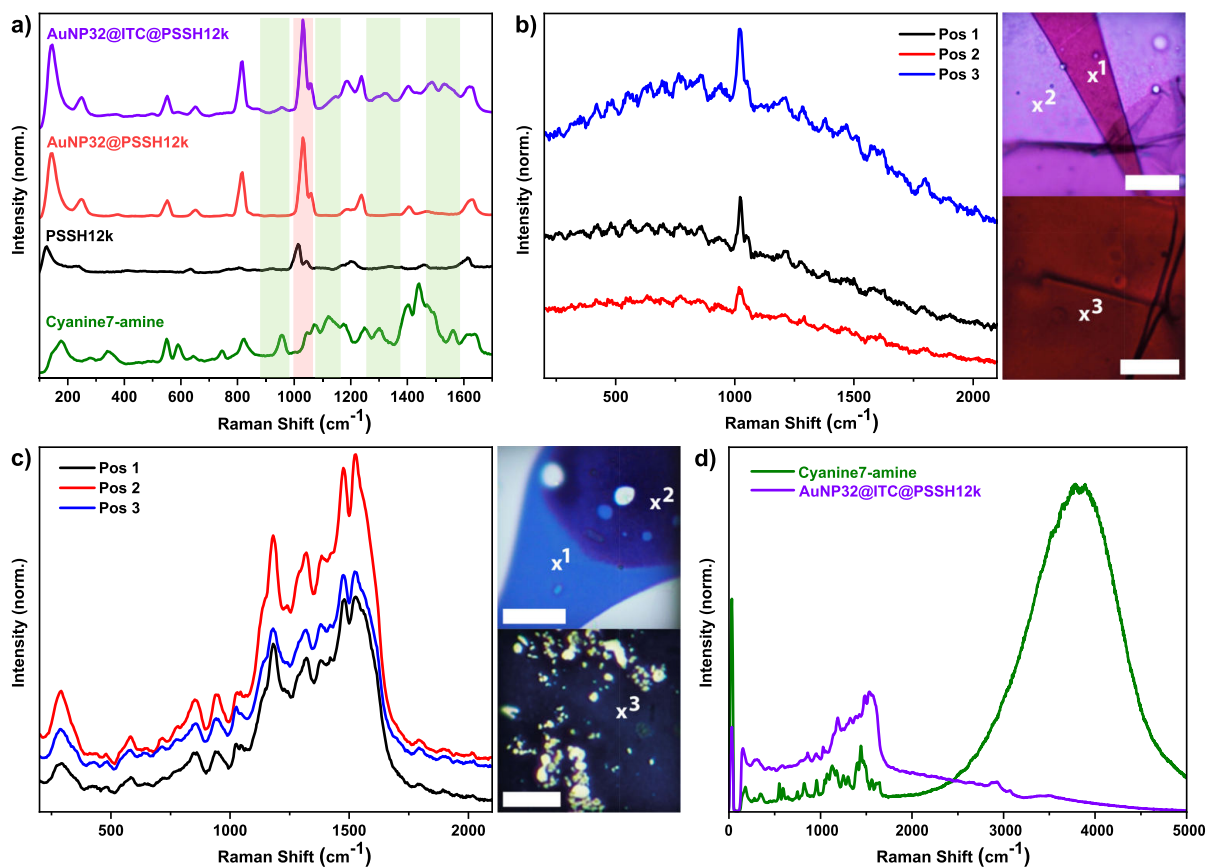


**FIG. 5.** (a) Raman spectra of cyanine7-amine, PSSH12k, AuNP32@PSSH12k, and AuNP32@ITC@PSSH12k, respectively. The green bars highlight specific dye-related vibrations; the characteristic Raman bands for PSSH are highlighted in red. (b) and (c) Transmission microscope images and Raman spectra from AuNP32@PSSH12k and AuNP32@ITC@PSSH12k supercrystals, respectively, measured on different layer thicknesses as labeled in the microscope images. The scale bars of the microscopic images are 10  $\mu\text{m}$  each. (d) Raman spectra of the cyanine7-amine dye and the AuNP32@ITC@PSSH12k crystal. The spectral range was chosen such that the PL from the cyanine7-amine is visible in the spectra. The strong quenching of the ITC PL around 3800  $\text{cm}^{-1}$  indicates that the ITC is bound to the AuNPs.

leads to a hot electron distribution, which effectively broadens the plasmon absorption. In TA, this can be observed as a bleach feature around the plasmon resonance accompanied by two positive absorption bands.<sup>30</sup> The thermalization of the hot electron distribution leads to a picosecond component in the bleach recovery dynamics. Heat transfer to the environment can be observed on a timescale of hundreds of picoseconds to some nanoseconds.<sup>31</sup>

Figure 6 compares the TA spectra of ITC, bare AuNP32@CTAC, and hybrid AuNP32@ITC@PSSH12k after excitation at 715 nm at different delay times. The TA spectra of the hybrid cannot be explained by the superposition of the bare AuNPs and ITC. In the hybrids, an additional bleach feature at longer probe wavelengths is observed, which red-shifts with increasing delay time. On the timescale of electron–phonon coupling, both the LSPR bleach feature of the hybrids as well as the new, red-shifted bleach

feature show similar bleach recovery dynamics, suggesting that the fast dynamics of the red-shifted feature are mainly governed by the evolution of the electronic temperature in the AuNP.<sup>32</sup> However, we find that for the bare AuNPs, complete bleach recovery is obtained after a few nanoseconds, whereas for the hybrid structures, long-lived bleach components are observed. This demonstrates that the strong gold–dye interaction leads to new, mixed electronic states and that energy is not solely dissipated quickly by Ohmic damping.

When mixing the unmodified dye (cyanine7-amine) with previously functionalized AuNP20@PSSH12k, we find that the TA spectra resemble the sum of both components (supplementary material, cf. Fig. S9), stressing the need to apply the dye to the AuNPs prior to the functionalization to PSSH for strong optical interaction of AuNPs and dye.

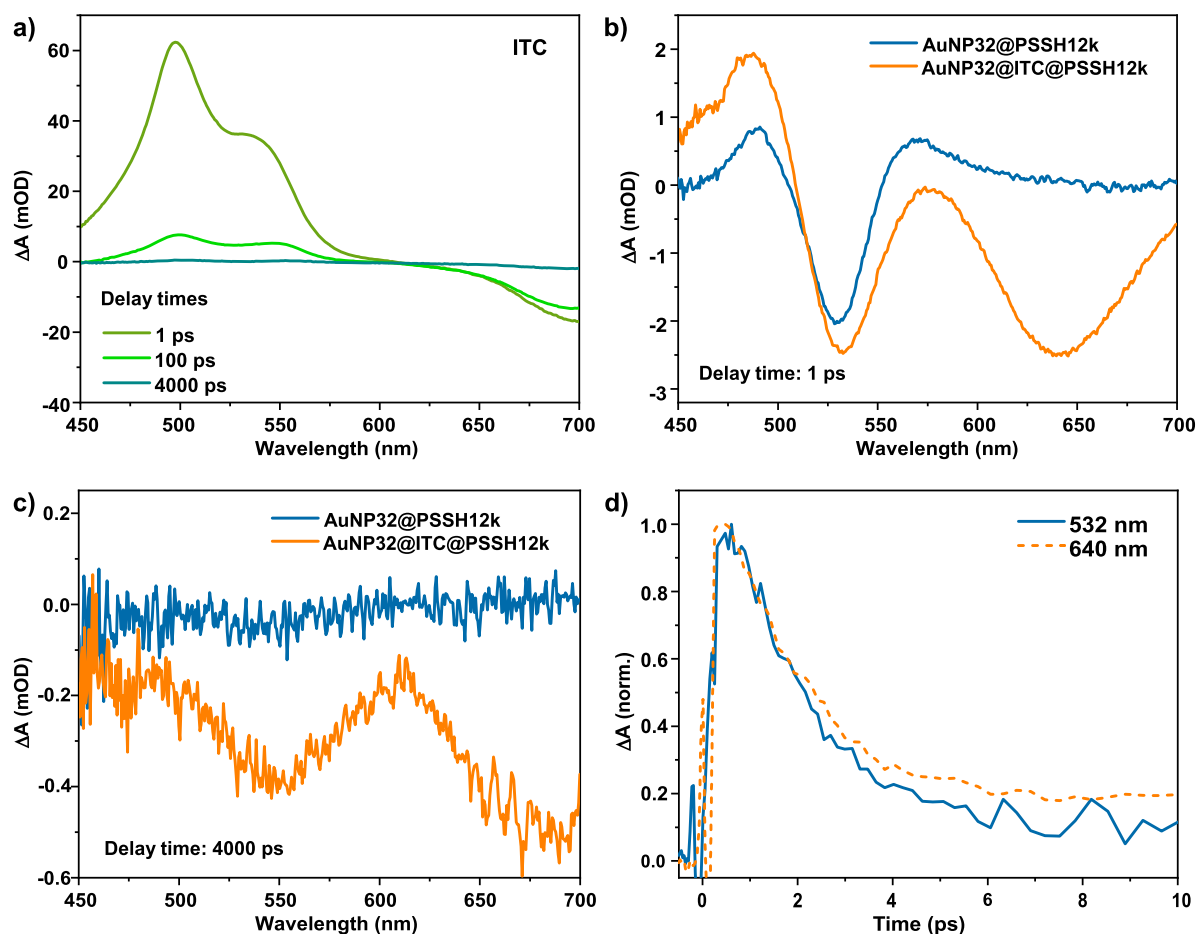


FIG. 6. (a) TA spectra of ITC after 715 nm excitation. (b) and (c) TA spectra of AuNP32@PSSH and AuNP32@ITC@PSSH12k under the same excitation conditions. (d) TA traces of AuNP32@ITC@PSSH12k after 715 nm excitation, probed at 532 and 640 nm.

#### IV. CONCLUSIONS

We have presented a strategy to incorporate an organic dye into AuNP supercrystals. The strategy employs dye modification with gold-binding isothiocyanate and further functionalization with assembly governing PSSH. We demonstrated quantitative control on the number of dye molecules per AuNP and the uniform dye distribution in assembled NP films. TA studies show significant changes in the dynamics of the combined material compared to the individual components, pointing toward a magnitude of strong emitter-supercrystal interactions. In principle, the dye modification approach is applicable to a broad range of commercial organic dyes, making it very flexible. As examples, the strong coupling between surface lattice resonances and Rhodamine 6G excitons observed by Rodriguez and co-workers could be enhanced with more strongly coupled plasmon-exciton-polaritons.<sup>33</sup> Using the dense supercrystals

in the context of long-range collective dipole-dipole interactions, reported by the Odom group, could effectively reduce the system dimensionality and tailor effective polariton stimulated emission.<sup>34,35</sup> However, our results also highlight the need for further parameter optimization, particularly regarding the size and concentrations of the components involved, such as AuNPs, dye, and PSSH. Fine-tuning these parameters will enhance the homogeneity and size of the hybrid supercrystals.

#### SUPPLEMENTARY MATERIAL

See the [supplementary material](#) for additional methodological details of material synthesis and characterization, as well as a complete tabulation of measured and calculated spectra and PL studies for 16 and 49 nm AuNPs.



## ACKNOWLEDGMENTS

This work was supported by the Deutsche Forschungsgemeinschaft (DFG) under Grant No. EXC 2056, Project ID 390715994, Project ID 504656879, and Project ID 408076438.

## AUTHOR DECLARATIONS

## Conflict of Interest

The authors have no conflicts to disclose.

## Author Contributions

**S. Kesarwani:** Conceptualization (equal); Data curation (lead); Visualization (lead); Writing – original draft (lead); Writing – review & editing (equal). **S. Juergensen:** Data curation (supporting); Writing – original draft (supporting); Writing – review & editing (supporting). **Y. U. Staechelin:** Data curation (supporting); Writing – review & editing (supporting). **S. Reich:** Conceptualization (supporting); Writing – review & editing (supporting). **F. Schulz:** Conceptualization (equal); Writing – original draft (supporting); Writing – review & editing (equal). **H. Lange:** Conceptualization (equal); Funding acquisition (lead); Writing – review & editing (equal).

## DATA AVAILABILITY

The data that supports the findings of this study are available within the article and its [supplementary material](#).

## REFERENCES

- 1 E. B. Barros, B. G. Vieira, N. S. Mueller, and S. Reich, “Plasmon polaritons in nanoparticle supercrystals: Microscopic quantum theory beyond the dipole approximation,” *Phys. Rev. B* **104**, 035403 (2021).
- 2 J. Kang, Z. M. Sherman, D. L. Conrad, H. S. Crory, M. N. Dominguez, S. A. Valenzuela, E. V. Anslin, T. M. Truskett, and D. J. Milliron, “Structural control of plasmon resonance in molecularly linked metal oxide nanocrystal gel assemblies,” *ACS Nano* **17**(23), 24218–24226 (2023).
- 3 A. M. Green, W. J. Chang, Z. M. Sherman, Z. Sakotic, K. Kim, D. Wasserman, D. J. Milliron, and T. M. Truskett, “Structural order and plasmonic response of nanoparticle monolayers,” *ACS Photonics* **11**, 1280 (2024).
- 4 N. J. Greybush, I. Liberal, L. Malassis, J. M. Kikkawa, N. Engheta, C. B. Murray, and C. R. Kagan, “Plasmon resonances in self-assembled two-dimensional Au nanocrystal metamolecules,” *ACS Nano* **11**(3), 2917–2927 (2017).
- 5 M. Brust, D. Bethell, C. J. Kiely, and D. J. Schiffrin, “Self-assembled gold nanoparticle thin films with nonmetallic optical and electronic properties,” *Langmuir* **14**(19), 5425–5429 (1998).
- 6 N. S. Mueller, Y. Okamura, B. G. M. Vieira, S. Juergensen, H. Lange, E. B. Barros, F. Schulz, and S. Reich, “Deep strong light–matter coupling in plasmonic nanoparticle crystals,” *Nature* **583**, 780–784 (2020).
- 7 J.-H. Song, T. Atay, S. Shi, H. Urabe, and A. V. Nurmikko, “Large enhancement of fluorescence efficiency from CdSe/ZnS quantum dots induced by resonant coupling to spatially controlled surface plasmons,” *Nano Lett.* **5**, 1557–1561 (2005).
- 8 B. S. Kim, L. Avila, L. E. Brus, and I. P. Herman, “Organic ligand and solvent kinetics during the assembly of CdSe nanocrystal arrays using infrared attenuated total reflection,” *Appl. Phys. Lett.* **76**, 3715–3717 (2000).
- 9 A. J. Hallock, P. L. Redmond, and L. E. Brus, “Optical forces between metallic particles,” *Proc. Natl. Acad. Sci. U. S. A.* **102**, 1280–1284 (2005).
- 10 Q. Li, U. Jonas, X. Zhao, and M. Kappl, “The forces at work in colloidal self-assembly: A review on fundamental interactions between colloidal particles,” *Asia-Pac. J. Chem. Eng.* **3**(3), 255–268 (2008).
- 11 N. Vogel, M. Retsch, C.-A. Fustin, A. Del Campo, and U. Jonas, “Advances in colloidal assembly: The design of structure and hierarchy in two and three dimensions,” *Chem. Rev.* **115**(13), 6265–6311 (2015).
- 12 F. Schulz, O. Pavelka, F. Lehmkuhler, F. Westermeier, Y. Okamura, N. S. Mueller, S. Reich, and H. Lange, “Structural order in plasmonic superlattices,” *Nat. Commun.* **11**(1), 3821 (2020).
- 13 Y. Zheng, X. Zhong, Z. Li, and Y. Xia, “Successive, seed-mediated growth for the synthesis of single-crystal gold nanospheres with uniform diameters controlled in the range of 5–150 nm,” *Part. Part. Syst. Charact.* **31**(2), 266–273 (2014).
- 14 A. Dong, J. Chen, P. M. Vora, J. M. Kikkawa, and C. B. Murray, “Binary nanocrystal superlattice membranes self-assembled at the liquid–air interface,” *Nature* **466**, 474–477 (2010).
- 15 X. Qian, S. R. Emory, and S. Nie, “Anchoring molecular chromophores to colloidal gold nanocrystals: Surface-enhanced Raman evidence for strong electronic coupling and irreversible structural locking,” *J. Am. Chem. Soc.* **134**(4), 2000–2003 (2012).
- 16 C.-Y. Lin, C.-H. Liu, and W.-L. Tseng, “Fluorescein isothiocyanate-capped gold nanoparticles for fluorescent detection of reactive oxygen species based on thiol oxidation and their application for sensing glucose in serum,” *Anal. Methods* **2**(11), 1810–1815 (2010).
- 17 I. Fratoddi, A. Cartoni, I. Venditti, D. Catone, P. O’Keeffe, A. Paladini, F. Toschi, S. Turchini, F. Sciubba, G. Testa *et al.*, “Gold nanoparticles functionalized by rhodamine B isothiocyanate: A new tool to control plasmonic effects,” *J. Colloid Interface Sci.* **513**, 10–19 (2018).
- 18 F. Schulz, W. Friedrich, K. Hoppe, T. Vossmeier, H. Weller, and H. Lange, “Effective pegylation of gold nanorods,” *Nanoscale* **8**(13), 7296–7308 (2016).
- 19 C. Kinnear, H. Dietsch, M. J. Clift, C. Endes, B. Rothen-Rutishauser, and A. Petri-Fink, “Gold nanorods: Controlling their surface chemistry and complete detoxification by a two-step place exchange,” *Angew. Chem.* **125**, 1988 (2013).
- 20 M. J. Hore, X. Ye, J. Ford, Y. Gao, J. Fei, Q. Wu, S. J. Rowan, R. J. Composto, C. B. Murray, and B. Hammouda, “Probing the structure, composition, and spatial distribution of ligands on gold nanorods,” *Nano Lett.* **15**(9), 5730–5738 (2015).
- 21 S. Gomez-Grana, F. Hubert, F. Testard, A. Guerrero-Martinez, I. Grillo, L. M. Liz-Marzan, and O. Spalla, “Surfactant (bi)layers on gold nanorods,” *Langmuir* **28**(2), 1453–1459 (2012).
- 22 F. Schulz, S. Tober, and H. Lange, “Size-dependent phase transfer functionalization of gold nanoparticles to promote well-ordered self-assembly,” *Langmuir* **33**(50), 14437–14444 (2017).
- 23 F. Stete, W. Koopman, and M. Bargheer, “Signatures of strong coupling on nanoparticles: Revealing absorption anticrossing by tuning the dielectric environment,” *ACS Photonics* **4**, 1669–1676 (2017).
- 24 K. G. Thomas and P. V. Kamat, “Chromophore-functionalized gold nanoparticles,” *Acc. Chem. Res.* **36**, 888–898 (2003).
- 25 A. Vujacic, V. Vasic, M. Dramicanin, S. P. Sovilj, N. Bibic, S. Milonjic, and V. Vodnik, “Fluorescence quenching of 5,5’-Disulfopropyl-3,3’-dichlorothiacyanine dye adsorbed on gold nanoparticles,” *J. Phys. Chem. C* **117**, 6567–6577 (2013).
- 26 F. Schulz and H. Lange, “Optimizing interparticle gaps in large-scale gold nanoparticle supercrystals for flexible light–matter coupling,” *Adv. Opt. Mater.* **10**, 2202064 (2022).
- 27 B. Jasse, R. Chao, and J. Koenig, “Laser Raman scattering in uniaxially oriented atactic polystyrene,” *J. Polym. Sci., Polym. Phys. Ed.* **16**(12), 2157–2169 (1978).
- 28 C. Liang and S. Krimm, “Infrared spectra of high polymers. VI. Polystyrene,” *J. Polym. Sci.* **27**(115), 241–254 (1958).
- 29 N. S. Mueller, E. Pitzner, Y. Okamura, G. Gordeev, P. Kusch, H. Lange, J. Heberle, F. Schulz, and S. Reich, “Surface-enhanced Raman scattering

and surface-enhanced infrared absorption by plasmon polaritons in three-dimensional nanoparticle supercrystals," *ACS Nano* **15**(3), 5523–5533 (2021).

<sup>30</sup>Y. U. Staechelin, D. Hoening, F. Schulz, and H. Lange, "Size-dependent electron-phonon coupling in monocrystalline gold nanoparticles," *ACS Photonics* **8**, 752–757 (2021).

<sup>31</sup>G. V. Hartland, "Optical studies of dynamics in noble metal nanostructures," *Chem. Rev.* **111**, 3858–3887 (2011).

<sup>32</sup>F. Stete, M. Bargheer, and W. Koopman, "Ultrafast dynamics in plasmon-exciton core-shell systems: The role of heat," *Nanoscale* **15**(40), 16307–16313 (2023).

<sup>33</sup>S. Rodriguez and J. G. Rivas, "Surface lattice resonances strongly coupled to rhodamine 6G excitons: Tuning the plasmon-exciton-polariton mass and composition," *Opt. Express* **21**(22), 27411–27421 (2013).

<sup>34</sup>A. D. Sample, J. Guan, J. Hu, T. Reese, C. R. Cherqui, J.-E. Park, F. Freire-Fernández, R. D. Schaller, G. C. Schatz, and T. W. Odom, "Strong coupling between plasmons and molecular excitons in metal-organic frameworks," *Nano Lett.* **21**(18), 7775–7780 (2021).

<sup>35</sup>A. K. Boddeti, Y. Wang, X. G. Juarez, A. Boltasseva, T. W. Odom, V. Shalaev, H. Alaeian, and Z. Jacob, "Reducing effective system dimensionality with long-range collective dipole-dipole interactions," *Phys. Rev. Lett.* **132**(17), 173803 (2024).

## 6. Unpublished results

### 6.1 Terahertz-induced Stark effect in CdSe nanoplatelets

Applying an electric field to a semiconductor leads to a change in the energy levels of its charge carriers. This, in turn, leads to a change in the energies of both the valence and conduction bands, effectively altering the band gap energy. This phenomenon is referred to as the Stark effect. High static electric fields may cause a dielectric breakdown. Electric fields of laser pulses, having much lower duty cycles, circumvent this problem. If the applied electric field is provided by sub-band-gap photons, the term optical Stark effect (OSE) is used. Semiconducting nanomaterials show pronounced Stark shifts (quantum confined Stark effect (QCSE)).<sup>290–292</sup> Depending on the nanomaterials size, shape and composition, the band edge absorption might shift to either higher or lower photon energies.<sup>293</sup> The effect is used in electro-optical modulators<sup>294</sup> and to study the properties of excitons in nanomaterials.<sup>295,296</sup> The Franz-Keldysh effect describes the modification of the absorption edge of semiconductors under an applied electric field. In nanostructures, it is known to broaden excitonic lines.<sup>297</sup> Laser pulses allow inducing ultrafast changes in the absorption spectra of nanomaterials. THz pulses are especially useful since the low photon energy prevents both damaging of the sample as well as optical excitation *via* multiphoton absorption.

The optical properties of two-dimensional nanoplatelets have been described in Chapter 4.2. Achtstein *et al.* conducted static electroabsorption measurements on CdSe NCs of different geometries and could show that the Stark effect-induced changes in absorption in nanoplatelets are more than ten times larger than in QDs.<sup>298</sup> OSE in CdSe nanoplatelets was reported with mostly optical or NIR driving pulses with photon energies below the band gap,<sup>295,299</sup> although Diroll recently expanded to the mid-IR region.<sup>300</sup> THz-driven Stark effect on colloidal Cd-based NCs was first reported by Hoffmann *et al.* in 2010.<sup>301</sup> Pein *et al.* employed lithographic gold structures for THz field enhancement in experiments on QDs.<sup>302,303</sup> Recently, Gollner *et al.* reported transmission changes of up to 15 % in CdSe-CdS core-shell QDs under illumination with intense THz radiation.<sup>304</sup>

So far, the THz-induced Stark effect in Cd-based nanoplatelets has not been studied, although it can be expected that optical changes can be observed at relatively low THz field strengths. Here, measurements of the THz-induced Stark effect in 3 monolayer (ML) CdSe nanoplatelets are presented and compared to OSE measurements with vis and NIR pump pulses.

### Materials and experimental methods

The studied 3 ML CdSe nanoplatelets were synthesized and provided by Julia Funk (Weller Research Group, Institute of Physical Chemistry, Universität Hamburg).

The sample was synthesized *via* a one-pot approach. 1-Octadecen, oleic acid, cadmium oxide, acetic acid and selenium were mixed and heated to 240° C. The reaction was terminated after 20 minutes and the nanoplatelets were purified *via* centrifugation with n-hexane and ethanol.<sup>305</sup> Figure 6.1 shows a TEM image and the absorption spectrum of the sample. The light hole absorption peak is at 434 nm, the heavy hole absorption peak is at 462 nm. At 509 nm, a third absorption feature is observed, which probably stems from QDs, that are produced during the synthesis as a by-product. For the TPOP measurements, the sample was dropcasted onto a quartz substrate. The measurements with vis and NIR pump pulses were conducted with the sample in solution in 2 mm thick cuvettes.

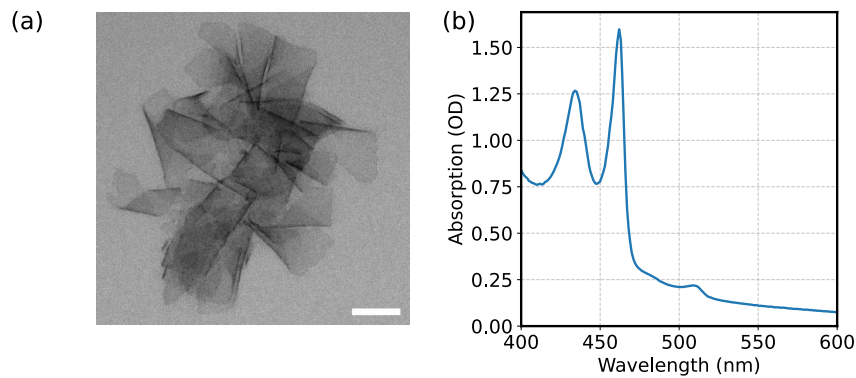


**Figure 6.1:** (a) TEM image of the studied 3 ML CdSe nanoplatelets. The scale bar corresponds to 50 nm. (b) Absorption spectrum of the sample.

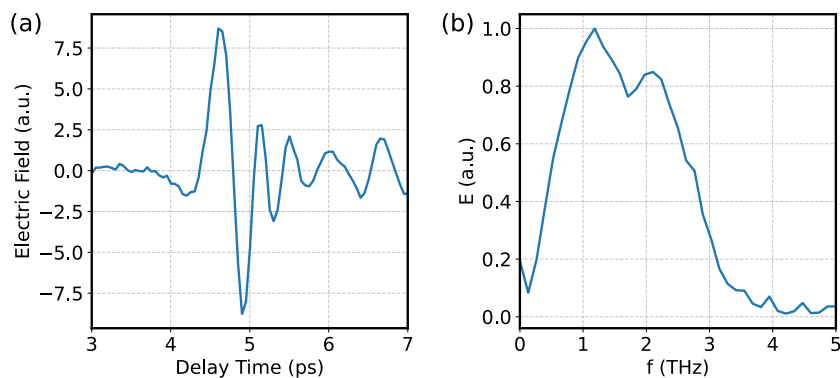


**Figure 6.2:** (a) EOS timetrace of the employed THz pulse. (b) THz spectrum obtained by Fourier transformation of the EOS timetrace.

For the TPOP setup, a THz source was installed into the pump beam path of the commercial TA setup also used in other studies presented in this thesis (*HELIOS*, *Ultrafast Instruments*). A calcium fluoride crystal was used to generate the probing white-light, which spectrally

### 6.1. Terahertz-induced Stark effect in CdSe nanoplatelets

covered both the heavy hole and light hole transition of the nanoplatelets. A commercial spintronic THz emitter (*T-Spin2*, *TeraSpinTec*) was pumped with 2.6 mJ, 800 nm, 35 fs pulses, yielding a THz spectrum with a peak intensity at 1.2 THz and a spectral bandwidth of 2.4 THz (FWHM) (*cf.* Figure 6.2). An ITO-coated THz-visible broadband beamsplitter in combination with a Teflon disk was used to separate the THz beam from the 800 nm beam. The THz beam was focused to the sample position using a gold-coated OAP with a reflective focal length of 50.8 mm. The white-light probe beam was spatially overlaid with the THz beam through a centered hole in the OAP. The ITO beamsplitter reflects minor parts of the 800 nm beam. When removing the Teflon disk, this 800 nm residue is focused by the OAP onto the sample. Its intensity is high enough to optically excite the nanoplatelets and conduct 800 nm-pump-optical-probe experiments, that give much higher contrast than the TPOP experiment. This can be used to align the spatio-temporal overlap of the THz pump and optical probe beam and ensure the sample is placed in focus. When reinserting the 1 mm thick Teflon disk, the temporal overlap shifts by 4-5 ps. The THz pulse energy  $E_{pulse}$  was measured using a pyroelectric detector (*MPY-RS*, *WiredSense*). The THz focal radius  $\omega_0$  ( $1/e^2$  radius) was measured using the knife-edge technique. The pulse energy was 230 nJ, and the focal radius was 1.5 mm. The peak electric field can be calculated from<sup>306</sup>

$$E_{peak} = \sqrt{2Z_0 I_0}, \quad (6.1)$$

where  $Z_0$  is the impedance of free space ( $Z_0 \approx 376.730 \Omega$ ) and  $I_0$  is the peak intensity for Gaussian pulses

$$I_0 = \frac{2F_0}{\Delta t} \sqrt{\frac{\ln(2)}{\pi}} \approx \frac{0.94F_0}{\Delta t}. \quad (6.2)$$

$\Delta t$  is the pulse duration, which is approximately the inverse of the center THz frequency.  $F_0$  is given by

$$F_0 = \frac{2E_{pulse}}{\pi\omega_0^2}. \quad (6.3)$$

For the TPOP experiments shown, the peak THz electric field was 86 kV/cm. Due to dielectric screening, the actual electric field received by the nanoplatelets will be smaller.<sup>304</sup>

For the vis-pump and NIR-pump experiments, an OPA (*TOPAS-PRIME*, *Light Conversion*) was used to generate the 720 nm and 1300 nm pump beams. The spot sizes of the pump beams were measured using the knife-edge technique. A variable ND filter was used to adjust the pump beam fluences.

## Results and discussion

Figure 6.3 shows the THz-induced differential absorption of 3 ML CdSe nanoplatelets. A GSB of the lowest-energy excitonic absorption feature, accompanied by two PIA features at both the high and low energy side of the GSB is observed. In the temporal TPOP trace, two maxima separated by a few hundred femtoseconds are found. Around 509 nm, where the linear absorption spectrum shows a peak that can not be assigned to any transition in the nanoplatelets, no differential absorption is observed, hence this absorption feature can safely

be ignored for the following discussion. Figure 6.4 shows the EOS signal of the employed THz pump pulse. The change in absorption of the nanoplatelets follows the THz intensity dynamics, which is calculated as the square of the EOS signal. For comparison, TA of the sample was measured with an excitation wavelength of 400 nm. Optical excitation leads to GSB and PIA features in the same spectral region as observed in the TPOP experiment. However, the GSB is much more long-lived in the TA experiment, as expected for the excitation of electrons above the band gap. Comparison of the measured dynamics with the EOS and TA signal confirms that the experimental contrast is induced by the THz electric field intensity and not optically (*e.g.* by multiphoton absorption or leaking 800 nm photons from THz sources driving pulse).

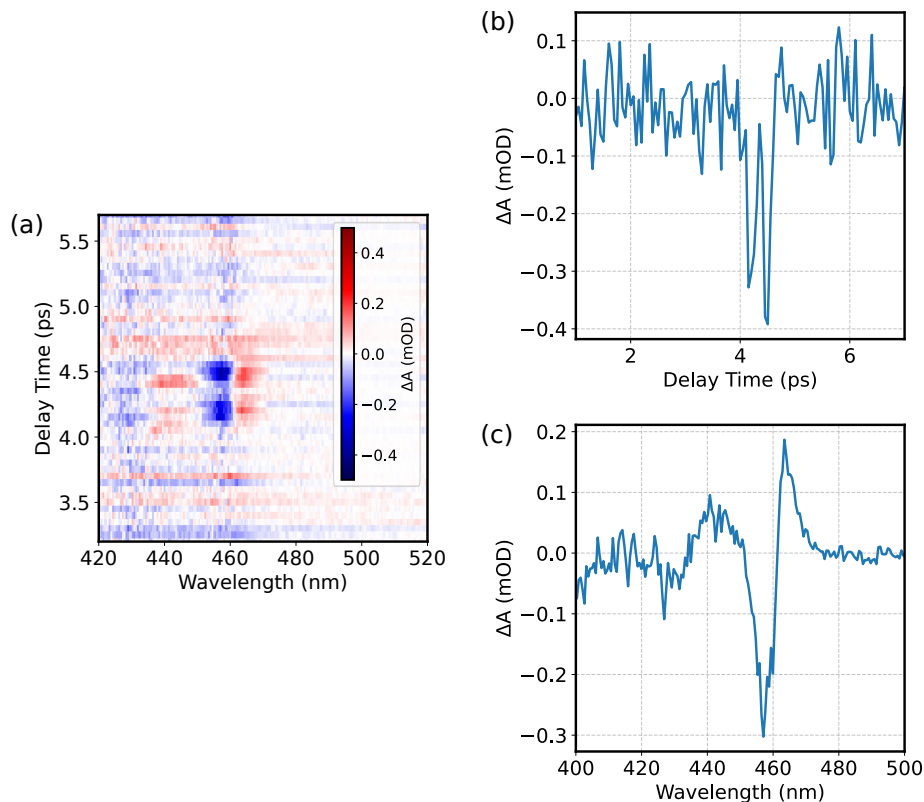


**Figure 6.3:** TPOP data of 3 ML CdSe nanoplatelets. (a) TPOP-map. (b) TPOP time trace at the probe wavelength of maximum signal (457 nm). (c) Differential TPOP spectrum at the delay time of maximum signal (4.42 ps).

For comparison, measurements with a sub-band-gap visible (720 nm) and NIR pump (1300 nm) pulse were conducted. Figure 6.5 shows the obtained differential spectra at the temporal overlap of pump and probe pulse as well as the differential spectra at 15 ps delay. At visible and NIR photon energies, multiple photon absorption can lead to the excitation of charge carriers above the band gap. For the visible excitation, this leads to a resolvable long-lasting GSB of the heavy hole absorption feature at a pump fluence of 460  $\mu\text{J}/\text{cm}^2$  and higher. Figure 6.5(e) shows how this GSB feature's intensity depends on the employed pump fluence. A linear dependency is usually observed for one-photon

### 6.1. Terahertz-induced Stark effect in CdSe nanoplatelets

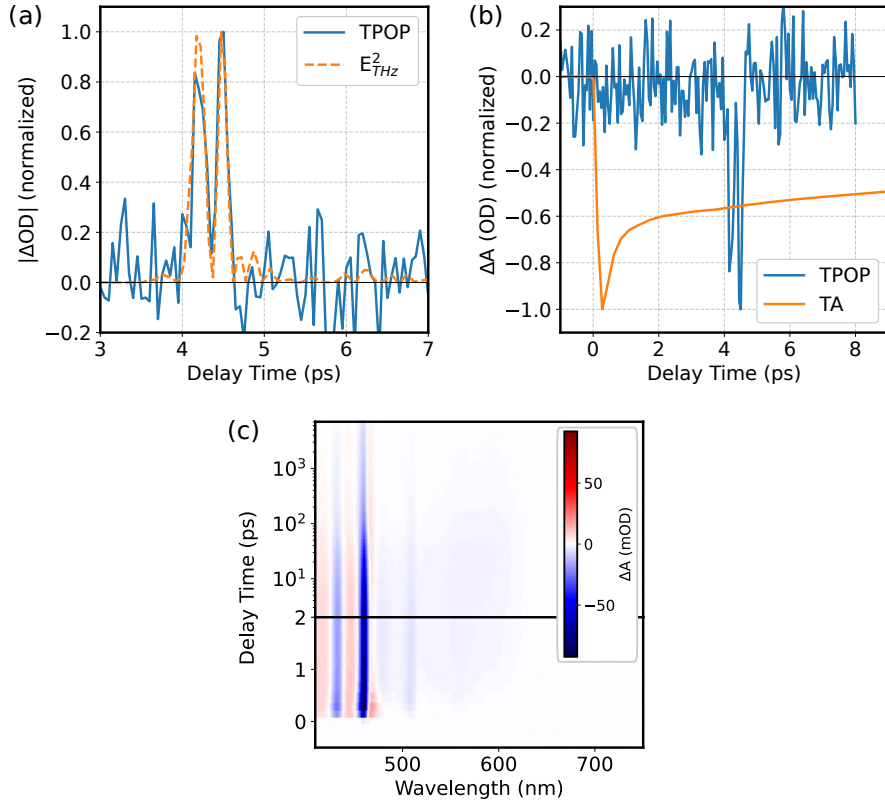


**Figure 6.4:** (a) Normalized differential absorption and THz intensity (obtained by taking the square of the EOS timetrace). (b) Comparison of TPOP time trace at the probe wavelength of maximum signal (457 nm) with TA GSB recovery dynamics at the same probe wavelength. (c) TA-map of CdSe nanoplatelets after excitation with 400 nm and 150  $\mu\text{J}/\text{cm}^2$ .

absorption, which is not expected here, as the employed photon energy is below the band gap. A quadratic dependency points towards two-photon absorption behavior,<sup>299,307</sup> which is indeed observed here. In the case of the NIR pump beam, a weak GSB can only be seen at the highest employed pump fluence of 1920  $\mu\text{J}/\text{cm}^2$ . The OSE signal only lasts for around 100 fs during the temporal overlap of pump and probe pulse (*cf.* Figure 6.5(f)).

The differential absorption  $\Delta A$  that would stem from a pure shift in absorption photon energy  $\Delta E$ , as would be expected from the Stark effect, can be approximated using the first derivative of the absorption spectrum  $A$

$$\Delta A = -\Delta E \frac{\partial A}{\partial E}, \quad (6.4)$$

as  $\partial E$  is much smaller than  $\Delta E$ .<sup>300,308</sup> Figure 6.6 shows the first derivative of the absorption spectrum versus the measured  $\Delta A$  signals for vis, NIR and THz pump. The obtained differential spectra with vis and NIR pump resemble the first derivative very well, which is in agreement with results reported by Geiregat *et al.* for non-resonant optical pumping (*cf.* Figure 3b in Reference<sup>295</sup>) and Diroll for NIR to mid-IR pumping (*cf.* Figure 2c and e in Reference<sup>300</sup>) Interestingly, the first derivative of the absorption spectrum is not able to describe the THz-induced shift in absorption. In this case, the measured differential absorp-

tion is much more symmetric around the center wavelength of the heavy hole absorption peak. Clearly, the change in absorption is described much better by a line broadening rather than a hypsochromic shift.

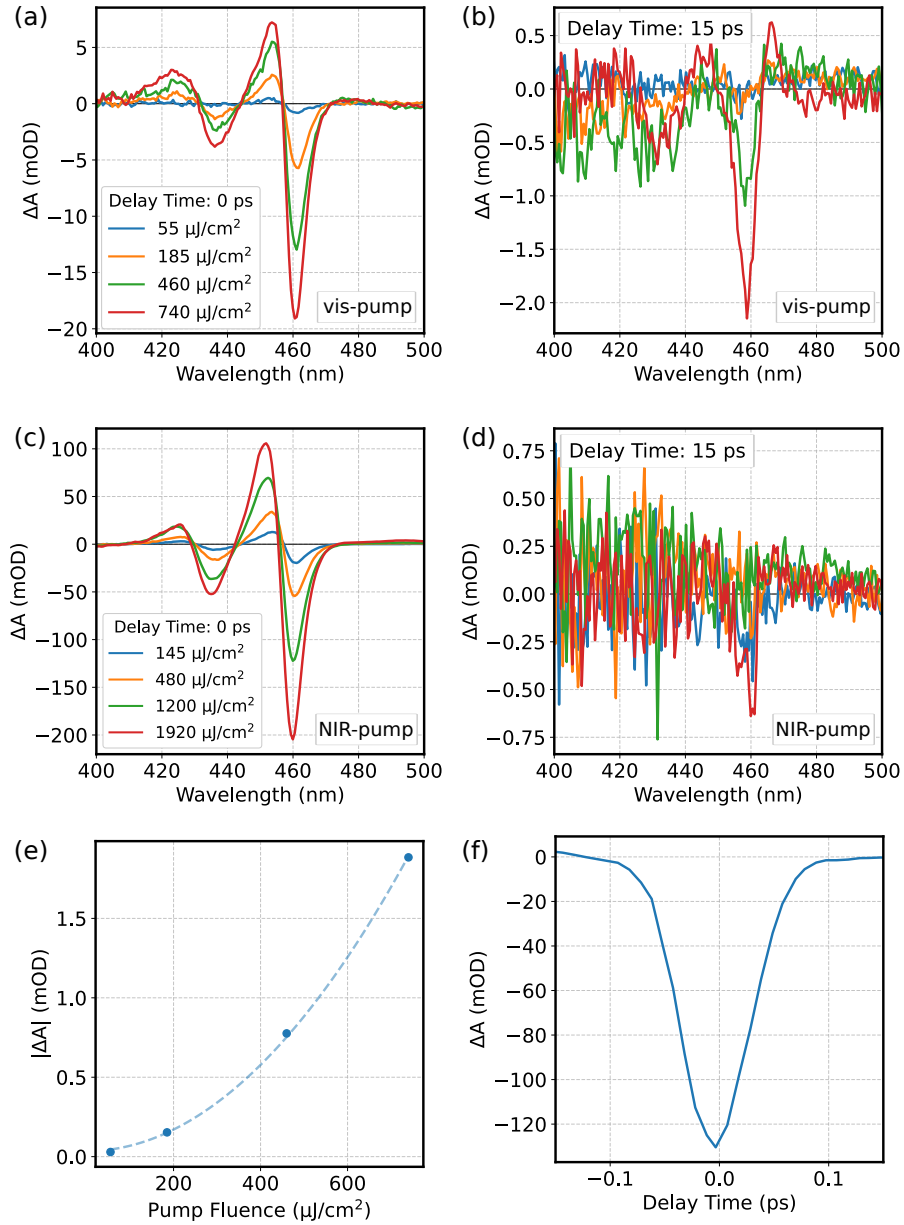


**Figure 6.5:** (a) Differential absorption with a sub-band-gap visible pump pulse at temporal overlap of pump and probe at different pump fluences. (b) Differential absorption with sub-band-gap visible pump pulse at 15 ps delay. For high pump fluences, long-lived GSB of the heavy hole absorption feature is observed. (c),(d) Same as (a),(b) for NIR pump pulse. (e) The GSB maximum at long delay times for the vis-pump depends quadratically on the pump fluence, indicating two-photon absorption. (f) The OSE signal has a lifetime on the order of 100 fs, confirming that it is only apparent during temporal overlap of pump and probe (shown for the NIR pump).



### 6.1. Terahertz-induced Stark effect in CdSe nanoplatelets

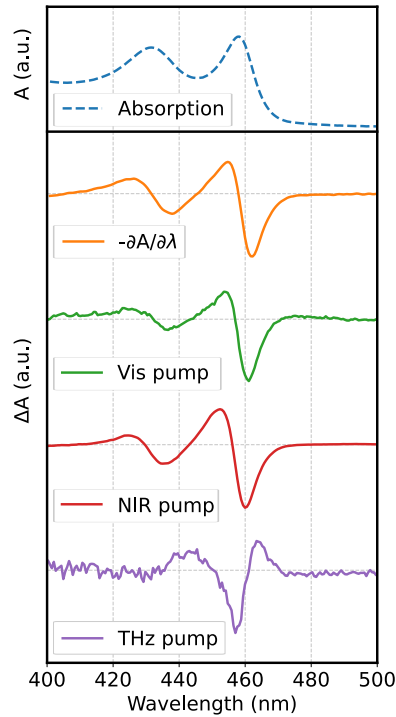


**Figure 6.6:** Absorption and differential absorption of the CdSe nanoplatelets. The differential absorption obtained from the vis and NIR pump pulses resembles the first derivative of the linear absorption spectrum, indicating a shift of the heavy and light hole resonances. The differential absorption obtained from THz pumping differs from that behavior. Spectra are normalized and vertically offset for clarity.

#### Outlook

It was shown that THz transient fields can change the optical properties of NCs, namely CdSe nanoplatelets, at very low THz field strengths without the use of field enhancement structures. Gollner *et al.* recently reported THz-induced OSE in CdSe/CdS QDs with field strengths in the MV/cm regime,<sup>304</sup> whereas the field strength employed here was only 86 kV/cm. The field-induced absorption changes depend on the employed pump pulse, with visible and NIR pump yielding a differential absorption that can well be explained by the first derivative, as expected from OSE. However, employing a THz pump pulse, the differential absorption can be described by a broadening of the heavy-hole absorption peak rather than a shift. This might be due to the Franz-Keldysh effect dominating over the OSE.<sup>296</sup> THz-field-dependent measurements might allow differentiating between Franz-Keldysh and OSE contributions, as different field dependencies of the two electro-optical effects were reported.<sup>309</sup>

## 6.2 Collective properties of giant-shell quantum dots

Assembling NCs into close-packed structures enables electronic and optical interaction between them, which can result in properties differing from those of the sum of the individual NCs.<sup>310</sup> Various synthetic strategies are used for the assembly, such as self-assembly on liquid-liquid interfaces,<sup>311–313</sup> the clustering of NCs in polymeric micelles,<sup>313,314</sup> or emulsion templating.<sup>315,316</sup>

Strong electronic coupling between NCs in dense NC arrays can lead to band-like energy structures.<sup>163,317–319</sup> This so-called miniband formation was shown for perovskite NCs.<sup>320,321</sup> Somewhat weaker electronic coupling can still influence charge carrier dynamics substantially, as faster carrier cooling and smaller biexciton binding energies were observed in dense NC clusters as compared to colloiddally dispersed NCs.<sup>322,323</sup>

In dense ensembles of perovskite NCs, not only miniband formation was observed, but also strongly altered emission properties. Rainò *et al.* reported superfluorescence from lead halide perovskite superlattices.<sup>20</sup> Superfluorescence describes the cooperative spontaneous emission of close-packed emitters. The spontaneous emission of one of the emitters induces a macroscopic dipole.<sup>324</sup> The excitonic dipoles of the remaining emitters align along this macroscopic dipole, resulting in a coherent burst of emission.<sup>324,325</sup> This superfluorescent emission can be distinguished from independent spontaneous emission of all the emitters and from amplified spontaneous emission in the time domain.<sup>326</sup> The peak of the superfluorescent emission occurs with a certain time delay, effectively the time it takes for the excitonic dipoles to align. Also, time-dependent oscillations in the emission intensity, so-called Burnham-Chiao ringing, can be observed.<sup>325,327,328</sup> Cd-based NCs are less well suited to exhibit superfluorescence due to the long excitonic lifetimes and fast excitonic dephasing.<sup>326</sup>

Ensembles of NCs exhibit a distribution of band gap energies due to their size distributions. Hence, Förster resonance energy transfer occurs in NC ensembles, as smaller NCs with a larger band gap transfer their energy to larger NCs with a smaller band gap.<sup>314,329</sup> This dipole-dipole interaction is strongly distance-dependent and hence mainly occurs in dense ensembles. In TA and PL experiments, resonance energy transfer can be observed as a red-shift of the GSB or emission, respectively.

Here, the collective optical properties of CdSe-CdS giant shell QDs encapsulated into polymeric micelles were studied. TA and PL experiments were employed to investigate resonant energy transfer, electronic coupling, excitonic coupling and stimulated emission properties of the densely-packed QDs.

### Materials and experimental methods

*The studied giant-shell QDs were synthesized and characterized by Sonja Krohn (Fraunhofer IAP-CAN), Artur Feld and Agnes Weimer (both working in the Weller Research Group, Institute of Physical Chemistry, Universität Hamburg) encapsulated the QDs into polymer shells.*

## 6.2. Collective properties of giant-shell quantum dots

The CdSe-CdS giant-shell QDs were synthesized following the approach reported by Chen *et al.*<sup>185</sup> The QDs had a diameter of 13.9 nm ( $\pm 1.5$  nm) and a PL-QY of 76 % after shell excitation. The QDs were encapsulated in OH-terminated polyisopren-b-polyethylenoxid following the procedure described by Schmidtke *et al.*<sup>313</sup> The polymer-encapsulated QDs were separated size-selectively using a glycerol gradient to separate single QDs from polymer capsules carrying multiple QDs.

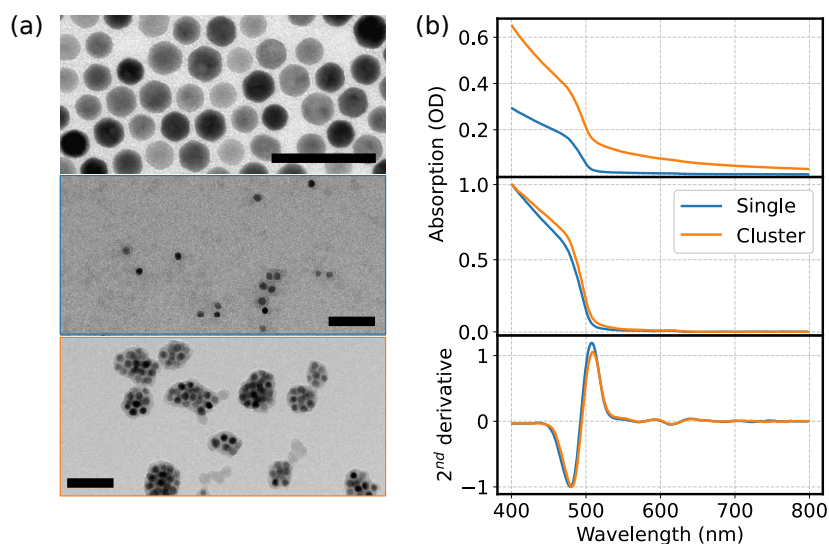


**Figure 6.7:** (a) TEM images of employed giant-shell QDs before the encapsulation, single encapsulated QDs and clustered QDs (top to bottom). All scale bars correspond to 50 nm. (b) UV-vis absorption spectra of the single encapsulated QDs and the clustered QDs (top), after scattering correction (middle) and the second derivative of the scattering-corrected absorption spectra.

Figure 6.7 shows TEM images of the employed QDs before encapsulation, individually encapsulated QDs and polymer-capsules containing multiple QDs, *i.e.* clustered QDs. From the TEM image, it can be seen that the clustered QD sample contained a certain cluster size distribution, ranging from a few QDs per cluster to tens of QDs per cluster. In all the optical experiments discussed hereafter, the clustered QDs are compared to individually encapsulated QDs (referred to as *single* QDs) rather than the QDs before encapsulation to ensure the comparison of samples in similar chemical environments. Figure 6.7(b) shows the UV-vis absorption spectra of the two samples. Due to the larger size of the polymer capsule, the clustered QD sample showed stronger scattering than the single QDs. A scattering correction was applied, subtracting a  $\lambda^{-4}$  dependent function fitted to the below-bandgap part of the spectrum. Exact determination of the position of the excitonic absorption peaks can be impeded by the overlap of the band edge absorption in QDs. Hence, the second derivative of the absorption spectra was calculated, in which excitonic absorption peaks appear as minima.

PL decay was measured using a fluorescence lifetime spectrometer (*PicoQuant GmbH, FluoTime 300*). PL decay curves were measured for emission wavelengths from 550 to 700 nm with a step width of 2 nm using a monochromator with a bandwidth of 2 nm. An excitation wavelength of 440 nm was chosen for all shown PL measurements.

TA measurements were conducted on the setup described in Chapter 2.2. Excitation wavelengths of 400 nm and 570 nm were generated *via* SHG and an OPA, respectively.

## Results and discussion

From the second derivative of the absorption spectra, the following excitonic absorption peak positions were derived: For the single QDs, the CdS and CdSe excitonic peaks occurred at 478 nm and 614 nm, respectively. For the clustered QDs, both absorption peaks occurred red-shifted at 481 nm (CdS) and 615 nm (CdSe). Tang *et al.* reported a red-shift in absorption of about 10 meV upon the formation of supercrystals from perovskite NCs, which they attributed to the electronic coupling between the densely packed NCs.<sup>322</sup> Here, the red-shift falls into the same order of magnitude, as it amounts to approximately 15 meV for the CdS absorption and 3 meV for the CdSe absorption.

Figure 6.8 shows that the PL spectrum of the clusters is not shifted relative to the spectrum of the single QDs. This is in disagreement with the observed red-shift in the absorption spectrum. In the case of effective electronic coupling, a red-shift would be expected in both absorption and emission. However, faster PL decay is observed in the clusters. Exponential functions were fitted to the decay curves at each emission wavelength. Slower PL decay is observed for longer emission wavelengths in both the single and clustered QDs. Efficient resonant energy transfer has been observed in densely-packed clusters of NCs, which is characterized by the accelerated PL decay of the blue part of the emission spectrum, as smaller particles can resonantly transfer their energy onto larger particles.<sup>314,329,330</sup> However, Pal *et al.* reported that the efficiency of resonant energy transfer in CdSe-CdS QDs depends on the shell thickness, observing fast energy transfer in ensembles of thin-shell QDs, but not in ensembles of thick-shell QDs.<sup>331</sup> Resonant energy transfer is highly distance-dependent. Thick shells keep the core-localized excitons of neighboring QDs apart from each other, hence prohibiting efficient energy transfer. In the measurements on giant-shell QDs shown here, although the clustered QDs show overall faster PL decay than the single QDs, the wavelength-resolved decay curves do not point towards strong resonant energy transfer, in agreement with the results reported by Pal *et al.*

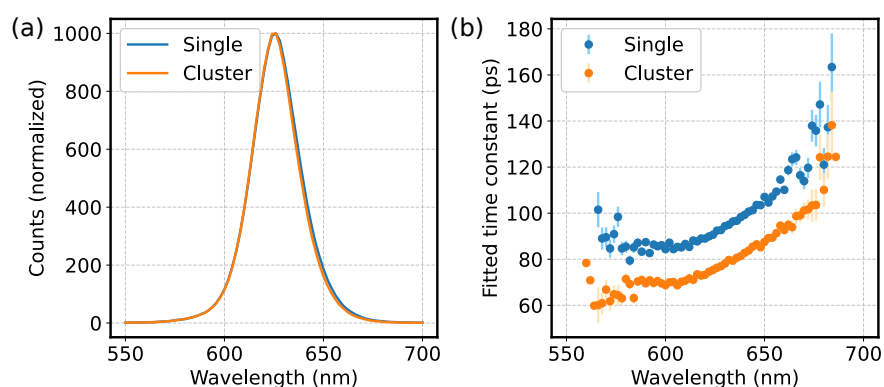


**Figure 6.8:** (a) PL spectra of the single QDs and the clustered QDs. (b) Fitted decay time constant versus emission wavelength.

TA at an excitation wavelength of 400 nm was measured on the single and clustered QDs to study the electronic behavior in more detail. First, Poisson excitation statistics were evaluated from measurement rows with varying pump fluence following the procedure described in Chapter 4.3.1. The CdS GSB feature was used for evaluating the excitation statistics, as in the giant-shell QDs, the CdS shell volume is much larger than the CdSe core volume (*cf.* Figure A7). At an excitation wavelength of 400 nm, absorption cross sections of approximately  $5 \cdot 10^{-15} \text{ cm}^2$  were found for both the single QDs and clustered QDs, which is consistent with reported values for Cd-based QDs.<sup>332</sup> The constant  $C_{ex}$ , which relates the pump fluence  $J$  to the mean exciton number  $\langle N \rangle$  was found to be  $0.01 (\mu\text{J}/\text{cm}^2)^{-1}$ .

At low excitation fluences of  $10 \mu\text{J}/\text{cm}^2$ , which corresponds to a mean exciton number  $\langle N \rangle$  of 0.1, single and clustered QDs show similar TA behavior. Figure 6.9(a) compares the differential spectra at relatively short (5 ps) and long (6 ns) delay times. The CdS GSB feature of the clustered QDs is slightly red-shifted as compared to the single QDs, which is consistent with the linear absorption spectra. The GSB recovery dynamics of the CdSe feature coincide on both short and long timescales (*cf.* Figure 6.9(c) and Figure A8). Since the TA data at low exciton densities and the observed absorption cross-sections match, it can be concluded that the two samples can be well compared and the slightly different chemical environments of individually encapsulated QDs and QDs encapsulated in clusters do not alter their general optical properties. However, at exciton densities of around 10 excitons per particle ( $1000 \mu\text{J}/\text{cm}^2$ ), significant differences between single and clustered QDs are observed (*cf.* Figure 6.9(b) and (d)). For the clustered QDs, an additional fast decay component is observed in the CdSe GSB recovery dynamics on the picosecond timescale. The single QDs, on the other hand, show an additional rise component rather than a decay component. On longer timescales, the GSB recovery dynamics of single and clustered QDs again coincide (*cf.* Figure A8). Also, at short delay times, the CdS GSB feature of the clustered QDs is red-shifted much stronger relative to the single QDs than at low excitation densities.

Figure 6.10 shows the CdSe GSB recovery dynamics of the two samples at various pump fluences, *i.e.* mean initial exciton numbers. Up until a mean exciton number of 1, where about 63 % of all QDs carry at least one exciton, the dynamics for single and clustered QDs coincide. At mean exciton numbers of 2.5 and higher, at which nearly every QD carries at least one exciton, the additional fast decay component in the clustered QDs builds up. The single QDs show their additional rise component at mean exciton numbers of 7.5 and higher.

In Figure 6.11, the TA data at long probe wavelengths is shown. The single QDs show a PIA feature in the spectral region from approximately 650 nm to 750 nm. As described in Chapter 4.3.2 and shown in Figure 4.11, this feature is well-known for Cd-based QDs and is usually assigned to surface-trapped holes.<sup>211,227</sup> At low excitation densities, the PIA does not show any picosecond decay dynamics. However, at high excitation densities, a fast decay component on the timescale of tens of picoseconds is observed (*cf.* Figure A9). The surface-trapped hole PIA feature is known to be spectrally broad and extend down to wavelengths of 600 nm (*cf.* Figure 4.11). Hence, at the probe wavelength of 615 nm displayed in Figure 6.9 and 6.10, the PIA will overlap with the CdSe GSB feature. Exponential fitting revealed a rise time of 18 ps in the CdSe GSB and a decay time of 23 ps in the surface-trapped-hole-induced

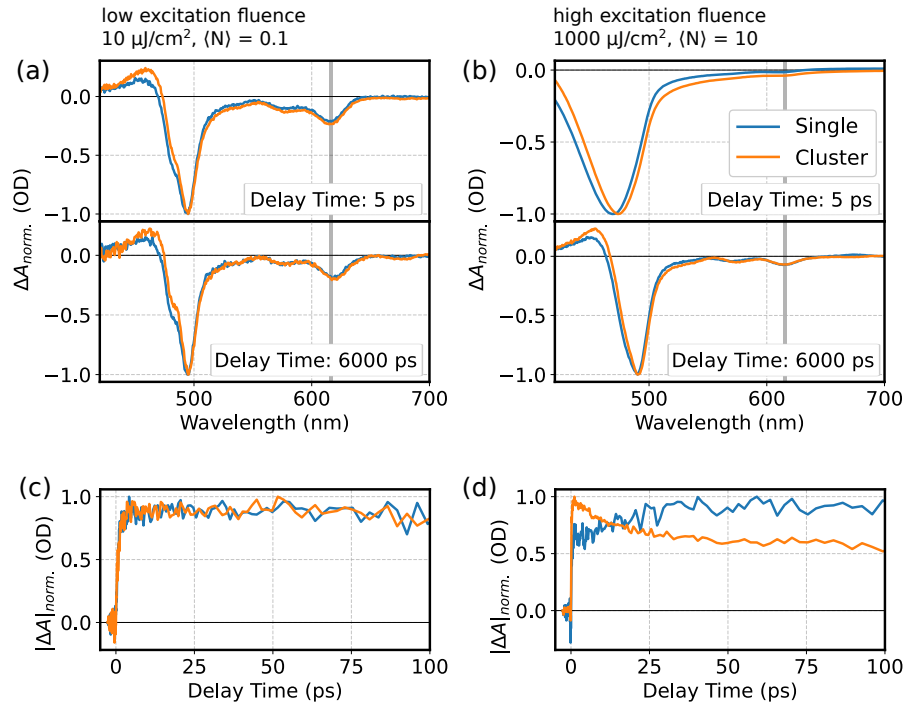


**Figure 6.9:** TA data of single and clustered QDs at low and high excitation fluences at an excitation wavelength of 400 nm. (a),(c) At low exciton densities, apart from a minor red-shift of the clustered QDs' CdS GSB, both the differential spectra as well as the bleach recovery dynamics of the two samples coincide. (b),(d) At high exciton densities, the clustered QDs show an additional decay component in their CdSe GSB recovery dynamics, whereas the single QDs show an additional rise component both not observed at low excitation densities. The probe wavelength was 615 nm for all displayed GSB recovery dynamics.

PIA. Hence, the rise in the GSB observed in single QDs might be caused by the spectral overlap with the PIA feature. As GSB and PIA differ in sign, the overlapping decay in PIA will appear as a rise in GSB.

The clustered QDs, on the other hand, show a broad negative  $\Delta A$  at long probe wavelengths, ranging from the CdSe GSB at around 615 nm to 750 nm. The negative  $\Delta A$  feature decays with a time constant of 13 ps. This decay time matches with the additional decay component observed for the CdSe GSB, hence it can be assumed that there is a broad negative feature that ranges from the spectral region of the CdSe GSB to longer probe wavelengths. As the QDs do not show any absorption at longer wavelengths than the lowest CdSe absorption feature (*cf.* Figure 6.7), the negative  $\Delta A$  feature does not stem from GSB, but must originate from stimulated emission. Indeed, Klimov *et al.* reported Auger-assisted sub-band-gap gain in compositionally graded QDs at excitation densities of  $\langle N \rangle \geq 2$ , consistent with the data shown here.<sup>18</sup>

In TA experiments with core excitation, a similar picosecond decay component of the CdSe GSB of the clustered QDs was observed. The rise component of the single QDs was however not observed under core excitation. The measurements under core excitation are summarized in Figure A10.

## 6.2. Collective properties of giant-shell quantum dots

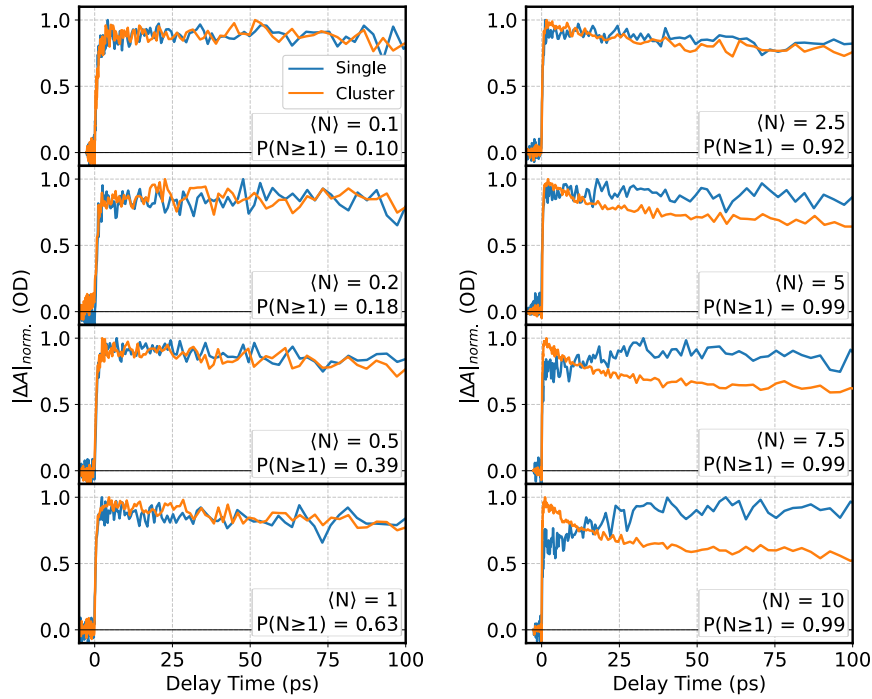


**Figure 6.10:** CdSe GSB recovery dynamics (probe wavelength 615 nm) at several excitation densities. The additional decay component observed in clustered QDs occurs at mean exciton numbers of 2.5 and higher. The additional rise component observed in single QDs occurs at mean exciton numbers of 7.5 and higher.

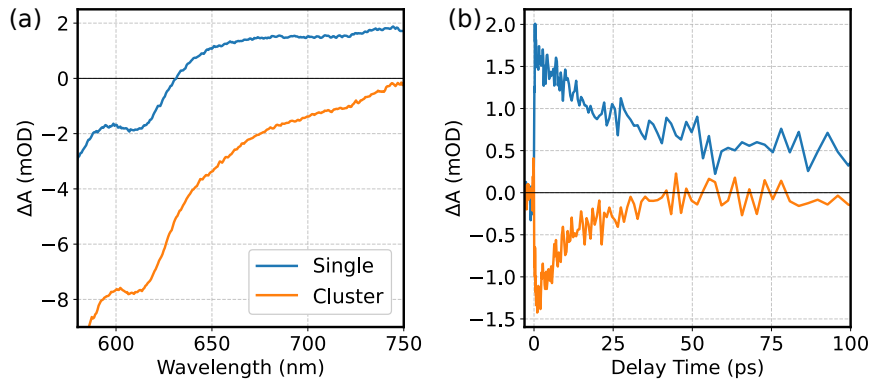


**Figure 6.11:** (a) TA spectra of single and clustered QDs at 2 ps delay time at long probe wavelengths after excitation with 400 nm and 1000  $\mu\text{J}/\text{cm}^2$ . (b) TA dynamics probed at 700 nm under the same excitation conditions.

In QDs, the biexcitonic binding energy  $\Delta_{XX}$  can be deduced from the TA data. At a low excitation density, the probe pulse either interacts with a non-excited QD (no contribution to the TA signal) or with a QD containing one exciton. In this case, the biexciton binding energy between the exciton generated by the pump pulse and the exciton generated by the probe pulse shifts the excitonic absorption to lower energies, *i.e.* longer wavelengths, generating a derivative-like spectral shape in the differential spectrum (*cf.* Figure 4.6), which can be used to calculate the biexciton binding energy. However, once the exciton generated by the pump pulse populates the band edge states, GSB outweighs the spectral shift. Hence, the

biexcitonic binding energies are deduced from the shift after excitation with above band gap photon energies and at short delay times, when the electrons did not yet relax to the band edge. Klimov suggested a method to analyze the biexciton binding energy from the maximum amplitudes of the biexcitonic shift ( $A$ ) and GSB feature ( $B$ ).<sup>205</sup> Figure 6.12 exemplarily shows the biexcitonic shift feature of the clustered QDs after excitation with 400 nm at a low excitation density ( $\langle N \rangle = 0.1$ ). Figure 6.12(c) shows the relationship between the ratio of  $A/B$  and the biexcitonic binding energy  $\Delta_{XX}$ , whereby the line width of the 1s transition  $\Gamma_{1s}$  has to be taken into account. For the single and clustered QDs, the line widths (half-width at half maximum) were deduced from the linear absorption spectra and the biexciton binding energies were determined to be 12 meV and 9 meV, respectively. The obtained values are in line with biexcitonic binding energies reported in literature<sup>205,213,323</sup> and point towards excitonic coupling in the clustered QDs. Marino *et al.* reported comparable changes in the biexcitonic binding energy for CdSe QDs when clustering them into supercrystals.<sup>323</sup> Here, the biexcitonic shift feature can only be observed at the CdS-shell resonance, but not at the CdSe-core resonance. As shown in Chapter 5.3, fast exciton formation in the CdSe core upon shell excitation is observed in giant-shell QDs. The observed decrease in biexciton binding energy upon clustering of the QDs suggests delocalization of the excitons between the CdS shell of neighboring QDs prior to the exciton localization into the CdSe core.

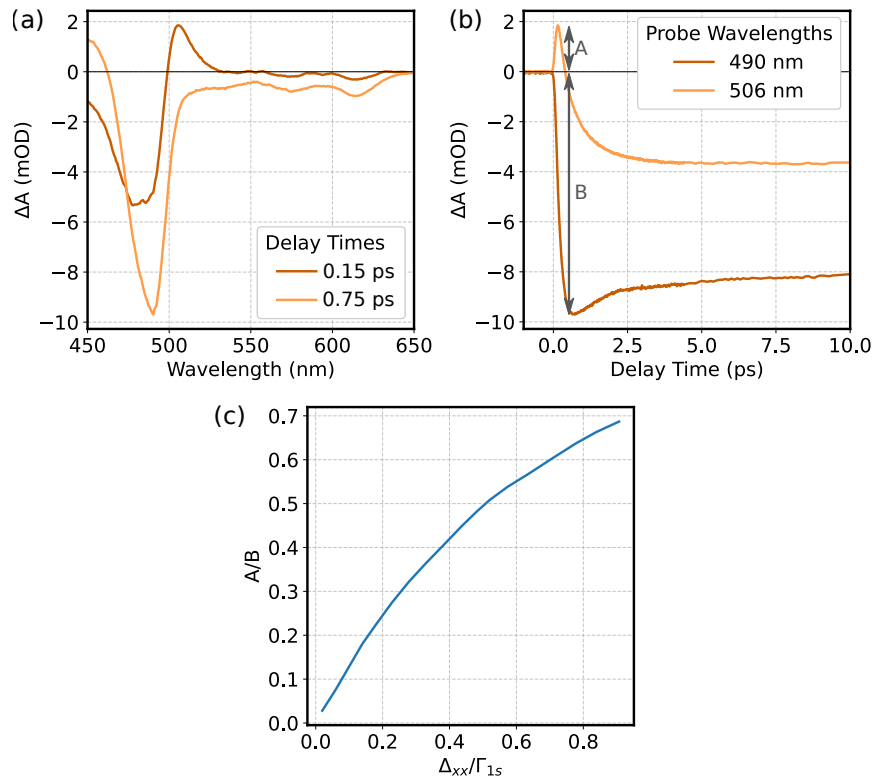


**Figure 6.12:** (a) TA spectra after excitation with 400 nm at a low excitation density. (b) TA dynamics probed at the wavelengths of maximum contrast of the biexcitonic shift and the GSB. (c) Relationship of the ratio  $A/B$  and the biexcitonic binding energy  $\Delta_{XX}$ . Reproduced with permission from Klimov.<sup>205</sup>



## Outlook

Summarizing, it could be shown how dense packing of giant-shell CdSe-CdS QDs alters their optical properties and charge carrier dynamics. Absorption spectra point towards electronic coupling (or miniband formation) as it is observed in ensembles of perovskite QDs. However, emission spectra contradict this interpretation. Although the PL lifetime of clustered QDs is overall faster than in single QDs, efficient resonant energy transfer could not be observed. The most significant differences occurred in the TA measurement at high excitation densities. Whereas in the single QDs, the CdSe GSB and the broad wavelengths are covered by the well-known PIA of surface-trapped holes, the clustered QDs show an additional fast decay component. Broad negative  $\Delta A$  at wavelengths below the band gap of the employed QDs point towards Auger-assisted stimulated emission. Also, weakened biexciton binding was observed in clustered QDs.

To study the collective properties of densely packed giant-shell QDs in more detail, better-defined samples have to be synthesized. Here, the sample contained clusters filled with different numbers of QDs. Also, interparticle distances were not characterized. Synthetically controlling the number of particles per cluster and the interparticle distance within a cluster, combined with careful characterization of these quantities, would enable parameter studies. Such would provide further insight into the collective phenomena described above, which are expected to depend on the geometrical properties of the sample (*e.g.* excitonic coupling depends on the interparticle distance<sup>323</sup>).

To get a better understanding of the Auger-assisted sub-band gap stimulated emission, the TA spectra should be directly compared to the absorption spectra of the very sample used for TA. From this, gain efficiencies and gain lifetimes can be determined.<sup>333–336</sup>



## 7. Summary

Pump-probe spectroscopic experiments driven by ultrafast laser pulses allow to study charge carrier dynamics after light absorption in colloidal NCs. Especially TA spectroscopy with sub-picosecond time resolution is indispensable in modern NC research, as it is employed in various subfields, such as NC photocatalysis,<sup>337,338</sup> NC solar cells<sup>339</sup> or in the study of fundamental physical processes.<sup>148,340</sup> Whereas TA probes the occupation of electronic states, OPTP probes the electronic properties of excited charge carriers. When conducted under comparable excitation conditions, OPTP can therefore be a valuable supplement to TA.<sup>264,275</sup>

The optical properties of AuNPs are mainly governed by their LSPR. Both resonant excitation of the LSPR as well as interband excitation leads to the generation of few non-thermal electrons, which relax *via* a cascade of events. Initial thermalization of the electrons is followed by electron-phonon coupling until eventually the absorbed energy is dissipated to the environment.

Semiconductor NCs exhibit size-dependent optical properties due to the quantum confinement effect. Depending on the design of the NCs, the excitation of electrons into the conduction band can lead to efficient charge separation, which is beneficial for photocatalytic applications, or efficient charge recombination, which is desired in light-emitting devices.

The main findings of this thesis can be summarized as follows:

**Size-dependent electron-phonon coupling in monocrystalline gold nanoparticles:** In the first project presented in this thesis, electron-phonon coupling in AuNPs was studied. It has long been under discussion whether the electron-phonon coupling constant is size-dependent. If electron-surface scattering would contribute significantly to electron-phonon coupling,  $G$  should decrease with increasing particle size due to the decreasing surface-to-volume ratio. A plethora of studies on this subject have been published, some of which observe size-dependent electron-phonon coupling,<sup>134,341</sup> whereas others were not able to find any size dependency.<sup>137,342–344</sup> Here, it could be shown that  $G$  is indeed size-dependent, however, this can only be observed in monocrystalline AuNPs. In polycrystalline AuNPs, which for a long time were the most intensely studied AuNPs, the size dependency is blurred due to electron-surface scattering at internal grain boundaries. Only with the development of new synthesis protocols,<sup>98</sup> which allow easy access to monocrystalline particles, the size dependency of electron-phonon coupling in AuNPs could be resolved.

**Carrier localization in zero-dimensional and one-dimensional CdSe-CdS heterostructures:** The second project studied the charge carrier dynamics in CdSe-CdS core-shell QDs and CdSe-CdS DRs employing both TA and OPTP. It could be shown that in DRs, shell-located electrons are mobile and contribute to measurable photoconductivity for hundreds of picoseconds before localizing into the core or being trapped at the particle surface. Despite the shallow confinement in the quasi-type II structure, core-located electrons are immobile, as they are bound into excitons with the core-located holes. In contrast, immobile excitons are formed in core-shell QDs within less than 2 ps after both core and shell excitation. It was shown that when carefully ensuring identical excitation conditions in TA and OPTP, the data acquired in the two experiments can be directly compared, allowing to correlate charge carrier localization (from TA) with mobility (from OPTP).

**Impact of pump beam spot size on semiconductor carrier dynamics in optical-pump-terahertz-probe spectroscopy:** The third project of this thesis focuses on an experimental error in OPTP that distorts the obtained differential THz spectra and hence the measured photoconductivity. As the wavelength of low-frequency THz radiation is in the millimeter range, in OPTP, the probe pulse can only be focused to a certain, frequency-dependent spot size. Due to experimental constraints, the pump beam spot size is often not large enough to ensure homogeneous excitation of the rather large probed sample region. Here, it is shown that inhomogeneous excitation distorts the obtained differential THz spectra towards higher frequencies. A model was set up to compensate for these distortions. Guidelines for the careful design of OPTP setups are given.

**Cation exchange during the synthesis of colloidal type-II ZnSe-dot/CdS-rod nanocrystals:** The fourth project presented in this thesis deals with the cation exchange during the shell growth of ZnSe-CdS DRs. Aliquots were taken at different times from the reaction solution. Besides TEM and numerical calculations based on the effective mass approximation, optical spectroscopy was used to study the cation exchange. TA was employed to follow the evolution of the spectral positions of the excitonic GSB features with reaction times. Conclusions about the evolution of the band structure could be drawn from the rise times. Also, Auger recombination times were investigated. It could be shown that cation exchange from Zn to Cd inevitably occurs during the initial stages of the shell growth, altering the band structure and hence the optical properties of the particles. As about 50 % of the Zn ions in the core are exchanged to Cd, this can not be neglected when describing the properties of ZnSe-CdS DRs.

**Electron donor-specific surface interactions promote the photocatalytic activity of metal-semiconductor nanohybrids:** Hybrid semiconductor-metal nanoparticles are well-studied model systems for photocatalytic hydrogen generation with nano-photocatalysts. In Pt-tipped CdSe-CdS DRs, the DR acts as a light-absorbing antenna. The hole locates in the semiconductor domain, whereas the excited electron is transferred to the metal tip, thereby establishing long-lived charge separation. The Pt tip then acts as a catalytic surface for hydrogen generation.<sup>11,168</sup> It is well known that the hydrogen production yield strongly depends on the choice of the electron-donating agent, which is added to remove the hole from the CdSe core.<sup>198,345,346</sup> However, the EDA's interaction with the particle's surface has not yet been taken into account. In the fifth project presented in this thesis, the surface activity of a row of well-established EDAs was studied. It was shown that ionic EDAs replace

the stabilizing ligands from the particle's surface, thereby lowering the colloidal stability and enabling fast hole transfer to the EDA. Alcoholic EDAs, on the other hand, act in a diffusion-limited way. Performing TA on the Pt-tipped DRs with different EDAs, faster hole removal in the case of surface-active EDAs as compared to diffusion-limited EDAs could be proven, which is in line with higher hydrogen production rates. The work will help to understand the working principles of the EDAs.

**Incorporation strategy for organic dyes into gold nanoparticle superlattices:** The sixth project of this thesis presents a strategy to incorporate organic dyes into plasmonic superlattices. TA was used to study the interaction of the dye and the plasmonic AuNPs. It was shown that strong optical interaction of the dye with the AuNPs could only be established when carefully binding the dye to the AuNPs surface before the ligand exchange from CTAC to PSSH, which is crucial for supercrystal formation.

**Terahertz-induced Stark effect in CdSe nanoplatelets (unpublished):** In a yet unpublished project presented in this thesis, OSE in CdSe nanoplatelets was studied. THz-induced OSE occurred at very low THz field strengths in this sample. It was shown that by employing NIR and sub-band-gap optical pump pulses, the OSE signal could be well described as the first derivative of the absorption spectrum. However, the THz-induced OSE signal could rather be described by a broadening of the heavy hole absorption band. Further measurements are required to separate Franz-Keldysh and OSE contributions.

**Collective properties of giant-shell quantum dots (unpublished):** In another unpublished study, the collective properties of densely-packed giant-shell CdSe-CdS QDs were studied. It was shown that Auger-assisted sub-band-gap stimulated emission occurs in such dense ensembles at high excitation densities. Also, excitonic coupling leads to weaker biexciton binding in dense ensembles as compared to single QDs.

In conclusion, metal and semiconductor NCs as well as hybrid colloidal NCs were studied using pump-probe spectroscopic methods. New findings on fundamental processes are presented, such as the contribution of electron-surface scattering to electron-phonon coupling in AuNPs, yielding to size-dependent electron-phonon coupling constant in monocrystalline AuNPs. The charge carrier localization in CdSe-CdS NCs depends on the NCs' shape. It could be shown that electrons in DRs remain mobile for hundreds of picoseconds, whereas they are bound to excitons in QDs within a few picoseconds. In hybrid nanomaterials, it could be proven that the surface activity of the employed EDA alters the charge carrier dynamics in Pt-tipped CdSe-CdS DRs, which in turn influences the hydrogen production rates. Besides the well-established TA technique, OPTP experiments were carried out, which are less well-known in the NC community. The usefulness of a combined experimental approach of TA and OPTP could be demonstrated. Guidelines to conduct reliable OPTP experiments were provided, which paves the way towards further studies of the properties of optically excited charge carriers in colloidal NCs employing a combination of TA and OPTP.



# References

- (1) Efros, A. L.; Brus, L. E. *ACS Nano* **2021**, *15*, 6192–6210.
- (2) Linic, S.; Christopher, P.; Ingram, D. B. *Nature Materials* **2011**, *10*, 911–921.
- (3) Zhao, J.; Wang, J.; Brock, A. J.; Zhu, H. *Journal of Photochemistry and Photobiology C: Photochemistry Reviews* **2022**, *52*, 100539.
- (4) Burke, R.; Bren, K. L.; Krauss, T. D. *The Journal of Chemical Physics* **2021**, *154*, 030901.
- (5) Li, X.-B.; Tung, C.-H.; Wu, L.-Z. *Nature Reviews Chemistry* **2018**, *2*, 160–173.
- (6) Takata, T.; Domen, K. *ACS Energy Letters* **2019**, *4*, 542–549.
- (7) Zhao, P.; Li, N.; Astruc, D. *Coordination Chemistry Reviews* **2013**, *257*, 638–665.
- (8) Li, N.; Zhao, P.; Astruc, D. *Angewandte Chemie International Edition* **2014**, *53*, 1756–1789.
- (9) Carbone, L.; Cozzoli, P. D. *Nano Today* **2010**, *5*, 449–493.
- (10) Donegá, C. D. M. *Chemical Society Reviews* **2011**, *40*, 1512–1546.
- (11) Wu, K.; Lian, T. *Chemical Society Reviews* **2016**, *45*, 3781–3810.
- (12) Waiskopf, N.; Ben-Shahar, Y.; Banin, U. *Advanced Materials* **2018**, *30*, 1706697.
- (13) García De Arquer, F. P.; Talapin, D. V.; Klimov, V. I.; Arakawa, Y.; Bayer, M.; Sargent, E. H. *Science* **2021**, *373*, eaaz8541.
- (14) Shu, Y.; Lin, X.; Qin, H.; Hu, Z.; Jin, Y.; Peng, X. *Angewandte Chemie International Edition* **2020**, *59*, 22312–22323.
- (15) Panfil, Y. E.; Oded, M.; Banin, U. *Angewandte Chemie International Edition* **2018**, *57*, 4274–4295.
- (16) Park, Y.-S.; Roh, J.; Diroll, B. T.; Schaller, R. D.; Klimov, V. I. *Nature Reviews Materials* **2021**, *6*, 382–401.
- (17) Jung, H.; Ahn, N.; Klimov, V. I. *Nature Photonics* **2021**, *15*, 643–655.
- (18) Ahn, N.; Livache, C.; Pinchetti, V.; Klimov, V. I. *Chemical Reviews* **2023**, *123*, 8251–8296.
- (19) Zhou, C.; Zhong, Y.; Dong, H.; Zheng, W.; Tan, J.; Jie, Q.; Pan, A.; Zhang, L.; Xie, W. *Nature Communications* **2020**, *11*, 329.
- (20) Rainò, G.; Becker, M. A.; Bodnarchuk, M. I.; Mahrt, R. F.; Kovalenko, M. V.; Stöferle, T. *Nature* **2018**, *563*, 671–675.

## References

- (21) Sekh, T. V. et al. *ACS Nano* **2024**, *18*, 8423–8436.
- (22) Proppe, A. H.; Berkinsky, D. B.; Zhu, H.; Šverko, T.; Kaplan, A. E. K.; Horowitz, J. R.; Kim, T.; Chung, H.; Jun, S.; Bawendi, M. G. *Nature Nanotechnology* **2023**, *18*, 993–999.
- (23) *Quantum Dots for Quantum Information Technologies*, 1st ed. 2017; Michler, P., Ed.; Nano-Optics and Nanophotonics; Springer International Publishing: Cham, 2017.
- (24) Mueller, N. S.; Okamura, Y.; Vieira, B. G. M.; Juergensen, S.; Lange, H.; Barros, E. B.; Schulz, F.; Reich, S. *Nature* **2020**, *583*, 780–784.
- (25) Cao, E.; Lin, W.; Sun, M.; Liang, W.; Song, Y. *Nanophotonics* **2018**, *7*, 145–167.
- (26) Stete, F.; Koopman, W.; Henkel, C.; Benson, O.; Kewes, G.; Bargheer, M. *ACS Photonics* **2023**, *10*, 2511–2520.
- (27) Shah, J., *Ultrafast spectroscopy of semiconductors and semiconductor nanostructures*, 2. enlarged ed; Springer series in solid-state sciences 115; Springer: Berlin Heidelberg, 1999.
- (28) *An introduction to laser spectroscopy*, 2. ed; Andrews, D. L., Demidov, A. A., Eds.; Springer Science + Business Media: New York, NY, 2012.
- (29) Porter, G. *Proceedings of the Royal Society of London. Series A. Mathematical and Physical Sciences* **1950**, *200*, 284–300.
- (30) The Nobel Prize in Chemistry 1967, <https://www.nobelprize.org/prizes/chemistry/1967/summary/>, Accessed: 2023-10-22.
- (31) Ramasesha, K.; Leone, S. R.; Neumark, D. M. *Annual Review of Physical Chemistry* **2016**, *67*, 41–63.
- (32) The Nobel Prize in Physics 2023, <https://www.nobelprize.org/prizes/physics/2023/summary/>, Accessed: 2023-10-22.
- (33) Ekimov, A. I.; Onushchenko, A. *JETP Lett.* **1981**, *34*, 345.
- (34) Rossetti, R.; Nakahara, S.; Brus, L. E. *The Journal of Chemical Physics* **1983**, *79*, 1086–1088.
- (35) Murray, C. B.; Norris, D. J.; Bawendi, M. G. *Journal of the American Chemical Society* **1993**, *115*, 8706–8715.
- (36) The Nobel Prize in Chemistry 2023 - Quantum dots — seeds of nanoscience, <https://www.nobelprize.org/prizes/chemistry/2023/advanced-information/>, Accessed: 2023-12-28.
- (37) The Nobel Prize in Chemistry 2023, <https://www.nobelprize.org/prizes/chemistry/2023/summary/>, Accessed: 2023-12-28.
- (38) Perenboom, J.; Wyder, P.; Meier, F. *Physics Reports* **1981**, *78*, 173–292.
- (39) Halperin, W. P. *Reviews of Modern Physics* **1986**, *58*, 533–606.
- (40) Kambhampati, P. *The Journal of Physical Chemistry Letters* **2021**, *12*, 4769–4779.
- (41) Freestone, I.; Meeks, N.; Sax, M.; Higgitt, C. *Gold Bulletin* **2007**, *40*, 270–277.
- (42) Faraday, M. *Philosophical Transactions of the Royal Society of London* **1857**, *147*, 145–181.



- (43) Thompson, D. *Gold Bulletin* **2007**, *40*, 267–269.
- (44) Mie, G. *Annalen der Physik* **1908**, *330*, 377–445.
- (45) Khurgin, J.; Bykov, A. Y.; Zayats, A. V. **2023**, DOI: 10.48550/ARXIV.2302.10247.
- (46) Hartland, G. V.; Besteiro, L. V.; Johns, P.; Govorov, A. O. *ACS Energy Letters* **2017**, *2*, 1641–1653.
- (47) Verma, R.; Belgamwar, R.; Polshettiwar, V. *ACS Materials Letters* **2021**, *3*, 574–598.
- (48) Kumar, A.; Choudhary, P.; Kumar, A.; Camargo, P. H. C.; Krishnan, V. *Small* **2022**, *18*, 2101638.
- (49) Smith, A. M.; Nie, S. *Accounts of Chemical Research* **2010**, *43*, 190–200.
- (50) Ben-Shahar, Y.; Stone, D.; Banin, U. *Chemical Reviews* **2023**, *123*, 3790–3851.
- (51) *Femtosecond laser pulses: principles and experiments*, 2nd ed; Rullière, C., Ed.; Advanced texts in physics; Springer: New York, 2005.
- (52) Demtroeder, W., *Laser spectroscopy 2: experimental techniques*, 5th edition. 2015; Springer Berlin Heidelberg: New York, NY, 2015.
- (53) Pickering, J. D., *Ultrafast Lasers and Optics for Experimentalists*; IOP Publishing: 2021.
- (54) Haus, H. *IEEE Journal of Selected Topics in Quantum Electronics* **2000**, *6*, 1173–1185.
- (55) Maine, P.; Strickland, D.; Bado, P.; Pessot, M.; Mourou, G. *IEEE Journal of Quantum Electronics* **1988**, *24*, 398–403.
- (56) The Nobel Prize in Physics 2018, <https://www.nobelprize.org/prizes/physics/2018/summary/>, Accessed: 2023-12-20.
- (57) Murti, Y. V. G. S.; Vijayan, C., *Physics of nonlinear optics*, Second edition; Springer: Cham, Switzerland, 2021.
- (58) Calendron, A.-L.; Çankaya, H.; Cirmi, G.; Kärtner, F. X. *Optics Express* **2015**, *23*, 13866.
- (59) *Terahertz Spectroscopy: Principles and Applications*; Dexheimer, S. L., Ed.; Optical science and engineering 131; CRC Press: Boca Raton, 2008.
- (60) Coutaz, J.-L.; Garet, F.; Wallace, V. P., *Principles of terahertz time-domain spectroscopy*; Pan Stanford publ: Singapore, 2018.
- (61) Neu, J.; Schmuttenmaer, C. A. *Journal of Applied Physics* **2018**, *124*, 231101.
- (62) Neu, J. *APL Photonics* **2023**, *8*, 071103.
- (63) *Terahertz spectroscopy and imaging*; Peiponen, K.-E., Zeitler, J. A., Kuwata-Gonokami, M., Eds.; Springer series in optical sciences v. 171; Springer: Berlin ; New York, 2013.
- (64) Jepsen, P.; Cooke, D.; Koch, M. *Laser & Photonics Reviews* **2011**, *5*, 124–166.
- (65) Nahata, A.; Weling, A. S.; Heinz, T. F. *Applied Physics Letters* **1996**, *69*, 2321–2323.

## References

- (66) Girod, B.; Rabenstein, R.; Stenger, A., *Signals and systems*; Wiley: Chichester ; New York, 2001.
- (67) Hecht, E., *Optics*, 5 ed.; Pearson: Boston Columbus Indianapolis New York San Francisco Amsterdam Cape Town Dubai London Madrid Milan Munich, 2017.
- (68) Orfanidis, S. J., *Electromagnetic Waves and Antennas*; Rutgers University: 2016.
- (69) Cunningham, P. D. *IEEE Transactions on Terahertz Science and Technology* **2013**, *3*, 494–498.
- (70) Xing, X.; Zhao, L.; Zhang, Z.; Liu, X.; Zhang, K.; Yu, Y.; Lin, X.; Chen, H. Y.; Chen, J. Q.; Jin, Z.; Xu, J.; Ma, G.-h. *The Journal of Physical Chemistry C* **2017**, *121*, 20451–20457.
- (71) Joyce, H. J.; Boland, J. L.; Davies, C. L.; Baig, S. A.; Johnston, M. B. *Semiconductor Science and Technology* **2016**, *31*, 103003.
- (72) Neu, J.; Regan, K. P.; Swierk, J. R.; Schmuttenmaer, C. A. *Applied Physics Letters* **2018**, *113*, 233901.
- (73) Glover, R. E.; Tinkham, M. *Physical Review* **1957**, *108*, 243–256.
- (74) Duvillaret, L.; Garet, F.; Coutaz, J.-L. *Applied Optics* **1999**, *38*, 409.
- (75) Cassar, Q.; Chopard, A.; Fauquet, F.; Guillet, J.-P.; Pan, M.; Perraud, J.-B.; Mounaix, P. *IEEE Transactions on Terahertz Science and Technology* **2019**, *9*, 684–694.
- (76) Tayvah, U.; Spies, J. A.; Neu, J.; Schmuttenmaer, C. A. *Analytical Chemistry* **2021**, *93*, 11243–11250.
- (77) Kužel, P.; Němec, H. *Journal of Physics D: Applied Physics* **2014**, *47*, 374005.
- (78) Ostatnický, T.; Pushkarev, V.; Němec, H.; Kužel, P. *Physical Review B* **2018**, *97*, 085426.
- (79) Lloyd-Hughes, J.; Jeon, T.-I. *Journal of Infrared, Millimeter, and Terahertz Waves* **2012**, *33*, 871–925.
- (80) Kužel, P.; Němec, H. *Advanced Optical Materials* **2020**, *8*, 1900623.
- (81) Drude, P. *Annalen der Physik* **1900**, *306*, 566–613.
- (82) Drude, P. *Annalen der Physik* **1900**, *308*, 369–402.
- (83) Fox, M., *Optical properties of solids*, 2nd ed; Oxford master series in condensed matter physics v. 3; Oxford University Press: Oxford, New York, 2010.
- (84) Ulbricht, R.; Hendry, E.; Shan, J.; Heinz, T. F.; Bonn, M. *Reviews of Modern Physics* **2011**, *83*, 543–586.
- (85) Nienhuys, H.-K.; Sundström, V. *Applied Physics Letters* **2005**, *87*, 012101.
- (86) Bohren, C. F.; Huffman, D. R., *Absorption and Scattering of Light by Small Particles*, 1st ed.; Wiley: 1998.
- (87) Maier, S. A., *Plasmonics: fundamentals and applications*; Springer: New York, 2007.
- (88) Ashcroft, N. W.; Mermin, N. D., *Solid state physics*; Holt, Rinehart and Winston: New York, 1976.

- (89) Rangel, T.; Kecik, D.; Trevisanutto, P. E.; Rignanese, G.-M.; Van Swygenhoven, H.; Olevano, V. *Physical Review B* **2012**, *86*, 125125.
- (90) Johnson, P. B.; Christy, R. W. *Physical Review B* **1972**, *6*, 4370–4379.
- (91) Zeman, E. J.; Schatz, G. C. *The Journal of Physical Chemistry* **1987**, *91*, 634–643.
- (92) Raether, H., *Excitation of plasmons and interband transitions by electrons*; Springer tracts in modern physics 88; Springer: Berlin Heidelberg, 1980.
- (93) Kurosawa, K.; Pierce, R. M.; Ushioda, S.; Hemminger, J. C. *Physical Review B* **1986**, *33*, 789–798.
- (94) Foteinopoulou, S.; Devarapu, G. C. R.; Subramania, G. S.; Krishna, S.; Wasserman, D. *Nanophotonics* **2019**, *8*, 2129–2175.
- (95) Amendola, V.; Pilot, R.; Frascioni, M.; Maragò, O. M.; Iatì, M. A. *Journal of Physics: Condensed Matter* **2017**, *29*, 203002.
- (96) Han, X. X.; Rodriguez, R. S.; Haynes, C. L.; Ozaki, Y.; Zhao, B. *Nature Reviews Methods Primers* **2022**, *1*, 87.
- (97) Mueller, N. S.; Pfitzner, E.; Okamura, Y.; Gordeev, G.; Kusch, P.; Lange, H.; Heberle, J.; Schulz, F.; Reich, S. *ACS Nano* **2021**, *15*, 5523–5533.
- (98) Zheng, Y.; Zhong, X.; Li, Z.; Xia, Y. *Particle & Particle Systems Characterization* **2014**, *31*, 266–273.
- (99) Staechelin, Y. U.; Hoeing, D.; Schulz, F.; Lange, H. *ACS Photonics* **2021**, *8*, 752–757.
- (100) Link, S.; El-Sayed, M. A. *International Reviews in Physical Chemistry* **2000**, *19*, 409–453.
- (101) Toropov, A. A.; Shubina, T. V., *Plasmonic effects in metal-semiconductor nanostructures*, First edition; Oxford science publications 19; Oxford University Press: Oxford, 2015.
- (102) Sumlin, B. J.; Heinson, W. R.; Chakrabarty, R. K. *Journal of Quantitative Spectroscopy and Radiative Transfer* **2018**, *205*, 127–134.
- (103) Sumlin, B. J. Online user's guide for the Python Mie Scattering package (PyMieScatt), <https://pymiescatt.readthedocs.io/en/latest>, Accessed: 2024-01-31.
- (104) Haiss, W.; Thanh, N. T. K.; Aveyard, J.; Fernig, D. G. *Analytical Chemistry* **2007**, *79*, 4215–4221.
- (105) Brown, A. M.; Sundararaman, R.; Narang, P.; Goddard, W. A.; Atwater, H. A. *Physical Review B* **2016**, *94*, 075120.
- (106) Kreibig, U.; Frangstein, C. V. *Zeitschrift für Physik* **1969**, *224*, 307–323.
- (107) Kreibig, U.; Vollmer, M., *Optical properties of metal clusters*; Springer series in materials science 25; Springer: Berlin Heidelberg, 2010.
- (108) Jiang, N.; Zhuo, X.; Wang, J. *Chemical Reviews* **2018**, *118*, 3054–3099.
- (109) Mayer, K. M.; Hafner, J. H. *Chemical Reviews* **2011**, *111*, 3828–3857.

## References

- (110) Halas, N. J.; Lal, S.; Chang, W.-S.; Link, S.; Nordlander, P. *Chemical Reviews* **2011**, *111*, 3913–3961.
- (111) Ghosh, S. K.; Pal, T. *Chemical Reviews* **2007**, *107*, 4797–4862.
- (112) Yeshchenko, O.; Bondarchuk, I.; Gurin, V.; Dmitruk, I.; Kotko, A. *Surface Science* **2013**, *608*, 275–281.
- (113) Kim, S.; Yoon, S. *Bulletin of the Korean Chemical Society* **2021**, *42*, 1058–1065.
- (114) Khurgin, J.; Tsai, W.-Y.; Tsai, D. P.; Sun, G. *ACS Photonics* **2017**, *4*, 2871–2880.
- (115) Stamatopoulou, P. E.; Tserkezis, C. *Optical Materials Express* **2022**, *12*, 1869.
- (116) *Quantum Plasmonics*; Bozhevolnyi, S. I., Martin-Moreno, L., Garcia-Vidal, F., Eds.; Springer Series in Solid-State Sciences, Vol. 185; Springer International Publishing: Cham, 2017.
- (117) Shahbazyan, T. V. *Physical Review B* **2016**, *94*, 235431.
- (118) Besteiro, L. V.; Yu, P.; Wang, Z.; Holleitner, A. W.; Hartland, G. V.; Wiederrecht, G. P.; Govorov, A. O. *Nano Today* **2019**, *27*, 120–145.
- (119) Hartland, G. V. *Chemical Reviews* **2011**, *111*, 3858–3887.
- (120) Wu, N. *Nanoscale* **2018**, *10*, 2679–2696.
- (121) Zhang, Y.; He, S.; Guo, W.; Hu, Y.; Huang, J.; Mulcahy, J. R.; Wei, W. D. *Chemical Reviews* **2018**, *118*, 2927–2954.
- (122) Brongersma, M. L.; Halas, N. J.; Nordlander, P. *Nature Nanotechnology* **2015**, *10*, 25–34.
- (123) Hodak, J. H.; Henglein, A.; Hartland, G. V. *The Journal of Physical Chemistry B* **2000**, *104*, 9954–9965.
- (124) Hubenthal, F. *Progress in Surface Science* **2007**, *82*, 378–387.
- (125) Sun, Q.; Yu, H.; Ueno, K.; Kubo, A.; Matsuo, Y.; Misawa, H. *ACS Nano* **2016**, *10*, 3835–3842.
- (126) Fann, W. S.; Storz, R.; Tom, H. W. K.; Bokor, J. *Physical Review B* **1992**, *46*, 13592–13595.
- (127) Fann, W. S.; Storz, R.; Tom, H. W. K.; Bokor, J. *Physical Review Letters* **1992**, *68*, 2834–2837.
- (128) Vallée, F. *Comptes Rendus de l'Académie des Sciences - Series IV - Physics* **2001**, *2*, 1469–1482.
- (129) Link, S.; El-Sayed, M. A. *The Journal of Physical Chemistry B* **1999**, *103*, 8410–8426.
- (130) Brown, A. M.; Sundararaman, R.; Narang, P.; Goddard, W. A.; Atwater, H. A. *ACS Nano* **2016**, *10*, 957–966.
- (131) Bernardi, M.; Mustafa, J.; Neaton, J. B.; Louie, S. G. *Nature Communications* **2015**, *6*, 7044.
- (132) Della Valle, G.; Conforti, M.; Longhi, S.; Cerullo, G.; Brida, D. *Physical Review B* **2012**, *86*, 155139.

- (133) Heilpern, T.; Manjare, M.; Govorov, A. O.; Wiederrecht, G. P.; Gray, S. K.; Harutyunyan, H. *Nature Communications* **2018**, *9*, 1853.
- (134) Guzelturk, B. et al. *ACS Nano* **2020**, *14*, 4792–4804.
- (135) Ortolani, M.; Mancini, A.; Budweg, A.; Garoli, D.; Brida, D.; De Angelis, F. *Physical Review B* **2019**, *99*, 035435.
- (136) Voisin, C.; Christofilos, D.; Del Fatti, N.; Vallée, F.; Prével, B.; Cottancin, E.; Lermé, J.; Pellarin, M.; Broyer, M. *Physical Review Letters* **2000**, *85*, 2200–2203.
- (137) Link, S.; Burda, C.; Wang, Z. L.; El-Sayed, M. A. *The Journal of Chemical Physics* **1999**, *111*, 1255–1264.
- (138) Karaman, C. O.; Bykov, A. Y.; Kiani, F.; Tagliabue, G.; Zayats, A. V. *Nature Communications* **2024**, *15*, 703.
- (139) O’Keeffe, P.; Catone, D.; Di Mario, L.; Toschi, F.; Magnozzi, M.; Bisio, F.; Alabastri, A.; Proietti Zaccaria, R.; Toma, A.; Della Valle, G.; Paladini, A. *Laser & Photonics Reviews* **2021**, *15*, 2100017.
- (140) Aruda, K. O.; Tagliazucchi, M.; Sweeney, C. M.; Hannah, D. C.; Schatz, G. C.; Weiss, E. A. *Proceedings of the National Academy of Sciences* **2013**, *110*, 4212–4217.
- (141) Huang, W.; Qian, W.; El-Sayed, M. A.; Ding, Y.; Wang, Z. L. *The Journal of Physical Chemistry C* **2007**, *111*, 10751–10757.
- (142) Tang, Y.; Ouyang, M. *Nature Materials* **2007**, *6*, 754–759.
- (143) Rouxel, R.; Diego, M.; Maioli, P.; Lascoux, N.; Vialla, F.; Rossella, F.; Banfi, F.; Vallée, F.; Del Fatti, N.; Crut, A. *The Journal of Physical Chemistry C* **2021**, *125*, 23275–23286.
- (144) Anisimov, S.; Kapeliovich, B.; Perelman, T. *Soviet Journal of Experimental and Theoretical Physics* **1974**, *39*, 375–377.
- (145) Hashimoto, S.; Werner, D.; Uwada, T. *Journal of Photochemistry and Photobiology C: Photochemistry Reviews* **2012**, *13*, 28–54.
- (146) Hartland, G. V. *Annual Review of Physical Chemistry* **2006**, *57*, 403–430.
- (147) Crut, A.; Maioli, P.; Del Fatti, N.; Vallée, F. *Physics Reports* **2015**, *549*, 1–43.
- (148) Hoening, D. et al. *Nano Letters* **2023**, *23*, 5943–5950.
- (149) Salzwedel, R.; Knorr, A.; Hoening, D.; Lange, H.; Selig, M. *The Journal of Chemical Physics* **2023**, *158*, 064107.
- (150) Matzdorf, R.; Gerlach, A.; Theilmann, F.; Meister, G.; Goldmann, A. *Applied Physics B: Lasers and Optics* **1999**, *68*, 393–395.
- (151) Chiang, W.-Y.; Bruncz, A.; Ostovar, B.; Searles, E. K.; Brasel, S.; Hartland, G.; Link, S. *The Journal of Physical Chemistry C* **2023**, *127*, 21176–21185.
- (152) Hu, M.; Hartland, G. V. *The Journal of Physical Chemistry B* **2002**, *106*, 7029–7033.
- (153) Klingshirn, C. F., *Semiconductor optics*; Advanced texts in physics; Springer: Berlin ; New York, 2005.

## References

- (154) Yu, P. Y.; Cardona, M., *Fundamentals of semiconductors: physics and materials properties*, 4th ed; Graduate texts in physics; Springer: Berlin, New York, 2010.
- (155) Brus, L. E. *The Journal of Chemical Physics* **1983**, *79*, 5566–5571.
- (156) Brus, L. E. *The Journal of Chemical Physics* **1984**, *80*, 4403–4409.
- (157) Wheeler, D. A.; Zhang, J. Z. *Advanced Materials* **2013**, *25*, 2878–2896.
- (158) Zhang, C.; Do, T. N.; Ong, X.; Chan, Y.; Tan, H.-S. *Chemical Physics* **2016**, *481*, 157–164.
- (159) Nasir, J. A.; Rehman, Z. U.; Shah, S. N. A.; Khan, A.; Butler, I. S.; Catlow, C. R. A. *Journal of Materials Chemistry A* **2020**, *8*, 20752–20780.
- (160) Yu, W. W.; Peng, X. *Angewandte Chemie International Edition* **2002**, *41*, 2368–2371.
- (161) Yu, W. W.; Qu, L.; Guo, W.; Peng, X. *Chemistry of Materials* **2003**, *15*, 2854–2860.
- (162) Peng, X.; Wickham, J.; Alivisatos, A. P. *Journal of the American Chemical Society* **1998**, *120*, 5343–5344.
- (163) Talapin, D. V.; Lee, J.-S.; Kovalenko, M. V.; Shevchenko, E. V. *Chemical Reviews* **2010**, *110*, 389–458.
- (164) Talaat, H.; Abdallah, T.; Mohamed, M.; Negm, S.; El-Sayed, M. A. *Chemical Physics Letters* **2009**, *473*, 288–292.
- (165) Hu, J.; Li, L.-s.; Yang, W.; Manna, L.; Wang, L.-W.; Alivisatos, A. P. *Science* **2001**, *292*, 2060–2063.
- (166) Drake, G. A.; Keating, L. P.; Shim, M. *Chemical Reviews* **2023**, *123*, 3761–3789.
- (167) Zhu, H.; Chen, Z.; Wu, K.; Lian, T. *Chemical Science* **2014**, *5*, 3905–3914.
- (168) Wu, K.; Zhu, H.; Lian, T. *Accounts of Chemical Research* **2015**, *48*, 851–859.
- (169) Li, H.; Cheng, C.; Yang, Z.; Wei, J. *Nature Communications* **2022**, *13*, 6466.
- (170) Zhu, H.; Song, N.; Lv, H.; Hill, C. L.; Lian, T. *Journal of the American Chemical Society* **2012**, *134*, 11701–11708.
- (171) Nasilowski, M.; Mahler, B.; Lhuillier, E.; Ithurria, S.; Dubertret, B. *Chemical Reviews* **2016**, *116*, 10934–10982.
- (172) Ithurria, S.; Tessier, M. D.; Mahler, B.; Lobo, R. P. S. M.; Dubertret, B.; Efron, A. L. *Nature Materials* **2011**, *10*, 936–941.
- (173) Achtstein, A. W.; Schliwa, A.; Prudnikau, A.; Hardzei, M.; Artemyev, M. V.; Thomsen, C.; Woggon, U. *Nano Letters* **2012**, *12*, 3151–3157.
- (174) Yu, J.; Chen, R. *InfoMat* **2020**, *2*, 905–927.
- (175) She, C.; Fedin, I.; Dolzhenkov, D. S.; Demortière, A.; Schaller, R. D.; Pelton, M.; Talapin, D. V. *Nano Letters* **2014**, *14*, 2772–2777.
- (176) Luo, Y.; Wang, L.-W. *ACS Nano* **2010**, *4*, 91–98.
- (177) Eshet, H.; Grünwald, M.; Rabani, E. *Nano Letters* **2013**, *13*, 5880–5885.
- (178) Steiner, D.; Dorfs, D.; Banin, U.; Della Sala, F.; Manna, L.; Millo, O. *Nano Letters* **2008**, *8*, 2954–2958.

- (179) Sitt, A.; Sala, F. D.; Menagen, G.; Banin, U. *Nano Letters* **2009**, *9*, 3470–3476.
- (180) She, C.; Bryant, G. W.; Demortière, A.; Shevchenko, E. V.; Pelton, M. *Physical Review B* **2013**, *87*, 155427.
- (181) Müller, J.; Lupton, J. M.; Lagoudakis, P. G.; Schindler, F.; Koeppe, R.; Rogach, A. L.; Feldmann, J.; Talapin, D. V.; Weller, H. *Nano Letters* **2005**, *5*, 2044–2049.
- (182) Borys, N. J.; Walter, M. J.; Huang, J.; Talapin, D. V.; Lupton, J. M. *Science* **2010**, *330*, 1371–1374.
- (183) Hines, M. A.; Guyot-Sionnest, P. *The Journal of Physical Chemistry* **1996**, *100*, 468–471.
- (184) Bryant, G. W.; Jaskolski, W. *The Journal of Physical Chemistry B* **2005**, *109*, 19650–19656.
- (185) Chen, Y.; Vela, J.; Htoon, H.; Casson, J. L.; Werder, D. J.; Bussian, D. A.; Klimov, V. I.; Hollingsworth, J. A. *Journal of the American Chemical Society* **2008**, *130*, 5026–5027.
- (186) Ghosh, Y.; Mangum, B. D.; Casson, J. L.; Williams, D. J.; Htoon, H.; Hollingsworth, J. A. *Journal of the American Chemical Society* **2012**, *134*, 9634–9643.
- (187) Banin, U.; Ben-Shahar, Y.; Vinokurov, K. *Chemistry of Materials* **2014**, *26*, 97–110.
- (188) Wu, K.; Zhu, H.; Liu, Z.; Rodríguez-Córdoba, W.; Lian, T. *Journal of the American Chemical Society* **2012**, *134*, 10337–10340.
- (189) Amirav, L.; Alivisatos, A. P. *The Journal of Physical Chemistry Letters* **2010**, *1*, 1051–1054.
- (190) Choi, J. Y.; Park, W.-W.; Park, B.; Sul, S.; Kwon, O.-H.; Song, H. *ACS Catalysis* **2021**, *11*, 13303–13311.
- (191) Ben-Shahar, Y.; Scotognella, F.; Kriegel, I.; Moretti, L.; Cerullo, G.; Rabani, E.; Banin, U. *Nature Communications* **2016**, *7*, 10413.
- (192) Nakibli, Y.; Mazal, Y.; Dubi, Y.; Wächtler, M.; Amirav, L. *Nano Letters* **2018**, *18*, 357–364.
- (193) Bang, J. U.; Lee, S. J.; Jang, J. S.; Choi, W.; Song, H. *The Journal of Physical Chemistry Letters* **2012**, *3*, 3781–3785.
- (194) Kalisman, P.; Houben, L.; Aronovitch, E.; Kauffmann, Y.; Bar-Sadan, M.; Amirav, L. *Journal of Materials Chemistry A* **2015**, *3*, 19679–19682.
- (195) Wächtler, M.; Kalisman, P.; Amirav, L. *The Journal of Physical Chemistry C* **2016**, *120*, 24491–24497.
- (196) Wu, K.; Chen, Z.; Lv, H.; Zhu, H.; Hill, C. L.; Lian, T. *Journal of the American Chemical Society* **2014**, *136*, 7708–7716.
- (197) Berr, M. J.; Wagner, P.; Fischbach, S.; Vaneski, A.; Schneider, J.; Susha, A. S.; Rogach, A. L.; Jäckel, F.; Feldmann, J. *Applied Physics Letters* **2012**, *100*, 223903.
- (198) Simon, T.; Bouchonville, N.; Berr, M. J.; Vaneski, A.; Adrović, A.; Volbers, D.; Wyrwich, R.; Döblinger, M.; Susha, A. S.; Rogach, A. L.; Jäckel, F.; Stolarczyk, J. K.; Feldmann, J. *Nature Materials* **2014**, *13*, 1013–1018.

## References

- (199) Chen, S.; Wang, L.-W. *Chemistry of Materials* **2012**, *24*, 3659–3666.
- (200) Kalisman, P.; Nakibli, Y.; Amirav, L. *Nano Letters* **2016**, *16*, 1776–1781.
- (201) Wolff, C. M.; Frischmann, P. D.; Schulze, M.; Bohn, B. J.; Wein, R.; Livadas, P.; Carlson, M. T.; Jäckel, F.; Feldmann, J.; Würthner, F.; Stolarczyk, J. K. *Nature Energy* **2018**, *3*, 862–869.
- (202) Gramlich, M.; Bohn, B. J.; Tong, Y.; Polavarapu, L.; Feldmann, J.; Urban, A. S. *The Journal of Physical Chemistry Letters* **2020**, *11*, 5361–5366.
- (203) Klimov, V. I. *The Journal of Physical Chemistry B* **2000**, *104*, 6112–6123.
- (204) Klimov, V. I.; Mikhailovsky, A. A.; McBranch, D. W.; Leatherdale, C. A.; Bawendi, M. G. *Science* **2000**, *287*, 1011–1013.
- (205) Klimov, V. I. *Annual Review of Physical Chemistry* **2007**, *58*, 635–673.
- (206) Morgan, D. P.; Kelley, D. F. *The Journal of Physical Chemistry C* **2020**, *124*, 8448–8455.
- (207) Grimaldi, G.; Geuchies, J. J.; Van Der Stam, W.; Du Fossé, I.; Brynjarsson, B.; Kirkwood, N.; Kinge, S.; Siebbeles, L. D.; Houtepen, A. J. *Nano Letters* **2019**, *19*, 3002–3010.
- (208) Taheri, M. M.; Elbert, K. C.; Yang, S.; Diroll, B. T.; Park, J.; Murray, C. B.; Baxter, J. B. *The Journal of Physical Chemistry C* **2021**, *125*, 31–41.
- (209) Morgan, D. P.; Maddux, C. J. A.; Kelley, D. F. *The Journal of Physical Chemistry C* **2018**, *122*, 23772–23779.
- (210) Yan, C.; Weinberg, D.; Jasarasaria, D.; Kolaczowski, M. A.; Liu, Z.-j.; Philbin, J. P.; Balan, A. D.; Liu, Y.; Schwartzberg, A. M.; Rabani, E.; Alivisatos, A. P. *ACS Nano* **2021**, *15*, 2281–2291.
- (211) Jasarasaria, D.; Philbin, J. P.; Yan, C.; Weinberg, D.; Alivisatos, A. P.; Rabani, E. *The Journal of Physical Chemistry C* **2020**, *124*, 17372–17378.
- (212) McArthur, E. A.; Morris-Cohen, A. J.; Knowles, K. E.; Weiss, E. A. *The Journal of Physical Chemistry B* **2010**, *114*, 14514–14520.
- (213) Klimov, V.; Hunsche, S.; Kurz, H. *Physical Review B* **1994**, *50*, 8110–8113.
- (214) Rabouw, F. T.; De Mello Donega, C. *Topics in Current Chemistry* **2016**, *374*, 58.
- (215) Inoshita, T.; Sakaki, H. *Physical Review B* **1992**, *46*, 7260–7263.
- (216) Kambhampati, P. *Accounts of Chemical Research* **2011**, *44*, 1–13.
- (217) Cooney, R. R.; Sewall, S. L.; Dias, E. A.; Sagar, D. M.; Anderson, K. E. H.; Kambhampati, P. *Physical Review B* **2007**, *75*, 245311.
- (218) Efros, A. L.; Kharchenko, V.; Rosen, M. *Solid State Communications* **1995**, *93*, 281–284.
- (219) Cooney, R. R.; Sewall, S. L.; Anderson, K. E. H.; Dias, E. A.; Kambhampati, P. *Physical Review Letters* **2007**, *98*, 177403.
- (220) Guyot-Sionnest, P.; Wehrenberg, B.; Yu, D. *The Journal of Chemical Physics* **2005**, *123*, 074709.



- (221) Wang, L.; Chen, Z.; Liang, G.; Li, Y.; Lai, R.; Ding, T.; Wu, K. *Nature Communications* **2019**, *10*, 4532.
- (222) Boehme, S. C.; Brinck, S. T.; Maes, J.; Yazdani, N.; Zapata, F.; Chen, K.; Wood, V.; Hodgkiss, J. M.; Hens, Z.; Geiregat, P.; Infante, I. *Nano Letters* **2020**, *20*, 1819–1829.
- (223) Cao, W.; Yuan, L.; Patterson, R.; Wen, X.; Tapping, P. C.; Kee, T.; Veetil, B. P.; Zhang, P.; Zhang, Z.; Zhang, Q.; Reece, P.; Bremner, S.; Shrestha, S.; Conibeer, G.; Huang, S. *Nanoscale* **2017**, *9*, 17133–17142.
- (224) Price, M. B.; Butkus, J.; Jellicoe, T. C.; Sadhanala, A.; Briane, A.; Halpert, J. E.; Broch, K.; Hodgkiss, J. M.; Friend, R. H.; Deschler, F. *Nature Communications* **2015**, *6*, 8420.
- (225) Houtepen, A. J.; Hens, Z.; Owen, J. S.; Infante, I. *Chemistry of Materials* **2017**, *29*, 752–761.
- (226) Giansante, C.; Infante, I. *The Journal of Physical Chemistry Letters* **2017**, *8*, 5209–5215.
- (227) Schnitzenbaumer, K. J.; Labrador, T.; Dukovic, G. *The Journal of Physical Chemistry C* **2015**, *119*, 13314–13324.
- (228) Wu, K.; Du, Y.; Tang, H.; Chen, Z.; Lian, T. *Journal of the American Chemical Society* **2015**, *137*, 10224–10230.
- (229) Klimov, V. I.; McBranch, D. W.; Leatherdale, C. A.; Bawendi, M. G. *Physical Review B* **1999**, *60*, 13740–13749.
- (230) Wei, H. H.-Y.; Evans, C. M.; Swartz, B. D.; Neukirch, A. J.; Young, J.; Prezhdoo, O. V.; Krauss, T. D. *Nano Letters* **2012**, *12*, 4465–4471.
- (231) Utterback, J. K.; Grennell, A. N.; Wilker, M. B.; Pearce, O. M.; Eaves, J. D.; Dukovic, G. *Nature Chemistry* **2016**, *8*, 1061–1066.
- (232) Utterback, J. K.; Hamby, H.; Pearce, O. M.; Eaves, J. D.; Dukovic, G. *The Journal of Physical Chemistry C* **2018**, *122*, 16974–16982.
- (233) Utterback, J. K.; Ruzicka, J. L.; Hamby, H.; Eaves, J. D.; Dukovic, G. *The Journal of Physical Chemistry Letters* **2019**, *10*, 2782–2787.
- (234) Utterback, J. K.; Cline, R. P.; Shulenberger, K. E.; Eaves, J. D.; Dukovic, G. *The Journal of Physical Chemistry Letters* **2020**, *11*, 9876–9885.
- (235) Jasieniak, J.; Mulvaney, P. *Journal of the American Chemical Society* **2007**, *129*, 2841–2848.
- (236) Keene, J. D.; McBride, J. R.; Orfield, N. J.; Rosenthal, S. J. *ACS Nano* **2014**, *8*, 10665–10673.
- (237) Wilker, M. B.; Utterback, J. K.; Greene, S.; Brown, K. A.; Mulder, D. W.; King, P. W.; Dukovic, G. *The Journal of Physical Chemistry C* **2018**, *122*, 741–750.
- (238) Utterback, J. K.; Wilker, M. B.; Mulder, D. W.; King, P. W.; Eaves, J. D.; Dukovic, G. *The Journal of Physical Chemistry C* **2019**, *123*, 886–896.
- (239) Utterback, J. K.; Wilker, M. B.; Brown, K. A.; King, P. W.; Eaves, J. D.; Dukovic, G. *Physical Chemistry Chemical Physics* **2015**, *17*, 5538–5542.

## References

- (240) Okano, M.; Sakamoto, M.; Teranishi, T.; Kanemitsu, Y. *The Journal of Physical Chemistry Letters* **2014**, *5*, 2951–2956.
- (241) Hewa-Kasakarage, N. N.; El-Khoury, P. Z.; Tarnovsky, A. N.; Kirsanova, M.; Nemitz, I.; Nemchinov, A.; Zamkov, M. *ACS Nano* **2010**, *4*, 1837–1844.
- (242) McDaniel, H.; Pelton, M.; Oh, N.; Shim, M. *The Journal of Physical Chemistry Letters* **2012**, *3*, 1094–1098.
- (243) Grennell, A. N.; Utterback, J. K.; Pearce, O. M.; Wilker, M. B.; Dukovic, G. *Nano Letters* **2017**, *17*, 3764–3774.
- (244) Shulenberg, K. E.; Jilek, M. R.; Sherman, S. J.; Hohman, B. T.; Dukovic, G. *Chemical Reviews* **2023**, *123*, 3852–3903.
- (245) Melnychuk, C.; Guyot-Sionnest, P. *Chemical Reviews* **2021**, *121*, 2325–2372.
- (246) Klimov, V. I. *Annual Review of Condensed Matter Physics* **2014**, *5*, 285–316.
- (247) Robel, I.; Gresback, R.; Kortshagen, U.; Schaller, R. D.; Klimov, V. I. *Physical Review Letters* **2009**, *102*, 177404.
- (248) Park, Y.-S.; Bae, W. K.; Baker, T.; Lim, J.; Klimov, V. I. *Nano Letters* **2015**, *15*, 7319–7328.
- (249) Park, Y.-S.; Malko, A. V.; Vela, J.; Chen, Y.; Ghosh, Y.; García-Santamaría, F.; Hollingsworth, J. A.; Klimov, V. I.; Htoon, H. *Physical Review Letters* **2011**, *106*, 187401.
- (250) Cragg, G. E.; Efros, A. L. *Nano Letters* **2010**, *10*, 313–317.
- (251) García-Santamaría, F.; Brovelli, S.; Viswanatha, R.; Hollingsworth, J. A.; Htoon, H.; Crooker, S. A.; Klimov, V. I. *Nano Letters* **2011**, *11*, 687–693.
- (252) Bae, W. K.; Padilha, L. A.; Park, Y.-S.; McDaniel, H.; Robel, I.; Pietryga, J. M.; Klimov, V. I. *ACS Nano* **2013**, *7*, 3411–3419.
- (253) Nasilowski, M.; Spinicelli, P.; Patriarce, G.; Dubertret, B. *Nano Letters* **2015**, *15*, 3953–3958.
- (254) Jang, E.; Jang, H. *Chemical Reviews* **2023**, *123*, 4663–4692.
- (255) Lakowicz, J. R., *Principles of fluorescence spectroscopy*, 3rd ed; Springer: New York, 2006.
- (256) Lo, S. S.; Mirkovic, T.; Chuang, C.-H.; Burda, C.; Scholes, G. D. *Advanced Materials* **2011**, *23*, 180–197.
- (257) Nirmal, M.; Dabbousi, B. O.; Bawendi, M. G.; Macklin, J. J.; Trautman, J. K.; Harris, T. D.; Brus, L. E. *Nature* **1996**, *383*, 802–804.
- (258) Rabouw, F. T.; Antolinez, F. V.; Brechbühler, R.; Norris, D. J. *The Journal of Physical Chemistry Letters* **2019**, *10*, 3732–3738.
- (259) Efros, A. L.; Nesbitt, D. J. *Nature Nanotechnology* **2016**, *11*, 661–671.
- (260) Yuan, G.; Gómez, D. E.; Kirkwood, N.; Boldt, K.; Mulvaney, P. *ACS Nano* **2018**, *12*, 3397–3405.
- (261) Efros, A. L.; Rosen, M. *Physical Review Letters* **1997**, *78*, 1110–1113.

- (262) Wang, X.; Ren, X.; Kahen, K.; Hahn, M. A.; Rajeswaran, M.; Maccagnano-Zacher, S.; Silcox, J.; Cragg, G. E.; Efros, A. L.; Krauss, T. D. *Nature* **2009**, *459*, 686–689.
- (263) Banin, U. et al. *Nanotechnology* **2021**, *32*, 042003.
- (264) Bergren, M. R.; Palomaki, P. K. B.; Neale, N. R.; Furtak, T. E.; Beard, M. C. *ACS Nano* **2016**, *10*, 2316–2323.
- (265) Li, M.; Wu, B.; Ekahana, S. A.; Utama, M. I. B.; Xing, G.; Xiong, Q.; Sum, T. C.; Zhang, X. *Applied Physics Letters* **2012**, *101*, 091104.
- (266) Mics, Z.; Němec, H.; Rychetský, I.; Kužel, P.; Formánek, P.; Malý, P.; Němec, P. *Physical Review B* **2011**, *83*, 155326.
- (267) Gorris, F. E. S.; Deffner, M.; Priyadarshi, S.; Klinke, C.; Weller, H.; Lange, H. *Advanced Optical Materials* **2020**, *8*, 1901058.
- (268) Efros, A. L.; Rosen, M. *Annual Review of Materials Science* **2000**, *30*, 475–521.
- (269) Müller, T.; Parz, W.; Unterrainer, K.; Sauvage, S.; Houel, J.; Boucaud, P.; Miard, A.; Lemaître, A. *Physical Review B* **2008**, *77*, 035314.
- (270) Cooke, D. G.; Jepsen, P. U.; Lek, J. Y.; Lam, Y. M.; Sy, F.; Dignam, M. M. *Physical Review B* **2013**, *88*, 241307.
- (271) Lauth, J.; Failla, M.; Klein, E.; Klinke, C.; Kinge, S.; Siebbeles, L. D. A. *Nanoscale* **2019**, *11*, 21569–21576.
- (272) Kaindl, R. A.; Hägele, D.; Carnahan, M. A.; Chemla, D. S. *Physical Review B* **2009**, *79*, 045320.
- (273) Wang, F.; Shan, J.; Islam, M. A.; Herman, I. P.; Bonn, M.; Heinz, T. F. *Nature Materials* **2006**, *5*, 861–864.
- (274) Dakovski, G. L.; Lan, S.; Xia, C.; Shan, J. *The Journal of Physical Chemistry C* **2007**, *111*, 5904–5908.
- (275) Pijpers, J. J. H.; Milder, M. T. W.; Delerue, C.; Bonn, M. *The Journal of Physical Chemistry C* **2010**, *114*, 6318–6324.
- (276) Yang, Y.; Wu, K.; Shabaev, A.; Efros, A. L.; Lian, T.; Beard, M. C. *ACS Energy Letters* **2016**, *1*, 76–81.
- (277) Momper, R.; Zhang, H.; Chen, S.; Halim, H.; Johannes, E.; Yordanov, S.; Braga, D.; Blülle, B.; Doblas, D.; Kraus, T.; Bonn, M.; Wang, H. I.; Riedinger, A. *Nano Letters* **2020**, *20*, 4102–4110.
- (278) Kunneman, L. T.; Zanella, M.; Manna, L.; Siebbeles, L. D. A.; Schins, J. M. *The Journal of Physical Chemistry C* **2013**, *117*, 3146–3151.
- (279) Quick, M. T.; Owschimikow, N.; Achtstein, A. W. *The Journal of Physical Chemistry Letters* **2021**, *12*, 7688–7695.
- (280) Guyot-Sionnest, P. *The Journal of Physical Chemistry Letters* **2012**, *3*, 1169–1175.
- (281) Beard, M. C.; Turner, G. M.; Murphy, J. E.; Micic, O. I.; Hanna, M. C.; Nozik, A. J.; Schmittenmaer, C. A. *Nano Letters* **2003**, *3*, 1695–1699.
- (282) Guglietta, G. W.; Diroll, B. T.; Gaulding, E. A.; Fordham, J. L.; Li, S.; Murray, C. B.; Baxter, J. B. *ACS Nano* **2015**, *9*, 1820–1828.

## References

- (283) Sarkar, S.; Banerjee, S.; Swarnkar, A.; Mandal, P. *The Journal of Physical Chemistry C* **2021**, *125*, 10539–10548.
- (284) Talgorn, E.; Gao, Y.; Aerts, M.; Kunneman, L. T.; Schins, J. M.; Savenije, T. J.; Van Huis, M. A.; Van Der Zant, H. S. J.; Houtepen, A. J.; Siebbeles, L. D. A. *Nature Nanotechnology* **2011**, *6*, 733–739.
- (285) Staechelin, Y. U.; Deffner, M.; Krohn, S.; Castillo Delgadillo, C.; Niehaus, J. S.; Lange, H. *The Journal of Chemical Physics* **2022**, *156*, 061102.
- (286) Staechelin, Y. U.; Kroh, T.; Kärtner, F. X.; Lange, H. *Journal of the Optical Society of America B* **2023**, *40*, 2058.
- (287) Rebmann, J.; Werners, H.; Johst, F.; Dohrmann, M.; Staechelin, Y. U.; Strelow, C.; Mews, A.; Kipp, T. *Chemistry of Materials* **2023**, *35*, 1238–1248.
- (288) Wengler-Rust, S.; Staechelin, Y. U.; Lange, H.; Weller, H. *Small* **2024**, *20*, 2401388.
- (289) Kesarwani, S.; Juergensen, S.; Staechelin, Y. U.; Reich, S.; Schulz, F.; Lange, H. *The Journal of Chemical Physics* **2024**, *161*, 044702.
- (290) Miller, D. A. B.; Chemla, D. S.; Damen, T. C.; Gossard, A. C.; Wiegmann, W.; Wood, T. H.; Burrus, C. A. *Physical Review Letters* **1984**, *53*, 2173–2176.
- (291) Wen, G. W.; Lin, J. Y.; Jiang, H. X.; Chen, Z. *Physical Review B* **1995**, *52*, 5913–5922.
- (292) Combescot, M. *Physics Reports* **1992**, *221*, 167–249.
- (293) Park, K.; Deutsch, Z.; Li, J. J.; Oron, D.; Weiss, S. *ACS Nano* **2012**, *6*, 10013–10023.
- (294) Chaisakul, P.; Marris-Morini, D.; Rouifed, M.-S.; Isella, G.; Chrastina, D.; Frigerio, J.; Le Roux, X.; Edmond, S.; Coudevylle, J.-R.; Vivien, L. *Optics Express* **2012**, *20*, 3219.
- (295) Geiregat, P.; Rodá, C.; Tanghe, I.; Singh, S.; Di Giacomo, A.; Lebrun, D.; Grimaldi, G.; Maes, J.; Van Thourhout, D.; Moreels, I.; Houtepen, A. J.; Hens, Z. *Light: Science & Applications* **2021**, *10*, 112.
- (296) Scott, R.; Achtstein, A. W.; Prudnikau, A. V.; Antanovich, A.; Siebbeles, L. D. A.; Artemyev, M.; Woggon, U. *Nano Letters* **2016**, *16*, 6576–6583.
- (297) Schmitt-Rink, S.; Chemla, D.; Miller, D. *Advances in Physics* **1989**, *38*, 89–188.
- (298) Achtstein, A. W.; Prudnikau, A. V.; Ermolenko, M. V.; Gurinovich, L. I.; Gaponenko, S. V.; Woggon, U.; Baranov, A. V.; Leonov, M. Y.; Rukhlenko, I. D.; Fedorov, A. V.; Artemyev, M. V. *ACS Nano* **2014**, *8*, 7678–7686.
- (299) Diroll, B. T. *Nano Letters* **2020**, *20*, 7889–7895.
- (300) Diroll, B. T. *Nanotechnology* **2023**, *34*, 245706.
- (301) Hoffmann, M. C.; Monozon, B. S.; Livshits, D.; Rafailov, E. U.; Turchinovich, D. *Applied Physics Letters* **2010**, *97*, 231108.
- (302) Pein, B. C.; Chang, W.; Hwang, H. Y.; Scherer, J.; Coropceanu, I.; Zhao, X.; Zhang, X.; Bulović, V.; Bawendi, M.; Nelson, K. A. *Nano Letters* **2017**, *17*, 5375–5380.
- (303) Pein, B. C.; Lee, C. K.; Shi, L.; Shi, J.; Chang, W.; Hwang, H. Y.; Scherer, J.; Coropceanu, I.; Zhao, X.; Zhang, X.; Bulović, V.; Bawendi, M. G.; Willard, A. P.; Nelson, K. A. *Nano Letters* **2019**, *19*, 8125–8131.

- (304) Gollner, C.; Jutas, R.; Kreil, D.; Dirin, D. N.; Boehme, S. C.; Baltuška, A.; Kovalenko, M. V.; Pugžlys, A. *Advanced Optical Materials* **2022**, *10*, 2102407.
- (305) Funk, J. I. M.; Sochor, B.; Weller, H. *in Preparation*, Insights of the formation of CdSe nanoplatelets using a flow reactor.
- (306) Saleh, B. E. A.; Teich, M. C., *Fundamentals of photonics*; Wiley series in pure and applied optics; Wiley: New York, 1991.
- (307) Giovanni, D.; Chong, W. K.; Dewi, H. A.; Thirumal, K.; Neogi, I.; Ramesh, R.; Mhaisalkar, S.; Mathews, N.; Sum, T. C. *Science Advances* **2016**, *2*, e1600477.
- (308) Yang, Y.; Yang, M.; Zhu, K.; Johnson, J. C.; Berry, J. J.; Van De Lagemaat, J.; Beard, M. C. *Nature Communications* **2016**, *7*, 12613.
- (309) Cotter, D.; Girdlestone, H. P.; Moulding, K. *Applied Physics Letters* **1991**, *58*, 1455–1457.
- (310) Boles, M. A.; Engel, M.; Talapin, D. V. *Chemical Reviews* **2016**, *116*, 11220–11289.
- (311) Dong, A.; Chen, J.; Vora, P. M.; Kikkawa, J. M.; Murray, C. B. *Nature* **2010**, *466*, 474–477.
- (312) Schulz, F.; Pavelka, O.; Lehmkuhler, F.; Westermeier, F.; Okamura, Y.; Mueller, N. S.; Reich, S.; Lange, H. *Nature Communications* **2020**, *11*, 3821.
- (313) Schmidtke, C.; Eggers, R.; Zierold, R.; Feld, A.; Kloust, H.; Wolter, C.; Ostermann, J.; Merkl, J.-P.; Schotten, T.; Nielsch, K.; Weller, H. *Langmuir* **2014**, *30*, 11190–11196.
- (314) Rafipoor, M.; Koll, R.; Merkl, J.-P.; Fruhner, L. S.; Weller, H.; Lange, H. *Small* **2019**, *15*, 1803798.
- (315) Marino, E.; Keller, A. W.; An, D.; Van Dongen, S.; Kodger, T. E.; MacArthur, K. E.; Heggen, M.; Kagan, C. R.; Murray, C. B.; Schall, P. *The Journal of Physical Chemistry C* **2020**, *124*, 11256–11264.
- (316) Marino, E.; Kodger, T. E.; Wegdam, G. H.; Schall, P. *Advanced Materials* **2018**, *30*, 1803433.
- (317) Lee, J.-S.; Kovalenko, M. V.; Huang, J.; Chung, D. S.; Talapin, D. V. *Nature Nanotechnology* **2011**, *6*, 348–352.
- (318) Scheele, M. *Zeitschrift für Physikalische Chemie* **2015**, *229*, 167–178.
- (319) Kagan, C. R.; Murray, C. B. *Nature Nanotechnology* **2015**, *10*, 1013–1026.
- (320) Khatun, M. F.; Okamoto, T.; Biju, V. *Chemical Communications* **2023**, *59*, 13831–13834.
- (321) Tong, Y.; Yao, E.-P.; Manzi, A.; Bladt, E.; Wang, K.; Döblinger, M.; Bals, S.; Müller-Buschbaum, P.; Urban, A. S.; Polavarapu, L.; Feldmann, J. *Advanced Materials* **2018**, *30*, 1801117.
- (322) Tang, Y.; Poonia, D.; Van Der Laan, M.; Timmerman, D.; Kinge, S.; Siebbeles, L. D. A.; Schall, P. *ACS Applied Energy Materials* **2022**, *5*, 5415–5422.
- (323) Marino, E.; Sciortino, A.; Berkhout, A.; MacArthur, K. E.; Heggen, M.; Gregorkiewicz, T.; Kodger, T. E.; Capretti, A.; Murray, C. B.; Koenderink, A. F.; Messina, F.; Schall, P. *ACS Nano* **2020**, *14*, 13806–13815.

## References

- (324) Gross, M.; Haroche, S. *Physics Reports* **1982**, *93*, 301–396.
- (325) Cong, K.; Zhang, Q.; Wang, Y.; Noe, G. T.; Belyanin, A.; Kono, J. *Journal of the Optical Society of America B* **2016**, *33*, C80.
- (326) Rainò, G.; Utzat, H.; Bawendi, M.; Kovalenko, M. *MRS Bulletin* **2020**, *45*, 841–848.
- (327) Liu, Z.; Qin, X.; Chen, Q.; Jiang, T.; Chen, Q.; Liu, X. *Advanced Materials* **2023**, *35*, 2209279.
- (328) Yan, D.; Shan, Q.; Dong, Y.; Han, L.; Wu, X.; Peng, Y.; Zeng, H. *Chemical Communications* **2023**, *59*, 5365–5374.
- (329) Montanarella, F.; Biondi, M.; Hinterding, S. O. M.; Vanmaekelbergh, D.; Rabouw, F. T. *Nano Letters* **2018**, *18*, 5867–5874.
- (330) Lunz, M.; Bradley, A. L.; Chen, W.-Y.; Gerard, V. A.; Byrne, S. J.; Gun'ko, Y. K.; Lesnyak, V.; Gaponik, N. *Physical Review B* **2010**, *81*, 205316.
- (331) Pal, B. N.; Ghosh, Y.; Brovelli, S.; Laocharoensuk, R.; Klimov, V. I.; Hollingsworth, J. A.; Htoon, H. *Nano Letters* **2012**, *12*, 331–336.
- (332) Leatherdale, C. A.; Woo, W.-K.; Mikulec, F. V.; Bawendi, M. G. *The Journal of Physical Chemistry B* **2002**, *106*, 7619–7622.
- (333) Tomar, R.; Kulkarni, A.; Chen, K.; Singh, S.; Van Thourhout, D.; Hodgkiss, J. M.; Siebbeles, L. D.; Hens, Z.; Geiregat, P. *The Journal of Physical Chemistry C* **2019**, *123*, 9640–9650.
- (334) Liao, C.; Xu, R.; Xu, Y.; Zhang, C.; Xiao, M.; Zhang, L.; Lu, C.; Cui, Y.; Zhang, J. *The Journal of Physical Chemistry Letters* **2016**, *7*, 4968–4976.
- (335) Rodà, C.; Salzmann, B. B. V.; Wagner, I.; Ussembayev, Y.; Chen, K.; Hodgkiss, J. M.; Neyts, K.; Moreels, I.; Vanmaekelbergh, D.; Geiregat, P. *Nano Letters* **2021**, *21*, 10062–10069.
- (336) Tanghe, I.; Samoli, M.; Wagner, I.; Cayan, S. A.; Khan, A. H.; Chen, K.; Hodgkiss, J.; Moreels, I.; Thourhout, D. V.; Hens, Z.; Geiregat, P. *Nature Nanotechnology* **2023**, *18*, 1423–1429.
- (337) Brooks, J. L.; Warkentin, C. L.; Saha, D.; Keller, E. L.; Frontiera, R. R. *Nanophotonics* **2018**, *7*, 1697–1724.
- (338) Miao, T. J.; Tang, J. *The Journal of Chemical Physics* **2020**, *152*, 194201.
- (339) Halpert, J. E.; Morgenstern, F. S. F.; Ehrler, B.; Vaynzof, Y.; Credginton, D.; Greenham, N. C. *ACS Nano* **2015**, *9*, 5857–5867.
- (340) Hoeng, D.; Schulz, F.; Mueller, N. S.; Reich, S.; Lange, H. *The Journal of Chemical Physics* **2020**, *152*, 064710.
- (341) Arbouet, A.; Voisin, C.; Christofilos, D.; Langot, P.; Fatti, N. D.; Vallée, F.; Lermé, J.; Celep, G.; Cottancin, E.; Gaudry, M.; Pellarin, M.; Broyer, M.; Maillard, M.; Pileni, M. P.; Treguer, M. *Physical Review Letters* **2003**, *90*, 177401.
- (342) Hodak, J. H.; Martini, I.; Hartland, G. V. *The Journal of Physical Chemistry B* **1998**, *102*, 6958–6967.
- (343) Hodak, J. H.; Henglein, A.; Hartland, G. V. *The Journal of Chemical Physics* **2000**, *112*, 5942–5947.

- (344) Minutella, E.; Schulz, F.; Lange, H. *The Journal of Physical Chemistry Letters* **2017**, *8*, 4925–4929.
- (345) Simon, T.; Carlson, M. T.; Stolarczyk, J. K.; Feldmann, J. *ACS Energy Letters* **2016**, *1*, 1137–1142.
- (346) Amirav, L.; Alivisatos, A. P. *Journal of the American Chemical Society* **2013**, *135*, 13049–13053.
- (347) Lorenc, M.; Ziolk, M.; Naskrecki, R.; Karolczak, J.; Kubicki, J.; Maciejewski, A. *Applied Physics B: Lasers and Optics* **2002**, *74*, 19–27.
- (348) Lapini, A.; Vázquez, S. M.; Touceda, P. T.; Lima, M. *Journal of Molecular Structure* **2011**, *993*, 470–473.
- (349) Iliopoulos, K.; Potamianos, D.; Kakkava, E.; Aloukos, P.; Orfanos, I.; Couris, S. *Optics Express* **2015**, *23*, 24171.
- (350) Kovalenko, S. A.; Dobryakov, A. L.; Ruthmann, J.; Ernsting, N. P. *Physical Review A* **1999**, *59*, 2369–2384.
- (351) Beckwith, J. S.; Rumble, C. A.; Vauthey, E. *International Reviews in Physical Chemistry* **2020**, *39*, 135–216.
- (352) Liebel, M.; Schnedermann, C.; Wende, T.; Kukura, P. *The Journal of Physical Chemistry A* **2015**, *119*, 9506–9517.
- (353) Ziolk, M.; Naskrecki, R.; Karolczak, J. *Optics Communications* **2004**, *241*, 221–229.
- (354) UltrafastSystems Surface Xplorer Manual, <https://ultrafast.systems/wp-content/uploads/2021/07/SurfaceXplorerManual.pdf>, Accessed: 2024-3-14, 2015.
- (355) Megerle, U.; Pugliesi, I.; Schriever, C.; Sailer, C. F.; Riedle, E. *Applied Physics B* **2009**, *96*, 215–231.
- (356) Rasmusson, M.; Tarnovsky, A. N.; Akesson, E.; Sundström, V. *Chemical Physics Letters* **2001**, *335*, 201–208.
- (357) Surface Xplorer: Data Analysis Software by Ultrafast Systems, <https://ultrafast.systems/products/spectrometers-accessories/surface-xplorer/>, Accessed: 2023-12-20.





# A. Appendix

## A.1 Technical aspects of transient absorption spectroscopy

In this chapter, some more technical aspects of TA spectroscopy will be discussed. TA measurements on pure solvents were conducted to collect exemplary data of the so-called coherent artifact. These measurements are also used to demonstrate chirp correction and the examination of the instrument response function, which serves as an estimate for the time resolution. All measurements were performed on pure water in cuvettes with an optical path length of 2 mm, an excitation wavelength of 515 nm and an excitation fluence of 150  $\mu\text{J}/\text{cm}^2$  if not stated otherwise.

### Coherent artifact

As pump and probe pulses overlap temporarily in the sample, TA experiments suffer from unwanted signals, which overlay the actual sample response and thus complicate the evaluation of the data around zero delay time. Several non-linear processes can contribute to these unwanted signals. Cross-phase modulation (XPM) is usually regarded as the main contribution.<sup>347,348</sup> An intense laser pulse changes the refractive index of a medium when propagating through it. This phenomenon is termed the optical Kerr effect. The change in refractive index is linearly dependent on the optical intensity  $I(t)$  and leads to the redistribution of frequencies in the intense pulse itself (SPM) or any other co-propagating pulse (XPM).<sup>306</sup> As in TA experiments the probe pulse intensity is weak, only XPM between the pump and probe pulse affects the measured signal, while SPM of the probe pulse is negligible.<sup>348</sup> The change in the refractive index  $n(t)$  of the material (here: solvent and cuvette-material) can be described as

$$n(t) = n + n_2 I(t), \quad (\text{A.1})$$

where  $I(t)$  is the temporal envelope of the pump pulses intensity and  $n_2$  is the materials nonlinear refractive index.  $n_2$  depends on the third-order optical susceptibility  $\chi^{(3)}$  of the material<sup>306</sup>

$$n_2 = \frac{3\eta_0}{n^2\epsilon_0}\chi^{(3)}, \quad (\text{A.2})$$

where  $\eta_0$  is the impedance of free space and  $\epsilon_0$  is the electric permittivity of free space. Toluene exhibits a comparably high  $\chi_3$  value and therefore shows more pronounced XPM signals in TA measurements as n-hexane, which has a lower  $\chi_3$  value.<sup>349</sup> Figure A1 shows

qualitative agreement between the simulated XPM feature following reference<sup>347</sup> and the measured coherent artifact in water with a pump wavelength of 515 nm, indicating that XPM is the main contribution to the coherent artifact in this specific experimental configuration.

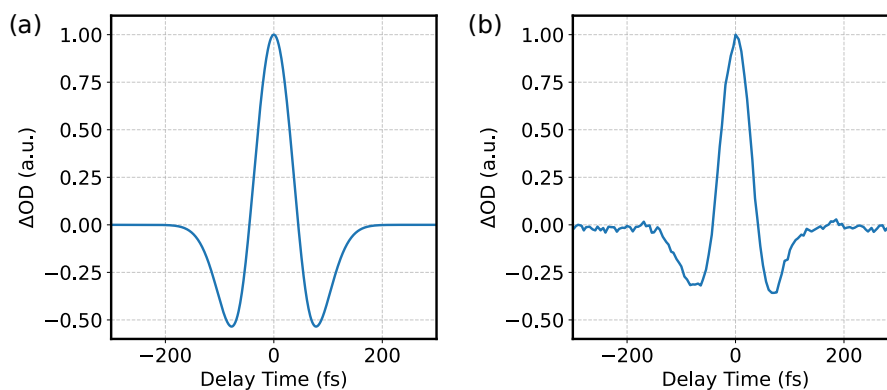


**Figure A1:** (a) Simulated XPM feature following Lorenc *et al.*<sup>347</sup> (b) Measured coherent artifact in pure water with a pump wavelength of 515 nm at a probe wavelength of 550 nm.

Two-photon absorption and stimulated Raman amplification can further contribute to the coherent artifact.<sup>347</sup> The spectral and temporal shape of the coherent artifact depend on many experimental parameters such as the used solvent and cuvette material, the pump pulses wavelength and duration as well as the probe pulses spectrum and chirp. For example, the occurrence of a Raman-induced artifact depends on the employed pump wavelength and is more pronounced if the difference between pump and probe wavelength is small.<sup>350,351</sup> Figure A2 exemplarily shows the coherent artifact measured with the setup employed in this work with several experimental configurations. Impulsive stimulated Raman scattering can produce an oscillating signal that lasts longer than the temporal pump-probe overlap and therefore, strictly speaking, cannot be considered a coherent artifact.<sup>352</sup> Still, it shall be mentioned here, as it is an unwanted signal originating from the cuvette material, the solvent or the substrate material (and not from the sample), which complicates data interpretation at earlier delay times.

### Chirp correction

Due to the group velocity dispersion on the probe pulse, the different spectral components of the probe pulse arrive at the sample at different times. This does not influence the measured dynamics but leads to a spectrally dependent time zero. As expected, the white-light probe pulse exhibits positive chirp, *i.e.* the longer wavelength components (low frequencies) travel faster than the shorter wavelength components (high frequencies).<sup>353</sup>

Every TA measurement begins at "negative delay times", *i.e.* the probe pulse travels through the sample before the pump pulse excites the sample. The pump pulse beam path is fixed, whereas the probe pulse passes the delay stage. The delay stage is now scanned towards positive delay times, extending the beam path of the probe pulse. At one point, the fast components of the probe pulse (longer wavelengths) are still ahead of the pump pulse, whereas

### A.1. Technical aspects of transient absorption spectroscopy

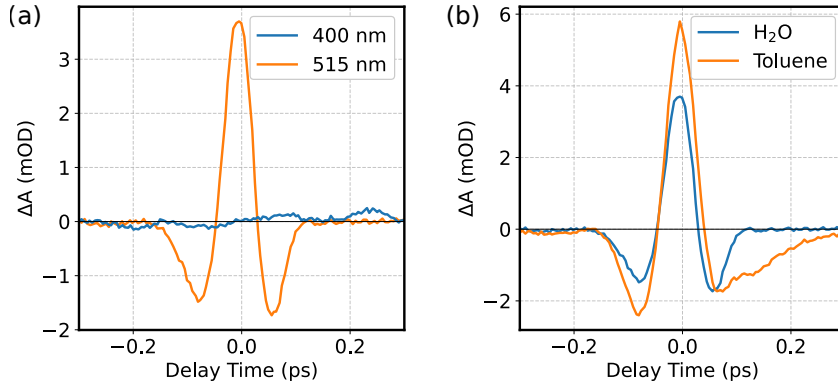


**Figure A2:** Coherent artifact measured in TA with different experimental conditions at a probe wavelength of 550 nm. (a) Coherent artifact measured in pure water with pump wavelengths of 400 nm and 515 nm at the same excitation fluence of 150  $\mu\text{J}/\text{cm}^2$ . (b) Coherent artifact in pure water and pure toluene with a pump wavelength of 515 nm and an excitation fluence of 150  $\mu\text{J}/\text{cm}^2$ .

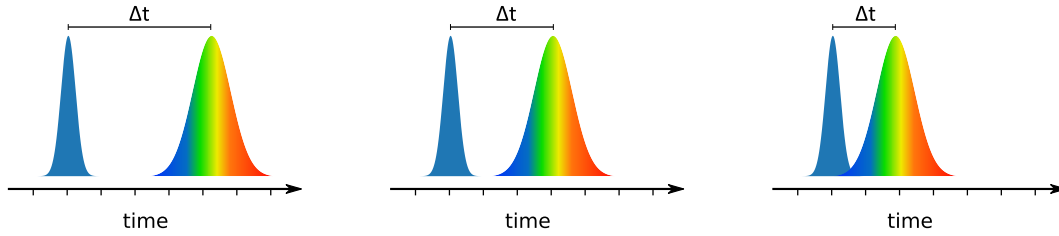


**Figure A3:** Visual representation of why the short wavelength part of the spectrum exhibits earlier time zero points. As the delay stage is scanned from negative delay time towards more positive delay times, the slow components of the probe pulse (short wavelengths) overlap with the pump pulse, while the fast components of the probe pulse (long wavelengths) are still ahead of the pump pulse.

the slow components of the probe pulse (shorter wavelengths) overlap with the pump pulse. This leads to an earlier time zero point for shorter wavelengths (*cf.* Figure A3). Figure A5 shows exemplarily that the chirp in the employed setup is approximately linear with the probe photon energy.

The software Surface Xplorer (Ultrafast Systems) was used to correct the measurements for this chirp. It allows to manually choose the time zero at certain wavelengths, interpolates the values with Equation (A.3) and shifts the data along the time-axis, yielding a data set with spectrally uniform time zero.<sup>354</sup> To manually choose time zero, the first point in time, at which there is contrast above the noise level, is used. In measurements that show a significant contribution of the coherent artifact, its maximum can also be used for this purpose. Figure A4 exemplarily shows the coherent artifact in a TA measurement before and after chirp correction.

$$t_0 = a \cdot \sqrt{\frac{b \cdot w^2 - 1}{c \cdot w^2 - 1}} + d \quad (\text{A.3})$$

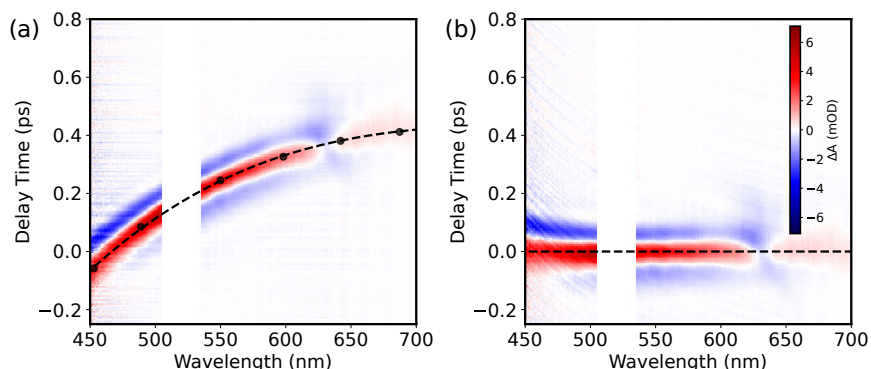


**Figure A4:** TA data of pure water with 515 nm excitation. Data around the excitation wavelength is omitted as it is disturbed by scattered pump photons reaching the spectrometer. (a) Before chirp correction. The manually chosen time zero points at several probe wavelengths are plotted as well as the fit of Equation (A.3) to these data points. (b) Same measurement after chirp correction.

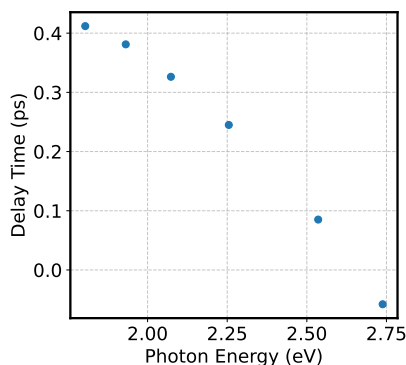


**Figure A5:** Time zero points at several probe wavelengths (same data as in Figure A4(a)) versus probe photon energy. The chirp on the white-light probe pulse is approximately linear with photon energy (and thus frequency).

## Time resolution

The temporal response function of a pump-probe experiment equals the pump-probe cross-correlation function.<sup>355,356</sup> The temporal envelope of the coherent artifact can be utilized to determine this cross-correlation function. Here, the temporal envelope of the coherent artifact at a probe wavelength of 550 nm was fitted with a Gaussian function to assess the FWHM of the temporal response function of the employed setup (see Figure A6). The determined temporal FWHM is 123 fs, but it is important to note that this value is dependent on the specific experimental conditions employed. Various schemes for the generation of pump and probe pulses were utilized in this work, resulting in variations in the FWHM of the temporal response function throughout the measurements. It is safe to assume that the temporal FWHM was well below 1 ps for all measurements presented in this work.

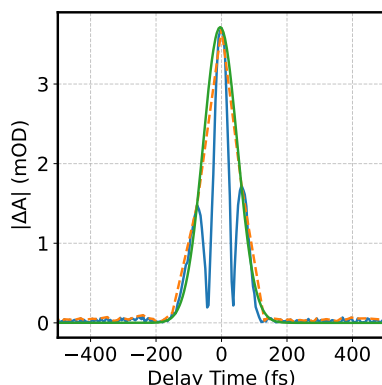


**Figure A6:** Absolute  $\Delta A$  signal of the coherent artifact (blue) with its temporal envelope (orange dotted line) and the Gaussian fit (green).

### Data correction

TA data was routinely processed using Surface Xplorer, a software provided by the manufacturer of the TA spectrometer, Ultrafast Systems,<sup>357</sup> according to the following sequence:

1. *Crop data to spectral range exhibiting acceptable signal-to-noise.* The Helios spectrometer records a broad spectral range, usually exceeding the actual white-light spectrum. Therefore, at both the blue and red end of the spectrum, data is unusable. Usually, the white-light generated inside a calcium fluoride crystal in the employed setup covers the spectral range from 340 to 700 nm, while the white-light generated inside a sapphire crystal covers the spectral range from 440 nm to 750 nm.
2. *Subtract scattered light.* In case the employed pump wavelength falls within the probe spectral range, scattered light from the pump pulse will hit the spectrometer and lead to a negative  $\Delta A$  signal. The same holds true for light emitted by the samples at wavelengths within the probe spectral range. As these signals are delay time-independent, they can be subtracted from the measurement by using differential spectra at negative delay times, which should always be recorded for this purpose. The subtraction usually works fine for the sample emission. The scattered pump pulse signal fluctuates with the pump laser fluence, whereby the correction often cannot be performed well, rendering the data in this spectral range unusable.
3. *Chirp correction.* The temporal chirp on the white-light pulse is corrected as described above.
4. *Time zero correction.* In some cases it might additionally be necessary to correct the time zero point of the measurement, effectively shifting the data along the delay time axis by a fixed delay. Usually after performing a chirp correction, this step is not needed, as correcting the chirp effectively means correcting the time zero point for every spectral component of the probe pulse.

Further data evaluation was conducted using self-written Python scripts.

## A.2 Supporting information for Chapter 5.2

### Size-dependent electron-phonon coupling in monocrystalline gold nanoparticles

This supporting information is reprinted with permission from Yannic U. Staechelin, Dominik Hoening, Florian Schulz and Holger Lange, *ACS Photonics* **2021**, 8, 752-757 - published by the American Chemical Society (ACS).

DOI: [10.1021/acsp Photonics.1c00078](https://doi.org/10.1021/acsp Photonics.1c00078)

# Size-dependent Electron-Phonon Coupling in Monocrystalline Gold Nanoparticles - Supporting Information

Yannic U. Staechelin,<sup>\*,†</sup> Dominik Hoening,<sup>†,‡</sup> Florian Schulz,<sup>†</sup> and Holger Lange<sup>†,‡</sup>

<sup>†</sup>*Institute of Physical Chemistry, Universität Hamburg, Martin-Luther-King-Platz 6, 20146*

*Hamburg, Germany*

<sup>‡</sup>*CUI: Advanced Imaging of Matter, Luruper Chaussee 146, 22761 Hamburg, Germany*

E-mail: [yannic.staechelin@chemie.uni-hamburg.de](mailto:yannic.staechelin@chemie.uni-hamburg.de)

Number of pages: 13

Number of figures: 6

Number of tables: 1

## Syntheses

### Materials

Ultrapure water was used for all syntheses. Tetrachloroauric(III)acid ( $\geq 99.0$  % trace metal basis), Cetrimoniumbromide (CTAB,  $\geq 99.0$  %), Cetrimoniumchloride (CTAC,  $\geq 98.0$  %), Sodium borohydrate ( $\text{NaBH}_4$ ,  $\geq 99.0$  %) and Ascorbic Acid ( $\geq 99.0$  %) were obtained from Sigma-Aldrich.

### Synthesis of the polycrystalline AuNPs

The polycrystalline PEGMUA-coated AuNPs were synthesized via seeded growth as described by Bastús *et al.*<sup>1</sup> and PEGylated as described previously.<sup>2</sup>

### Synthesis of the nearly monocrystalline AuNPs

Monocrystalline CTAC-coated AuNPs were synthesized via a slightly modified version of the protocol of Zheng *et al.*<sup>3</sup> To a 10 mL aqueous solution of  $\text{HAuCl}_4$  (0.25 mM) and CTAB (100 mM), 0.6 mL of an aqueous solution of  $\text{NaBH}_4$  (10 mM) was added via one-shot-injection while rapidly stirring the solution to obtain CTAB-capped Au clusters. The reaction mixture was stirred for 3 min with 1000 rpm. The solution was kept undisturbed for 3 h. *First growth step:* To an aqueous solution of CTAC (200 mM, 20 mL) and Ascorbic Acid (100 mM, 15 mL), 0.5 mL of the CTAB-capped Au clusters were added. An aqueous solution of  $\text{HAuCl}_4$  (0.5 mM, 20 mL) was added via one-shot-injection. The reaction mixture was stirred for 15 min at 300 rpm. After washing with water once, monocrystalline AuNPs with a diameter of 10.6 nm were obtained. Those were used for TA measurements and as seeds for further growth steps. *Second growth step:* A certain volume of the 10.6 nm seeds was added to an aqueous solution of CTAC (100 mM, 20 mL). This mixture was sonicated for 10 min. An aqueous solution of Ascorbic Acid (100 mM, 130  $\mu\text{L}$ ) was added rapidly. After stirring the solution for 1 min, an aqueous solution of  $\text{HAuCl}_4$  (0.5 mM, 20 mL) was added



dropwise within 1 h via a syringe pump at 27 °C. The reaction was kept stirring for 10 min and washed with water once to obtain nearly monocrystalline AuNPs of different diameters, depending on the used volume of seed solution. The concentration of the seed solution was determined via the method described by Haiss *et al.*<sup>4</sup> The needed amount of seed particles was calculated with (cf. Bastús *et al.*<sup>1</sup>)

$$d_{product}^3 = \frac{6m \cdot (Au)}{\pi \cdot \rho_{Au} \cdot N_{AuNP}} + d_{seed}^3, \quad (S1)$$

where  $d_{product}^3$  and  $d_{seed}^3$  are the diameters of the product and seed particles, respectively,  $m(Au)$  is the mass of added gold,  $\rho_{Au}$  is the density of gold and  $N_{AuNP}$  is the number of gold particles.

AuNPs of 21.5 nm, 25.8 nm, 31.0 nm, 36.6 nm, 38.9 nm and 74.4 nm diameter were obtained from the second growth step. The 74.4 nm particles were not used for transient absorption measurements, as XRD data indicated that the particles were not monocrystalline, having a mean crystallite size of  $43.1 \pm 13.6$  nm.

PEG and CTAC were used as stabilizing ligands to ensure sample stability during the transient absorption measurements. Influences of the ligand sphere on electron dynamics are not expected on the timescales investigated in this work.<sup>5</sup>

## Sample Characterization

### TEM

Size distributions were determined via TEM analysis, using a Joel JEM-1011 instrument operating at 100 kV. TEM images of all employed samples are shown in Figures S1 and S2. HR-TEM measurements were performed using a JEOL JEM 2200 FS (UHR) with a

CESCOR and a CETCOR corrector.

## Powder XRD

X-Ray diffraction was carried out on a Panalytical MPD X'Pert Pro using Cu K  $\alpha$  radiation. Crystallite sizes  $D$  were determined via the Scherrer equation<sup>8</sup>

$$D = \frac{K \cdot \lambda}{h \cdot \cos(\theta)}, \quad (\text{S2})$$

where  $K = 0.94$ ,  $\lambda$  is the wavelength of the X-ray radiation,  $h$  is the FWHM of the respective reflection at  $2\theta$ . The reflections were fitted with a pseudo-voigt function to determine the FWHM. (111), (200), (220) and (311) reflections of the gold fcc lattice were analyzed. The four obtained sizes were averaged. Table S1 shows the calculated values for all employed samples.

Table S1: Particle diameters determined via TEM-analysis and crystallite sizes derived from Powder-XRD measurements via Scherrer equation for the employed mono- and polycrystalline AuNPs.

monocrystalline AuNPs		polycrystalline AuNPs	
particle diameter	averaged crystallite size	particle diameter	averaged crystallite size
$10.6 \pm 1.0$	$9.3 \pm 2.5$	$12.3 \pm 0.8$	$4.9 \pm 2.1$
$21.5 \pm 0.9$	$20.0 \pm 2.2$	$18.6 \pm 1.4$	$8.4 \pm 2.8$
$25.8 \pm 0.7$	$23.4 \pm 1.9$	$27.9 \pm 2.5$	$13.1 \pm 3.5$
$31.0 \pm 1.0$	$27.2 \pm 6.5$	$44.6 \pm 2.8$	$17.6 \pm 6.8$
$36.6 \pm 1.0$	$28.9 \pm 3.8$	$56.2 \pm 5.6$	$21.5 \pm 13.7$
$38.9 \pm 1.6$	$33.5 \pm 7.5$	$71.8 \pm 7.1$	$25.1 \pm 15.0$

## UV-Vis

Linear Absorption spectra were recorded using a Varian Cary 50 spectrometer. The Python package Pymiescatt<sup>6</sup> was used to calculate the linear absorption spectra of all employed samples under consideration of their size distribution using Mie theory. The complex refractive index of gold was taken from Johnson and Christy.<sup>7</sup> The simulated spectra are compared to the measured spectra in Figure S4.

## Transient Absorption Spectroscopy

The TA setup was described previously.<sup>2</sup> The excitation wavelength was set to 330 nm. The pump beam was focused to a diameter of approximately 500  $\mu\text{m}$ . The optical density of the samples at the excitation wavelength was tuned to similar values for all the investigated samples to ensure comparability, since more absorbed energy leads to a higher electron temperature and therefore longer electron-phonon-coupling times. As the bleach shifts to shorter wavelengths with increasing time delay, the bleach maxima were determined by fitting a sum of three Gaussian functions to the transient absorption spectra. The bleach recovery dynamic was fitted using Equation S3. A Heaviside function  $H(t)$  was used for the rise. The electron-electron coupling time  $\tau_{th}$  was set to 450 fs.<sup>9-11</sup>

$$\Delta A = H(t) \cdot \left\{ a \cdot \left[ 1 - \exp\left(-\frac{t}{\tau_{th}}\right) \right] \cdot \exp\left(-\frac{t}{\tau_{el-ph}}\right) + d \cdot \left[ 1 - \exp\left(\frac{t}{\tau_{el-ph}}\right) \right] \right\} \quad (\text{S3})$$

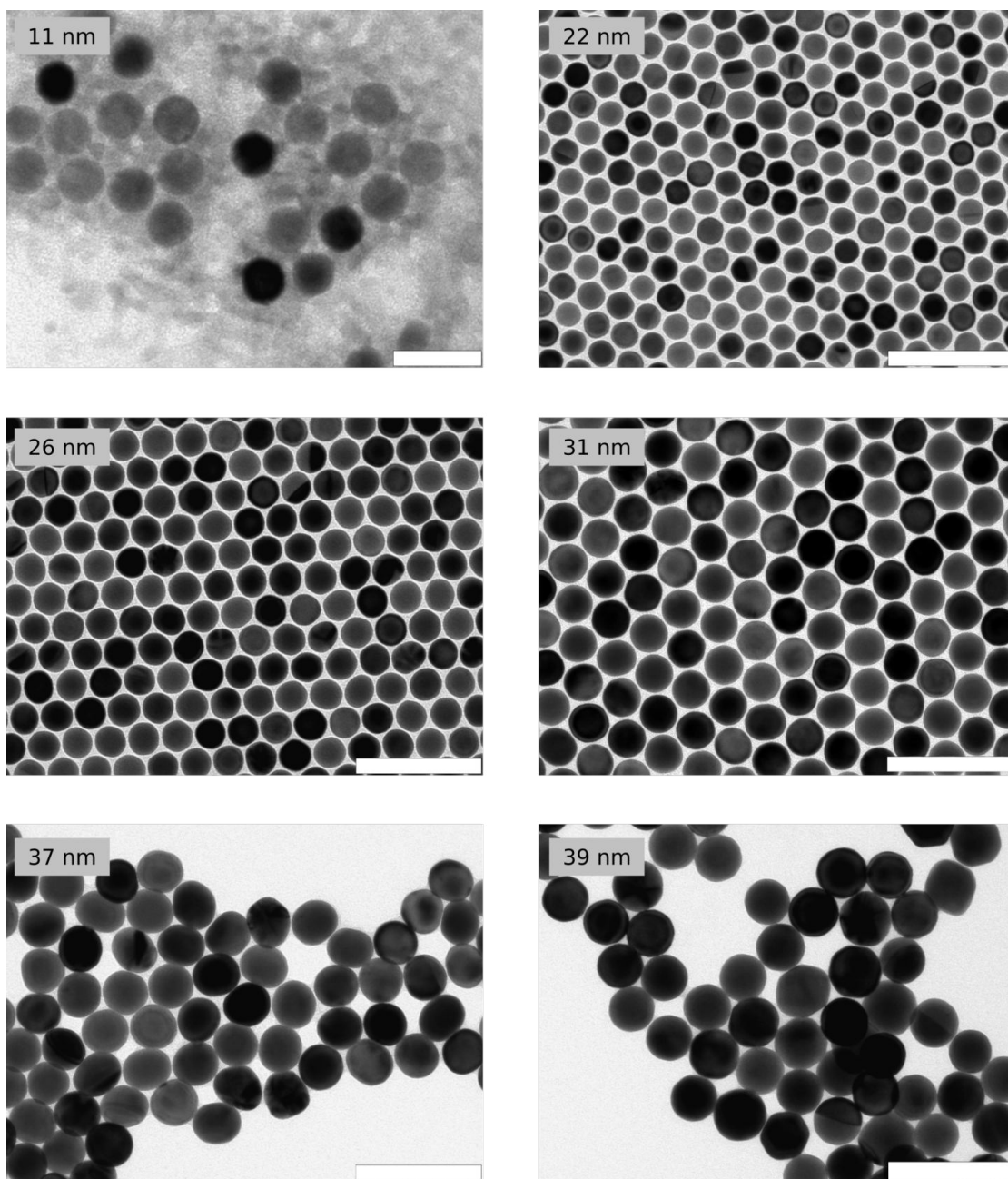


Figure S1: TEM images of the employed monocrystalline AuNPs. The scale bar corresponds to 20 nm for the 11 nm AuNPs and 100 nm for the other samples.

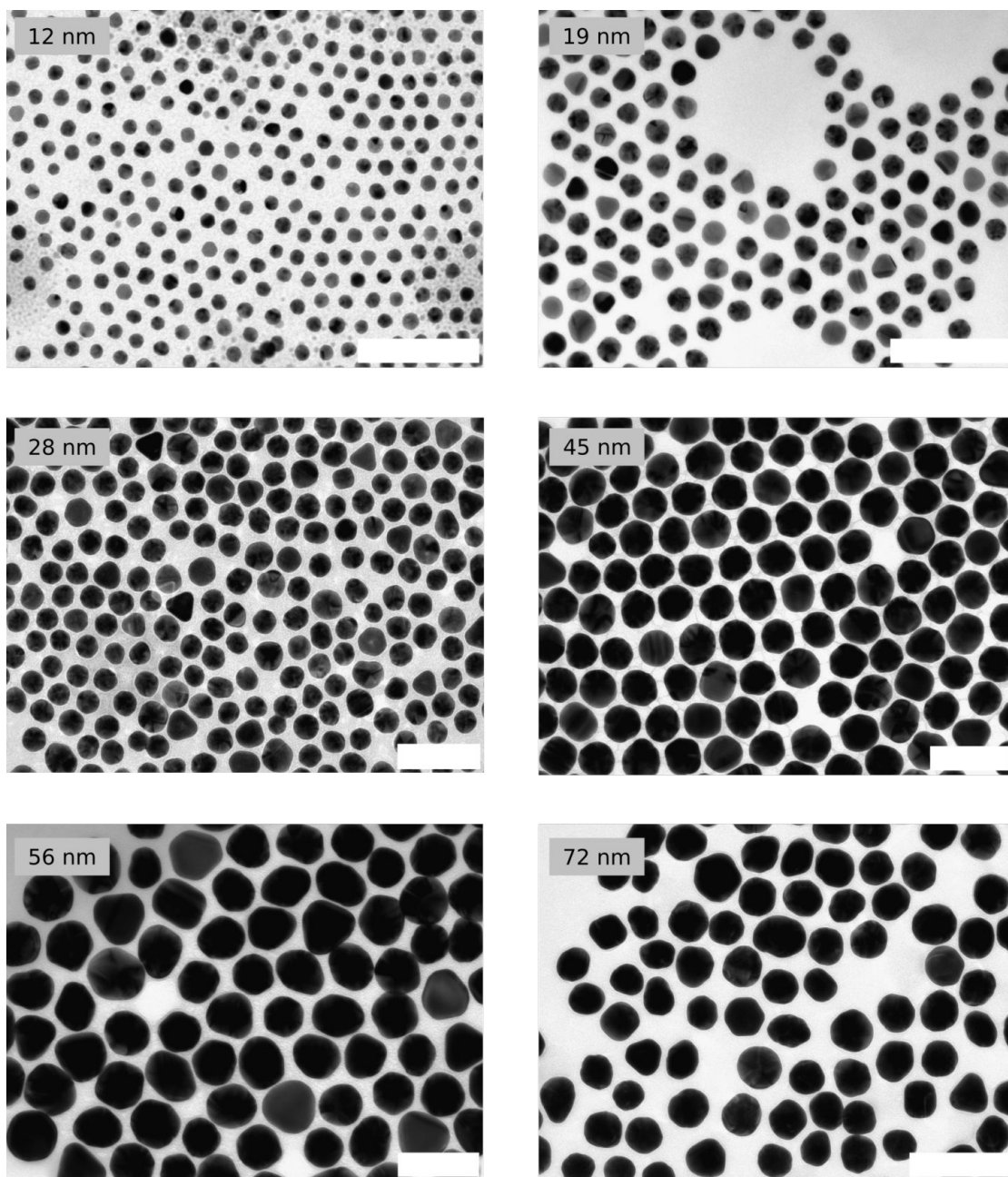


Figure S2: TEM images of the employed polycrystalline AuNPs. The scale bar corresponds to 200 nm for the 72 nm AuNPs and 100 nm for the other samples.

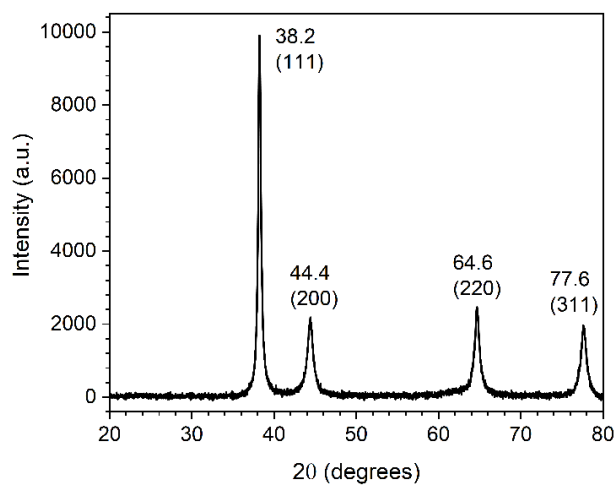


Figure S3: Exemplary XRD-pattern of polycrystalline AuNPs (45 nm diameter). The four reflections correspond to the Bragg reflections (111), (200), (220) and (311) of the face centered cubic (fcc) gold lattice.

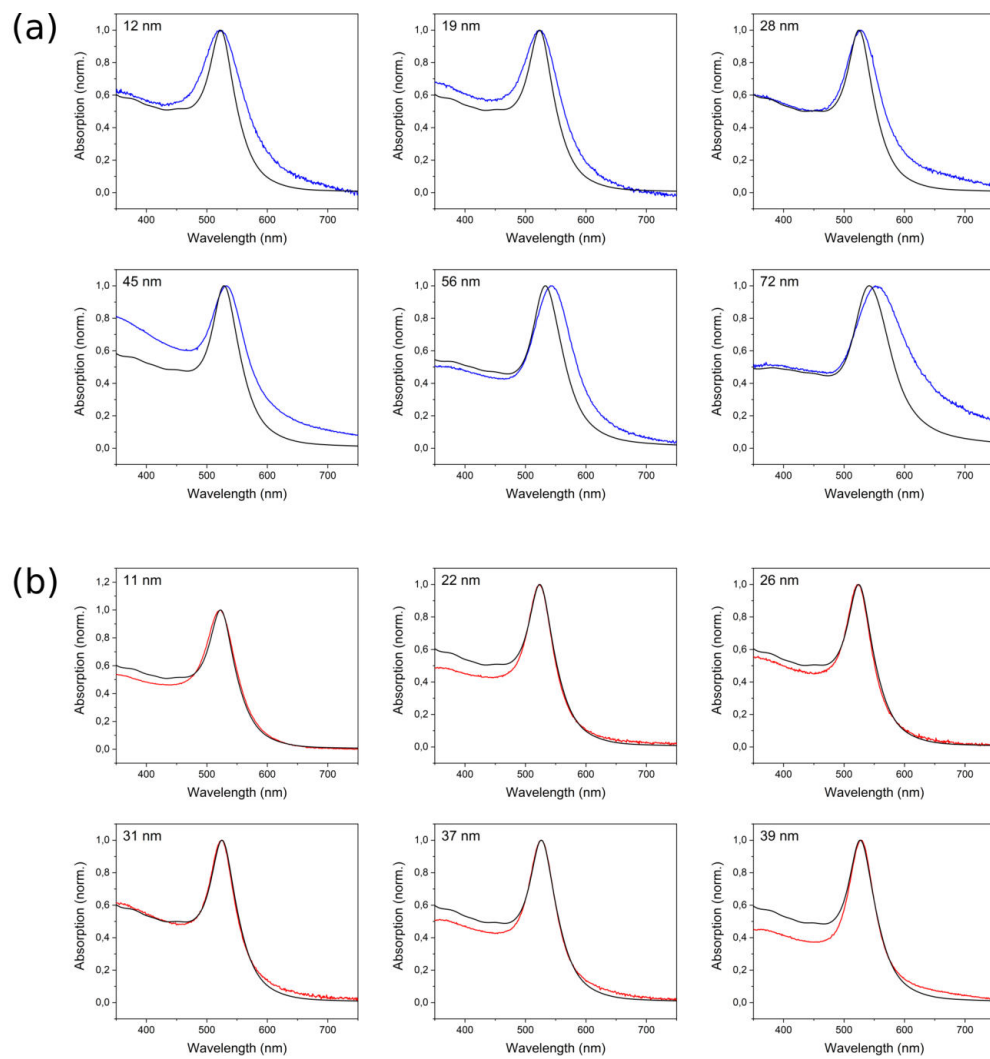


Figure S4: Comparison of experimental linear absorption spectra and simulated spectra using Pymiescatt (black) of (a) polycrystalline AuNPs (blue) and (b) monocrystalline AuNPs (red).

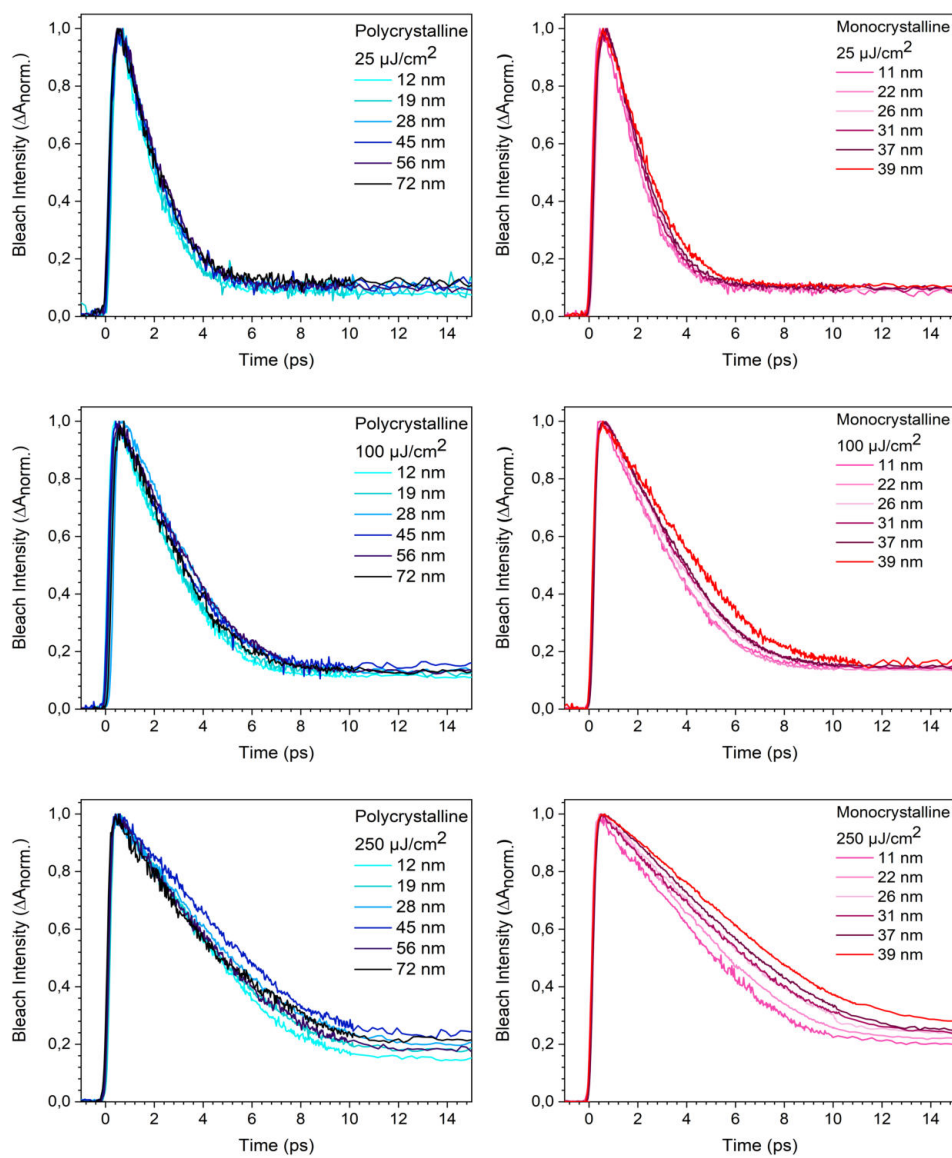


Figure S5: Normalized dynamics of the bleach recovery of poly- and monocrystalline AuNPs of different sizes. The pump fluences are indicated in the figure. The excitation wavelength was kept constant at 330 nm.



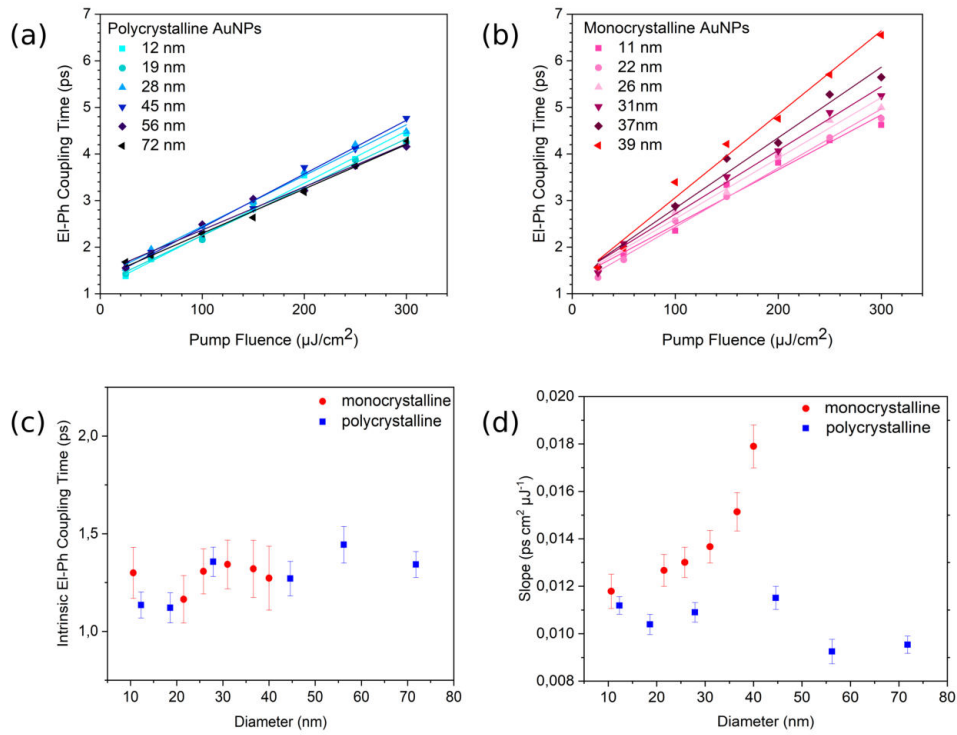


Figure S6: (a), (b) Electron-phonon coupling time versus pump fluence for poly- and monocrystalline samples. (c) intrinsic electron-phonon coupling time, determined by extrapolation of the linear fit in (a) and (b) to zero pump fluence. All observed values are in the range of 1.1 ps to 1.4 ps and a size dependency can neither be observed for mono- nor for polycrystalline AuNPs. (d) slope of the linear fits in (a) and (b).

## References

- (1) Bastús, N. G.; Comenge, J.; Puentes, V. Kinetically controlled seeded growth synthesis of citrate-stabilized gold nanoparticles of up to 200 nm: size focusing versus Ostwald ripening. *Langmuir* **2011**, *27*, 11098–11105.
- (2) Minutella, E.; Schulz, F.; Lange, H. Excitation-Dependence of Plasmon-Induced Hot Electrons in Gold Nanoparticles. *J. Phys. Chem. Lett.* **2017**, *8*, 4925–4929.
- (3) Zheng, Y.; Zhong, X.; Li, Z.; Xia, Y. Successive, Seed-Mediated Growth for the Synthesis of Single-Crystal Gold Nanospheres with Uniform Diameters Controlled in the Range of 5-150 nm. *Part. Part. Syst. Charact.* **2014**, *31*, 266–273.
- (4) Haiss, W.; Thanh, N. T. K.; Aveyard, J.; Fernig, D. G. Determination of size and concentration of gold nanoparticles from UV-vis spectra. *Anal. Chem.* **2007**, *79*, 4215–4221.
- (5) Arbouet, A.; Voisin, C.; Christofilos, D.; Langot, P.; Fatti, N. D.; Vallée, F.; Lermé, J.; Celep, G.; Cottancin, E.; Gaudry, M.; Pellarin, M.; Broyer, M.; Maillard, M.; Pileni, M. P.; Treguer, M. Electron-phonon scattering in metal clusters. *Phys. Rev. Lett.* **2003**, *90*, 177401.
- (6) Sumlin, B. J.; Heinson, W. R.; Chakrabarty, R. K. Retrieving the aerosol complex refractive index using PyMieScatt: A Mie computational package with visualization capabilities. *J. Quant. Spectrosc. Radiat. Transfer* **2018**, *205*, 127–134.
- (7) Johnson, P. B.; Christy, R. W. Optical Constants of the Noble Metals. *Phys. Rev. B* **1972**, *6*, 4370–4379.
- (8) Scherrer, P. Bestimmung der Größe und der inneren Struktur von Kolloidteilchen mittels Röntgenstrahlen. *Nachr. Ges. Wiss. Goettingen* **1918**, 98–100.

- (9) Del Fatti, N.; Voisin, C.; Achermann, M.; Tzortzakis, S.; Christofilos, D.; Vallée, F. Nonequilibrium electron dynamics in noble metals. *Phys. Rev. B* **2000**, *61*, 16956–16966.
- (10) Sun, C. K.; Vallée, F.; Acioli, L. H.; Ippen, E. P.; Fujimoto, J. G. Femtosecond-tunable measurement of electron thermalization in gold. *Phys. Rev. B: Condens. Matter Mater. Phys.* **1994**, *50*, 15337–15348.
- (11) Voisin, C.; Christofilos, D.; Loukakos, P. A.; Del Fatti, N.; Vallée, F.; Lermé, J.; Gaudry, M.; Cottancin, E.; Pellarin, M.; Broyer, M. Ultrafast electron-electron scattering and energy exchanges in noble-metal nanoparticles. *Phys. Rev. B* **2004**, *69*, 365.

### **A.3 Supporting information for Chapter 5.4**

#### **Impact of pump beam spot size on semiconductor carrier dynamics in optical-pump-terahertz-probe spectroscopy**

This supporting information is reprinted from Yannic U. Staechelin, Tobias Kroh, Franz X. Kärtner and Holger Lange, *Journal of the Optical Society of America B* **2023**, 40 (8), 2058-2063, CC BY 4.0 - published by Optica.

DOI: [10.6084/m9.figshare.23596269](https://doi.org/10.6084/m9.figshare.23596269)

## Impact of pump beam spot size on semiconductor carrier dynamics in optical-pump-terahertz-probe spectroscopy: supplement

**YANNIC U. STAEHELIN,<sup>1,\*</sup>  TOBIAS KROH,<sup>2,3</sup>  FRANZ X. KÄRTNER,<sup>2,3</sup>  AND HOLGER LANGE<sup>3,4</sup> **

<sup>1</sup>*Institute of Physical Chemistry, Universität Hamburg, Martin-Luther-King-Platz 6, 20146 Hamburg, Germany*

<sup>2</sup>*Center for Free-Electron Laser Science CFEL, Deutsches Elektronen-Synchrotron DESY, Hamburg, Germany*

<sup>3</sup>*The Hamburg Centre for Ultrafast Imaging, Luruper Chaussee 149, 22761 Hamburg, Germany*

<sup>4</sup>*Institute of Physics and Astronomy, University of Potsdam, Karl-Liebknecht-Straße 24, Potsdam, Germany*

\*[yannic.staechelin@uni-hamburg.de](mailto:yannic.staechelin@uni-hamburg.de)

---

This supplement published with Optica Publishing Group on 17 July 2023 by The Authors under the terms of the [Creative Commons Attribution 4.0 License](https://creativecommons.org/licenses/by/4.0/) in the format provided by the authors and unedited. Further distribution of this work must maintain attribution to the author(s) and the published article's title, journal citation, and DOI.

Supplement DOI: <https://doi.org/10.6084/m9.figshare.23596269>

Parent Article DOI: <https://doi.org/10.1364/JOSAB.496228>

# Impact of Pump Beam Spot Size on Semiconductor Carrier Dynamics in Optical-Pump-THz-Probe Spectroscopy: supplemental document

## 1. CALCULATION OF THE OVERLAP FACTOR

To calculate how much the effective THz probe spectrum is distorted by the spatially inhomogeneous excitation density of the sample in the measurement of a thin photoexcited film, the frequency-dependent spot size of the THz probe beam at the sample position is required. This spot size  $w(\nu)$  can be obtained in two different ways: (i) By mapping out the focused beam directly, as we did in this study, or alternatively (ii) by mapping out the collimated beam and computing the focused beamsize based on that result.

For (i), the THz focus was knife-edged while the THz time-domain signal ( $E(t)$ , TDS) was recorded (see Figure S1(a)). The measured THz-electric field was Fourier-transformed to obtain the corresponding knife-edged THz spectra  $E(\nu)$ , shown in Figure S1(b). As highlighted by Figure S1(c), this dataset contains a knife-edge scan for each frequency component of the probe pulse. The beam size  $w_1(\nu)$  at each frequency is then obtained by fitting to  $E(\nu)^2$  using

$$E^2(x) = E_0^2 + \frac{E_{max}^2}{2} \left( 1 - \operatorname{erf} \left( \frac{\sqrt{2}(x - x_0)}{w_0} \right) \right), \quad (S1)$$

where  $E^2$  is the position-dependent THz intensity,  $E_0^2$  is the background THz intensity,  $E_{max}^2$  is the maximal THz intensity,  $x$  is the position of the knife-edge,  $x_0$  is the knife-edge position with half of the maximal power, erf is the error function and  $w_0$  is the  $1/e^2$  beam radius of the focused beam. The obtained widths  $w_0(\nu)$  are shown in Figure S1(d).

Alternatively, the radius of the collimated beam between the first and second OAP  $w_1$  could be measured. The radius of the focused beam  $w_0$  could be calculated from that using [1]

$$w_0(\nu) = \frac{M^2 \cdot f \cdot c}{\pi \cdot w_1 \cdot \nu}, \quad (S2)$$

where  $M^2$  is the laser beam quality factor,  $f$  is the focal length of the employed off-axis parabolic mirror and  $\lambda$  is the wavelength of the THz radiation.  $w_1$  is the  $1/e^2$  radius of the intensity, which equals the  $1/e$  radius of the electric field. Note, this assumes  $f \gg w_1$  and the input beam to be a collimated Gaussian beam.

The spatial THz electric field distribution at the focus can be modelled using a spherical two-dimensional Gaussian function for each frequency component of the THz spectrum.

$$E(x, y, \nu) = \exp \left( - \left( \frac{(x - x_0)^2}{2\sigma(\nu)^2} + \frac{(y - y_0)^2}{2\sigma(\nu)^2} \right) \right) \quad (S3)$$

The variance  $\sigma$  is calculated from the  $1/e$  radius of the electric field  $w_1$  via  $\sigma(\nu) = 1/\sqrt{2} w_1(\nu)$  [2]. We assume low excitation density, at which the spatial distribution of charge carriers in the sample resembles the spatial intensity profile of the optical pump pulse. In analogy to the probe-beam characterization, the pump beam size was also determined by a knife-edge scan. The spatial charge carrier distribution can also be described by a two-dimensional gaussian function:

$$F(x, y) = \exp \left( - \left( \frac{(x - x_0)^2}{2\sigma_{pump}^2} + \frac{(y - y_0)^2}{2\sigma_{pump}^2} \right) \right) \quad (S4)$$

with  $\sigma_{pump} = 0.5 w_{pump}$ , where  $w_{pump}$  is the  $1/e^2$  radius of the intensity of the pump beam. Now we weight the electric field Gaussian functions of each frequency component of the THz probe pulse with the distribution of charge carriers to take into account that the sample is inhomogeneously excited.

$$E_{eff}(x, y, \nu) = E(x, y, \nu) \cdot F(x, y) \quad (S5)$$

$$E_{eff}(x, y, \nu) = \exp\left(-\left(\frac{(x-x_0)^2}{2\sigma(\nu)^2} + \frac{(y-y_0)^2}{2\sigma(\nu)^2}\right)\right) \cdot \exp\left(-\left(\frac{(x-x_0)^2}{2\sigma_{pump}^2} + \frac{(y-y_0)^2}{2\sigma_{pump}^2}\right)\right) \quad (S6)$$

$$E_{eff}(x, y, \nu) = \exp\left(-\frac{(x-x_0)^2}{2\sigma(\nu)^2\sigma_{pump}^2(\sigma(\nu)^2 + \sigma_{pump}^2)^{-1}} - \frac{(y-y_0)^2}{2\sigma(\nu)^2\sigma_{pump}^2(\sigma(\nu)^2 + \sigma_{pump}^2)^{-1}}\right) \quad (S7)$$

Integration over the whole sample area now gives the pump-profile weighted THz electric field

$$G(\nu) = \int_{-\infty}^{\infty} \int_{-\infty}^{\infty} E_{eff}(x, y, \nu) dx dy \quad (S8)$$

The volume under a two-dimensional gaussian curve is given by

$$V = \int_{-\infty}^{\infty} \int_{-\infty}^{\infty} A \exp\left(-\left(\frac{(x-x_0)^2}{2\sigma_x^2} + \frac{(y-y_0)^2}{2\sigma_y^2}\right)\right) dx dy = 2\pi A\sigma_x\sigma_y. \quad (S9)$$

Using

$$\sigma_x^2 = \sigma_y^2 = \frac{1}{\sigma(\nu)^2\sigma_{pump}^2(\sigma(\nu)^2 + \sigma_{pump}^2)}, \quad (S10)$$

this leads to

$$G(\nu) = 2\pi \left(\frac{\sigma(\nu)^2\sigma_{pump}^2}{\sigma(\nu)^2 + \sigma_{pump}^2}\right)^2. \quad (S11)$$

Now dividing G by the actual THz electric field H, where H is

$$H(\nu) = \int_{-\infty}^{\infty} \int_{-\infty}^{\infty} E(x, y, z) dx dy = 2\pi\sigma(\nu)^2, \quad (S12)$$

gives the overlap factor OF.

$$OF = \frac{G(\nu)}{H(\nu)} = \frac{2\pi \left(\frac{\sigma(\nu)^2\sigma_{pump}^2}{\sigma(\nu)^2 + \sigma_{pump}^2}\right)^2}{2\pi\sigma(\nu)^2} = \frac{\sigma_{pump}^2}{\sigma(\nu)^2 + \sigma_{pump}^2} \quad (S13)$$

With  $\sigma(\nu) = 1/\sqrt{2} w_0(\nu)$  and  $\sigma_{pump} = 0.5 w_{pump}$ , this yields

$$OF(\nu) = \frac{1}{2} \left(\frac{w_{pump}^2}{w_0(\nu)^2 + \frac{1}{2}w_{pump}^2}\right). \quad (S14)$$

## 2. KNIFE-EDGE MEASUREMENT OF THE THz BEAM

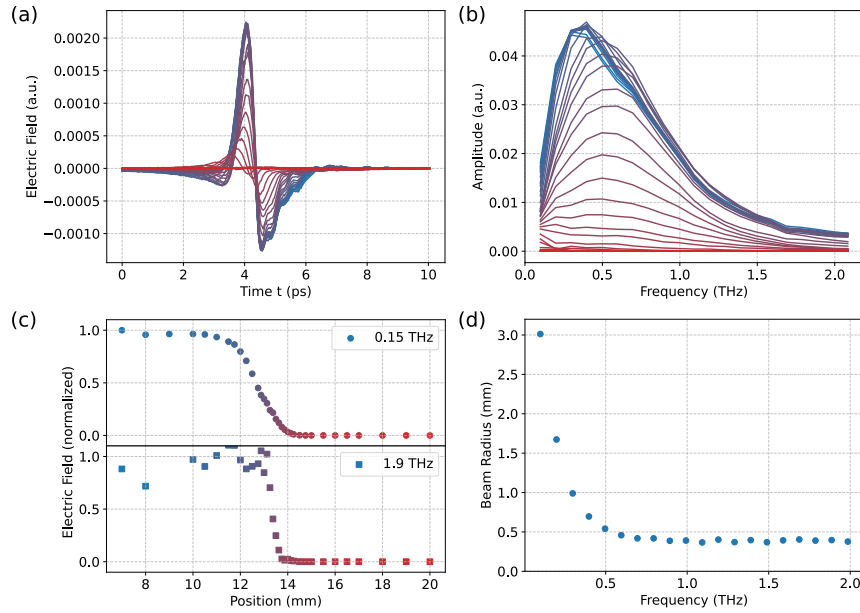


**Fig. S1.** Knife-edge data of the focused THz beam. (a) Measured THz pulses at different knife-edge positions. From blue to red: knife-edge did not block THz beam at all to knife-edge did block THz beam completely. (b) Fourier-transformed THz spectra of pulses plotted in (a). (c) Relative electric field amplitude for three exemplary frequencies. (d) Beam radii as determined for each THz frequency.

## 3. SAMPLES

Hexagonal CdS nanowires were synthesized using a solvothermal approach with cadmium diethyldithiocarbamate ( $\text{Cd}(\text{DDTC})_2$ ) as single-source precursor and ethylenediamine (en) as coordinating solvent. Nanowires with a diameter of around 50 nm and lengths exceeding 25  $\mu\text{m}$  were obtained after a reaction time of 48 h at 200  $^\circ\text{C}$  [3]. For THz measurements a concentrated dispersion of the nanowires in ethanol was dropcasted onto a 1" Teflon substrate and dried under nitrogen flow. The used 1" Si-wafer was obtained from Plano GmbH and had a thickness of 300  $\mu\text{m}$ .

## 4. MEASUREMENTS ON CADMIUM SELENIDE NANOWIRES

Pump beam radius dependent OPTP spectra were also measured on CdS nanowires to validate our results. The same trends as for the Si wafer are observed and can be described by our calculated overlap factors.



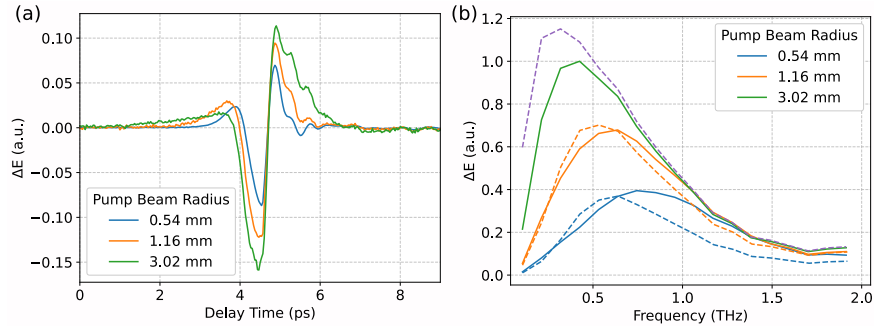


**Fig. S2.** (a) Photoinduced changes in the THz waveform  $\Delta E$  transmitted through a CdS nanowire sample 100 ps after excitation with  $\lambda = 400$  nm. (b) The solid lines show the differential electric field after excitation with pump beam of different radii (Fourier-transform of data in (a)). Dashed lines show data based on the simulation. Using the overlap factors plotted in Figure 2(c), the purple dashed line shows the actual differential electric field for an infinite large pump beam spot size, calculated from the data measured with a pump beam radius of 3.02 nm. From this, we can calculate the differential electric field for the pump beam radii of 0.54 nm and 1.16 nm (dashed orange and green lines).

## REFERENCES

1. E. Hecht, *Optics* (Pearson, Boston, 2017).
2. B. E. A. Saleh and M. C. Teich, *Fundamentals of Photonics* (Wiley, New York, 1991).
3. T. Dufaux, J. Boettcher, M. Burghard, and K. Kern, "Photocurrent Distribution in Graphene-CdS Nanowire Devices," *Small* **6**, 1868–1872 (2010).

## A.4 Supporting information for Chapter 5.6

### **Electron donor-specific surface interactions promote the photocatalytic activity of metal-semiconductor nanohybrids**

This supporting information is reprinted from Soenke Wengler-Rust, Yannic U. Staechelin, Holger Lange and Horst Weller, *Small*, **2024**, 20, 2401388, CC BY 4.0 Deed - published by Wiley-VCH GmbH.

DOI: [10.1002/sml.202401388](https://doi.org/10.1002/sml.202401388)



## Supporting Information

for *Small*, DOI 10.1002/smll.202401388

Electron Donor-Specific Surface Interactions Promote the Photocatalytic Activity of  
Metal-Semiconductor Nanohybrids

*Soenke Wengler-Rust\**, *Yannic U. Staechelin*, *Holger Lange* and *Horst Weller\**

# Supporting Information

## Electron Donor-Specific Surface Interactions Promote the Photocatalytic Activity of Metal-Semiconductor Nanohybrids

Soenke Wengler-Rust<sup>1</sup>, Yannic U. Staechelin<sup>1</sup>, Holger Lange<sup>1,2</sup>, and Horst  
Weller<sup>1,2,3</sup>

<sup>1</sup>Institut für Physikalische Chemie, Universität Hamburg, Hamburg, Germany

<sup>2</sup>The Hamburg Centre for Ultrafast Imaging, Hamburg, Germany

<sup>3</sup>Fraunhofer IAP-CAN, Hamburg, Germany

### **S1 Synthetic Parameters of Pt-tipped CdSe/CdS Dot-in-Rods**

The CdSe/CdS dot-in-rods (DRs) were synthesized by a seeded-growth procedure according to the report by Carbone et al.<sup>[1]</sup> The CdSe/CdS DRs used for all measurements, except the measurement row investigating the charge-separated state (CSS) feature, had an average length of  $29.3 \pm 3.4$  nm and a diameter of  $4.1 \pm 0.4$  nm and were prepared from CdSe seeds with a diameter of 2.3 nm (cf. Figure S1a). The diameters of the CdSe seeds were deduced from their absorption spectra based on the calculations by Mulvaney et al.<sup>[2;3]</sup>, whereas the CdSe/CdS DRs dimensions were determined from transmission electron microscopy (TEM) measurements (400 nanoparticles (NPs) were evaluated). Platinum tips were grown on the DRs by thermal decomposition of Pt(II) acetylacetonate, following known reports.<sup>[4]</sup> This hot-injection synthesis always yields a distribution of DRs with a single, two or more and

no Pt tip.<sup>[5;4]</sup> The amount of added Pt precursor, reaction time and temperature were kept low, in order to favor the growth of single Pt tips over the growth of especially large or multiple Pt domains on a single DR. We opted for the deposition of single tips, as single-tipped DRs were shown to achieve higher quantum efficiency in hydrogen production ( $QE_{H_2}$ ) compared to DRs with multiple tips due to faster electron transfer to the acceptor and reduced probability of charge recombination.<sup>[6;7]</sup> Besides that, large Pt-NPs induce scattering, thus complicating optical experiments. After conducting the Pt deposition, 48% of the DRs had a single, large Pt tip (tip diameter  $\geq 2$  nm - left inset Figure S1a), 24% had a single, small Pt tip (tip diameter  $< 2$  nm - right inset Figure S1a), only 1% had two Pt tips at both ends of the DR and 27% had no Pt tip. The number and size of Pt tips was derived from TEM micrographs ( $>200$  NPs were evaluated). In Figure S1b+c a high-angle annular dark field scanning TEM (HAADF STEM) measurement and a high resolution TEM (HRTEM) micrograph of the Pt-tipped DRs are shown, evidencing that the small tips on the DRs consist of Pt.

After the synthesis, the CdSe/CdS DRs and the Pt-tipped CdSe/CdS DRs were dispersed in toluene and passivated with phosphonate ligands, while the latter were additionally capped with oleic acid and oleylamine. These native ligands were exchanged by 11-mercaptoundecanoic acid (MUA) in order to transfer the NPs to aqueous suspension, following literature-known procedures.<sup>[8;9]</sup>

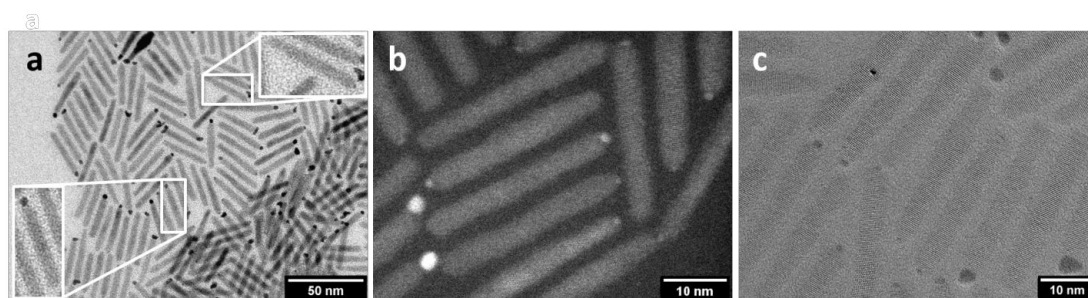


Figure S1: a) Transmission electron microscopy (TEM), b) high-angle annular dark field scanning TEM (HAADF STEM) and c) high resolution TEM (HRTEM) measurement of the Pt-tipped DRs. The left and right inset in a) show a DR with a single, large and small Pt tip, respectively. It is clearly visible that the domains grown on the DRs tips consist of Pt, having a higher atomic number ( $Z$ ) than Cd, S and Se and thus appearing brighter in the dark-field measurement and darker in the HRTEM.

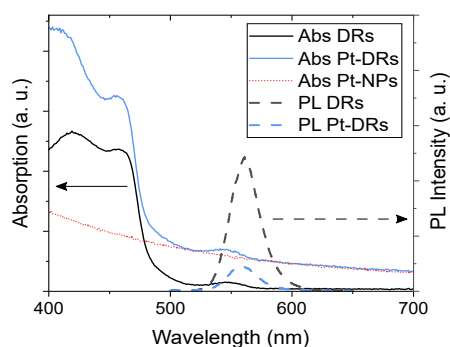


Figure S2: Static absorption spectra of bare CdSe/CdS DRs (black line), Pt-tipped DRs (blue line) and Pt-NPs (red, dotted line) and photoluminescence (PL) spectra of bare DRs (black, dashed line) and Pt-tipped DRs (blue, dashed line) in toluene.

## S2 Electron Donor-Induced Agglomeration of Colloidal Pt-CdSe/CdS DRs

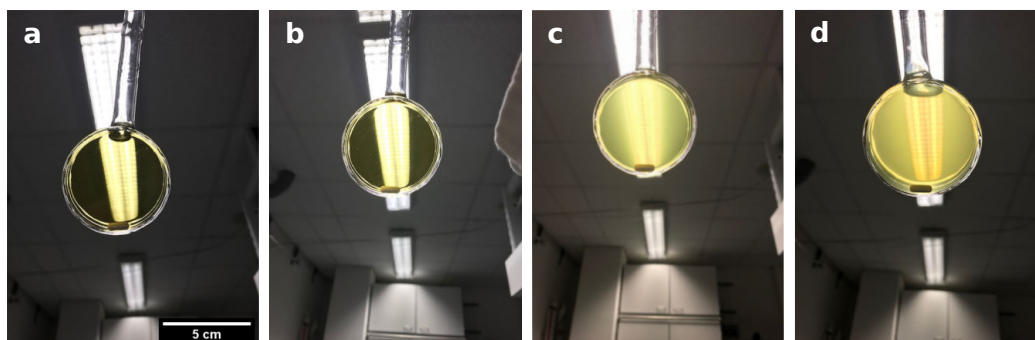


Figure S3: Photos of the colloidal Pt-CdSe/CdS DRs in water with a) MeOH, b)  $\text{Na}_2\text{SO}_3$ , c)  $\text{Na}_2\text{S}$  &  $\text{Na}_2\text{SO}_3$  and d) KOH & MeOH as EDA added in the quartz-glass cuvette right before illumination. The suspensions scatter light in the presence of  $\text{Na}_2\text{S}$  &  $\text{Na}_2\text{SO}_3$  and KOH & MeOH, caused by EDA-induced agglomeration of the NPs. An approximate scale bar is shown in a).

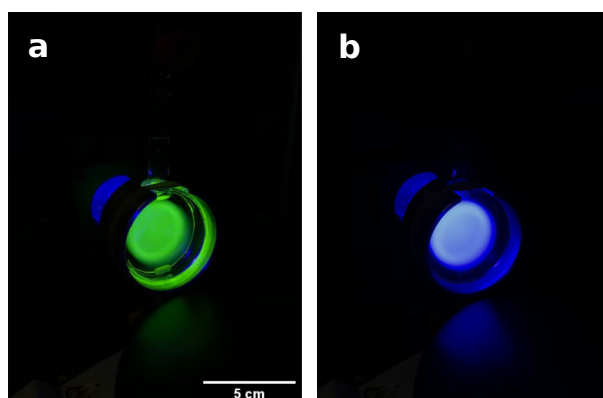


Figure S4: Photos of the colloidal Pt-CdSe/CdS DRs in water with a) MeOH and b)  $\text{Na}_2\text{S}$  &  $\text{Na}_2\text{SO}_3$  as EDAs added in the quartz-glass cuvette under illumination during steady-state hydrogen production measurements. While the NPs emit green light in the presence of the alcohol, the agglomerated NPs only scatter the blue LED light in the presence of sulfide & sulfite. An approximate scale bar is shown in a).

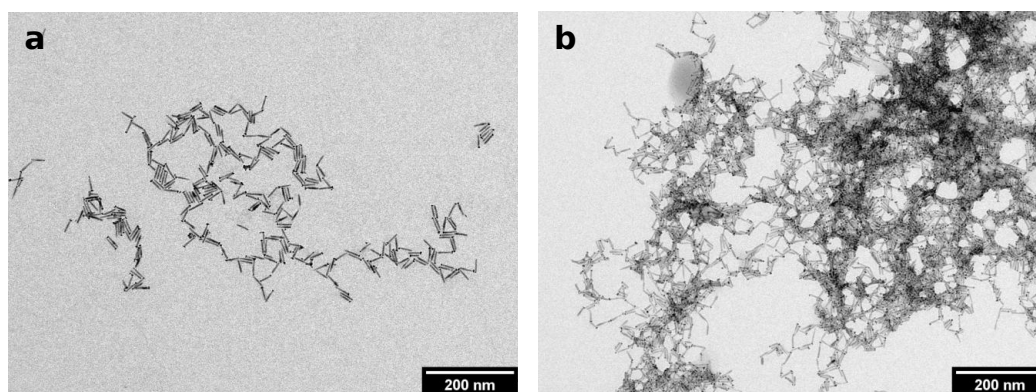


Figure S5: TEM measurements of MUA-capped Pt-CdSe/CdS DRs in water in the presence of IPA at a) neutral pH and b) pH 11. At increased pH the NPs agglomerate. The agglomeration is even stronger at pH 14, however the large amount of KOH inhibits imaging via TEM.

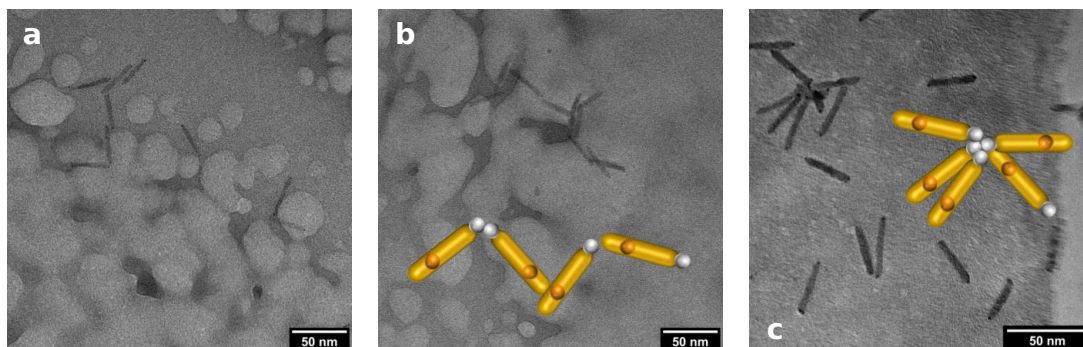


Figure S6: Cryo-TEM measurements of MUA-capped and Pt-tipped CdSe/CdS DRs a),b) in water and c) in the presence of hydroxide, after precipitation and redispersion at pH 6.9 and 9.8, respectively. Many DRs assembled tip-to-tip in the aqueous suspension. The sketches of attached Pt-DRs are a guide to the eye.

### S3 Static and Time-Resolved Absorption and Photoluminescence of Pt-Tipped CdSe/CdS DRs

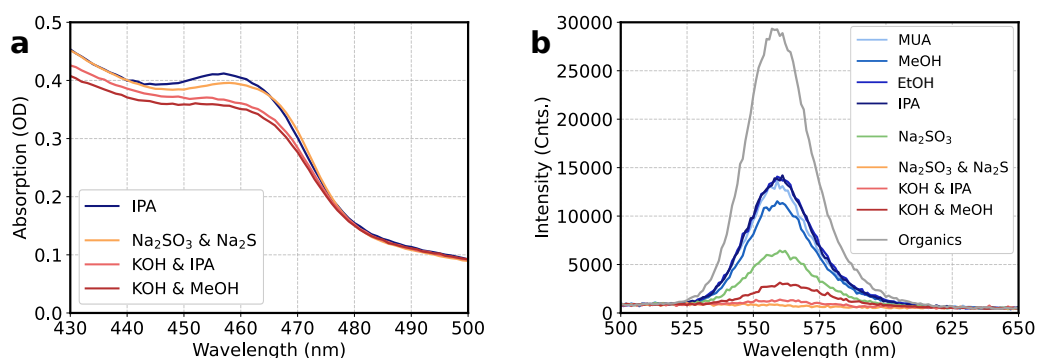


Figure S7: a) Static absorption and b) PL spectra of MUA-capped, Pt-tipped CdSe/CdS DRs in water (MUA), in the presence of different EDAs (IPA, MeOH, EtOH, KOH & IPA, KOH & MeOH, Na<sub>2</sub>SO<sub>3</sub>, Na<sub>2</sub>S & Na<sub>2</sub>SO<sub>3</sub>) and in toluene, capped with non-polar, organic ligands (organics). The PL originates from the CdSe core and all PL peaks are shifted bathochromically with respect to the CdSe core feature due to the Stokes shift (cf. Figures 2a,b and 4a).<sup>[10]</sup> In the presence of the EDA mixture of Na<sub>2</sub>S & Na<sub>2</sub>SO<sub>3</sub> and the mixture of KOH & alcohol an additional bathochromic shift occurs. The PL peaks are located at 558-560 nm in the presence of alcohols, Na<sub>2</sub>SO<sub>3</sub> and without EDA (MUA), whereas 562 and 563 nm for KOH & IPA and KOH & MeOH, no clear peak for Na<sub>2</sub>S & Na<sub>2</sub>SO<sub>3</sub>.



Electron Donor	MUA	MeOH	EtOH	IPA
QY <sub>PL</sub> (%)	3	3	3	4

Table S1: PL quantum yields of MUA-capped, Pt-tipped CdSe/CdS DRs in water (MUA) and in the presence of different diffusion-limited EDAs (MeOH, EtOH, IPA).

Electron Donor	KOH & IPA	KOH & MeOH	Na <sub>2</sub> SO <sub>3</sub>	Na <sub>2</sub> S & Na <sub>2</sub> SO <sub>3</sub>
QY <sub>PL</sub> (%)	0	0	1	0

Table S2: PL quantum yields of MUA-capped, Pt-tipped CdSe/CdS DRs in water in the presence of surface-active EDAs (KOH & IPA, KOH & MeOH, Na<sub>2</sub>SO<sub>3</sub>, Na<sub>2</sub>S & Na<sub>2</sub>SO<sub>3</sub>).

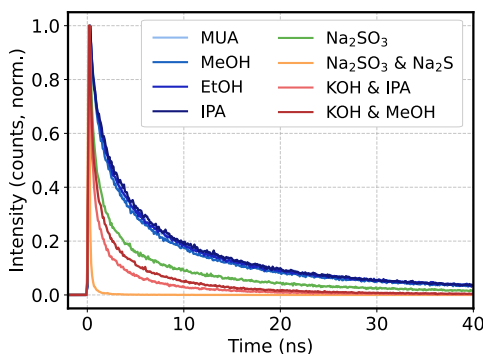


Figure S8: PL decay kinetics of MUA-capped, Pt-tipped CdSe/CdS DRs in the presence of different EDAs.

## S4 Steady-State Hydrogen Production Measurements

By plotting the measured hydrogen volumes against time and fitting the data points linearly, the hydrogen production rate was derived (Figure S9 - the error bars were derived from the relative error of the hydrogen calibration measurements (see Section S4.3)). Following, the quantum efficiency for hydrogen generation  $QE_{H_2}$  was calculated from this hydrogen production rate  $\frac{N_{H_2}}{t}$  (molecules H<sub>2</sub> per second) and the number of absorbed photons per time  $\frac{N_{Photons}}{t}$ :

$$QE_{H_2} = \frac{\frac{N_{H_2}}{t} * 2}{\frac{N_{Photons}}{t}}$$

The number of absorbed photons per time was calculated from the power of the LED, the optical density (OD) of the sample and the energy of a single photon at 445 nm. For

determining the OD of the respective sample, a spectrometer equipped with an integrating sphere was used (see experimental section).

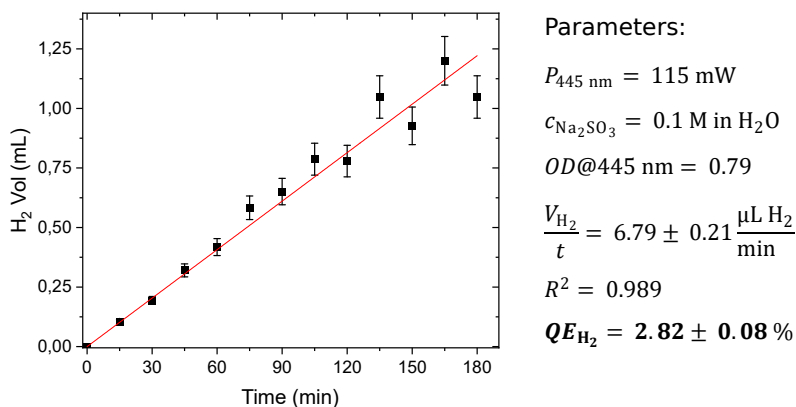


Figure S9: Steady-state hydrogen production measurement of Pt-tipped CdSe/CdS DRs using sodium sulfite as a sacrificial EDA. The measurement was conducted using a GC. The datapoints were fitted linearly for determining the hydrogen production rate. Measurement and fitting parameters, as well as calculated  $QE_{\text{H}_2}$  are listed.

#### S4.1 Calibration of Hydrogen Volumes in Gas Chromatography

A GC calibration was conducted to enable precise determination of the unknown hydrogen volumes inside the cuvette during the steady-state hydrogen generation measurements. For this purpose, distinct volumes of pure hydrogen gas were injected into the cuvette, which was filled with 45 mL water and 5 mL IPA and previously purged with nitrogen. Subsequently, gas aliquots were taken from the cuvette and injected into the GC for generating a calibration curve. By taking the gas aliquots for calibration directly from the cuvette, the experimental conditions and the process of aliquot withdrawal are precisely reproduced and therefore incorporated into the calibration.

#### S4.2 Calibration of LED Power

The power of the LED was calibrated using a power meter sensor (Thorlabs S425C Thermal Power Sensor Head, 0.19-20  $\mu\text{m}$ , 10 W and digital console Thorlabs PM100D Compact Power and Energy Meter Console). A plano-convex lens (Thorlabs N-BK7 Plano-Convex Lens, AR

Coating 350 - 700 nm) was used for focusing the LED beam onto the power meter sensor head. Since the entire beam is focused on the sensor head, the small divergence and the slightly non-uniform power density along the cross-section of the beam are irrelevant (cf. Figure S10a). Light scattering at the second cuvette window was determined and subtracted by repeating the measurement, using cuvettes of different optical paths length and without a cuvette inside. The power of the LED beam was measured 1. after passing a cuvette filled with water and 2 cm optical path length ( $P_{2\text{cm}}$ , Figure S10a), 2. after passing a cuvette filled with water and 4 cm optical path length ( $P_{4\text{cm}}$ , Figure S10b), 3. without a cuvette in the beam path ( $P_0$ , Figure S10c). The first measurement considers the attenuation of the excitation power at the first cuvette window and due to the solvent, however it also contains an attenuation of power due to the second cuvette window. The measured power  $P_{2\text{cm}}$  is therefore slightly lower than the power that actually excites the NP sample ( $P_{\text{PC}}$ ). The power that would have passed an empty cuvette was calculated first:

$$P_{\text{EmptyCuvette}} = P_{2\text{cm}} - P_{4\text{cm}} + P_{2\text{cm}}$$

Eventually, the power that hits the sample ( $P_{\text{PC}}$ ) without the contribution of the second cuvette window ( $\frac{P_0 - P_{\text{EmptyCuvette}}}{2}$ ) is obtained:

$$P_{\text{PC}} = \frac{P_0 - P_{\text{EmptyCuvette}}}{2} + P_{2\text{cm}}$$

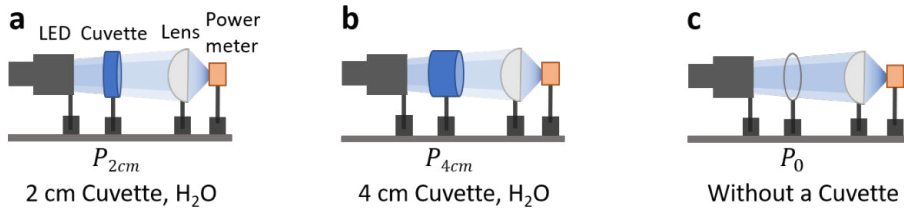


Figure S10: Three measurements conducted for calibrating the excitation power. A power meter was used for measuring the power of the LED beam a) after passing a cuvette filled with water and 2 cm optical path length, b) after passing a cuvette filled with water and 4 cm optical path length, c) without a cuvette in the beam path.

### S4.3 Error Bars in Steady-State Hydrogen Production Measurements

The error bars are generally derived from the standard error of the fit used for determining the hydrogen production rate. However, for the sample without added EDA (MUA) another batch of Pt-DRs was used, showing a comparable photocatalytic activity (see Section S5). The error bar of the MUA measurement was derived from the measurement with the largest difference in  $QE_{H_2}$ : the IPA sample ( $\frac{3\%}{2.6\%} = 1.15 \rightarrow$  error bar of 15 %).

## S5 Alternative Batch of Pt-Tipped CdSe/CdS DRs

For the static UV-Vis spectroscopy and the steady-state hydrogen measurements on the sample without added electron donating agent (EDA) (MUA-sample) another batch of Pt-DRs was used. This alternative batch showed comparable photocatalytic activity (see Figure S11a, the obtained  $QE_{H_2}$  in the presence of IPA, KOH & IPA and KOH & MeOH are very similar to the ones of the original batch displayed in Figure 3), as well as static absorption and absorbance (Figure S11b+c).

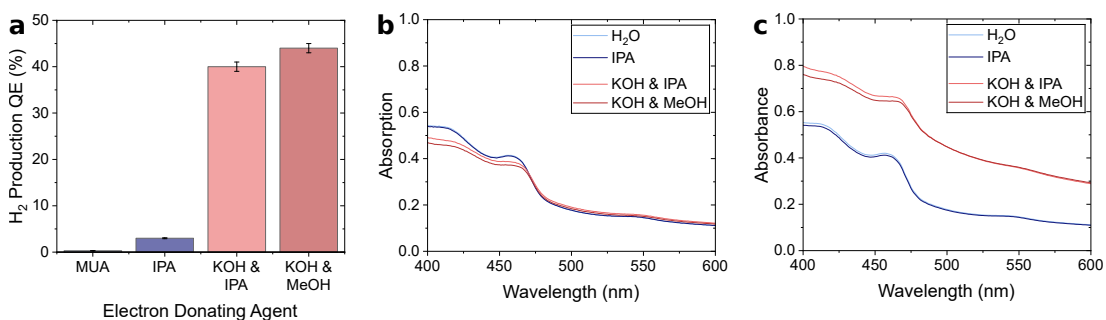


Figure S11: a) Hydrogen production quantum efficiencies, b) static absorption and c) absorbance spectra for an alternative batch of Pt-tipped CdSe/CdS DRs in the presence of different EDAs.

## S6 Charge-Separated State Feature

The Pt-CdSe/CdS DRs used for the charge-separated state (CSS) measurements were synthesized using the same CdSe seeds as for the DRs used for the other measurements (seed diameter of 2.3 nm). The rods had an average length of  $36.7 \pm 2.7$  nm and a diameter of  $4.2 \pm 0.3$  nm. For determining the rods size parameters, 200 NPs were evaluated in TEM

micrographs. After tipping, 71% of the NPs had a single Pt tip, 20% had two tips, 9% had no tip (150 Pt-DRs were evaluated in TEM micrographs - cf. Figure S12). The shoulder that eventually develops into the positive CSS feature occurs already after 1 ps, as would be expected from the fast electron transfer into the Pt tip (cf. Figure S13).<sup>[11]</sup>

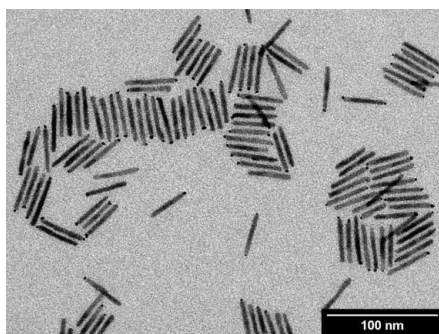


Figure S12: TEM micrograph of Pt-CdSe/CdS DRs used for the CSS measurements.

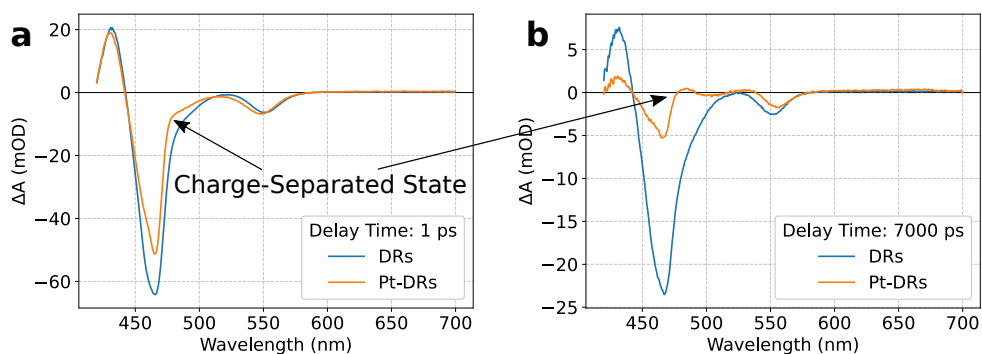
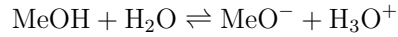


Figure S13: Transient absorption spectra of Pt-tipped CdSe/CdS DRs (orange line) and bare CdSe/CdS DRs (blue line) in water at a) 1 ps and b) 7 ns delay time. The shoulder, that eventually develops into the positive CSS-feature for the Pt-tipped DRs is already visible at 1 ps.

## S7 Dissociation of Alcoholic EDAs at pH 14

For the KOH & IPA and KOH & MeOH mixtures at pH 14, some of the alcoholic EDAs dissociate. In the case of MeOH the following equilibrium results:



with  $\text{MeO}^-$  as the methoxide anion. For this equilibrium the  $\text{p}K_a$  value can be determined:

$$\text{p}K_a = -\log \left( \frac{[\text{H}_3\text{O}^+] * [\text{MeO}^-]}{[\text{MeOH}]} * 1 \frac{\text{L}}{\text{mol}} \right)$$

with the square brackets indicating the concentration of the respective species.

$$\Rightarrow 10^{-\text{p}K_a} = \frac{[\text{H}_3\text{O}^+] * [\text{MeO}^-]}{[\text{MeOH}]} * 1 \frac{\text{L}}{\text{mol}}$$

Eventually, the concentration of formed methoxide can be calculated:

$$[\text{MeO}^-] = 10^{-\text{p}K_a} * \frac{[\text{MeOH}]}{[\text{H}_3\text{O}^+]} * 1 \frac{\text{mol}}{\text{L}}$$

The  $\text{p}K_a$  value of MeOH is 15.3,<sup>[12]</sup> and 10 vol% of MeOH were introduced, which corresponds to a concentration of  $2.48 \frac{\text{mol}}{\text{L}}$ .

$$[\text{MeO}^-] = 10^{-15.3} * \frac{2.48 \frac{\text{mol}}{\text{L}}}{10^{-14} \frac{\text{mol}}{\text{L}}} * 1 \frac{\text{mol}}{\text{L}} = 1.24 * 10^{-1} \frac{\text{mol}}{\text{L}}$$

Analogous in the presence of IPA ( $\text{p}K_a = 17.1$ ,<sup>[12]</sup>  $[\text{IPA}] = 1.31 \frac{\text{mol}}{\text{L}}$ ):

$$[\text{IPA}^-] = 10^{-17.1} * \frac{1.31 \frac{\text{mol}}{\text{L}}}{10^{-14} \frac{\text{mol}}{\text{L}}} * 1 \frac{\text{mol}}{\text{L}} = 1.04 * 10^{-3} \frac{\text{mol}}{\text{L}}$$

with  $[\text{IPA}^-]$  as the concentration of the IPA alkoxide.

## References

- [1] L. Carbone, C. Nobile, M. De Giorgi, F. D. Sala, G. Morello, P. Pompa, M. Hytch, E. Snoeck, A. Fiore, I. R. Franchini, M. Nadasan, A. F. Silvestre, L. Chiodo, S. Kudera, R. Cingolani, R. Krahne, L. Manna, *Nano Letters* **2007**, *7*, 10 2942.
- [2] J. Jasieniak, L. Smith, J. Van Embden, P. Mulvaney, M. Califano, *The Journal of Physical Chemistry C* **2009**, *113*, 45 19468.
- [3] W. W. Yu, L. Qu, W. Guo, X. Peng, *Chemistry of Materials* **2003**, *15*, 14 2854.
- [4] S. E. Habas, P. Yang, T. Mokari, *Journal of the American Chemical Society* **2008**, *130*, 11 3294.
- [5] J. K. Utterback, J. L. Ruzicka, H. R. Keller, L. M. Pellows, G. Dukovic, *Annual review of physical chemistry* **2020**, *71* 335.
- [6] Y. Nakibli, P. Kalisman, L. Amirav, *The Journal of Physical Chemistry Letters* **2015**, *6*, 12 2265.
- [7] T. Simon, M. T. Carlson, J. K. Stolarczyk, J. Feldmann, *ACS Energy Letters* **2016**, *1*, 6 1137.
- [8] R. Costi, A. E. Saunders, E. Elmalem, A. Salant, U. Banin, *Nano Letters* **2008**, *8*, 2 637.
- [9] L. Amirav, A. P. Alivisatos, *The Journal of Physical Chemistry Letters* **2010**, *1*, 7 1051.
- [10] J. R. Lakowicz, *Principles of Fluorescence Spectroscopy*, Springer, **2006**.
- [11] T. O'Connor, M. S. Panov, A. Mereshchenko, A. N. Tarnovsky, R. Lorek, D. Perera, G. Diederich, S. Lambright, P. Moroz, M. Zamkov, *ACS Nano* **2012**, *6*, 9 8156.
- [12] E. P. Serjeant, B. Dempsey, *IUPAC Chemical Data Series* **1979**, *23*.

## A.5 Supporting information for Chapter 5.7

### Incorporation strategy for organic dyes into gold nanoparticle superlattices

This supporting information is reprinted with permission from Shivani Kesarwani, Sabrina Juergensen, Yannic U. Staechelin, Stephanie Reich, Florian Schulz and Holger Lange, *The Journal of Chemical Physics* **2024**, 161, 044702 - published by the American Institute of Physics (AIP Publishing).

DOI: [10.1063/5.0209021](https://doi.org/10.1063/5.0209021)



## Supplementary Material

for

### Incorporation strategy for organic dyes into gold nanoparticle superlattices

S. Kesarwani,<sup>1</sup> S. Juergensen,<sup>2</sup> Y. U. Staechelin,<sup>1</sup> S. Reich,<sup>2</sup> F. Schulz,<sup>3</sup> H. Lange<sup>4,5</sup>

<sup>1</sup> Institut für Physikalische Chemie, Universität Hamburg, 20146 Hamburg, Germany

<sup>2</sup> Department of Physics, Freie Universität Berlin, 14195 Berlin, Germany

<sup>3</sup> Institute of Nanostructure and Solid State Physics, University of Hamburg, Hamburg, Germany

<sup>4</sup> The Hamburg Centre for Ultrafast Imaging, Universität Hamburg, 22761 Hamburg, Germany

<sup>5</sup> Department of Physics and Astronomy, Universität Potsdam, Potsdam, Germany

(\*Electronic mail: holger.lange@uni-hamburg.de)

## S1. ITC ANALYSIS

### Experimental

*<sup>1</sup>H-NMR spectroscopy*- All NMR experiments were carried out on a Bruker 600 MHz Avance III HD spectrometer (14.09 T, 600.13 MHz for <sup>1</sup>H) at 298 K in deuterated dimethyl sulfoxide (DMSO-d<sub>6</sub>). One-dimensional <sup>1</sup>H spectra were obtained utilizing a 30° excitation pulse and a relaxation delay of 1.0 s. The spectra were acquired with a spectral width of 12019.23 Hz and 65536 time domain data points by recording 64 scans. <sup>1</sup>H chemical shifts were referenced to the solvent signal. All spectra were processed utilizing Topspin Version 4.1.4., applying zero filling and an exponential multiplication of the FID with a line broadening factor of 0.3 Hz. The samples were suspended in 0.6 mL of DMSO-d<sub>6</sub>.

*Mass spectrometry*- Mass spectrometry was done with an Agilent 6224 LC-TOF system in high resolution mode. Samples were dissolved in deuterated chloroform (CDCl<sub>3</sub>), 1 mg/mL). Spectra were recorded in a m/z-range of 110-3200.

*Fourier transform infrared (FTIR) spectroscopy*- Fourier transform infrared (FTIR) spectra were recorded using a Varian 660 FT-infrared spectrometer equipped with an Attenuated Total Reflectance (ATR) unit. Samples were dissolved in deuterated chloroform and were used in liquid state.

### Structure

Fig. S1 and Fig. S2 show the structure of cyanine7-amine and ITC. The NMR-spectra of the modified dye (ITC) included some impurities from the synthesis, but could unambiguously be assigned based on the data from the unmodified dye (Cy7) and the 2D-NMR spectra. The shift of the methylene protons at C-47 and their coupling to C-49 at 127 ppm evidenced in HMBC-2D-data confirmed the formation of the isothiocyanate. After binding to the AuNP, all non-binding impurities are removed in the subsequent purification steps.

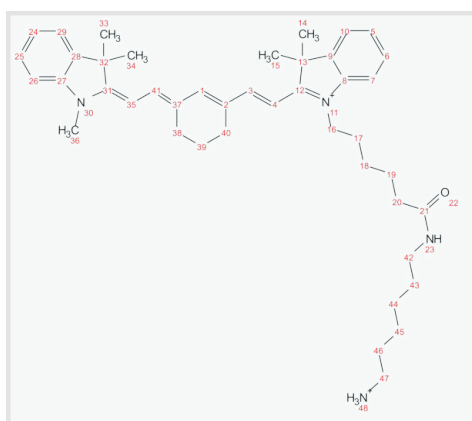


FIG. S1. Structure of Cyanine7-amine.

$^1\text{H}$  NMR (600 MHz, DMSO- $d_6$ )  $\delta$ [ppm] : 7.90-7.72 (b, m, 4H, 48-H and 23-H), 7.72 – 7.64 (m, 3H, 1-H, 3-H and 41-H), 7.62-7.17 (m, 8H, 24-H, 25-H, 26-H, 29-H, 5-H, 6-H, 7-H, 10-H), 6.15 (t,  $J = 13.6$  Hz, 2H, 4-H and 35-H), 4.15 – 4.07 (m, 2H, 16-H), 3.62 (s, 3H, 36-H), 2.99 (dt,  $J = 6.6$  Hz, 2H, 42-H), 2.79-2.69 (m, 2H, 47-H), 2.05 (t,  $J = 7.3$  Hz, 2H, 20-H), 1.84 – 1.78 (m, 2H, 39-H), 1.74-1.67 (m, 2H, 17-H), 1.66-1.65 (2s, 12H, 33-H, 34-H, 14-H and 15-H), 1.59-1.46 (m, 4H, 46-H and 19-H), 1.39-1.31 (m, 4H, 18-H and 43-H), 1.31-1.18 (m, 2H, 44-H and 45-H). The assignments were confirmed with 2D-NMR spectra.

MS (ESI,  $m/z$ ) : 324 [ $\text{M}^{2+}$ ], 649 [ $\text{M}+\text{H}^+$ ].

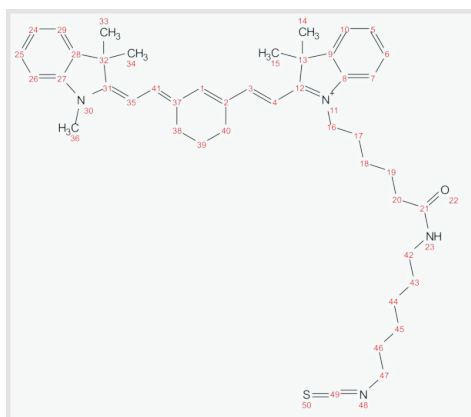


FIG. S2. Structure of ITC.

$^1\text{H}$  NMR (600 MHz, DMSO- $d_6$ )  $\delta$ [ppm] : 7.72 – 7.64 (m, 4H, 23-H, 1-H, 3-H and 41-H), 7.62-7.17 (m, 8H, 24-H, 25-H, 26-H, 29-H, 5-H, 6-H, 7-H, 10-H), 6.15 (t,  $J = 13.6$  Hz, 2H, 4-H and 35-H), 4.15 – 4.05 (m, 2H, 16-H), 3.62 (s, 3H, 36-H), 2.99 (dt,  $J = 6.6$  Hz, 2H, 42-H), 3.64 (t, 2H, 47-H), 2.05 (t,  $J = 7.3$  Hz, 2H, 20-H), 1.84 – 1.78 (m, 2H, 39-H), 1.74-1.67 (m, 2H, 17-H), 1.66-1.65 (2s, 12H, 33-H, 34-H, 14-H and 15-H), 1.59-1.46 (m, 4H, 46-H and 19-H), 1.39-1.31 (m, 4H, 18-H and 43-H), 1.31-1.18 (m, 2H, 44-H and 45-H). The assignments were confirmed with 2D-NMR spectra.

MS (ESI,  $m/z$ ) : 344 [ $\text{M}^{2+}$ ], 689 [ $\text{M}^+$ ], 735 [ $\text{M}-\text{OC}_2\text{H}_5^+$ ].

**FTIR**

Fig. S3 displays FTIR spectra from cyanine7 -amine and ITC. The spectra show the characteristic bands at  $1637\text{ cm}^{-1}$ , due to C=O stretching of carbonyl group, and the band at  $3250\text{ cm}^{-1}$ , attributable to N-H stretching of amine group . Furthermore, both the bands at  $835\text{ cm}^{-1}$ , attributed to (C-S) and  $2099\text{ cm}^{-1}$  (N=C=S).<sup>1</sup>

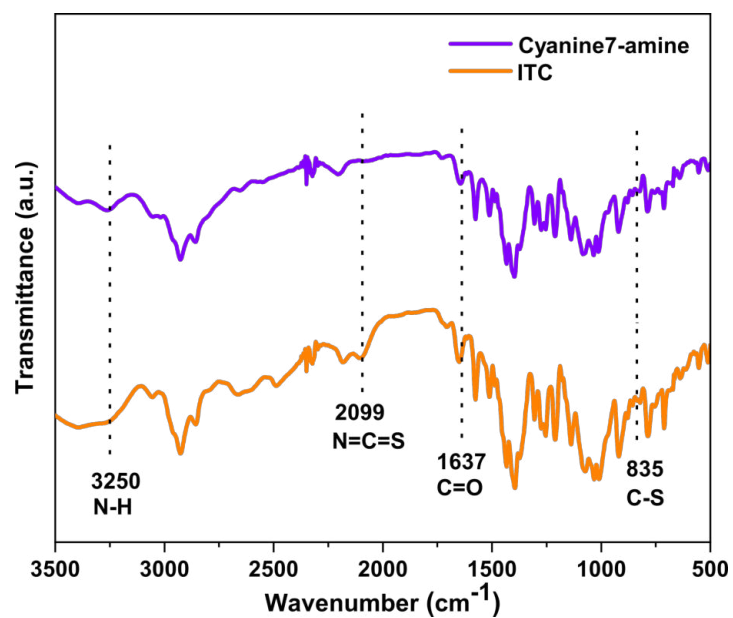


FIG. S3. FTIR spectra of Cyanine7-amine and ITC respectively.

## S2. DYE CONCENTRATION STUDIES

To optimize the ITC concentration range for the experiments with dye-AuNP hybrid systems, the concentration-dependent PL of ITC was investigated. At concentrations exceeding  $3 \mu\text{M}$ , the PL intensity does not scale linearly with concentration due to inner filter effects.

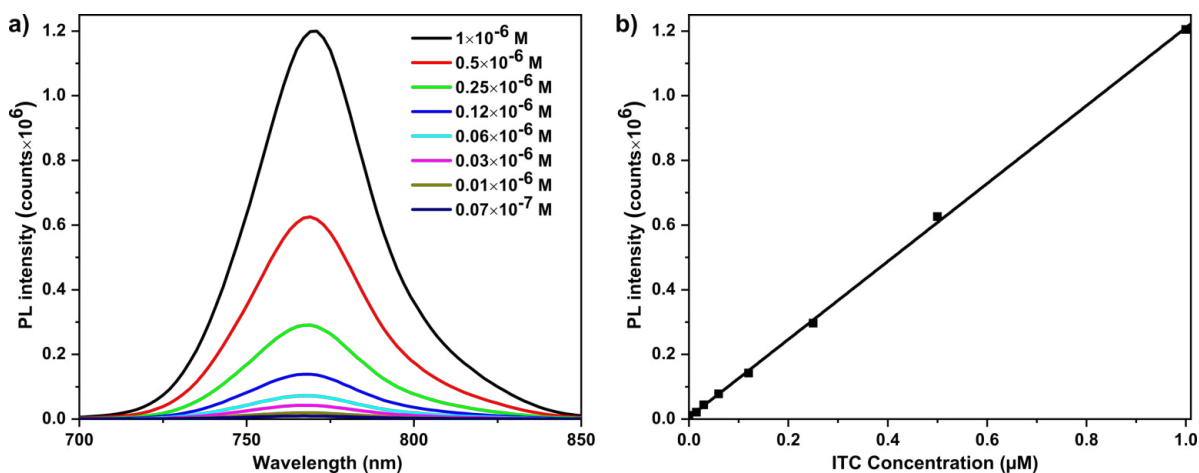


FIG. S4. (a) ITC PL spectra for different concentrations. (b) ITC PL intensity versus concentration (dots). The solid line is a linear fit.

## S3. PL STUDIES

The intensity of the dominant ITC PL peak at 773 nm can be taken as reference for the molar concentration of ITC. Assuming that  $I_o$  is the initial intensity of the pure ITC in ethanol and  $c_o$  is the corresponding initial (known) concentration of ITC, by measuring the final intensity  $I_u$  from the SN, the concentration of unbound ITC molecules  $c_u$  can be calculated from:  $I_o = Kc_o$ ,  $I_u = Kc_u$  and  $c_a = c_o - c_u$ , where  $c_a$  is the concentration of adsorbed molecules and  $K$  is a constant factor determined from the calibration. For the experiments, the AuNPs were centrifuged and the obtained pellets were mixed with ITC. The pellet volumes ( $10 \mu\text{L}$ ) are negligible compared to the total volume of ITC (3 mL) used. Fig. S5 to Figs. S8 summarize the PL study of

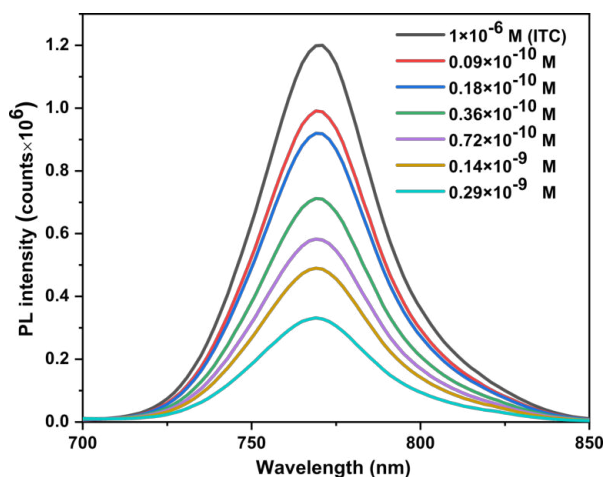


FIG. S5. ITC SN PL spectra ( $1 \times 10^{-6}$  M) for addition of AuNP32@CTAC pellets, doubling the AuNP concentration at each step.

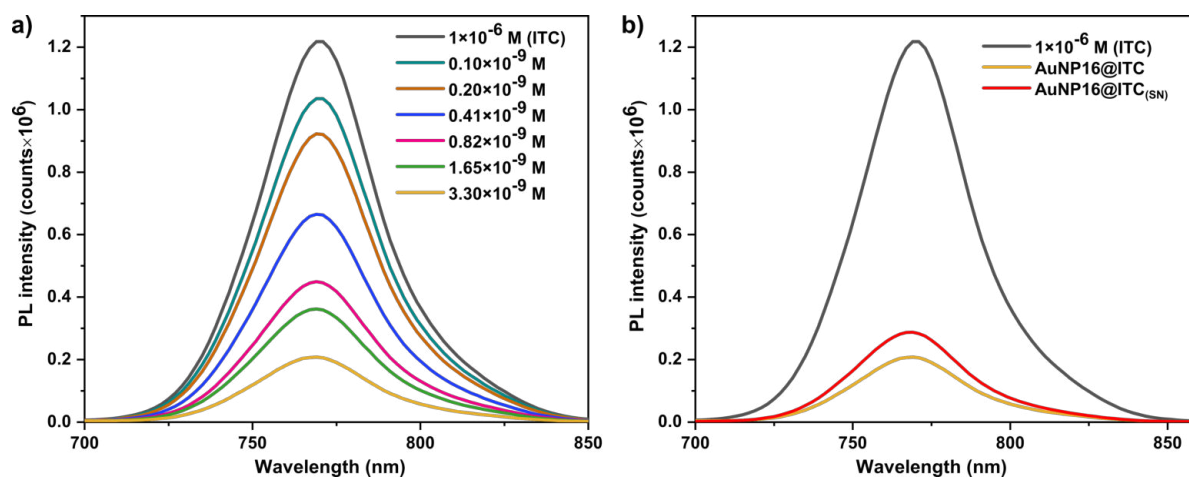


FIG. S6. ITC SN PL spectra ( $1 \times 10^{-6}$  M) (a) with addition of AuNP16@CTAC, doubling the concentration at each step. (b) after addition of AuNP16@CTAC ( $3.3 \times 10^{-9}$  M), and their respective SN.

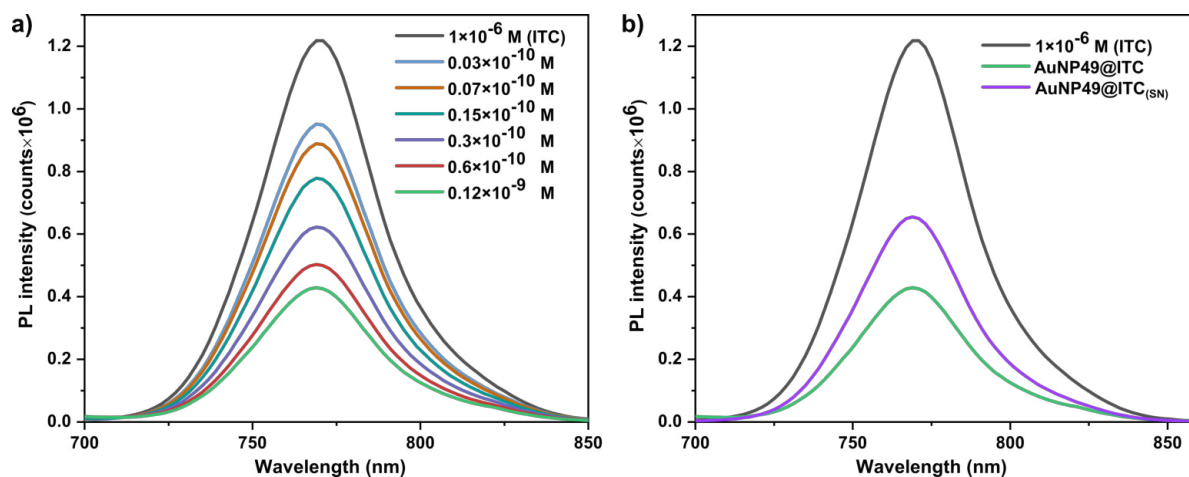


FIG. S7. ITC SN PL spectra ( $1 \times 10^{-6}$  M) (a) with addition of AuNP49@CTAC, doubling the concentration at each step. (b) after addition of AuNP49@CTAC ( $0.12 \times 10^{-9}$  M), and their respective SN.

AuNP16, AuNP32, and AuNP49, which was used as data basis for the calculation of the footprint. The resulting ITC footprints are summarized in tables TABLE T1 and T2.

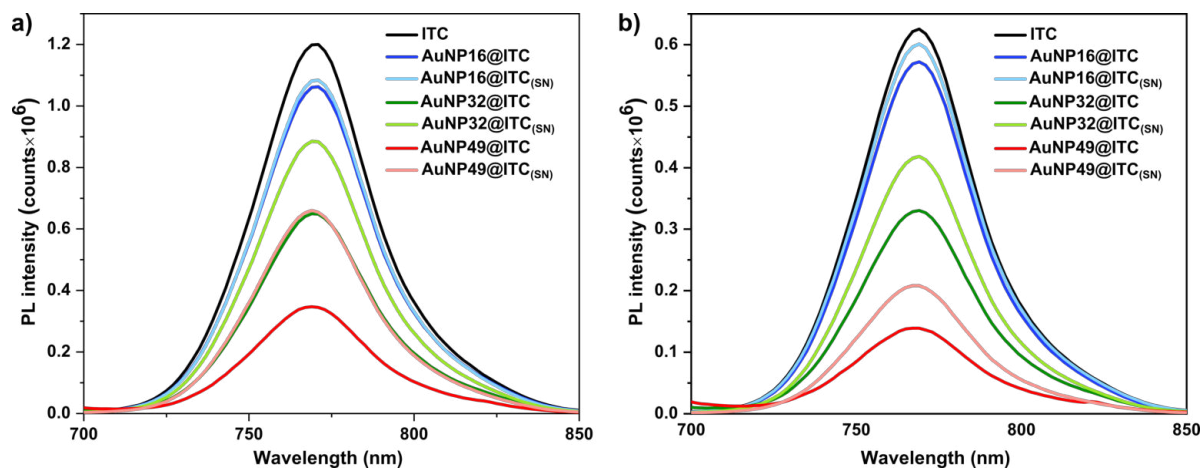


FIG. S8. (a) ITC SN PL spectra ( $1 \times 10^{-6}$  M) after addition of an equal number of AuNPs ( $1.3 \times 10^{11}$ ) for AuNP16, AuNP32 and AuNP49 and their respective SN. (b) ITC SN PL spectra ( $0.5 \times 10^{-6}$  M) after addition of an equal number of AuNPs ( $8.7 \times 10^{10}$ ) for 16 nm, 32 nm and 49 nm and their respective SN.

	16 nm	32 nm	49 nm
Number of ITC molecules per particle	$1061 \pm 92$	$3508 \pm 15$	$7017 \pm 835$
Footprint of ITC molecules ( $\text{nm}^{-2}$ )	$0.8 \pm 0.07$	$0.9 \pm 0.04$	$1.0 \pm 0.03$

TABLE T1. Summary of geometric parameters for ITC binding to AuNPs, calculated for mixing around ( $1.3 \times 10^{11}$ ) AuNPs with ITC ( $1 \times 10^{-6}$  M) (cf. Fig. S8 (a)). Here, the errors in number of dye molecules were estimated on the basis of concentration of AuNPs. To calculate the concentration of AuNPs we have used the mean of concentrations obtained with the methods given by Haiss *et al*<sup>2</sup> and Scarabelli *et al*<sup>3</sup>. The standard deviation in concentration calculation from both the methods are around 8.7% (AuNP16), 0.4% (AuNP32), 11.9% (AuNP49 nm) respectively.

	16 nm	32 nm	49 nm
Number of ITC molecules per particle	$1029 \pm 89$	$3810 \pm 15$	$7242 \pm 861$
Footprint of ITC molecules ( $\text{nm}^{-2}$ )	$0.8 \pm 0.07$	$0.8 \pm 0.01$	$1.0 \pm 0.06$

TABLE T2. Calculation of area occupied by one ITC molecules after mixing ( $8.7 \times 10^{10}$ ) number of nanoparticles with ITC ( $0.5 \times 10^{-6}$  M) (cf. Fig. S8 (b))

#### S4. TA SPECTROSCOPY

We measured TA of cyanine7-amine (Cy7) dye, 20 nm PSSH-coated AuNPs and a mixture (AuNPs were first functionalized with PSSH and then coated with unmodified cyanine7-amine) thereof under both 400 nm and 715 nm excitation (Fig. S9). At 400 nm excitation, the AuNPs show strong absorption due to interband transitions, whereas the cyanine dye hardly absorbs. At 715 nm, the AuNPs absorb very little, whereas the dye shows strong absorption. Under both 400 nm and 715 nm excitation, the TA spectra of the mixture can be described as the sum of the TA spectra of the AuNPs and the dye, being dominated by the AuNPs in case of 400 nm excitation and the dye in case of 715 nm excitation. In both cases, the TA spectra do not show the features observed for the gold-dye hybrid described in the main text. Hence, we conclude that mixing the unfunctionalized dye with PSSH-coated AuNPs does not lead to the strong optical interaction that is observed when modifying the dye and binding it to the AuNPs before the functionalization with PSSH.

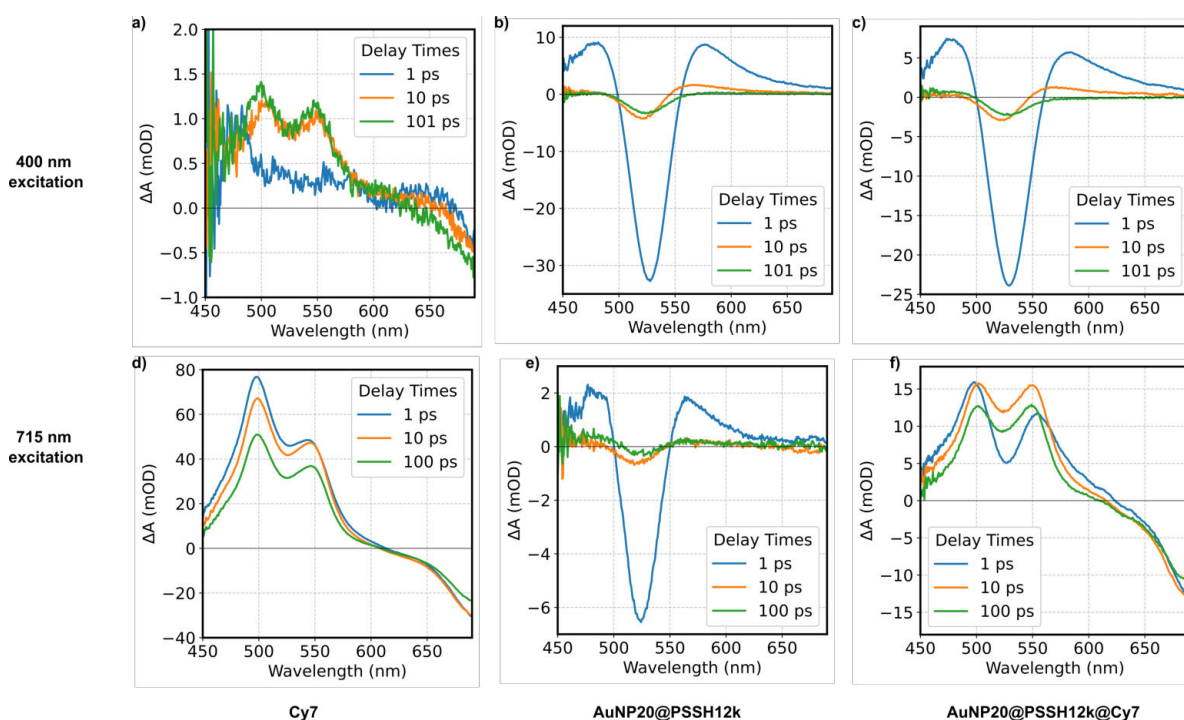
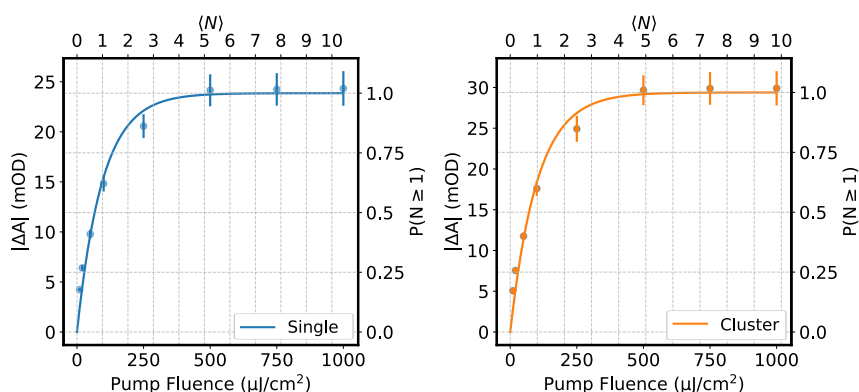


FIG. S9. TA spectra of cyanine7-amine, 20 nm PSSH functionalized AuNP, 20 nm PSSH functionalized AuNP mixed with cyanine7-amine at 400 nm excitation (a,b,c) and 715 nm excitation (d,e,f), respectively.

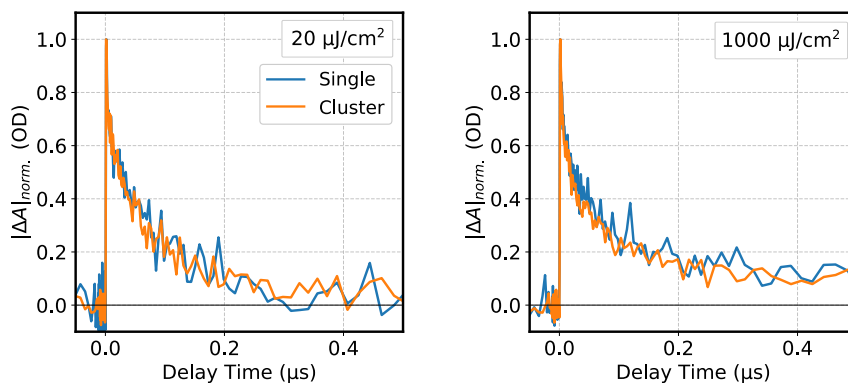
#### REFERENCES

- <sup>1</sup>D. Wiles, B. Gingras, and T. Suprunchuk, "The c=s stretching vibration in the infrared spectra of some thiosemicarbazones," *Canadian Journal of Chemistry*, vol. 45, no. 5, pp. 469–473, 1967.
- <sup>2</sup>W. Haiss, N. T. Thanh, J. Aveyard, and D. G. Fernig, "Determination of size and concentration of gold nanoparticles from uv-vis spectra," *Analytical chemistry*, vol. 79, no. 11, pp. 4215–4221, 2007.
- <sup>3</sup>L. Scarabelli, A. Sánchez-Iglesias, J. Pérez-Juste, and L. M. Liz-Marzán, "A "tips and tricks" practical guide to the synthesis of gold nanorods," 2015.

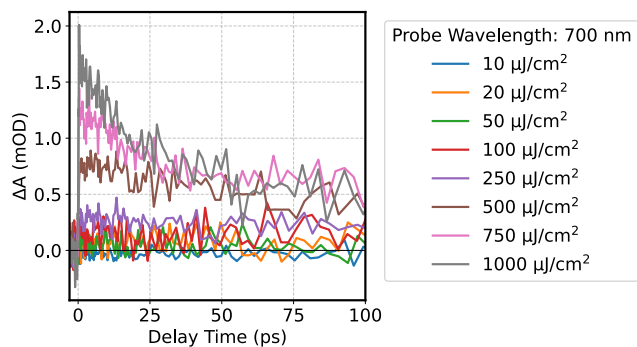
## A.6 Supporting information for Chapter 6.2



**Figure A7:** Poisson evaluation of the excitation statistics of single and clustered QDs. The determined absorption cross sections are  $(5.2 \pm 0.6) 10^{15} \text{ cm}^2$  and  $(4.9 \pm 0.5) 10^{15} \text{ cm}^2$  for single and clustered QDs, respectively.



**Figure A8:** Long delay time TA data of single and clustered QDs after excitation with 400 nm, probed at the CdSe GSB (615 nm probe wavelength). At both low and high pump fluences, the GSB recovery dynamics of the two samples coincide.







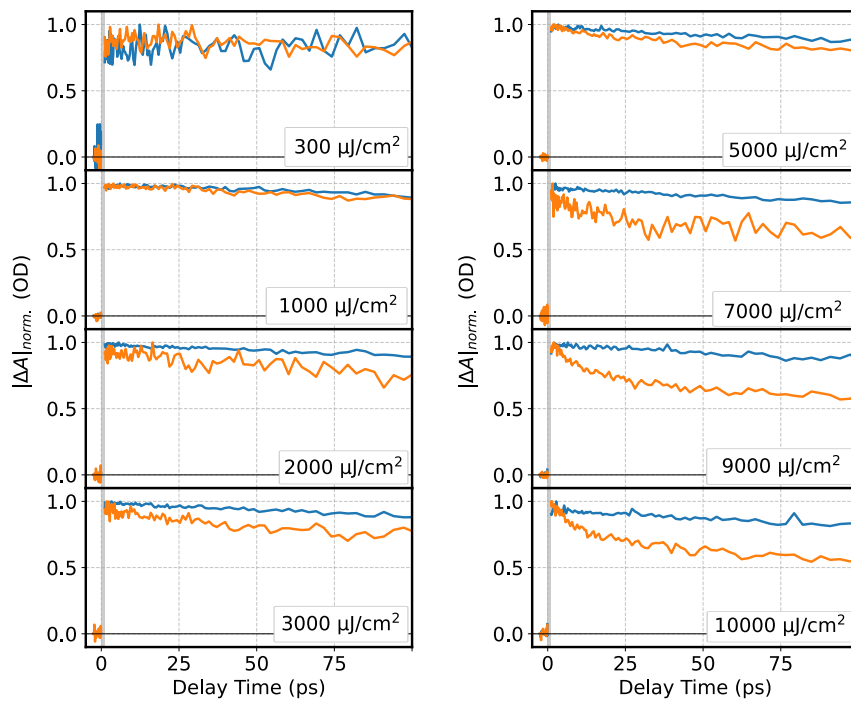









**Figure A9:** TA dynamics of the surface-trapped hole induced PIA in single QDs after 400 nm excitation, probed at 700 nm. For high excitation fluences, a picosecond decay component is observed.





**Figure A10:** TA dynamics of the CdSe GSB recovery in single and clustered QDs after core excitation (570 nm excitation), probed at 615 nm. Similar behavior as for the shell excitation at 400 nm is found. At low excitation fluences, no difference in the GSB recovery is observed. However, at high excitation fluences, the clustered QDs show an additional picosecond decay component that can be fitted with a single-exponential function, yielding a time constant of 18 ps.

## A.7 List of chemicals

Chemical	GHS pictogram	Hazard statements (H...)	Precautionary statements (P...)
11-Mercapto-undecanoic acid		315, 319, 335	261, 264, 271, 208, 302 + 352, 305 + 351 + 338
Acetone	 	225, 319, 336, EUH066	210, 240, 305 + 351 + 338, 403 + 233
Cadmium selenide	  	301 + 331, 312, 350, 373, 410	201, 261, 273, 301 + 310 + 330, 308 + 313, 403 + 233
Cadmium selenide, cadmium sulfide	  	302, 341, 350, 361, 372, 410	201, 273, 301 + 312 + 330, 308 + 313, 501
Cetrimonium bromide	   	302, 315, 318, 335, 373, 410	273, 280, 301 + 312, 302 + 352, 305 + 351 + 338, 314

A.7. List of chemicals

Chemical	GHS pictogram	Hazard statements (H...)	Precautionary statements (P...)
Cetrimonium chloride	  	302, 311, 314, 410	280, 301 + 330 + 331, 303 + 361 + 353, 305 + 351 + 338
Ethanol	 	225, 319	210, 233, 305 + 351 + 338
Hexane	   	225, 304, 315, 336, 361f, 373, 411	202, 280, 303 + 361 + 353, 304 + 340, 308 + 313
Isopropyl alcohol	 	225, 319, 336	210, 261, 312, 370 + 378, 403 + 233, 403 + 235, 501
Methanol	  	225, 301 + 311 + 331, 370	210, 270, 280, 303 + 361 + 353, 304 + 340, 308 + 311
Potassium hydroxide	 	290, 302, 314	280, 303 + 361 + 353, 305 + 351 + 338, 310














Chemical	GHS pictogram	Hazard statements (H...)	Precautionary statements (P...)
Sodium borohydrate	   	260, 301, 314, 360F, EUH014	201, 231 + 232, 280, 308 + 313, 370 + 378, 402 + 404
Sodium sulfide	 	290, 301 + 311, 314	260, 280, 301 + 310, 302 + 352, 303 + 361 + 353, 305 + 351 + 338
Tetrachloroauric(III) acid	   	290, 302, 314, 373, 411	260, 273, 280, 303 + 361 + 353, 305 + 351 + 338, 314
Toluene	  	225, 304, 315, 336, 361d, 373	210, 240, 301 + 310 + 330, 302 + 352, 314, 403 + 233

Table A.1: GHS information of the chemicals used in this work

Table A.2: All H, EUH, and P Statements.

<b>Identifier</b>	<b>Statement</b>
H200	Unstable explosives.
H201	Explosive; mass explosion hazard.
H202	Explosive, severe projection hazard.
H203	Explosive; fire, blast or projection hazard.
H204	Fire or projection hazard.
H205	May mass explode in fire.
H220	Extremely flammable gas.
H221	Flammable gas.
H222	Extremely flammable aerosol.
H223	Flammable aerosol.
H224	Extremely flammable liquid and vapour.
H225	Highly flammable liquid and vapour.
H226	Flammable liquid and vapour.
H228	Flammable solid.
H240	Heating may cause an explosion.
H241	Heating may cause a fire or explosion.
H242	Heating may cause a fire.
H250	Catches fire spontaneously if exposed to air.
H251	Self-heating: may catch fire.
H252	Self-heating in large quantities; may catch fire.
H260	In contact with water releases flammable gases which may ignite spontaneously.
H261	In contact with water releases flammable gases.
H270	May cause or intensify fire; oxidiser.
H271	May cause fire or explosion; strong oxidiser.
H272	May intensify fire; oxidiser.
H280	Contains gas under pressure; may explode if heated.
H281	Contains refrigerated gas; may cause cryogenic burns or injury.
H290	May be corrosive to metals.
H300	Fatal if swallowed.
H301	Toxic if swallowed.
H302	Harmful if swallowed.
H304	May be fatal if swallowed and enters airways.
H310	Fatal in contact with skin.

*continues on next page*

<b>Identifier</b>	<b>Statement</b>
H311	Toxic in contact with skin.
H312	Harmful in contact with skin.
H314	Causes severe skin burns and eye damage.
H315	Causes skin irritation.
H317	May cause an allergic skin reaction.
H318	Causes serious eye damage.
H319	Causes serious eye irritation.
H330	Fatal if inhaled.
H331	Toxic if inhaled.
H332	Harmful if inhaled.
H334	May cause allergy or asthma symptoms or breathing difficulties if inhaled.
H335	May cause respiratory irritation.
H336	May cause drowsiness or dizziness.
H340	May cause genetic defects.
H341	Suspected of causing genetic defects.
H350	May cause cancer.
H351	Suspected of causing cancer.
H360	May damage fertility or the unborn child.
H361	Suspected of damaging fertility or the unborn child.
H362	May cause harm to breast-fed children.
H370	Causes damage to organs.
H371	May cause damage to organs.
H372	Causes damage to organs through prolonged or repeated exposure.
H373	May cause damage to organs through prolonged or repeated exposure.
H400	Very toxic to aquatic life.
H410	Very toxic to aquatic life with long lasting effects.
H411	Toxic to aquatic life with long lasting effects.
H412	Harmful to aquatic life with long lasting effects.
H413	May cause long lasting harmful effects to aquatic life.
H350i	May cause cancer by inhalation.
H360F	May damage fertility.
H360D	May damage the unborn child.
H361f	Suspected of damaging fertility.

*continues on next page*

<b>Identifier</b>	<b>Statement</b>
H361d	Suspected of damaging the unborn child.
H360FD	May damage fertility. May damage the unborn child.
H361fd	Suspected of damaging fertility. Suspected of damaging the unborn child.
H360Fd	May damage fertility. Suspected of damaging the unborn child.
H360Df	May damage the unborn child. Suspected of damaging fertility.
EUH001	Explosive when dry.
EUH006	Explosive with or without contact with air.
EUH014	Reacts violently with water.
EUH018	In use may form flammable/explosive vapour-air mixture.
EUH019	May form explosive peroxides.
EUH044	Risk of explosion if heated under confinement.
EUH029	Contact with water liberates toxic gas.
EUH031	Contact with acids liberates toxic gas.
EUH032	Contact with acids liberates very toxic gas.
EUH066	Repeated exposure may cause skin dryness or cracking.
EUH070	Toxic by eye contact.
EUH071	Corrosive to the respiratory tract.
EUH059	Hazardous to the ozone layer.
EUH201	Contains lead. Should not be used on surfaces liable to be chewed or sucked by children.
EUH201A	Warning! contains lead.
EUH202	Cyanoacrylate. Danger. Bonds skin and eyes in seconds. Keep out of the reach of children.
EUH203	Contains chromium (VI). May produce an allergic reaction.
EUH204	Contains isocyanates. May produce an allergic reaction.
EUH205	Contains epoxy constituents. May produce an allergic reaction.
EUH206	Warning! Do not use together with other products. May release dangerous gases (chlorine).
EUH207	Warning! Contains cadmium. Dangerous fumes are formed during use. See information supplied by the manufacturer. Comply with the safety instructions.
EUH208	Contains <i>&lt;name of sensitising substance&gt;</i> . May produce an allergic reaction.
EUH209	Can become highly flammable in use.
EUH209A	Can become flammable in use.
EUH210	Safety data sheet available on request.

*continues on next page*

<b>Identifier</b>	<b>Statement</b>
EUH401	To avoid risks to human health and the environment, comply with the instructions for use.
P101	If medical advice is needed, have product container or label at hand.
P102	Keep out of reach of children.
P103	Read label before use.
P201	Obtain special instructions before use.
P202	Do not handle until all safety precautions have been read and understood.
P210	Keep away from heat/sparks/open flames/hot surfaces. — No smoking.
P211	Do not spray on an open flame or other ignition source.
P220	Keep/Store away from clothing/. . . /combustible materials.
P221	Take any precaution to avoid mixing with combustibles . . .
P222	Do not allow contact with air.
P223	Keep away from any possible contact with water, because of violent reaction and possible flash fire.
P230	Keep wetted with . . .
P231	Handle under inert gas.
P232	Protect from moisture.
P233	Keep container tightly closed.
P234	Keep only in original container.
P235	Keep cool.
P240	Ground/bond container and receiving equipment.
P241	Use explosion-proof electrical/ventilating/lighting/. . . equipment.
P242	Use only non-sparking tools.
P243	Take precautionary measures against static discharge.
P244	Keep reduction valves free from grease and oil.
P250	Do not subject to grinding/shock/. . . /friction.
P251	Pressurized container: Do not pierce or burn, even after use.
P260	Do not breathe dust/fume/gas/mist/vapours/spray.
P261	Avoid breathing dust/fume/gas/mist/vapours/spray.
P262	Do not get in eyes, on skin, or on clothing.
P263	Avoid contact during pregnancy/while nursing.
P264	Wash . . . thoroughly after handling.
P270	Do not eat, drink or smoke when using this product.

*continues on next page*



<b>Identifier</b>	<b>Statement</b>
P271	Use only outdoors or in a well-ventilated area.
P272	Contaminated work clothing should not be allowed out of the workplace.
P273	Avoid release to the environment.
P280	Wear protective gloves/protective clothing/eye protection/face protection.
P281	Use personal protective equipment as required.
P282	Wear cold insulating gloves/face shield/eye protection.
P283	Wear fire/flame resistant/retardant clothing.
P284	Wear respiratory protection.
P285	In case of inadequate ventilation wear respiratory protection.
P231 + P232	Handle under inert gas. Protect from moisture.
P235 + P410	Keep cool. Protect from sunlight.
P301	IF SWALLOWED:
P302	IF ON SKIN:
P303	IF ON SKIN (or hair):
P304	IF INHALED:
P305	IF IN EYES:
P306	IF ON CLOTHING:
P307	IF exposed:
P308	IF exposed or concerned:
P309	IF exposed or if you feel unwell:
P310	Immediately call a POISON CENTER or doctor/physician.
P311	Call a POISON CENTER or doctor/physician.
P312	Call a POISON CENTER or doctor/physician if you feel unwell.
P313	Get medical advice/attention.
P314	Get medical advice/attention if you feel unwell.
P315	Get immediate medical advice/attention.
P320	Specific treatment is urgent (see . . . on this label).
P321	Specific treatment (see . . . on this label).
P322	Specific measures (see . . . on this label).
P330	Rinse mouth.
P331	Do NOT induce vomiting.
P332	If skin irritation occurs:
P333	If skin irritation or rash occurs:
P334	Immerse in cool water/wrap in wet bandages.

*continues on next page*

<b>Identifier</b>	<b>Statement</b>
P335	Brush off loose particles from skin.
P336	Thaw frosted parts with lukewarm water. Do not rub affected area.
P337	If eye irritation persists:
P338	Remove contact lenses, if present and easy to do. Continue rinsing.
P340	Remove victim to fresh air and keep at rest in a position comfortable for breathing.
P341	If breathing is difficult, remove victim to fresh air and keep at rest in a position comfortable for breathing.
P342	If experiencing respiratory symptoms:
P350	Gently wash with plenty of soap and water.
P351	Rinse cautiously with water for several minutes.
P352	Wash with plenty of soap and water.
P353	Rinse skin with water/shower.
P360	Rinse immediately contaminated clothing and skin with plenty of water before removing clothes.
P361	Remove/Take off immediately all contaminated clothing.
P362	Take off contaminated clothing and wash before reuse.
P363	Wash contaminated clothing before reuse.
P370	In case of fire:
P371	In case of major fire and large quantities:
P372	Explosion risk in case of fire.
P373	DO NOT fight fire when fire reaches explosives.
P374	Fight fire with normal precautions from a reasonable distance.
P375	Fight fire remotely due to the risk of explosion.
P376	Stop leak if safe to do so.
P377	Leaking gas fire: Do not extinguish, unless leak can be stopped safely.
P378	Use . . . for extinction.
P380	Evacuate area.
P381	Eliminate all ignition sources if safe to do so.
P390	Absorb spillage to prevent material damage.
P391	Collect spillage.
P301 + P310	IF SWALLOWED: Immediately call a POISON CENTER or doctor/physician.

*continues on next page*

<b>Identifier</b>	<b>Statement</b>
P301 + P312	IF SWALLOWED: Call a POISON CENTER or doctor/physician if you feel unwell.
P301 + P330 + P331	IF SWALLOWED: rinse mouth. Do NOT induce vomiting.
P302 + P334	IF ON SKIN: Immerse in cool water/wrap in wet bandages.
P302 + P350	IF ON SKIN: Gently wash with plenty of soap and water.
P302 + P352	IF ON SKIN: Wash with plenty of soap and water.
P303 + P361 + P353	IF ON SKIN (or hair): Remove/Take off immediately all contaminated clothing. Rinse skin with water/shower.
P304 + P340	IF INHALED: Remove victim to fresh air and keep at rest in a position comfortable for breathing.
P304 + P341	IF INHALED: If breathing is difficult, remove victim to fresh air and keep at rest in a position comfortable for breathing.
P305 + P351 + P338	IF IN EYES: Rinse cautiously with water for several minutes. Remove contact lenses, if present and easy to do. Continue rinsing.
P306 + P360	IF ON CLOTHING: Rinse immediately contaminated clothing and skin with plenty of water before removing clothes.
P307 + P311	IF exposed: Call a POISON CENTER or doctor/physician.
P308 + P313	IF exposed or concerned: Get medical advice/attention.
P309 + P311	IF exposed or if you feel unwell: Call a POISON CENTER or doctor/physician.
P332 + P313	If skin irritation occurs: Get medical advice/attention.
P333 + P313	If skin irritation or rash occurs: Get medical advice/attention.
P335 + P334	Brush off loose particles from skin. Immerse in cool water/wrap in wet bandages.
P337 + P313	If eye irritation persists: Get medical advice/attention.
P342 + P311	If experiencing respiratory symptoms: Call a POISON CENTER or doctor/physician.
P370 + P376	In case of fire: Stop leak if safe to do so.
P370 + P378	In case of fire: Use . . . for extinction.
P370 + P380	In case of fire: Evacuate area.
P370 + P380 + P375	In case of fire: Evacuate area. Fight fire remotely due to the risk of explosion.
P371 + P380 + P375	In case of major fire and large quantities: Evacuate area. Fight fire remotely due to the risk of explosion.
P401	Store . . .
P402	Store in a dry place.
P403	Store in a well-ventilated place.

*continues on next page*

---

<b>Identifier</b>	<b>Statement</b>
P404	Store in a closed container.
P405	Store locked up.
P406	Store in corrosive resistant/. . . container with a resistant inner liner.
P407	Maintain air gap between stacks/pallets.
P410	Protect from sunlight.
P411	Store at temperatures not exceeding °C/°F.
P412	Store at temperatures not exceeding 50 °C/122 °F.
P413	Store bulk masses greater than kg/lbs at temperatures not exceeding °C/°F.
P420	Store away from other materials.
P422	Store contents under . . .
P402 + P404	Store in a dry place. Store in a closed container.
P403 + P233	Store in a well-ventilated place. Keep container tightly closed.
P403 + P235	Store in a well-ventilated place. Keep cool.
P410 + P403	Protect from sunlight. Store in a well-ventilated place.
P410 + P412	Protect from sunlight. Do not expose to temperatures exceeding 50 °C/122 °F.
P411 + P235	Store at temperatures not exceeding °C/°F. Keep cool.
P501	Dispose of contents/container to . . .

---

## A.8 List of abbreviations

AuNPs	gold nanoparticles
CB	conduction band
CPA	chirped-pulse amplification
DC	direct current
DFG	difference frequency generation
DR	dot-in-rod nanoparticle
EOS	electro-optical sampling
FWHM	full width at half maximum
GSB	ground-state bleach
HOMO	highest occupied molecular orbital
IR	infrared
LSPR	localized surface plasmon resonance
LUMO	lowest unoccupied molecular orbital
LED	light-emitting diode
ML	monolayer
MUA	11-mercaptoundecanoic acid
NC	nanocrystal
NIR	near-infrared
NR	nanorod
OAP	off-axis parabolic mirror
OPA	optical parametric amplifier
OPTP	optical-pump-terahertz-probe
OSE	optical Stark effect
PIA	photoinduced absorption
PL	photoluminescence
QD	quantum dot
QCSE	quantum-confined Stark effect
SHG	second-harmonic generation
SFG	sum frequency generation
SPM	self-phase modulation
TA	transient absorption
TEM	transmission electron microscopy
THz	terahertz
THz-TDS	terahertz time domain spectroscopy
TPOP	terahertz-pump-optical-probe
TTM	two-temperature model
VB	valence band
vis	visible
XPM	cross-phase modulation

## A.9 List of Figures

2.1	Generation of laser pulses by mode-locking . . . . .	6
2.2	Schematic time evolution of linearly chirped pulses. . . . .	7
2.3	Schematic of the TA setup used in this thesis . . . . .	9
2.4	Exemplary TA data of CdSe-CdS QDs . . . . .	10
2.5	Temporal overlap of fs- and $\mu$ s-TA. . . . .	11
2.6	THz generation <i>via</i> optical rectification . . . . .	13
2.7	Schematic representation of an EOS-setup . . . . .	13
2.8	Reconstruction of the electric field of a THz pulse using EOS . . . . .	14
2.9	Exemplary THz-TDS data . . . . .	16
2.10	Schematic representation of a THz-TDS and OPTP-setup . . . . .	17
2.11	Exemplary OPTP data . . . . .	18
2.12	Simulated OPTP data and its Fourier transform . . . . .	20
2.13	Drude photoconductivity in the THz frequency range . . . . .	21
2.14	Lorentz-Drude photoconductivity in the THz frequency range . . . . .	21
3.1	Real and imaginary part of the dielectric function of gold . . . . .	24
3.2	Schematic depiction of the different types of plasmons . . . . .	25
3.3	Exemplary TEM image of AuNPs . . . . .	26
3.4	Simulated and experimental absorption spectra of AuNPs. . . . .	27
3.5	Schematic depiction of the processes following LSPR excitation . . . . .	30
3.6	Measured and calculated differential absorption of AuNPs. . . . .	31
3.7	Landau damping and interband excitation in AuNPs . . . . .	32
3.8	Comparison of experimental TA data of AuNPs and the two-temperature model . . . . .	35
3.9	Breathing oscillation and phonon-phonon coupling in 16 nm AuNPs . . . . .	35
4.1	Absorption in bulk direct-band-gap semiconductors. . . . .	38
4.2	Discrete energy levels in semiconductor NCs. . . . .	39
4.3	Absorption in semiconductor NCs. . . . .	39
4.4	Exemplary TEM images of the 0D, 1D and 2D semiconductor NCs studied in this thesis. . . . .	40
4.5	Heterostructures and their band alignment . . . . .	41
4.6	Contrast giving mechanisms in TA experiments of semiconductor NCs . . . . .	43
4.7	Exemplary absorption and differential absorption spectrum of 3 nm CdSe QDs. . . . .	44
4.8	Poisson distributed excitation in semiconductor NCs . . . . .	44
4.9	Schematic overview over the processes happening in semiconductor NCs after light absorption. . . . .	46
4.10	Carrier cooling in semiconductor NCs . . . . .	47
4.11	Charge trapping in semiconductor NCs . . . . .	47
4.12	Charge localization in semiconductor NCs . . . . .	49
4.13	Auger recombination in semiconductor NCs . . . . .	50
4.14	Exciton polarizability probed by OPTP . . . . .	52

4.15	Overview over OPTP spectroscopic studies of ensembles of semiconductor NCs . . . . .	54
6.1	TEM and UV-vis of 3 ML CdSe nanoplatelets. . . . .	120
6.2	THz pulse employed for the TPOP measurements . . . . .	120
6.3	TPOP data of CdSe nanoplatelets . . . . .	122
6.4	TPOP data of CdSe nanoplatelets compared to the temporal THz intensity and TA data of the sample . . . . .	123
6.5	OSE in CdSe nanoplatelets induced by sub-band-gap visible and NIR excitation. . . . .	124
6.6	Absorption and differential absorption of the CdSe nanoplatelets with different excitation sources . . . . .	125
6.7	TEM and UV-vis of the studied giant-shell QDs . . . . .	127
6.8	PL spectra of single and clustered QDs . . . . .	128
6.9	TA data of single and clustered QDs at low and high excitation densities . . . . .	130
6.10	CdSe GSB recovery dynamics of single and clustered QDs at several excitation densities. . . . .	131
6.11	TA spectra of single and clustered QDs at long probe wavelengths . . . . .	131
6.12	Biexcitonic shift feature in the TA measurement of clustered QDs. . . . .	132
A1	XPM-induced coherent artifacts in TA . . . . .	158
A2	Coherent artifact in TA with different experimental conditions. . . . .	159
A3	Visual representation of chirp in TA . . . . .	159
A4	Chirp correction in TA . . . . .	160
A5	Linear chirp in TA . . . . .	160
A6	Absolute $\Delta A$ signal of the coherent artifact with its temporal envelope and the Gaussian fit . . . . .	161
A7	Poisson statistic of single and clustered QDs . . . . .	204
A8	Long delay time TA of single and clustered QDs. . . . .	204
A9	Dynamics of the surface-trapped hole induced PIA in single QDs. . . . .	204
A10	TA dynamics of single and clustered QDs after core excitation. . . . .	205





# Acknowledgements

This work would not have been possible without the help of others. Therefore, I thank . . .

. . . Holger Lange for his steady support throughout the four years of my PhD time.

. . . the members of the Lange research group, namely Dominik Höing, Florian Schulz, Michael Deffner, Sandra Zech, Shivani Kesarwani, Nour El Houda Chetoui, Claudio Pineda-Bosque and the students I worked with.

. . . the Research Training Group Nanohybrid for funding, its members for scientific support, Andreas Kolditz and Corinna Flügge for their help with all bureaucratic matters, and Vincent Mittag for his openness.

. . . the staff of the analytical and scientific services of the Department of Chemistry of the Universität Hamburg, namely Andrea Köppen, Robert Schön, Stefan Werner, Charlotte Ruhmlieb and Isabelle Nevoigt as well as Jan Flügge und Christian Strelow for their technical support.

. . . our collaboration partners at Universität Potsdam, Technische Universität Berlin, Freie Universität Berlin, Universiteit Gent, Technische Universität Wien and the Centre for Free-Electron Laser Science.

. . . all co-authors of the presented publications.

. . . Sönke Wengler-Rust, Artur Feld, Agnes Weimer, Sonja Krohn, Julia Funk, Finn Dobschall and Sophia Bittinger, who provided samples for various experiments.

Außerdem danke ich . . .

. . . meiner Familie, allen voran meiner Mutter, für die Unterstützung während der Zeit meines Bachelor-, Master- sowie Promotionsstudiums.

. . . meinen Sportteam für die Ablenkung vom Uni-Alltag.

. . . Nelly für ihre bedingungslose Unterstützung. Danke, dass du auch während der schweren Phasen der letzten Jahre für mich da warst. <3



# Eidesstattliche Versicherung

Hiermit versichere ich an Eides statt, die vorliegende Dissertationsschrift selbst verfasst und keine anderen als die angegebenen Quellen und Hilfsmittel benutzt zu haben. Sofern im Zuge der Erstellung der vorliegenden Dissertationsschrift generative Künstliche Intelligenz (gKI) basierte elektronische Hilfsmittel verwendet wurden, versichere ich, dass meine eigene Leistung im Vordergrund stand und dass eine vollständige Dokumentation aller verwendeten Hilfsmittel gemäß der Guten wissenschaftlichen Praxis vorliegt. Ich trage die Verantwortung für eventuell durch die gKI generierte fehlerhafte oder verzerrte Inhalte, fehlerhafte Referenzen, Verstöße gegen das Datenschutz- und Urheberrecht oder Plagiate.

Hamburg, den 23.07.2024

A handwritten signature in black ink, appearing to read 'J. Stachel', followed by a long horizontal flourish line.